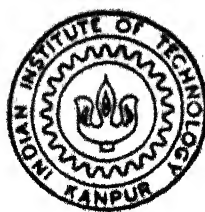


PHASE EQUILIBRIA AND STRUCTURAL STUDIES  
OF BORON-FREE AND BORON-DOPED  $\text{Ni}_3\text{Al}$   
AND  $\text{Ni}_3\text{Al}$  CONTAINING HAFNIUM

by  
R. R. NAGARAJAN



MME

1994

D

NAG

PHA

DEPARTMENT OF MATERIALS AND METALLURGICAL ENGINEERING

INDIAN INSTITUTE OF TECHNOLOGY KANPUR

April 1994

PHASE EQUILIBRIA AND STRUCTURAL STUDIES OF  
BORON-FREE AND BORON-DOPED  $\text{Ni}_3\text{Al}$  AND  
 $\text{Ni}_3\text{Al}$  CONTAINING HAFNIUM

*A Thesis Submitted*  
*in Partial fulfilment of the Requirements*  
*for the Degree of*  
DOCTOR OF PHILOSOPHY

*by*  
R. R. NAGARAJAN

*to the*  
DEPARTMENT OF MATERIALS AND METALLURGICAL ENGINEERING  
INDIAN INSTITUTE OF TECHNOLOGY KANPUR

APRIL, 1994

27 JUN 1996

CENTRAL LIBRARY  
I. I. T., KANPUR

Acc. No. A. 121716

MME-1994-D-NAG-PHA




A121716


## CERTIFICATE

15/4/94

It is certified that the work contained in the thesis entitled "PHASE EQUILIBRIA AND STRUCTURAL STUDIES OF BORON-FREE AND BORON-DOPED  $\text{Ni}_3\text{Al}$  AND  $\text{Ni}_3\text{Al}$  CONTAINING HAFNIUM", by R. R. Nagarajan, has been carried out under our supervision and that this work has not been submitted elsewhere for a degree.

  
(Dr. R.K. Ray)

Professor

  
(Dr. A.K. Jena)

Professor

Department of Materials and Metallurgical Engineering

Indian Institute of Technology

Kanpur



## ACKNOWLEDGEMENTS

It is my pleasant privilege to express my deep and sincere sense of gratitude and lasting indebtedness to my supervisors, Prof. A. K. Jena and Prof. R. K. Ray for their immense help and valuable guidance at all stages of this investigation. It was a great pleasure working under their guidance.

I express my deep gratitude to Prof. K. P. Gupta for giving valuable suggestions during the course of this investigation. With great sense of regard I express my gratitude to Dr. R. Balasubramaniam for allowing me to use his laboratory facilities. I express my sincere gratitude to all the Faculty members of IIT Kanpur who have taught me various courses during my academic programme.

I warmly acknowledge the everwilling cooperation extended to me by my friends Mr. M. N. Mungole, Mr. Banu P. Babu, Mr. S. G. Choudhury and Mr. Ashvini Gaur.

My sincere thanks are due to M/s V. Kumar, H. C. Srivastava, K. P. Mukherjee, Uma Shankar, V. P. Gupta, P. K. Pal, U. S. Lal, B. K. Jain and S. C. Bharthwal for their kind assistance. I am very much thankful to my friends Mr. Vijayan Rajan, Mr. Pandimani, Mr. Sampath, Mr. Padmanabhan, Mr. Biragi, Mr. Sanjay Nath, Mr. K. S. Rao and Mr. Vivek for their so kind help on many occasions.

I sincerely thank Mr. G. S. Thapa for his excellent drafting work.

Finally I express my gratitude to the Department of Science and Technology, Government of India, for financial support and the Defence Metallurgical Research Laboratory, Hyderabad, India for providing the material.

R. R. Nagarajan

# CONTENTS

	<u>Page</u>
LIST OF FIGURES	x
LIST OF TABLES	xix
ABSTRACT	xxi
CHAPTER I INTRODUCTION	1
CHAPTER II LITERATURE REVIEW	5
2.1. BINARY ALLOYS BETWEEN Ni, Al and Hf	5
2.1.1. Ni-Al system	5
2.1.2. Ni-Hf system	7
2.1.3. Al-Hf system	7
2.2. THE TERNARY Ni-Al-Hf SYSTEM	7
2.3. STRUCTURE OF $\gamma'$ ( $\text{Ni}_3\text{Al}$ ) PHASE	12
2.3.1. Unit cell	12
2.3.2. Ordering in $\text{Ni}_3\text{Al}$	13
2.3.3 Lattice parameter	20
2.4. ALLOYING BEHAVIOUR OF SOLUTES	21
2.4.1. Substitutional solutes	21
2.4.2. Interstitial solutes	31
2.4.2.1. Boron	31
2.4.2.2. Other interstitial solutes	33
2.5. DIFFUSION IN BORON-FREE AND BORON-DOPED $\text{Ni}_3\text{Al}$	34
2.6. YIELDING BEHAVIOUR OF $\gamma'$	37
2.6.1. Temperature dependence of yield stress	37
2.6.2. Mechanism of yielding	37
2.6.3. Grain size effect on the yield behaviour	43
2.6.4. Effect of alloy stoichiometry	47
2.6.5. Solid solution strengthening	49

2.7. DUCTILITY	55
2.7.1. Intrinsic brittleness of grain boundaries in $\text{Ni}_3\text{Al}$	55
2.7.2. Effect of boron	57
2.7.3. Mechanism of ductilization by boron	57
2.7.4. Effect of substitutional elements	65
2.7.5. Mechanism of enhanced ductility by substitutional solutes	66
2.7.6. Improvement in the ductility of hyper-stoichiometric alloys	68
2.7.7. Effect of environment and temperature	68
2.8. SUBSTRUCTURE	70
2.9. SCOPE OF THE PRESENT INVESTIGATION	76
CHAPTER III EXPERIMENTAL PROCEDURE	78
3.1. MATERIALS	78
3.2. ALLOY PREPARATION	78
3.3. HOMOGENIZATION	79
3.4. EQUILIBRATION	82
3.5. X-RAY DIFFRACTION	82
3.5.1. Powder sample preparation	82
3.5.2. X-ray diffraction conditions	82
3.6. OPTICAL MICROSCOPY	84
3.7. SCANNING ELECTRON MICROSCOPY	89
3.8. TRANSMISSION ELECTRON MICROSCOPY	89
3.9. HIGH TEMPERATURE COMPRESSION TEST	90

## CHAPTER IV PHASE EQUILIBRIA IN BORON-FREE AND BORON-DOPED

$\gamma'$ -RICH REGION OF THE Ni-Al-Hf SYSTEM	92
4.1. THE TRINICKEL ALUMINIDE $\gamma'$	92
4.1.1. Stoichiometric compound	92
4.1.2. Nickel-rich $\gamma'$ of nominal composition	
$\text{Ni}_{77}\text{Al}_{23}$	94
4.1.3. Aluminium-rich $\gamma'$ of nominal composition	
$\text{Ni}_{73}\text{Al}_{27}$	94
4.2. HAFNIUM CONTAINING TRINICKEL ALUMINIDES	97
4.2.1. Homogenization	97
4.2.2. The alloy of nominal composition	
$\text{Ni}_{75}\text{Al}_{22.5}\text{Hf}_{2.5}$	99
4.2.3. The alloy of nominal composition	
$\text{Ni}_{75}\text{Al}_{20}\text{Hf}_5$	99
4.2.4. The alloy of nominal composition	
$\text{Ni}_{75}\text{Al}_{17.5}\text{Hf}_{7.5}$	101
4.2.5. The alloy of nominal composition	
$\text{Ni}_{77.5}\text{Al}_{20.0}\text{Hf}_{2.5}$	103
4.2.6. The alloy of nominal composition	
$\text{Ni}_{77.5}\text{Al}_{17.5}\text{Hf}_{5.0}$	105
4.2.7. The alloy of nominal composition	
$\text{Ni}_{80.0}\text{Al}_{17.5}\text{Hf}_{2.5}$	105
4.2.8. The alloy of nominal composition	
$\text{Ni}_{80}\text{Al}_{15}\text{Hf}_5$	108
4.2.9. The alloy of nominal composition	
$\text{Ni}_{72.5}\text{Al}_{25.0}\text{Hf}_{2.5}$	108
4.2.10. The alloy of nominal composition	
$\text{Ni}_{72.5}\text{Al}_{22.5}\text{Hf}_{5.0}$	112

4.3. THE $\gamma'$ -RICH REGION OF THE BORON-FREE Ni-Al-Hf SYSTEM	114
4.3.1. Isothermal section	114
4.3.2. Comparison with literature	117
4.4. EFFECT OF BORON ON Ni <sub>3</sub> Al	119
4.4.1. Boron-doped stoichiometric Ni <sub>3</sub> Al	119
4.4.2. Boron-doped off-stoichiometric Ni <sub>3</sub> Al	119
4.5. EFFECT OF BORON ON TRINICKEL ALUMINIDE CONTAINING HAFNIUM	121
4.5.1. Boron-doped alloy of nominal composition Ni <sub>75</sub> Al <sub>22.5</sub> Hf <sub>2.5</sub>	121
4.5.2. Boron-doped alloy of nominal composition Ni <sub>75</sub> Al <sub>20</sub> Hf <sub>5</sub>	123
4.5.3. Boron-doped alloy of nominal composition Ni <sub>75</sub> Al <sub>17.5</sub> Hf <sub>7.5</sub>	123
4.5.4. Boron-doped alloy of nominal composition Ni <sub>72.5</sub> Al <sub>25</sub> Hf <sub>2.5</sub>	126
4.5.5. Boron-doped alloy of nominal composition Ni <sub>72.5</sub> Al <sub>22.5</sub> Hf <sub>5</sub>	126
4.5.6. Boron-doped alloy of nominal composition Ni <sub>70</sub> Al <sub>27.5</sub> Hf <sub>2.5</sub>	128
4.5.7. Boron-doped alloy of nominal composition Ni <sub>70</sub> Al <sub>25</sub> Hf <sub>5</sub>	128
4.5.8. Boron-doped alloy of nominal composition Ni <sub>77.5</sub> Al <sub>20</sub> Hf <sub>2.5</sub>	131
4.5.9. Boron-doped alloy of nominal composition Ni <sub>77.5</sub> Al <sub>17.5</sub> Hf <sub>5.0</sub>	131

4.6. THE $\gamma'$ -RICH REGION OF THE BORON-DOPED Ni-Al-Hf SYSTEM	134
4.6.1. Isothermal section	134
4.6.2. Comparison with boron-free constitutional diagram	137
CHAPTER V STRUCTURAL CHARACTERISTICS OF $\gamma'$	140
5.1. LATTICE PARAMETER	140
5.1.1. Stoichiometric $\gamma'$	140
5.1.2. Off-stoichiometric $\gamma'$	144
5.1.3. Hafnium containing $\gamma'$	145
5.1.4. Effect of boron	148
5.1.5. The $\gamma$ phase coexisting with $\gamma'$	152
5.2. STABILITY	152
5.2.1. Effect of temperature	152
5.2.2. Effect of composition	159
5.2.3. Effect of boron	169
5.2.4. Solute substitution and bonding characteristics	172
5.3. OCCURRENCE OF TWINS	186
5.3.1. Boron-free $\gamma'$	186
5.3.2. Effect of boron	188
5.4. SUBSTRUCTURE OF Ni <sub>3</sub> Al ( $\gamma'$ ) ALLOYS	188
5.4.1. Stoichiometric Ni <sub>3</sub> Al	189
5.4.2. Boron-doped Ni <sub>3</sub> Al	189
5.4.3. Hafnium containing $\gamma'$	193
5.4.4. Boron-doped $\gamma'$ containing hafnium	193
5.4.5. Boron-doped hafnium containing $\gamma'$ -rich alloy having two phase structure	196

Page

5.4.6. Discussion	196
CHAPTER VI MECHANICAL BEHAVIOUR OF $\gamma'$ IN COMPRESSION	200
6.1. INTRODUCTION	200
6.2. DEFORMATION OF STOICHIOMETRIC $\gamma'$	200
6.2.1. Stress-Strain behaviour	200
6.2.2. Effect of boron doping	204
6.3. DEFORMATION OF HAFNIUM-CONTAINING $\gamma'$	206
6.3.1. Stress-Strain behaviour	206
6.3.2. Effect of temperature	206
6.3.3. Effect of hafnium content	211
6.3.4. Effect of boron doping	211
6.4. FRACTURE BEHAVIOUR	211
6.5. DISCUSSION	218
CHAPTER VII SUMMARY AND CONCLUSIONS	222
REFERENCES	228
APPENDIX I	244

## LIST OF FIGURES

	<u>Page</u>
Fig. 2.1: The binary Ni-Al phase diagram [24].	6
Fig. 2.2: The binary Ni-Hf phase diagram [28].	8
Fig. 2.3: The binary Al-Hf phase diagram [33].	8
Fig. 2.4: Ni-Al-Hf 800°C isothermal section [34].	10
Fig. 2.5: Ni-Al-Hf 1200°C partial isothermal section [35].	11
Fig. 2.6: Ni-Al-Hf 1000°C partial isothermal section [35].	11
Fig. 2.7: Unit cell of $\text{Ni}_3\text{Al}$ ( $\text{L1}_2$ structure).	14
Fig. 2.8: Long-range order parameter, S, as a function of temperature for stoichiometric and off-stoichiometric $\text{Ni}_3\text{Al}$ [50].	16
Fig. 2.9: Long-range order parameter, S, as a function of temperature for stoichiometric $\text{Ni}_3\text{Al}$ [51].	18
Fig. 2.10: Long-range order parameter, S, as a function of temperature for stoichiometric $\text{Ni}_3\text{Al}$ (with and without boron). Order parameter, S : without B, $\Delta$ , (100/200); $\blacktriangle$ , (110/220); with B, $\circ$ , (100/200); $\bullet$ , (110/220); $\blacksquare$ , theoretical [54].	19
Fig. 2.11: Long-range order parameter, S, as a function of temperature for Ni-rich off-stoichiometric $\text{Ni}_3\text{Al}$ (with and without boron addition). Order parameter, S: without boron, $\Delta$ , (100/200); $\Delta$ , (110/220); with boron, $\circ$ , (100/200); $\bullet$ , (110/220); $\square$ , theoretical [54].	19
Fig. 2.12: Lattice parameter change in $\text{Ni}_3\text{Al}(\gamma')$ with additions of transition metals [58].	22
Fig. 2.13: The lattice parameter and the lattice strain as a function of the boron concentration in melt-spun $\text{Ni}_3\text{Al}$ . $\circ$ , measured on the wheel-contacting surface of the ribbons; $\square$ , measured on the non contacting surface of the ribbons [59].	23
Fig. 2.14: Lattice parameter of stoichiometric $\text{Ni}_3\text{Al}$ as a function of boron content. The squares and the line connecting them are for furnace-cooled samples. Other points are for air-cooled samples [60].	23
Fig. 2.15: Changes in lattice parameter of the $\text{Ni}_3\text{Al}$ with additions of C, B and Be atoms [52].	24



- Fig. 2.16: Effect of boron and heat treatment on lattice parameters at room temperature in  $\text{Ni}_3\text{Al}$ : (O)  $800^\circ\text{C}/3\text{h}$ ; (■)  $900^\circ\text{C}/5\text{h}$ ; (▲)  $900^\circ\text{C}/5\text{h}+1100^\circ\text{C}/5\text{h}$ ; (●) rapidly solidified material [56]. 24
- Fig. 2.17: Semischematic depiction of the solubility lobes of ternary  $\text{Ni}_3\text{Al}$  phase around  $1000^\circ\text{C}$  [63]. 26
- Fig. 2.18: The substitution behaviour of ternary addition in  $\text{Ni}_3\text{Al}$  [81]. 29
- Fig. 2.19: Temperature dependence of  $D_{\text{Ni}}^*$  in  $\text{Ni}_3\text{Al}$  [113]. 36
- Fig. 2.20: Yield strength as a function of temperature for  $\text{Ni}_3\text{Al}$  alloys (advanced aluminide alloy and  $\text{Ni}_3\text{Al}+0.2\text{B}$ ), compared with a few conventional commercial alloys (IN 713C, Hastelloy-X and 316 stainless steel) [120]. 38
- Fig. 2.21: Illustrations of successive positions for a superdislocation moving on the (111) plane by (a) bowing between cross-slip pinning (CSP) points as envisioned in the CSP models and (b) lateral motion of superkinks between Kear-Wilsdorf (KW) locks as envisioned in the superkinks models [144]. 41
- Fig. 2.22: Comparison of Hall-Petch relationships for alloys with and without boron [157]. 44
- Fig. 2.23: Changes in yield stress with temperature for boron-doped  $\text{Ni}_3\text{Al}$  with a grain size of 15.3, 85 and  $173\ \mu\text{m}$  [104]. 46
- Fig. 2.24: Effect of stoichiometry on flow stress of  $\text{Ni}_3\text{Al}$  at 77 K and room temperature [53]. 48
- Fig. 2.25: Temperature dependence of the 0.2% flow stress of the  $\text{Ni}_3\text{Al}$  alloys [53]. 48
- Fig. 2.26: Change in activation energy with solute concentration in ternary  $\text{Ni}_3\text{Al}$  with addition of transition metal elements [11]. 52
- Fig. 2.27: Relation between 0.2% flow stress measured at 77 K and the solute concentration in ternary  $\text{Ni}_3\text{Al}$  with addition of transition elements [11]. 54
- Fig. 2.28: Correlation of strengthening capacity,  $\delta\sigma_y/\delta C$ , to the lattice strain per atom fraction,  $\delta\epsilon/\delta C$ , for the addition of various ternary additions [171]. 54
- Fig. 2.29: Structure of the  $\Sigma=5(310)$  boundary in (a) stoichiometric  $\text{Cu}_2\text{Au}$ ; (b) stoichiometric  $\text{Ni}_2\text{Al}$  [194]. 58

Fig. 2.30: Effect of boron concentration on the ductility of $\text{Ni}_3\text{Al}$ [13].	59
Fig. 2.31: Effect of aluminium concentration on the ductility of boron-doped $\text{Ni}_3\text{Al}$ [13].	59
Fig. 2.32: Slip propagation across a boundary during TEM <i>in-situ</i> straining of boron-doped stoichiometric $\text{Ni}_3\text{Al}$ [208].	63
Fig. 2.33: Plot of room temperature tensile elongation as a function of aluminium concentration [245].	69
Fig. 2.34: Schematic variation of tensile elongation with temperature for boron-doped $\text{Ni}_3\text{Al}$ [104].	71
Fig. 2.35: Plot of tensile ductility as a function of test temperature for Ni-21.5% Al-0.5% Hf-0.1% B alloy tested in air and vacuum [236].	72
Fig. 2.36: Plot of tensile ductility as a function of air pressure for Ni-23% Al-0.5% Hf-0.07% B tested at 760°C [235].	72
Fig. 2.37: The atomic arrangement on the (111) plane in an $\text{A}_3\text{B}$ compound with the $\text{L1}_2$ structure. Large, medium and small circles represent atoms on A, B and C layers respectively [252].	74
Fig. 2.38: Atomic arrangement and possible dissociation schemes for $[\bar{1}10]$ dislocation on (111) in the $\text{L1}_2$ structure. (a) Types of dissociation, (b) six-fold, (c) four fold (d) two-fold (APB-splitting) and (e) two-fold (SISF-splitting) dissociations [253,254,255].	74
Fig. 3.1: X-ray diffraction pattern of boron-free stoichiometric $\text{Ni}_3\text{Al}$ , homogenized at 1100°C for 5 days and then annealed at 1000°C for 10 days, along with that of silicon standard peaks.	85
Fig. 3.2: Plot of Nelson-Riley function versus lattice parameter for boron-free stoichiometric $\text{Ni}_3\text{Al}$ .	88
Fig. 3.3: Schematic plot of arrangements of compression testing machine.	91
Fig. 4.1: Microstructure of stoichiometric $\text{Ni}_{75}\text{Al}_{25}$ alloy homogenized at 1100°C for 5 days and water quenched.	93
Fig. 4.2: Microstructure of the alloy $\text{Ni}_{77.4}\text{Al}_{22.6}$ homogenized at 1130°C for 20 days and water quenched.	95

- Fig. 4.3: Microstructure of the alloy of nominal composition  $\text{Ni}_{73}\text{Al}_{27}$  homogenized at  $1130^\circ\text{C}$  for 20 days and water quenched. 95
- Fig. 4.4: Lattice parameter of the  $\gamma'$  phase present in the alloy of nominal composition  $\text{Ni}_{75}\text{Al}_{17.5}\text{Hf}_{7.5}$  as a function of homogenization time at  $1130^\circ\text{C}$ . 98
- Fig. 4.5: Microstructure of the alloy  $\text{Ni}_{75.7}\text{Al}_{21.5}\text{Hf}_{2.8}$  homogenized at  $1130^\circ\text{C}$  for 20 days and water quenched. 100
- Fig. 4.6: Microstructure of the alloy  $\text{Ni}_{75.5}\text{Al}_{19.5}\text{Hf}_{5.0}$  homogenized at  $1130^\circ\text{C}$  for 20 days and water quenched. 100
- Fig. 4.7: Microstructure of the alloy of nominal composition  $\text{Ni}_{75}\text{Al}_{17.5}\text{Hf}_{7.5}$  homogenized at  $1130^\circ\text{C}$  for 20 days and water quenched;  
 (a). Optical microstructure;  
 (b). Scanning micrograph; 1 and 2 indicate the phases  $\gamma'$  and  $\eta_1$  respectively. 102
- Fig. 4.8: Microstructure of the alloy of nominal composition  $\text{Ni}_{77.5}\text{Al}_{20}\text{Hf}_{2.5}$  homogenized at  $1130^\circ\text{C}$  for 20 days and water quenched;  
 (a). Optical microstructure;  
 (b). Scanning micrograph; 1 and 2 indicate the phases  $\gamma'$  and  $\gamma$  respectively. 104
- Fig. 4.9: Microstructure of the alloy of nominal composition  $\text{Ni}_{77.5}\text{Al}_{17.5}\text{Hf}_5$  homogenized at  $1130^\circ\text{C}$  for 20 days and water quenched;  
 (a). Optical microstructure;  
 (b). Scanning micrograph; 1 and 2 indicate the phases  $\gamma'$  and  $\gamma$  respectively. 106
- Fig. 4.10: Microstructure of the alloy of nominal composition  $\text{Ni}_{80}\text{Al}_{17.5}\text{Hf}_{2.5}$  homogenized at  $1130^\circ\text{C}$  for 20 days and water quenched;  
 (a). Optical microstructure;  
 (b). Scanning micrograph; 1, 2 and 3 indicate the phases  $\gamma'$ ,  $\gamma'$  and  $\gamma$  respectively. 107
- Fig. 4.11: Microstructure of the alloy of nominal composition  $\text{Ni}_{80}\text{Al}_{15}\text{Hf}_5$  homogenized at  $1130^\circ\text{C}$  for 20 days and water quenched;  
 (a). Optical microstructure;

- (b). Scanning micrograph, 1, 2, 3 and 5 indicate the phases  $\gamma'$ ,  $\eta_1$ ,  $\gamma_1$  and  $\gamma$  respectively and 4 indicates the overall composition of the alloy.

109

Fig. 4.12: Microstructure of the alloy of nominal composition  $\text{Ni}_{72.5}\text{Al}_{25}\text{Hf}_{2.5}$  homogenized at  $1130^\circ\text{C}$  for 20 days and water quenched;

(a). Optical microstructure;

(b). Scanning micrograph; 1 indicates the phase  $\gamma'$  and 2 and 3 indicate the phase  $\beta$ .

111

Fig. 4.13: Microstructure of the alloy of nominal composition  $\text{Ni}_{72.5}\text{Al}_{22.5}\text{Hf}_5$  homogenized at  $1130^\circ\text{C}$  for 20 days and water quenched;

(a). Optical microstructure;

(b). Scanning micrograph; 1 indicates the phase  $\gamma'$  and 2 and 3 indicate the phases  $\beta$ .

113

Fig. 4.14: Constitution diagram of boron-free Ni-Al-Hf system in its  $\gamma'$ -rich region at  $1130^\circ\text{C}$ .

116

Fig. 4.15: Comparison of constitutional diagram of Ni-Al-Hf system determined in the present investigation with those reported in the literature.

118

Fig. 4.16: Microstructure of stoichiometric boron-doped  $\text{Ni}_{75}\text{Al}_{25}$  alloy homogenized at  $1100^\circ\text{C}$  for 5 days and water quenched;

(a). Alloy 'A' (see Table 3.1);

(b). Alloy 'B' (see Table 3.1).

120

Fig. 4.17: Microstructure of boron-doped alloy of nominal composition  $\text{Ni}_{77}\text{Al}_{23}$  homogenized at  $1130^\circ\text{C}$  for 20 days and water quenched;

122

Fig. 4.18: Microstructure of boron-doped alloy  $\text{Ni}_{73.2}\text{Al}_{26.8}$  homogenized at  $1130^\circ\text{C}$  for 20 days and water quenched.

122

Fig. 4.19: Microstructure of boron-doped alloy  $\text{Ni}_{75.3}\text{Al}_{22.3}\text{Hf}_{2.4}$  homogenized at  $1130^\circ\text{C}$  for 20 days and water quenched.

124

Fig. 4.20: Microstructure of boron-doped alloy  $\text{Ni}_{75.2}\text{Al}_{19.7}\text{Hf}_{5.1}$  homogenized at  $1130^\circ\text{C}$  for 20 days and water quenched.

124

Fig. 4.21: Microstructure of boron-doped alloy of nominal composition  $\text{Ni}_{75}\text{Al}_{17.5}\text{Hf}_{7.5}$  homogenized at  $1130^\circ\text{C}$  for 20 days and water quenched;

(a). Optical microstructure;

(b). Scanning micrograph; 1 and 2 indicate the phases  $\gamma'$  and  $\eta_1$  respectively.

125

Fig. 4.22: Microstructure of boron-doped alloy  $\text{Ni}_{72.5}\text{Al}_{25.2}\text{Hf}_{2.3}$  homogenized at  $1130^\circ\text{C}$  for 20 days and water quenched.

127

Fig. 4.23: Microstructure of boron-doped alloy  $\text{Ni}_{72.3}\text{Al}_{23.1}\text{Hf}_{4.6}$  homogenized at  $1130^\circ\text{C}$  for 20 days and water quenched.

127

Fig. 4.24: Microstructure of boron-doped alloy of nominal composition  $\text{Ni}_{70}\text{Al}_{27.5}\text{Hf}_{2.5}$  homogenized at  $1130^\circ\text{C}$  for 20 days and water quenched;

(a). Optical microstructure;

(b). Scanning micrograph; 1 and 2 indicate the phases  $\gamma'$  and  $\beta$  respectively.

129

Fig. 4.25: Microstructure of boron-doped alloy of nominal composition  $\text{Ni}_{70}\text{Al}_{25}\text{Hf}_5$  homogenized at  $1130^\circ\text{C}$  for 20 days and water quenched;

(a). Optical microstructure;

(b). Scanning micrograph; 1 and 2 indicate the phase  $\gamma'$  and 3, 4 and 5 indicate the phase  $\beta$ .

130

Fig. 4.26: Microstructure of boron-doped alloy of nominal composition  $\text{Ni}_{77.5}\text{Al}_{20}\text{Hf}_{2.5}$  homogenized at  $1130^\circ\text{C}$  for 20 days and water quenched;

(a). Optical microstructure;

(b). Scanning micrograph; 1 and 2 indicate the phases  $\gamma'$  and  $\gamma$  respectively.

132

Fig. 4.27: Microstructure of boron-doped alloy of nominal composition  $\text{Ni}_{77.5}\text{Al}_{17.5}\text{Hf}_5$  homogenized at  $1130^\circ\text{C}$  for 20 days and water quenched;

(a). Optical microstructure;

(b). Scanning micrograph; 1 and 2 indicate the phases  $\gamma'$  and  $\gamma$  respectively.

133

Fig. 4.28: Constitution diagram of boron-doped Ni-Al-Hf system in its  $\gamma'$ -rich region at  $1130^\circ\text{C}$ .

136

Fig. 4.29: Comparison of phase boundaries of boron-free and boron-doped Ni-Al-Hf system at  $1130^\circ\text{C}$ .

138

Fig. 5.1: Variation of lattice parameter of binary boron-free  $\text{Ni}_{75}\text{Al}_{25}$  as a function of equilibration temperature.

142

Fig. 5.2: Variation of lattice parameter of binary boron-free  $\text{Ni}_{75}\text{Al}_{25}$  as a function of aluminium content.

146

Fig. 5.3:	Variation of lattice parameter of binary boron-doped $\text{Ni}_3\text{Al}$ (Alloy B) as a function equilibration temperature; Dashed line shows the temperature dependence of lattice parameter of boron-free $\text{Ni}_3\text{Al}$ (from Figure 5.1).	150
Fig. 5.4.	Variation of lattice parameter of binary boron-doped $\text{Ni}_3\text{Al}$ (Alloy B) as function of aluminium content; Dashed line shows variation of lattice parameter of boron-free $\text{Ni}_3\text{Al}$ as function of aluminium content (from Figure 5.2).	153
Fig. 5.5:	Outline of body-centered tetragonal cell shown (dotted lines) inside the $\text{Ni}_3\text{Al}$ lattice using face-centered nickel atoms.	157
Fig. 5.6:	Schematic plot of the effect of temperature on the vacancy concentration ( $C_v$ ), the degree of order (S) and the lattice parameter.	160
Fig. 5.7:	Plot of experimental lattice parameter versus calculated lattice parameter for boron-free $\gamma'$ alloys.	163
Fig. 5.8:	Variation of specific and partial volumes as a function of atomic percent aluminium in boron-free binary $\text{Ni}_3\text{Al}$ alloys.	166
Fig. 5.9:	Variation of partial volumes as a function of atomic percent hafnium in boron-free ternary Ni-Al-Hf alloys.	167
Fig. 5.10:	Variation of partial volumes as a function of atomic percent aluminium in boron-free ternary Ni-Al-Hf alloys.	168
Fig. 5.11:	Plot of experimental lattice parameter versus calculated lattice parameter for boron-doped $\gamma'$ alloys.	171
Fig. 5.12:	Variation of specific and partial volumes as a function of atomic percent aluminium in boron-doped binary $\text{Ni}_3\text{Al}$ alloys.	174
Fig. 5.13:	Variation of partial volumes as a function of atomic percent hafnium in boron-doped ternary Ni-Al-Hf alloys.	175
Fig. 5.14:	Variation of partial volumes as a function of atomic percent aluminium in boron-doped ternary Ni-Al-Hf alloys.	176

Fig. 5.15: Two different octahedral sites for $\text{Ni}_3\text{Al}$ structure.	181
Fig. 5.16: Change in partial volumes ( $\Delta\bar{V}$ ) as a function of atomic percent hafnium in ternary Ni-Al-Hf alloys.	182
Fig. 5.17: Location of boron in one of the interstitial sites (Site II) on (100) plane of $\text{Ni}_3\text{Al}$	183
Fig. 5.18: Room temperature determination of the variation of the faulting probability, $\alpha$ , as a function of atomic percent solute in nickel-base alloys [277].	187
Fig. 5.19: Typical dislocation configurations in prestrained (2-3 %) boron-free $\text{Ni}_3\text{Al}$ ((a), (b) and (c))	190
Fig. 5.19: Typical dislocation configurations in prestrained (2-3 %) boron-free $\text{Ni}_3\text{Al}$ ((d), (e) and (f))	191
Fig. 5.20: Typical dislocation configurations in prestrained (2-3 %) boron-doped $\text{Ni}_3\text{Al}$ ((a), (b), (c) and (d))	192
Fig. 5.21: Typical dislocation configurations in prestrained (2-3 %) boron-free alloy $\text{Ni}_{75.5}\text{Al}_{19.5}\text{Hf}_5$ ((a), (b), (c) and d)	194
Fig. 5.22: Typical dislocation configurations in prestrained (2-3 %) boron-doped alloy $\text{Ni}_{75.2}\text{Al}_{19.7}\text{Hf}_{5.1}$ ((a) and (b))	195
Fig. 5.23: Typical microstructures of the boron-doped alloy of nominal composition $\text{Ni}_{75.0}\text{Al}_{17.5}\text{Hf}_{7.5}$ showing stacking faults in the $\eta_1$ phase ((a) and (b))	197
Fig. 6.1: Load versus change in length plot of boron-free stoichiometric $\text{Ni}_3\text{Al}$ alloy at $650^\circ\text{C}$ .	202
Fig. 6.2: True stress versus true strain plot of boron-free and boron-doped stoichiometric $\text{Ni}_3\text{Al}$ alloy at $650^\circ\text{C}$ .	203
Fig. 6.3: True stress versus true strain plot of boron-free and boron-doped stoichiometric $\text{Ni}_3\text{Al}$ alloy at $25^\circ\text{C}$ .	205
Fig. 6.4: Plot of peak temperature as a function of atomic percent hafnium [22].	207
Fig. 6.5: True stress versus true strain plot of boron-free alloy $\text{Ni}_{75.5}\text{Al}_{19.5}\text{Hf}_{5.0}$ at various temperatures.	208
Fig. 6.6: True stress versus true strain plot for boron-free alloy $\text{Ni}_{75.5}\text{Al}_{19.5}\text{Hf}_{5.0}$ and boron-doped alloy $\text{Ni}_{75.2}\text{Al}_{19.7}\text{Hf}_{5.1}$ at $25^\circ\text{C}$ .	209

	<u>Page</u>
Fig. 6.7: Plot of 0.2% flow stress as a function of temperature for boron-free alloy $\text{Ni}_{75.5}\text{Al}_{19.5}\text{Hf}_5$ and boron-doped alloy $\text{Ni}_{75.2}\text{Al}_{19.7}\text{Hf}_{5.1}$ .	210
Fig. 6.8: True stress versus true strain plot of boron-free alloy $\text{Ni}_{75.7}\text{Al}_{21.5}\text{Hf}_{2.8}$ at 600°C.	212
Fig. 6.9: Plot of 0.2% flow stress at peak temperature as a function of atomic percent hafnium.	213
Fig. 6.10: True stress versus true strain plot of boron-doped alloy $\text{Ni}_{75.2}\text{Al}_{19.7}\text{Hf}_{5.1}$ at various temperatures.	214
Fig. 6.11: SEM fractographs of the boron-free alloy $\text{Ni}_{75.5}\text{Al}_{19.5}\text{Hf}_5$ compression tested at 600°C ((a) and (b))	216
Fig. 6.12: SEM fractographs of the boron-free alloy $\text{Ni}_{75.5}\text{Al}_{19.5}\text{Hf}_5$ compression tested at 25°C ((a) and (b))	216
Fig. 6.13: SEM fractographs of the boron-doped alloy $\text{Ni}_{75.2}\text{Al}_{19.7}\text{Hf}_{5.1}$ compression tested at 700°C ((a) and (b))	217
Fig. 6.14: SEM fractographs of the boron-doped alloy $\text{Ni}_{75.2}\text{Al}_{19.7}\text{Hf}_{5.1}$ compression tested at 25°C ((a) and (b))	217
Fig. 6.15: Variation of the mechanical properties of boron-free $\gamma'$ alloys with hafnium content.	221



## LIST OF TABLES

	<u>Page</u>
Table 2.1: Substitutional behaviour of ternary additions in $\gamma'$ alloys	27
Table 3.1: List of alloys	80
Table 3.2: Homogenization temperature and time	81
Table 3.3: Calculation of errors using standard silicon sample	86
Table 3.4: Calculation of lattice parameter and Nelson-Riley function for boron-free $\text{Ni}_3\text{Al}$ using errors calculated for standard silicon sample	87
Table 4.1: EDAX analysis of the various phases present in the alloy of nominal composition $\text{Ni}_{80}\text{Al}_{15}\text{Hf}_5$	110
Table 4.2: Composition of the phases present in the boron-free Ni-Al-Hf system	115
Table 4.3: Composition of the phases present in the boron-doped Ni-Al-Hf system	135
Table 5.1: Lattice parameter of boron-free $\text{Ni}_3\text{Al}$ homogenized at $1100^\circ\text{C}$ for 5 days as a function of equilibration temperature	141
Table 5.2: Heat treatment and lattice parameter of boron-free $\gamma'$ available in the literature	143
Table 5.3: Lattice parameter of boron-free $\gamma'$ alloys at $25^\circ\text{C}$ quenched from $1130^\circ\text{C}$	147
Table 5.4: Lattice parameter of boron-doped $\text{Ni}_3\text{Al}$ homogenized at $1100^\circ\text{C}$ for 5 days as a function of equilibration temperature	149
Table 5.5: Heat treatment and lattice parameter of boron-doped $\gamma'$ available in the literature	151
Table 5.6: Lattice parameter of boron-doped $\gamma'$ alloys at $25^\circ\text{C}$ quenched from $1130^\circ\text{C}$	154
Table 5.7: Lattice parameter of boron-free $\gamma$ phase	155
Table 5.8: Calculated partial gram-atomic volumes of components in boron-free $\gamma'$	165
Table 5.9: Calculated partial gram-atomic volumes of components in boron-doped $\gamma'$	173

Page

Table 5.10: Atomic and covalent radii and related properties of nickel, aluminium and hafnium	178
Table 6.1: Results of the compression tests	219

## ABSTRACT

Superalloys were developed during the past few decades primarily for use in gas turbine engines of aircrafts which work at temperatures ranging from 650°C to 1100°C under adverse atmospheres. The need for ever increasing gas turbine combustion temperatures for enhanced efficiency and performance necessitated the development of materials that retain dimensional stability and resistance to surface attack. Ordered intermetallics have long been recognized as candidates for high temperature applications. Intermetallic compounds possess a number of properties that make them intrinsically more appealing. First and perhaps the most important one is that intermetallic compounds tend to be inherently very strong (high yield or fracture strength) and their strength tends to be maintained up to high temperatures. The strong tendency for chemical ordering in the intermetallic compounds reduces the atomic mobility at elevated temperatures and results in good structural stability and resistance to high temperature deformation. Intermetallic compounds may be expected to be better than the nickel-base superalloys which have been traditionally used for high temperature applications.

Among the intermetallic compounds,  $\text{Ni}_3\text{Al}$  is of special interest as it is the most important strengthening constituent of commercial nickel-base superalloys used extensively as high temperature structural materials for jet engine and aerospace applications. It is also responsible for the strength and creep resistance of the superalloys at elevated temperatures.  $\text{Ni}_3\text{Al}$  has an ordered cubic  $\text{L1}_2$  structure and is known as the  $\gamma'$  phase. Its mechanical properties are unique. The yield strength of  $\text{Ni}_3\text{Al}$  increases by more than a factor of five as the temperature is increased from room temperature to 700°C. One of the major difficulties in using  $\text{Ni}_3\text{Al}$  as an

engineering material is its low ductility and susceptibility to brittle fracture in its polycrystalline form.

Remarkable improvement in the ductility of polycrystalline  $\text{Ni}_3\text{Al}$  has been achieved by microalloying with boron. The properties of  $\text{Ni}_3\text{Al}$  can also be considerably improved by alloying with substitutional elements. Fortunately, a large number of alloying elements may be substituted for either of the constituent elements of  $\text{Ni}_3\text{Al}$  to a considerable degree. Substitutional solute, hafnium, has the maximum effect in increasing the high temperature strength of  $\text{Ni}_3\text{Al}$ -based alloys. It can increase the proof stress of  $\text{Ni}_3\text{Al}$  by more than 300% through solid solution strengthening. Hafnium is also shown to be one of the most effective solutes in improving high temperature creep resistance. The improvement of properties of any alloy system by the addition of solute atoms can be fully utilized and exploited if the relevant phase diagrams and structural characteristics are known. In spite of the fact that substantial information is available in the literature on boron-free and boron-doped  $\text{Ni}_3\text{Al}$  and related alloys, there is still a lot of scope of work especially in the promising hafnium containing alloys. In the present investigation, therefore, the phase equilibria and the structural and mechanical characteristics of boron-free and boron-doped  $\text{Ni}_3\text{Al}$  alloys containing hafnium have been investigated.

The alloys were prepared using a non-consumable tungsten electrode arc melting furnace under high purity argon atmosphere. Three boron and hafnium free alloys, four boron-doped hafnium free alloys, nine boron-free alloys with various hafnium contents ranging up to 7.5 at.% and nine boron-doped alloys with hafnium contents ranging up to 7.5 at.% were prepared. The arc melted alloys were vacuum sealed in fused quartz tubes and homogenized. For equilibration samples of the alloys were vacuum sealed in fused quartz tubes (vacuum of the order  $10^{-2}$  to  $10^{-3}$  torr), equilibrated at the required temperatures for predetermined lengths of

time and then quenched in water. Boron-free and boron-doped stoichiometric  $\text{Ni}_3\text{Al}$  alloys were equilibrated at  $1200^\circ\text{C}$  for 5 days, at  $1130^\circ\text{C}$  for 7 days, at  $1000^\circ\text{C}$  for 10 days and at  $800^\circ\text{C}$  for 20 days. The off-stoichiometric  $\text{Ni}_3\text{Al}$  alloys were equilibrated at  $1130^\circ\text{C}$  for 20 days. Hafnium containing  $\gamma'$  alloys with and without boron were also equilibrated at  $1130^\circ\text{C}$  for 20 days.

Microstructural analysis of the homogenized and equilibrated specimens was carried out by both optical microscopy and scanning electron microscopy. Transmission electron microscopic studies of foils were also carried out. The lattice parameters of the various phases present in the different alloys were accurately determined using X-ray diffraction tracings of powder samples of the alloys stress relieved at the equilibration temperatures. The composition of each phase present in an alloy was determined using EDAX facility attached to the scanning electron microscope. Compression tests on selected alloys were carried out using an MTS unit in the temperature range from room temperature to  $700^\circ\text{C}$ .

The compositions of various phases present in the equilibrated samples of the alloys yielded information on the phase equilibria in the  $\text{Ni}_3\text{Al}$ -rich part of the Ni-Al-Hf system. The ternary phase diagram around the  $\gamma'$  phase ( $\text{Ni}_3\text{Al}$ ) field at  $1130^\circ\text{C}$  was determined and the phase boundary of the  $\gamma'$  phase was established. The other phases,  $\gamma$ ,  $\gamma_1$ ,  $\beta$  and  $\eta_1$  were also found to coexist in equilibrium with  $\gamma'$  phase in a number of samples. The phase boundaries of these phases were determined. A number of tie lines for two phase equilibria, a tie triangle and a four phase equilibria were also established. The isothermal sections were drawn on the basis of these results. The literature contained very few experimental points. However, the present results yielded adequate data to establish the phase boundaries of  $\gamma'$  phase and the coexisting phases in Ni-Al-Hf system at  $1130^\circ\text{C}$ .

The phase equilibria in boron-doped Ni-Al-Hf system in its  $\gamma'$ -rich region was established on the basis of the analysis of phases present in the homogenized boron-doped hafnium containing  $\gamma'$  alloys. The phase boundary of the  $\gamma'$  phase was established. Here also, the phases,  $\gamma$ ,  $\beta$  and  $\eta_1$ , were found to coexist in equilibrium with  $\gamma'$  phase in a number alloys. Six tie lines for two phase equilibria were established. Isothermal section at  $1130^\circ\text{C}$  was drawn based on these results. The phase boundaries in the boron-doped alloys was found to shift appreciably with respect to those in the boron-free alloys. In the presence of boron, the solubility of nickel in  $\gamma'$  phase is reduced whereas that of aluminium in  $\gamma'$  phase is increased. It suggests that in the presence of boron, it is easier for aluminium and hafnium to occupy nickel sites while it is difficult for nickel to occupy the aluminium sublattice. The solubility of aluminium in the  $\gamma$  phase does not change appreciably while that of nickel in the  $\beta$  phase is reduced by about 1.25 at.% in the boron-doped state. The solubilities of nickel and aluminium are decreased by about 0.5 at.% in  $\eta_1$  phase in the presence of boron. It is also noted that although the boron content is very small (of the order of 0.1 at.%), the solubilities of the substitutional solutes showed changes of about 1 at.%. However, the presence of boron in Ni-Al-Hf system does not introduce any new phase or any new phase equilibria.

The stability characteristics of  $\gamma'$  phase in boron-free and boron-doped conditions were investigated in terms of the variation of the partial volumes of the components of the  $\gamma'$  phase. The specific volumes were determined on the basis of extensively and accurately measured lattice parameters of the  $\gamma'$  phase of the alloys. A mathematical model was developed by expressing the lattice parameters in terms of two variables, atom fraction,  $X$ , of nickel and aluminium. The lattice parameter,  $a$ , of the  $\gamma'$  phase was expressed in a polynomial equation truncated after the

second order terms. The best fit was obtained using the Minitab, Data Analysis Software. The relations obtained are as follows :

For boron-free alloys :

$$a = 4.839725 - 2.492X_{Ni} - 1.295X_{Al} + 1.54X_{Ni}^2 + 3.89X_{Al}^2 - 0.98X_{Ni}X_{Al}$$

For boron-doped alloys:

$$a = 6.998725 - 7.520X_{Ni} - 3.785X_{Al} + 4.47X_{Ni}^2 + 4.38X_{Al}^2 + 2.00X_{Ni}X_{Al}$$

Both experimental and calculated lattice parameters agreed well with each other in both boron-free and boron-doped systems. The partial volumes of the three components of the  $\gamma'$  phase, namely nickel, aluminium and hafnium, were calculated as functions of compositions of  $\gamma'$  using the above relations. Based on the partial volume calculations, the solute substitution and bonding characteristics in  $\gamma'$  phase containing 73 at.% Ni, 75 at.% Ni and 77 at.% Ni were investigated. In the hafnium free binary  $\gamma'$  phase, the partial volumes of aluminium and nickel are almost identical in nickel saturated  $\gamma'$  phase. As the aluminium content increases, the partial volume of aluminium increases rapidly while that of nickel decreases slightly. In hafnium containing ternary  $\gamma'$  phase the partial volume of aluminium changes significantly with change in composition compared with the partial volumes of nickel and hafnium. Some of the changes in the specific volumes are comparable with changes in atomic and covalent diameters. It is suggested that the results can be satisfactorily interpreted in the following manner. In hafnium containing alloys with 75 at.% Ni, hafnium seems to have considerable covalent character and the covalent character of aluminium increases appreciably as the hafnium content is increased from 0 to 5 at.%. In the boron-doped  $\gamma'$  alloy containing 75 at.% Ni, boron atoms occupy the edge-centered octahedral sites of the  $L1_2$  structure. Hafnium atoms occupy aluminium sites when hafnium content is low while it starts occupying nickel sites also as the hafnium content is increased. The alloying behaviour in the

nickel-rich  $\gamma'$  alloy (77 at.% Ni) and in the aluminium-rich  $\gamma'$  alloy (73 at.% Ni) is similar to that in the stoichiometric  $\gamma'$  alloy (75 at.% Ni). However, in the nickel-rich  $\gamma'$ , the boron atoms tend to occupy some of the body-centered octahedral sites in addition to occupying the edge-centered octahedral sites.

The lattice parameter of  $\gamma'$  phase of boron-free and boron-doped stoichiometric  $\text{Ni}_3\text{Al}$  tends to increase with increase in the quenching temperature up to about  $1000^\circ\text{C}$  and then decreases slightly beyond  $1000^\circ\text{C}$ . The decrease in the lattice parameter beyond  $1000^\circ\text{C}$  is more prominent in boron-doped alloy than in boron-free alloy. This unusual dependence of lattice parameter of  $\text{Ni}_3\text{Al}$  is due to the decrease in the degree of order with increase in equilibration temperature up to about  $1000^\circ\text{C}$  where the degree of order is expected to change rapidly with decrease in temperature and the thermal vacancy effect would be small. The slight decrease in the lattice parameter observed above  $1000^\circ\text{C}$  may be attributed to increase in the concentration of thermal vacancies as the effect of thermal vacancy at high temperature is appreciable and that of change in the degree of order would be negligible. In the presence of boron, the quenched-in thermal vacancy effect is slightly magnified because of higher quenched-in vacancies due to higher boron-vacancy binding energy.

Some of the structural characteristics of the boron-free and boron-doped  $\gamma'$  alloys, with and without hafnium and compressed by 2 to 3%, were examined through optical as well as transmission electron microscope. The occurrence of twins in boron-free stoichiometric and aluminium-rich  $\text{Ni}_3\text{Al}$  alloys and the absence of twins in boron-doped and hafnium containing alloys were attributed to the effect of alloying elements on the stacking fault probability. Typical microstructures of boron-free binary  $\text{Ni}_3\text{Al}$  consists of stacking fault like features and straight dislocations, two and three sets of which criss-cross one another at an



angle of  $60^\circ$ . Substructures of boron-doped binary  $\text{Ni}_3\text{Al}$  consist of short straight dislocation segments, dislocation dipoles and two sets of dislocation lines at angles of  $60^\circ$ . Boron-free  $\text{Ni}_3\text{Al}$  containing 5 at.% Hf showed long parallel dislocation lines and a criss-cross arrangement of two sets of dislocation lines at a few places. Boron-doped  $\text{Ni}_3\text{Al}$  containing 5 at.% Hf showed long dislocation lines. It was suggested that the faults observed in boron-free alloys are the superlattice intrinsic stacking faults (SISF). The addition of boron seems to effectively suppress the formation of SISFs in  $\text{Ni}_3\text{Al}$ . The effect of addition of hafnium to  $\text{Ni}_3\text{Al}$  has been found to be rather similar to that of boron in the sense that in the single phase  $\text{Ni}_3\text{Al}$  containing 5 at.% Hf, no stacking fault could be observed.

In order to compare the mechanical behaviour of the alloys investigated in the present study with those of the alloys of similar composition that have been reported in the literature, a limited number of mechanical testing (compression testing) was undertaken on a few selected alloy compositions. Although the stoichiometric  $\text{Ni}_3\text{Al}$  sample used in the present investigation showed good agreement between the values of proof stress at high temperature and the literature values, the alloy showed an unusually high value of proof stress at room temperature compared with the literature value. In the case of boron-doped  $\text{Ni}_3\text{Al}$ , higher proof stress values at high temperatures were obtained as compared with boron-free  $\text{Ni}_3\text{Al}$ . At room temperature, however, both have almost identical values. As far as the dependence of proof stress on temperature is concerned,  $\text{Ni}_3\text{Al}$  containing 5 at.% Hf, having the nominal composition  $\text{Ni}_{75}\text{Al}_{20}\text{Hf}_5$ , showed behaviour similar to that exhibited by alloys of similar composition reported in the literature. The values of the proof stress at peak temperature for various amounts of hafnium have also shown good agreement with those in the literature, although at room temperature, the

proof stress value of the experimental alloy is slightly lower than that reported in the literature. The effect of boron addition seems to increase the peak temperature,  $T_p$ , as well as the ductility of hafnium containing alloys. From the microstructural study of the fractured surfaces of the compression tested samples, it was concluded that the addition of boron to  $\gamma'$  was effective in suppressing intergranular fracture considerably.

On the basis of the present investigation it may be concluded that the  $\gamma'$  phase in its single phase state can retain up to about 7.4 at.% Hf. This alloy is about ten times stronger than the hafnium-free alloy at 500 K and possesses adequate ductility at high temperatures. After boron doping, the alloy can still be retained in a single phase state with up to 7.0 at.% Hf. Addition of boron also extends the usefulness of this alloy up to room temperature by improving its ductility and by suppressing intergranular fracture. Therefore, boron containing  $\gamma'$  alloys with hafnium appears to have considerable promise.

# CHAPTER I

## INTRODUCTION

Superalloys were developed during the past few decades primarily for use in gas turbine engines of aircrafts. The turbines of these engines operate at temperatures ranging from  $650^{\circ}\text{C}$  to  $1100^{\circ}\text{C}$  in an atmosphere consisting of products such as sodium and sulfur [1]. For operating satisfactorily in such a complex and severe environment, the superalloys used for the manufacture of turbines possess properties such as outstanding high temperature strength, creep and fatigue resistance, excellent ductility, good impact strength and adequate hot corrosion resistance. Because of this unique combination of properties, the superalloys have found application in a number of other areas as well such as gas cooled and fusion reactors [2], industrial power plants [3], coal gasification plants [4], chemical process industry [5], industrial gas turbines [6], heat exchangers [7], marine turbines [8], satellite propulsion systems [9] and exhaust valves [10]. Increasing demand for much superior properties has motivated considerable research and development activity for designing improved varieties of superalloys as well as other novel materials of promise.

The need for ever increasing gas turbine combustion temperatures for enhanced efficiency and performance necessitated the development of materials that retain dimensional stability and resistance to surface attack. Also, for better performance, the jet engines require materials which are low in density and can withstand higher temperature, thus increasing the thrust to weight ratio and engine efficiency. Ordered intermetallics have long been recognized as candidates for higher

temperature applications because thermally activated processes, such as diffusion, are inhibited by the ordered crystal structure. Intermetallic compounds are expected to be better than the nickel-base superalloys which have been traditionally used for high temperature applications.

Intermetallic compounds possess a number of properties that make them intrinsically more appealing. First and perhaps the most important one is that intermetallic compounds tend to be inherently very strong (high yield or fracture stress) and the strength tends to be maintained up to high temperatures. In addition, the modulus also tends to be high and decreases rather slowly with increasing temperature. Since, stiffness is the controlling property in many applications, especially in systems subjected to vibrations, a high modulus is an important benefit. The strong tendency for chemical ordering in the intermetallic compounds reduces the atomic mobility at elevated temperatures and results in good structural stability and resistance to high temperature deformation.

Among the intermetallic compounds,  $\text{Ni}_3\text{Al}$  is of special interest as it constitutes one of the important classes of intermetallic compounds and has unique mechanical properties. The temperature dependence of the yield strength of  $\text{Ni}_3\text{Al}$  is very unusual in the sense that the yield strength increases more than a factor of five as the temperature is increased from room temperature to about  $700^\circ\text{C}$  [11]. This property is put to good use in nickel-base superalloys for high temperature applications in which  $\text{Ni}_3\text{Al}$  content can be up to 60 volume percent. This makes  $\text{Ni}_3\text{Al}$ , a principal constituent responsible for the high temperature strength of nickel-base superalloys.

One of the major difficulties with  $\text{Ni}_3\text{Al}$  as an engineering material, however, is its low ductility and susceptibility to brittle fracture in polycrystalline form, although it is quite ductile in the

form of single crystals. Recently, the interest in  $\text{Ni}_3\text{Al}$  got renewed due to the remarkable improvement in ductility that has been achieved after microalloying with boron in hypostoichiometric  $\text{Ni}_3\text{Al}$  (less than 25 at.% Al) [12,13].

One of the major advantages with  $\text{Ni}_3\text{Al}$  is that a number of alloying elements may be substituted for either of the constituent elements of  $\text{Ni}_3\text{Al}$  to a considerable degree. The substitutional element hafnium is known to increase proof stress of  $\text{Ni}_3\text{Al}$  by more than 300% by way of solid solution hardening [11]. Some of the substitutional elements such as beryllium, copper, platinum, palladium and gold can improve the ductility of  $\text{Ni}_3\text{Al}$  [14,15,16]. Although the cold workability of nickel aluminides can be improved by adding suitable combinations of chromium and zirconium [17], hafnium has been found to be particularly beneficial for the improvement of elevated temperature ductility [18]. The elements, hafnium, chromium, zirconium and tantalum, also improve the creep resistance of  $\text{Ni}_3\text{Al}$ . Hafnium, however, has been shown to be the most effective in improving the creep resistance of  $\text{Ni}_3\text{Al}$  at high temperatures [19]. It is also known to improve combined creep-fatigue resistance [20]. The retention of creep-fatigue resistance with a decrease in yield strength is necessary if  $\text{Ni}_3\text{Al}(\text{B,Hf})$  is to be used as a monolith or as a composite matrix.

The improvement of mechanical properties of any alloy by the addition of solutes can be fully utilized and exploited if the relevant phase diagrams and the structural properties are known. The existing literature clearly indicates that the Ni-Al-Hf system is one of the most promising and hence needs to be investigated in detail. The substitutional behaviour of different amounts of hafnium in  $\text{Ni}_3\text{Al}$  is to be properly understood in order to predict the alloying effects. The different phases produced at different temperatures, their stability as

well as structural characteristics should also be thoroughly investigated. In view of the fact that boron plays a very crucial role in ductilizing  $\text{Ni}_3\text{Al}$ , the part played by this element in  $\text{Ni}_3\text{Al}$  alloys containing hafnium vis-a-vis their phase stability and mechanical behaviour should also be carefully looked into. Since, only a limited amount of information is available in the literature regarding the above, it has been decided to undertake further research in these directions. For this purpose, the constitution of the  $\gamma'$  ( $\text{Ni}_3\text{Al}$ )-rich region of boron-free and boron-doped Ni-Al-Hf alloy system has been investigated. The stability of these alloys and the substitutional behaviour of the solutes have been looked into and the results analyzed. Selected mechanical properties have been measured in order to note the effects of hafnium and boron additions on the properties of  $\gamma'$ . A number of experimental techniques have been used for the above purpose and these are enumerated in Chapter III.

## CHAPTER II

### LITERATURE REVIEW

#### 2.1. BINARY ALLOY SYSTEMS BETWEEN Ni, Al and Hf

##### 2.1.1. Ni-Al system

Since the first investigation of Ni-Al binary phase diagram which established its principal features, later work brought in considerable changes in phase relationships especially above 50 atom percent nickel. Most of the phase diagram work has been done by Alexander et al. [21], Hansen and Anderko [22], Taylor and Floyd [23], Massalski [24], Hilpert et al. [25] and Bremer et al. [26]. The phase diagram for Ni-Al system shown in Figure 2.1 [24] is largely based on X-ray, thermal and micrographic analysis.

The partial phase diagram for alloys with 0 to 50 at.% Ni is well established. There are only two intermediate peritectically formed phases, namely, (i)  $\text{NiAl}_3$  having  $\text{DO}_{11}$  type structure and (ii)  $\text{Ni}_2\text{Al}_3$  having  $\text{D}_{5_{13}}$  type structure. The  $\beta$  phase based on the composition  $\text{NiAl}$  has  $\text{B}_2$  type structure.

The partial phase diagram above 50 at.% Ni contains two intermediate phases, namely, (i)  $\text{Ni}_5\text{Al}_3$  having Pearson's symbol of oC16 and (ii)  $\text{Ni}_3\text{Al}$  having  $\text{L}_{12}$  type structure. The details of the crystal structures and lattice parameters of all solid phases in this system are listed in the literature [27].

According to Massalski [24], the invariant reactions  $\text{L} = (\text{Ni}) + \text{Ni}_3\text{Al}$  and  $\text{L} + \text{NiAl} = \text{Ni}_3\text{Al}$  take place at  $1385^\circ\text{C}$  (25 at.% Al) and  $1395^\circ\text{C}$  (25.5 at.% Al) respectively. On the other hand, Hilpert et al. [25] and Bremer et al. [26] found that the invariant reactions are

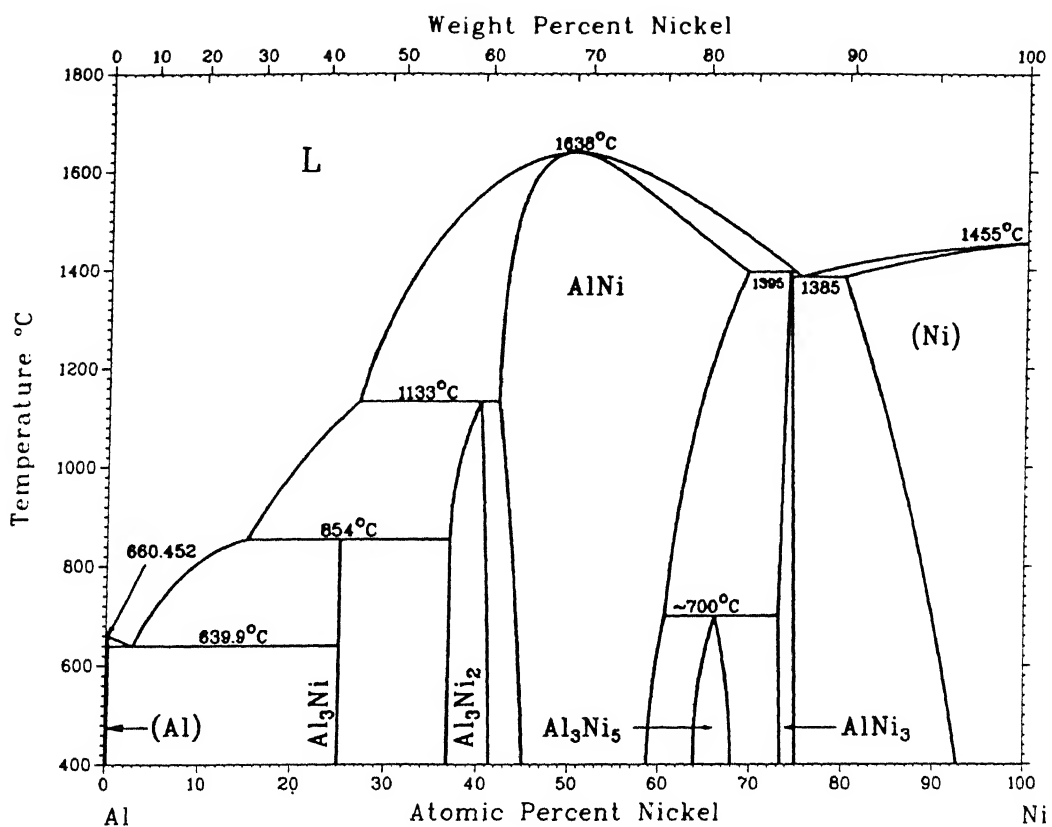


Fig. 2.1: The binary Ni-Al phase diagram [24].



$L + (Ni) = Ni_3Al$  and  $L = NiAl + Ni_3Al$  which take place at 1372 (24.5 at.% Al) and 1396°C (24.8 at.% Al) respectively.

### 2.1.2. Ni-Hf system

Ni-Hf system is analogous to Ni-Zr system. The phase diagram shown in Figure 2.2 was evaluated by Nash et al. [28] and is based mostly on the work of Bsenko [29] and Svechnikov et al. [30].

The intermediate phases which are reported in Ni-Hf system along with their crystal structures and available lattice parameters are listed in the literature [27].  $Ni_7Hf_2$  and NiHf are congruently melting and other intermediate phases such as  $Ni_5Hf$ ,  $Ni_3Hf$ ,  $Ni_7Hf_3$ ,  $Ni_{10}Hf_7$ ,  $Ni_{11}Hf_9$ ,  $NiHf_2$  and  $Ni_{21}Hf_8$  are formed peritectically. From the phase diagram, it is seen that the solid solubilities of Ni in (Hf) and Hf in (Ni) are limited. Based on the phase equilibria work by Elliott [31], Kaufman and Nesor [32] predicted large negative Gibbs energies of formation for Ni-Hf compounds using thermodynamic model calculation.

### 2.1.3. Al-Hf system

The microscopic and X-ray analyses of alloys in the range of 5 to 75 at.% Hf have made the tentative delineation of the equilibria possible. The Al-Hf phase diagram evaluated by Tsyganova et al. [33] is given in Figure 2.3. Among the seven intermediate phases,  $HfAl$ ,  $Hf_3Al_2$ ,  $HfAl_2$  and  $HfAl_3$  are supposed to be congruently melting.  $Hf_2Al$  and  $Hf_4Al_3$  are formed peritectoidally and  $Hf_2Al_3$  is formed peritectically. All the intermediate phases and their related structural informations are available in the literature [27].

## 2.2. THE TERNARY Ni-Al-Hf SYSTEM

Markiv et al. [34] were the first to report the isothermal section

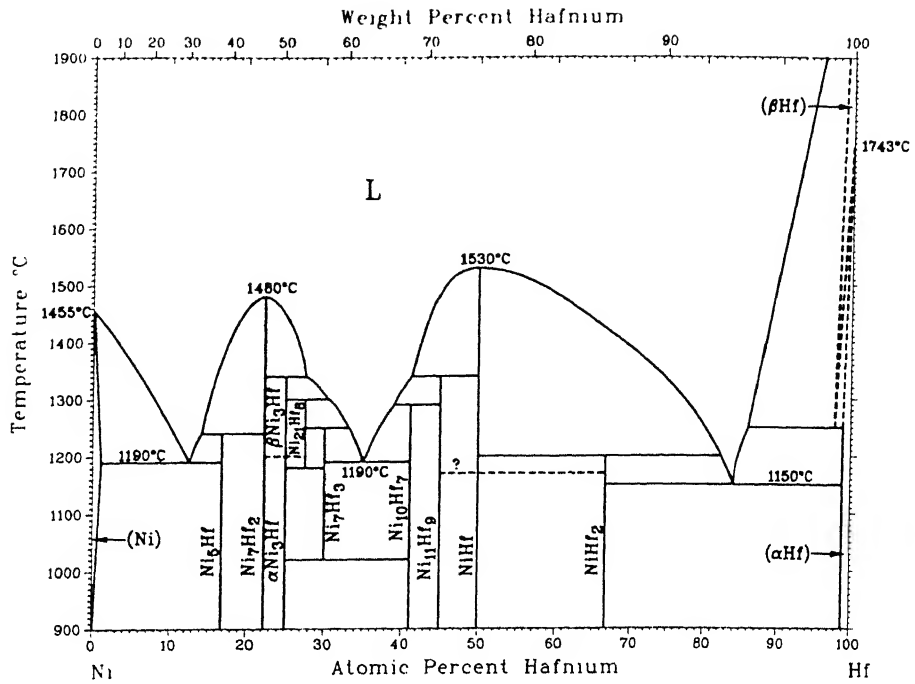


Fig. 2.2: The binary Ni-Hf phase diagram [28].

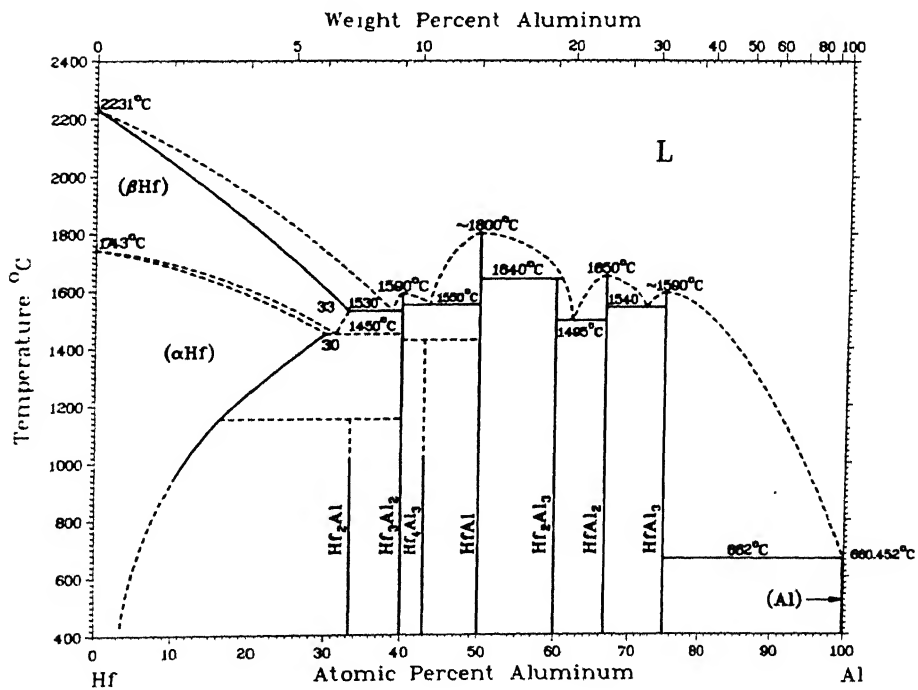


Fig. 2.3: The binary Al-Hf phase diagram [33].

of the entire system at 800°C which is shown in Figure 2.4. The phase analysis was performed by microstructural observations and X-ray diffraction techniques. The partial isothermal sections, evaluated by Nash and West [35] at 1200°C and 1000°C are shown in Figures 2.5 and 2.6 respectively. The phase analysis was carried out by optical microscopy, X-ray diffraction and electron probe microanalysis. Computer calculated isothermal sections in the range of Ni-50 at.% (Hf+Al) at 1423 and 1323°C [32,36], at 1223, 1123, 1023°C [32,36,37] and at 800°C [32,36] have also been reported. The thermodynamic description of the ternary system has been reported by Kaufman et al. [32,36]. The ternary system has been recently reviewed by Kumar [38] and Lee and Nash [39].

$\text{Ni}_3\text{Al}$  ( $\gamma'$  phase) is reported to dissolve about 8.5 at.% Hf at 1200°C [35] and 7 at.% Hf at 1000°C [35,40]. Nash and West [35] reported that  $\text{Ni}_7\text{Hf}_2$  can dissolve upto about 14 at.% Al with a width of 1.5 at.% Hf at 1200°C and 1000°C. On the other hand, Markiv et al. [34] found that none of the Ni-Hf binary compounds including  $\text{Ni}_7\text{Hf}_2$  can dissolve more than 1 at.% Al at 800°C.

At least ten ternary phases have been reported in this system, of which nine were first reported by Markiv and coworkers [34,41,42,43]. The details of the crystal structures and lattice parameters of the phases present in this system are listed in [27]. The ternary phase  $\text{Ni}_{19}\text{Hf}_{10}\text{Al}$  was reported to be stable above 1000°C but was not observed by Nash and West [35] in 1200°C and 1000°C isothermal sections. This phase was suggested to be an extension of  $\text{Ni}_2\text{Hf}$  into the ternary region [44] but it has been disproved by Bsenko [29]. Also, there is experimental evidence [29,35] suggesting that such a structure is not an equilibrium phase but most probably is stabilized by silica.  $\text{Ni}_{16}\text{Hf}_4\text{Al}_5$  ( $\lambda_3$  or L-phase) was reported to be present in the isothermal section at 800°C [34] but was not observed in the isothermal sections of 1000°C and

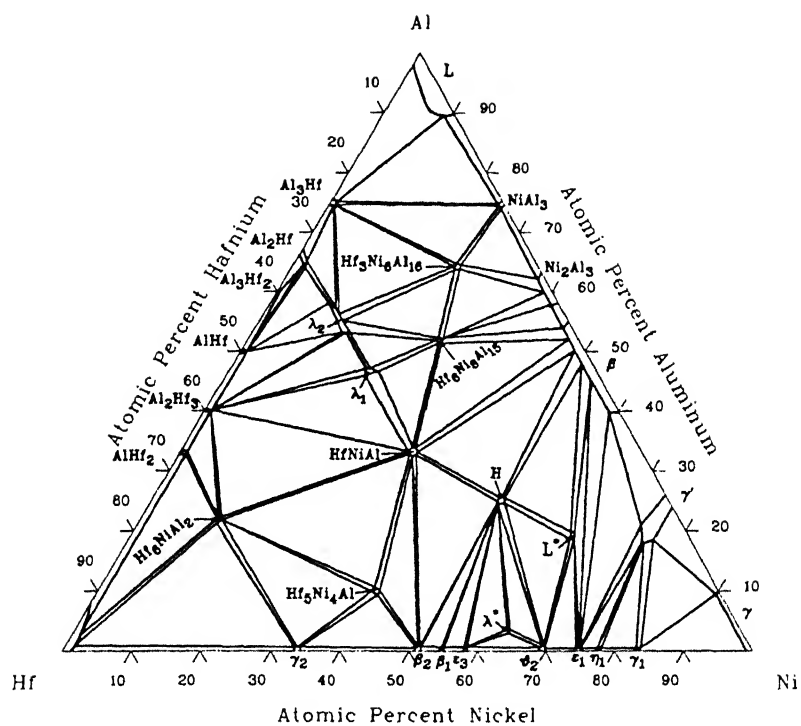


Fig. 2.4: Ni-Al-Hf 800°C isothermal section [34].

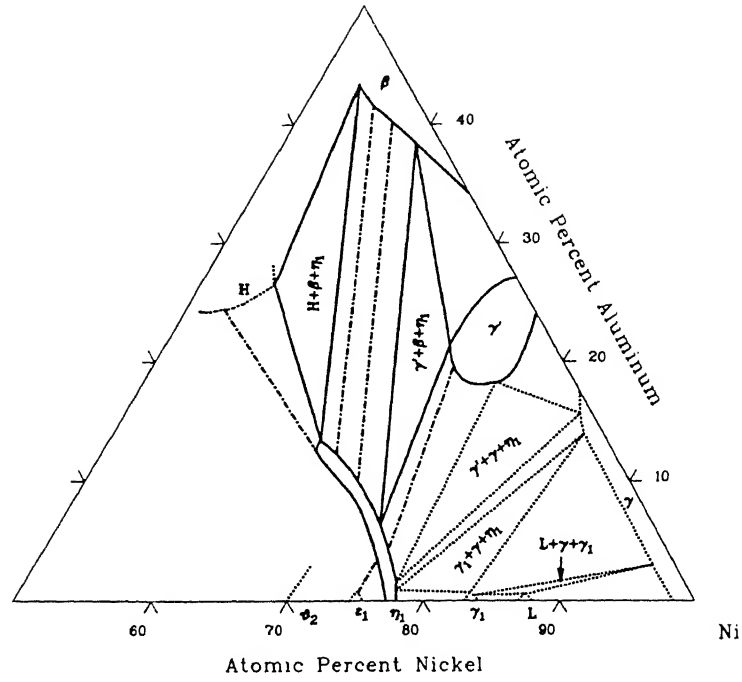


Fig. 2.5: Ni-Al-Hf 1200°C partial isothermal section [35].

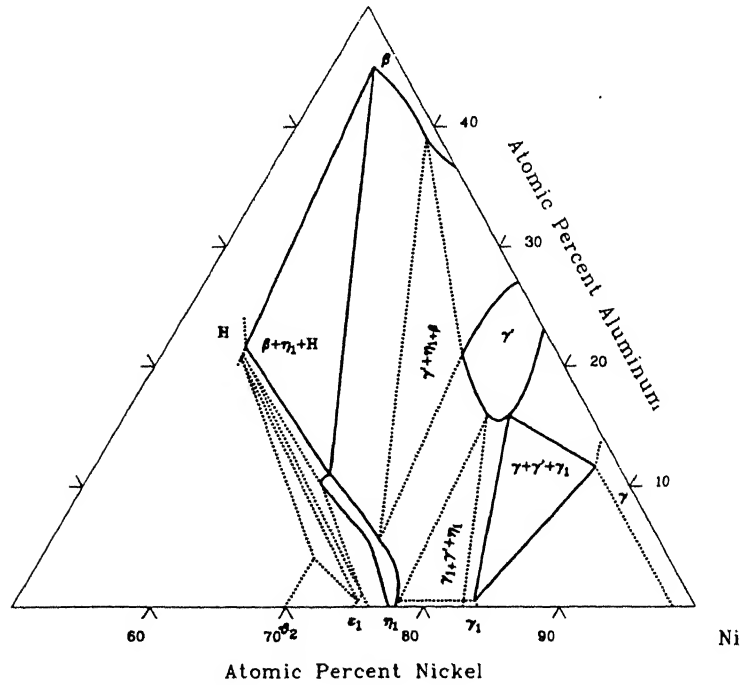
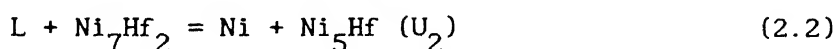
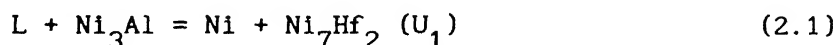


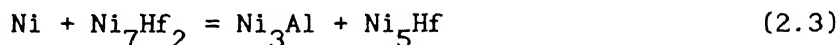
Fig. 2.6: Ni-Al-Hf 1000°C partial isothermal section [35].

1200°C [35]. Accordingly, it has been suggested that the  $\lambda_3$  phase is formed by a solid state reaction between 1000°C and 800°C [35]. The ternary phase  $\text{Ni}_2\text{HfAl}$  has been predicted to form by an invariant transition type reaction [35].

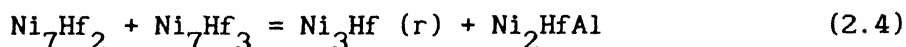
Two transition invariant reactions (Equations 2.1 and 2.2) have been reported by Nash and West [35] to take place during solidification of the nickel-rich alloys.



However, the temperatures of occurrence of the above invariant reactions were not reported but estimated to be between 1275 and 1200°C. Based on the observation of equilibria in the region  $\text{Ni-Ni}_3\text{Al-Ni}_7\text{Hf}_2$  between 1200°C and 1000°C, Nash and West [35] predicted the presence of invariant transition type reaction



at some temperature between 1200°C and 1000°C. In the same temperature range, Nash and West [35] predicted a possibility of another invariant transition type reaction



The three phase fields  $\text{Ni-Ni}_3\text{Al-Ni}_5\text{Hf}$  and  $\text{Ni}_3\text{Al-Ni}_5\text{Hf-Ni}_7\text{Hf}_2$  as reported in the 800°C isothermal section [34], were also found to be present in the 1000°C isothermal section [35]. The calculated isothermal section at 800°C [32,36] showed the presence of a  $\text{Ni-Ni}_5\text{Hf-Ni}_7\text{Hf}_2$  three phase field and thus does not take into account the above mentioned transition type reactions [35].

## 2.3. STRUCTURE OF $\gamma'$ ( $\text{Ni}_3\text{Al}$ ) PHASE

### 2.3.1. Unit cell

This is the intermediate compound which constitutes the principal

precipitating second phase in nickel base superalloys. It is denoted as  $\gamma'$  phase.  $\text{Ni}_3\text{Al}$  has  $\text{Cu}_3\text{Au}$  type structure and has Strukturbericht designation of  $\text{L1}_2$ . Figure 2.7 shows the schematic unit cell where nickel atoms occupy face centered positions and aluminium atoms are at the cube corners. The degree of order may differ from unity because the intermediate phase exists over a range of composition on both sides of the stoichiometry. Ordering in fcc materials can be conveniently described by considering the lattice as produced by four interpenetrating simple cubic sublattices of equal sizes. The lattice points at the cube corners of the fcc unit cell constitute one sublattice and each pair of points at the centres of the opposite faces generate one sublattice in combination with similar lattice points on the neighbouring unit cells. The  $\text{L1}_2$  structure of ordered  $\text{Ni}_3\text{Al}$  is generated when one of the four sublattices is occupied by only aluminium atoms.

Based on the lattice parameter and density variation with composition, Aoki et al. [45,46] concluded that in the nickel-rich side, all the aluminium atoms occupy cube corner sites and the nickel atoms occupy all face centre sites and vacant cube corner sites of the unit cell, while in the aluminium-rich side, all nickel atoms occupy face centre sites and aluminium atoms occupy all cube corner sites and vacant face centre sites of the unit cell. Consequently, these were respectively expressed as  $\text{Ni}_3(\text{Al}, \underline{\text{Ni}})$  and  $(\text{Ni}, \underline{\text{Al}})_3\text{Al}$  where underlined letters indicate type of excess atoms.

### 2.3.2. Ordering in $\text{Ni}_3\text{Al}$

Schramm [47] in 1941 obtained superlattice lines at room temperature in samples quenched from temperatures upto  $1300^\circ\text{C}$  (but it is possible that rapid ordering during quenching could mask any disorder

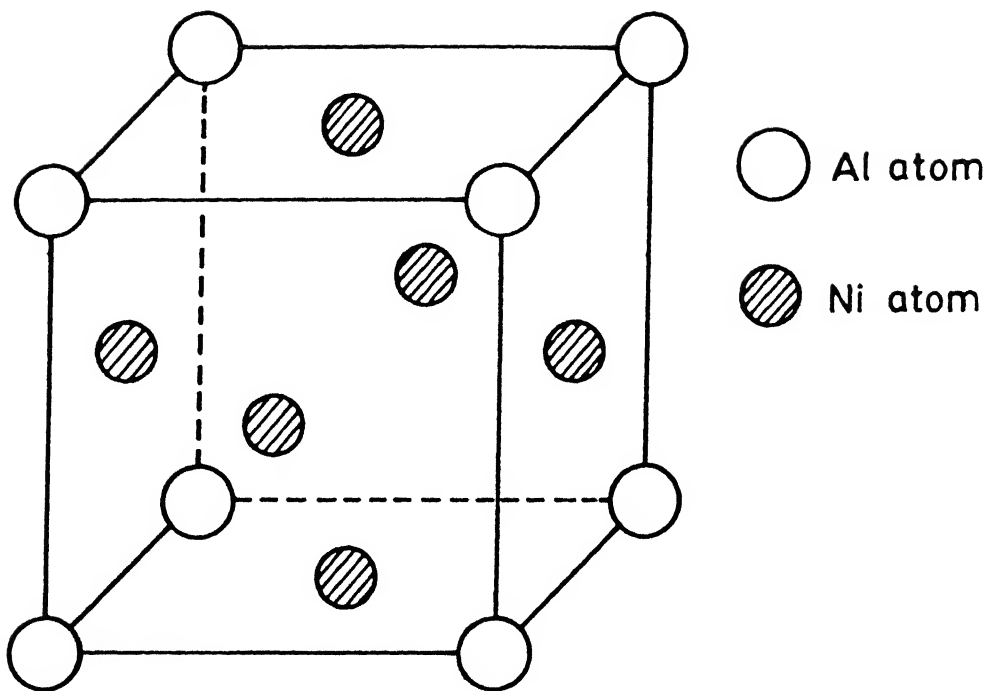


Fig. 2.7: Unit cell of  $\text{Ni}_3\text{Al}$  ( $\text{L1}_2$  structure).



present at higher temperatures). Measurements at elevated temperatures have shown that the (100) superlattice line becomes diffuse but is still present at 1000°C [48]. Corey and Lisowsky [49] in 1967 concluded that Ni<sub>3</sub>Al disorders between 1100°C and 1300°C. Since then, lot of research has been carried out on ordering in Ni<sub>3</sub>Al and related compounds. Stoeckinger and Newmann [50] studied ordering in Ni<sub>3</sub>Al in both stoichiometric and in off-stoichiometric nickel-rich alloys. The measurements were carried out on {h00} single crystals. They found a strong (100) line present in both cases at 1320°C. As can be seen from the constant values of the long range parameter, S, for both compositions (Figure 2.8), complete long range order is maintained upto the highest temperatures investigated. Theoretically, the maximum value which 'S' can attain is 1.00 for complete order and the values of 1.12 and 1.37 for the off-stoichiometric and stoichiometric Ni<sub>3</sub>Al respectively must be due to some error in calculating the structure factor for superlattice lines. Based on the electrical resistivity measurements [49], it has been claimed that off-stoichiometric Ni<sub>3</sub>Al with 22.5 at.% Al disorders in the temperature range from 1100°C and 1330°C. Stoeckinger and Newmann [50] rejected this due to the fact that  $\gamma'$  alloy with less than 23 at.% Al will enter ( $\gamma' + \gamma$ ) two phase region in the proximity of 1100°C [22]. The appearance of  $\gamma$  phase may be responsible for the decrease in the resistivity. A further indication can be found in the lattice parameter measurements. Upto about 1000°C, the lattice parameter of the off-stoichiometric Ni<sub>3</sub>Al increases linearly but above this temperature, the lattice parameter increases more rapidly. This again is indicative of changing from single to two phase region, since the composition of the off-stoichiometric crystal would change towards the stoichiometric composition which has a larger lattice parameter.

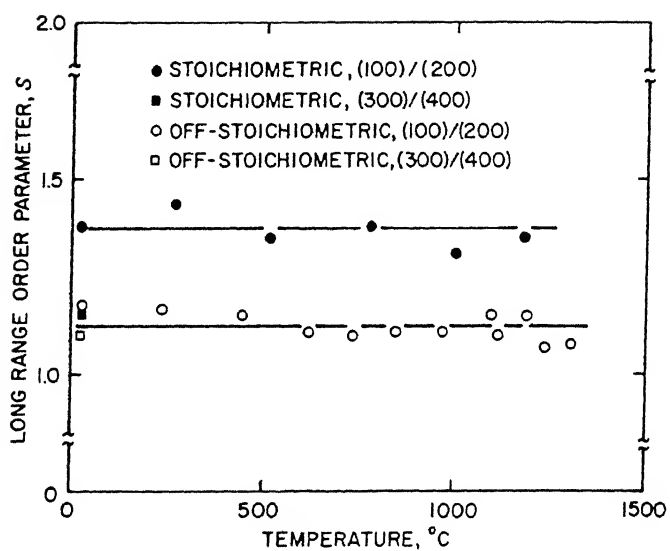


Fig. 2.8: Long-range order parameter,  $S$ , as a function of temperature for stoichiometric and off-stoichiometric  $\text{Ni}_3\text{Al}$  [50].

Even though Stoeckinger and Newmann [50] showed that stoichiometric and off-stoichiometric  $\text{Ni}_3\text{Al}$  maintain order upto the highest working temperatures, unfortunately, their results showed that the value of 'S' is substantially greater than one. This large values of 'S' casts some doubt on the validity of the measurements and hence, Pope and Garin [51] decided to carry out further measurements. They took extreme care to avoid extinction effects by using a fine particle size. They calculated the long range order parameter as a function of temperature. These values appear to be somewhat less than one but greater than 0.9 (Figure 2.9). They also concluded that 'S' remains constant below  $1300^\circ\text{C}$ .

Significant anomalies which exist in lattice parameter and order parameter determinations triggered further investigations. Masahashi et al. [52] observed that the  $\text{L1}_2$  structure gets further stabilized significantly with ternary additions such as carbon and boron even in off-stoichiometric compositions. Noguchi et al. [53] found that with an increasing alloy addition in the off-stoichiometric compositions within the phase region of  $\text{Ni}_3\text{Al}$  (23-27 at% Al), the phase stability of an  $\text{L1}_2$  structure with respect to the  $\text{DO}_{22}$  as well as  $\text{DO}_{19}$  is reduced. These two observations made Ramesh et al. [54] to do further research on this aspect. Ramesh et al. [54] also calculated the long range order parameter, S, for stoichiometric as well as nickel-rich off-stoichiometric  $\text{Ni}_3\text{Al}$  with and without boron addition (Figure 2.10 and 2.11). Systematic study was carried out on the (100/200) and (110/220) reflections at various temperatures. The split reflections seen at the (100), (110) and (200) locations could be indexed as the (100)(001), (110)(011) and (200)(002) reflections indicative of a tetragonal lattice with lattice constants 'a'  $\approx$  0.35786 nm and 'c'  $\approx$  0.35697 nm, whereas the lattice constant of the  $\text{L1}_2$  structure of

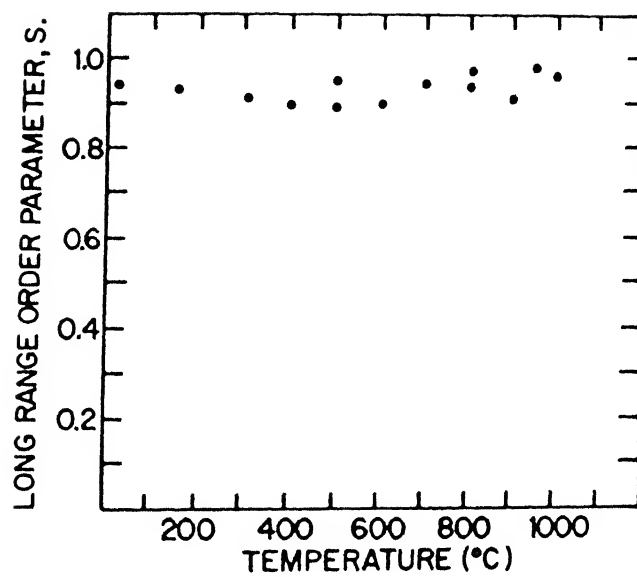


Fig. 2.9: Long-range order parameter,  $S$ , as a function of temperature for stoichiometric  $\text{Ni}_3\text{Al}$  [51].

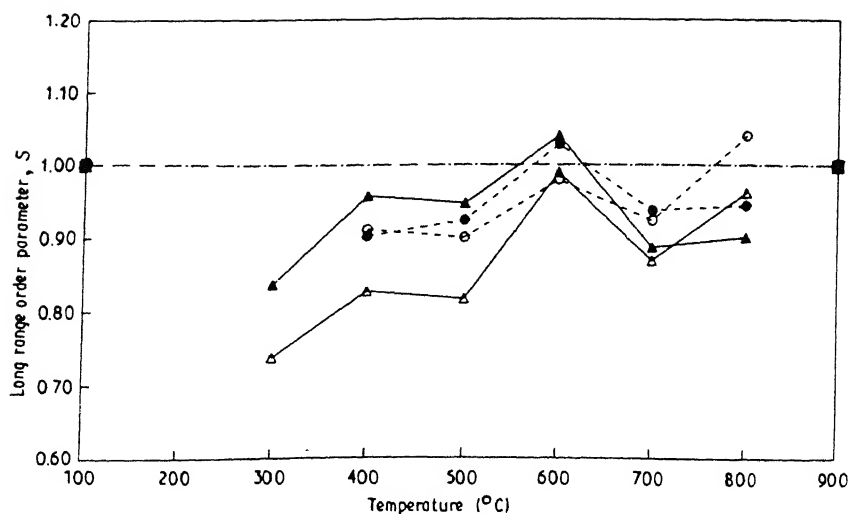


Fig. 2.10: Long-range order parameter,  $S$ , as a function of temperature for stoichiometric  $\text{Ni}_3\text{Al}$  (with and without boron). Order parameter,  $S$ : without B,  $\Delta$ , (100/200);  $\blacktriangle$ , (110/220); with B,  $\circ$ , (100/200);  $\bullet$ , (110/220);  $\blacksquare$ , theoretical [54].

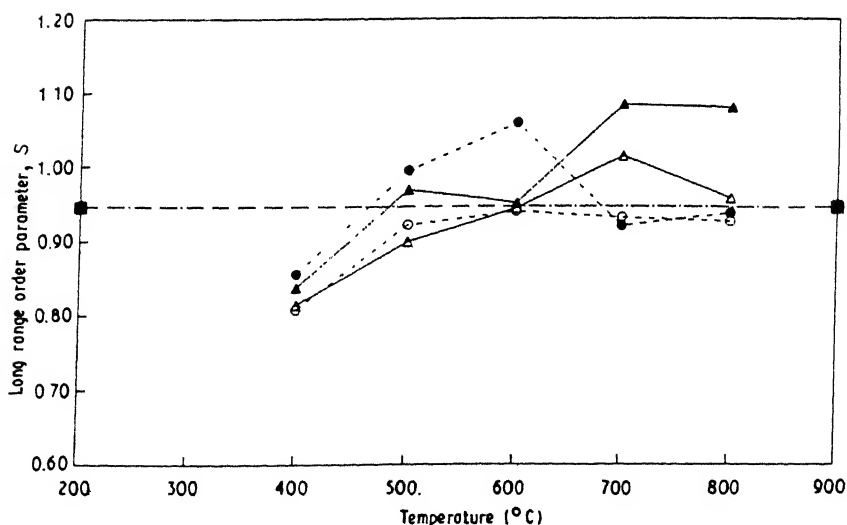


Fig. 2.11: Long-range order parameter,  $S$ , as a function of temperature for Ni-rich off-stoichiometric  $\text{Ni}_3\text{Al}$  (with and without boron addition). Order parameter,  $S$ : without boron,  $\Delta$ , (100/200);  $\blacktriangle$ , (110/220); with boron,  $\circ$ , (100/200);  $\bullet$ , (110/220);  $\blacksquare$ , theoretical [54].

this composition,  $\text{Ni}_{76}\text{Al}_{24}\text{B}_{0.1}$ , is 0.3571 nm. Similarly, indexing was also possible for other compositions and this led to the conclusion that the tetragonal structure identified could perhaps be the  $\text{DO}_{22}$  structure. It appears that this phase is more stable than the  $\text{L1}_2$ , not merely when there is an increased proportion of the minority component as stated by Noguchi et al. [53] but even otherwise when the temperature reaches a value close to  $1000^\circ\text{C}$ . The existence of two different structures was also confirmed by further experiments at  $1000^\circ\text{C}$  and  $600^\circ\text{C}$  [54]. Finally Ramesh et al. [54] concluded that the  $\text{L1}_2$  structure in  $\text{Ni}_3\text{Al}$  is not stable upto its melting point as has been widely believed to be the case. The  $\text{L1}_2$  structure attains a maximum stability at about  $600^\circ\text{C}$  where the order parameter attains the near theoretical value. As the temperature exceeds  $600^\circ\text{C}$ , the order parameter goes down and  $\text{L1}_2$  structure becomes unstable in relation to one or more other structures. These different structures appear to be thermodynamically stable and their exact crystal structures are difficult to ascertain at present.

### 2.3.3. Lattice parameter

A detailed study has been made on the effect of heat treatment and composition on the lattice parameter of  $\text{Ni}_3\text{Al}$  by Taylor et al. [23] and Bradley et al. [55]. Masahashi et al. [52], Ramesh et al. [54] and Young et al. [56] have also measured the lattice parameter of  $\text{Ni}_3\text{Al}$ . The available literature values of lattice parameters of  $\gamma'$  phase suggest a wide variation of lattice parameter with heat treatment [57]. For example, the lattice parameters of slow cooled and quenched samples of  $\gamma'$  phase containing 26.25 at.% Al have been found to vary by as much as 0.02 Å [55]. This clearly indicates that cooling rate has a strong effect on the lattice parameter of the  $\gamma'$  phase. The lattice parameters determined by Bradley et al. [55] and Young et al. [56] for  $\gamma'$  phase

containing 25 at.% Al, which were slow cooled, show a difference of as much as 0.02 Å. This only shows that further investigation needs to be made on the lattice parameter of  $\gamma'$  phase as a function of heat treatment parameters. The effect of heat treatment on the lattice parameter is thoroughly discussed in Chapter-V.

The effect of solute elements on the lattice parameter of  $\text{Ni}_3\text{Al}$  is shown in Figure 2.12 [58]. The effect of boron on the lattice parameter of  $\text{Ni}_3\text{Al}$  is shown in Figures 2.13 [59], 2.14 [60], 2.15 [52] and 2.16 [56].

## 2.4. ALLOYING BEHAVIOUR OF SOLUTES

### 2.4.1. Substitutional solutes

One of the main advantages of  $\text{Ni}_3\text{Al}$  is its ability to form solid solutions with many elements. It forms substitutional solid solutions with elements having large atomic diameters. The properties of substitutional solid solutions depend greatly on what site the ternary additions substitute. Accordingly, the substitutional solutes are broadly classified into three categories :

(i). Solute replacing nickel atoms : The solubility lobes of the ternary system shift from nickel side to ternary addition side.

(ii). Solute replacing aluminium atoms : The solubility lobes of the ternary system shift from aluminium side to ternary addition side.

(iii). Solute replacing both atoms: The solubility lobes extend almost bisecting the quasi-binary section  $\text{Ni}_3\text{Al.Ni}_3\text{X}$  and  $\text{Ni}_3\text{Al.X}_3\text{Al}$ .

There have been many attempts to predict the occupation site of ternary elements in  $\text{Ni}_3\text{Al}$ . Guard and Westbrook [61] studied the substitutional behaviour of various ternary elements from the direction of solubility lobe of  $\text{Ni}_3\text{Al}$  in ternary phase diagram which was later

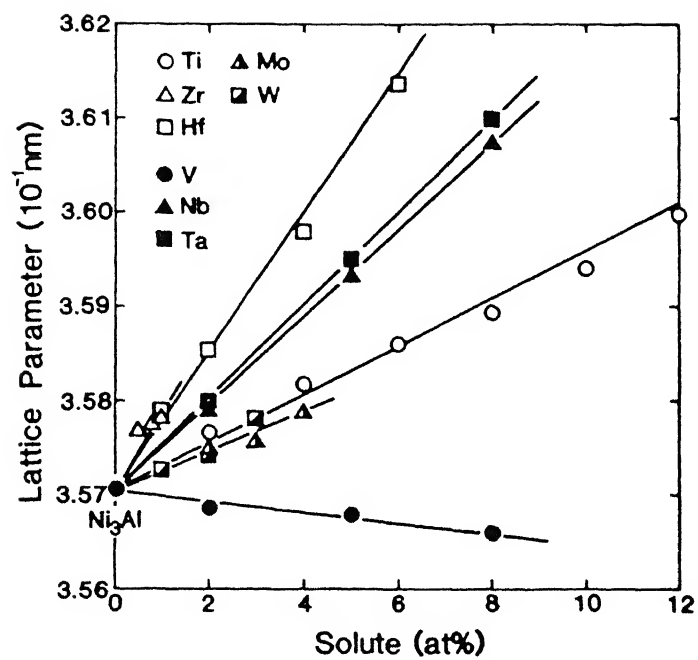


Fig. 2.12: Lattice parameter change in  $\text{Ni}_3\text{Al}(\gamma')$  with additions of transition metals [58].



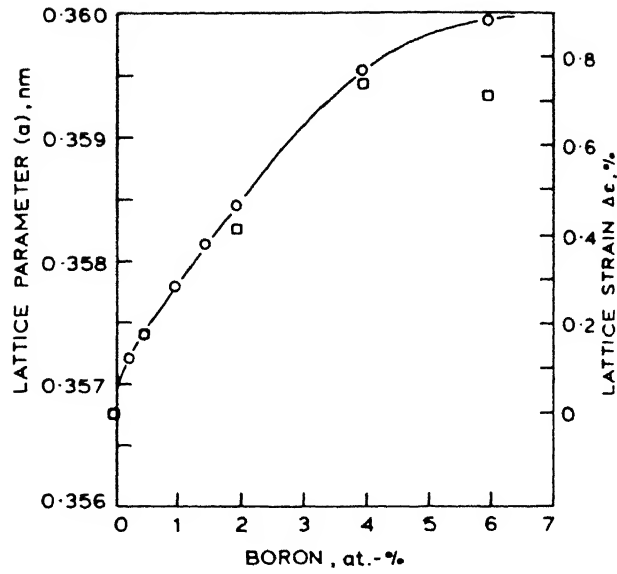


Fig. 2.13: The lattice parameter and the lattice strain as a function of the boron concentration in melt-spun  $\text{Ni}_3\text{Al}$ . O, measured on the wheel-contacting surface of the ribbons;  $\square$ , measured on the non contacting surface of the ribbons [59].

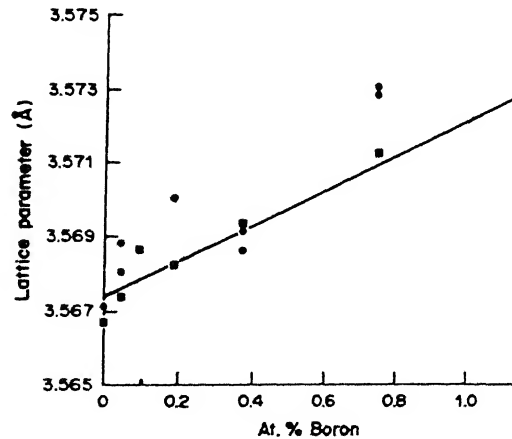


Fig. 2.14: Lattice parameter of stoichiometric  $\text{Ni}_3\text{Al}$  as a function of boron content. The squares and the line connecting them are for furnace-cooled samples. Other points are for air-cooled samples [60].

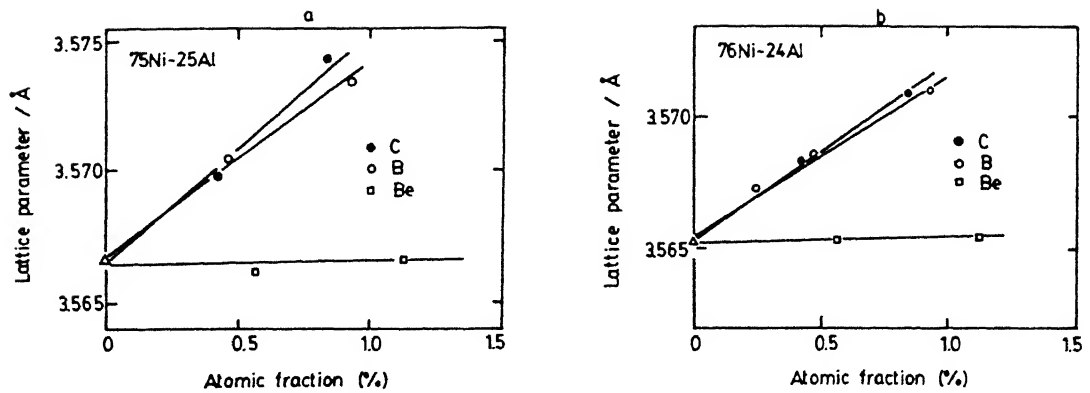


Fig. 2.15: Changes in lattice parameter of the  $\text{Ni}_3\text{Al}$  with additions of C, B and Be atoms [52].

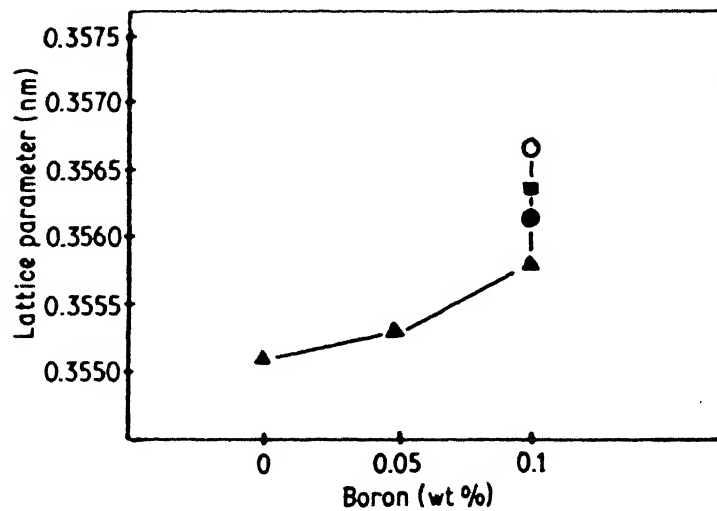


Fig. 2.16: Effect of boron and heat treatment on lattice parameters at room temperature in  $\text{Ni}_3\text{Al}$ : (O) 800°C/3h; (■) 900°C/5h; (▲) 900°C/5h+1100°C/5h; (●) rapidly solidified material [56].

extended by Rawlings et al. [62] and Ochiai et al. [63] and then subsequently reviewed by Stoloff [64]. The solubility lobes for various elements in  $\text{Ni}_3\text{Al}$  at 1273K [63,65] are shown in Figure 2.17.

Substitution behaviour of ternary elements in  $\text{Ni}_3\text{Al}$  is given in Table 2.1. An overwhelmingly large number of substitutional solutes replace aluminium atoms. There is a disagreement in the literature as to the site occupancy by hafnium, molybdenum, tungsten, tantalum and manganese. Although the expectation based on the phase diagram is that hafnium occupies aluminium sites [34], Ochiai et al. [63] suggest that hafnium can be found on aluminium as well as nickel sites; atom probe experiments by Miller and Horton [66,67] show a strong preference for aluminium sites. Bentley [68] has reached the same conclusion from zone-axis ALCHEMI results. Brenner and coworkers [69] using atom probe concluded that hafnium predominantly occupies the nickel sites; also in agreement with this are the results of RBS/ion-channeling experiments by Bohn et al. [70] and perturbed angular correlation (PAC) results of Bohn and coworkers [71]. While the X-ray results of Lin and Pope [72] show that tantalum occupy the aluminium sites for tantalum contents above 0.2 at.%; using ion-channeling technique with Rutherford back scattering (RBS) and nuclear reaction analyses, Lin et al. [73] concluded that tantalum predominantly occupies nickel sites. X-ray diffraction data indicate that chromium, molybdenum and tungsten substitute on both the sites [74,75], but chemical analysis of extracted precipitates suggest that molybdenum and tungsten substitute mainly for aluminium site [76,77]. Based on electronic consideration, Rawlings et al. [62] concluded that molybdenum and tungsten substitute for both the sites. X-ray results of Aigeltinger et al. [78] confirms that molybdenum substitutes for aluminium sites. Although manganese is expected to

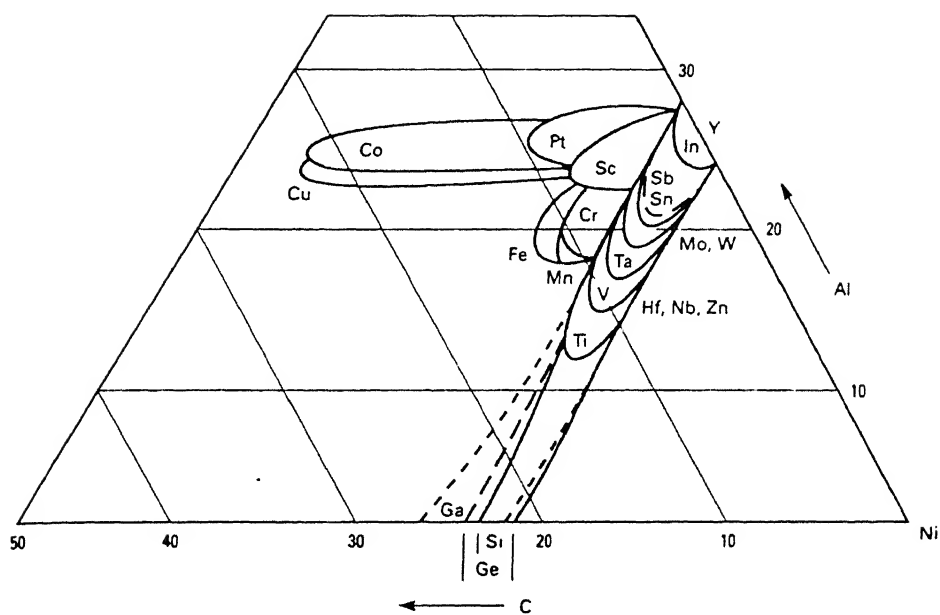


Fig. 2.17: Semischematic depiction of the solubility lobes of ternary  $\text{Ni}_3\text{Al}$  phase around  $1000^\circ\text{C}$  [63].

Table 2.1

Substitutional behaviour of ternary additions in  $\gamma'$  alloys

Sites substituted			Ref <sup>*</sup>	Remarks
Ni	Al	Ni and Al		
	Hf		34	Phase diagrams
Co, Cu	Si, Ti, V, Mn	Cr, Fe	61	Phase diagrams
Co, Cu	Si, Ti, V, Mn, Nb, Hf, Ta	Cr, Fe, Mo, W	62	Electronic consideration
	Ga, Ge, Hf, In, Mo, Nb, Sn, Sb, Si, Ta, Ti, V, W, Zr	Cr, Mn	63	Theoretical consideration involving the nearest neighbour interactions.
Co	Hf	Fe	66, 67	Atom probe field ion microscopy
	Hf		68	Zone axis ALCHEMI
Hf		Hf	69	Atom probe technique
			70	RBS/ion-channelling technique.
Hf			71	Perturbed angular correlation technique.
	Ta		72	X-ray diffraction
Ta			73	Ion-channelling technique with RBS and nuclear reaction analysis.
Co	Ti, V, Nb, Ta	Cr, Mo, W	74	X-ray diffraction
	Mo, W	Cr, Mo, W	75	X-ray diffraction
			76	Chemical analysis of extracted precipitates
Co, Fe	Ti, V, Nb, Mo, Ta, W	Cr	77	Analysis of $\gamma'$ precipitate
	Mo		78	X-ray diffraction method
Cu		Mn	79	Cluster variation method
	.	Fe	80	ALCHEMI
Pd			81	ALCHEMI
Cu			83	Atom probe field ion microscopy
	Nb		85	Phase diagrams
	Ti, Cr	W	86	X-ray diffraction
	Nb		87	Analysis of $\gamma'$ precipitate
		Fe	88, 89	Mossbauer spectroscopy
Pd			90	Cluster variation method

Ref<sup>\*</sup> : Reference.

substitute for aluminium sites based on the phase diagram [61], it has been also shown that manganese substitutes for both nickel as well as aluminium sites [63,79]. It is interesting to note that for 2.5 at.% Fe in  $\text{Ni}_3\text{Al}$ , 78% of iron atoms occupy sites on the aluminium sublattice while in  $\text{Ni}_3\text{Al}$  containing 9.3 at% Fe, only 54% of iron atoms occupy sites on the aluminium sublattice. This analysis shows that the proportions of iron on aluminium and nickel sublattices vary with iron content [89]. This has also been confirmed by Shindo et al. [80].

Ochiai et al. [63] investigated the substitution behaviour of transition metal elements in  $\text{L1}_2$  type compounds like  $\text{Ni}_3\text{Al}$  etc. based on Bragg-Williams approximation of 'Nearest Neighbour Interaction'. This was further revised by Chiba et al. [81]. Figure 2.18 [81] indicates the correlation between the pair interaction parameter ratios of  $V_{\text{NiC}}/V_{\text{NiAl}}$  and  $V_{\text{AlC}}/V_{\text{NiAl}}$  for various ternary elements with the site preferences in  $\text{Ni}_3\text{Al}$  compounds. The data points for various ternary elements were evaluated using the Miedema's semi-empirical formula [82]. Ochiai et al. [63] suggested a relation for evaluating the site preference of 'C' atom in  $\text{A}_3\text{B}$  intermetallic compounds, using a parameter 'K', as :

$$K = \frac{V_{\text{AC}}}{V_{\text{AB}}} - \frac{V_{\text{BC}}}{V_{\text{AB}}} - P \quad (2.5)$$

where

$V_{ij}$  = Pair interaction parameter of i and j species;

$V_{ij} = H_{ij} - (H_{ii} + H_{jj})/2$  ;

P = Asymmetric index which depends only on the nature of the

alloy =  $2 - 3/2(H_{ii} - H_{jj})V_{ij}$  ;

$H_{ii}$ ,  $H_{jj}$  and  $H_{ij}$  = The bond energies of 'ii', 'jj' and 'ij' respectively.

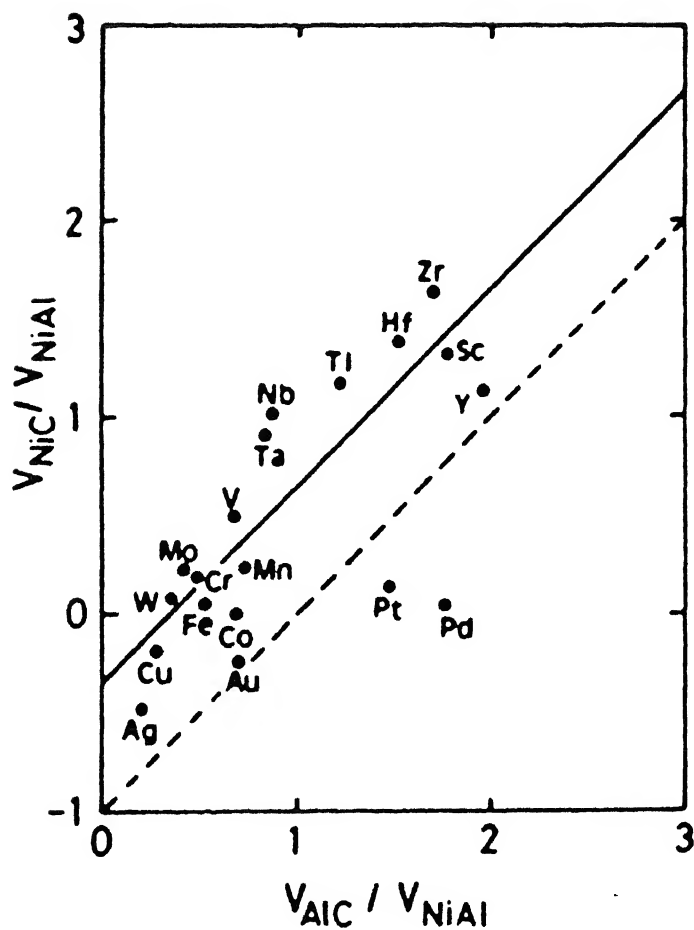


Fig. 2.18: The substitution behaviour of ternary addition in  $Ni_3Al$  [81].

The above condition was modified by Chiba et al. [81] as

$$\frac{V_{\text{NiC}}}{V_{\text{NiAl}}} < \frac{V_{\text{AlC}}}{V_{\text{NiAl}}} - 1 \quad (2.6)$$

According to Ochiai et al. [63], the elements situated above the solid line ( $K>0$ ) in Figure 2.18 substitute for aluminium sites independent of the composition whereas those below the solid line ( $K>0$ ) in Figure 2.18 substitute for nickel sites. Furthermore, the dotted line, after Chiba et al. [81] in Figure 2.18, divides the ternary elements substituting for the nickel site into two parts. That is, the elements situated below the dotted line always substitute for nickel site regardless of the composition of the host elements. On the other hand, the elements situated between the solid line and the dotted line substitute for the nickel site and the aluminium site if the ternary alloying elements are added in the compositions of  $\text{Ni}_{75-X}\text{Al}_{25}\text{C}_X$  and  $\text{Ni}_{75}\text{Al}_{25-X}\text{C}_X$  respectively. According to this diagram, copper is supposed to have a composition dependence in its site preference. However, copper has been predicted to prefer the nickel site based on its electronic similarity with nickel [62], the direction of the solubility lobe [61] and a more elaborate evaluation by the cluster variation method [79]. The recent atom probe field ion microscopy work [83] also showed that copper has very strong site preference to the nickel even in nickel-rich  $\text{Ni}_3\text{Al}$ . So, it has been concluded that the accuracy of the pair interaction parameters evaluated from Miedema's formula may not be satisfactory for predicting the site preference for some of the species [83].

It has been suggested that the stronger the tendency for a ternary element to substitute for nickel site, the more the ordering energy of  $\text{Ni}_3\text{Al}$  degrades [79,84]. A further investigation [16] revealed that the improvement in the ductility of  $\text{Ni}_3\text{Al}$  could be achieved by the addition



of elements, such as platinum, copper, cobalt as well as palladium, all of which have strong preference to nickel sites.

## 2.4.2. Interstitial solutes

### 2.4.2.1. Boron

As for the small atoms which substitute interstitially in  $\text{Ni}_3\text{Al}$ , extensive research has been done on boron because of its beneficial effect of improving ductility of polycrystalline  $\text{Ni}_3\text{Al}$ . Using Debye-Scherrer technique and X-ray diffractometry, Masahashi et al. [52] showed that boron prefers to occupy the interstitial body centred position of  $\text{L1}_2$  structure, that is, to form the Perovskite structure (or the  $\text{L}'1_2$  structure). Using ion-channelling technique with nuclear reaction products analysis, Bohn et al. [70] came to the definite conclusion that boron occupies the octahedral interstitial sites.

The effect of boron doping can be considered as if the boron atom acts as an electron donor where the electronic charge distribution is deficient. It has been suggested that in a grain boundary of pure nickel, boron acts as an electron donor and thereby strengthens the atomic bond at the grain boundary [91]. Also, the beneficial effect of boron on the grain boundary cohesive strength of  $\text{Ni}_3\text{Al}$  alloys was indicated by first principle cluster variation [92], cluster calculation of density of state [93], tight binding electron theory [94] and embedded atom potentials [95].

In polycrystalline  $\text{Ni}_3\text{Al}$  containing 24 at.% Al, the tensile elongation is found to be maximum (about 53%) for a concentration of about 0.1 wt.% boron ( $\approx 4700$  at.p.p.m.) [13] which is well within the solubility limit. Chaki [96] has calculated that the optimum concentration of boron atoms necessary to obtain maximum ductility in  $\text{Ni}_{76}\text{Al}_{24}$  is 3900 at.p.p.m. which is in reasonable agreement with the

experimental value of 4700 at.p.p.m. by Liu et al. [13]. Using X-ray diffraction, differential thermal analysis and transmission electron microscopy, it is shown that by rapid solidification melt spinning process, upto 1.5 atom percent boron can be held in solution in the aluminide without formation of boride [59]. However, at boron doping levels greater than 1.5 atom percent,  $M_{23}B_6$  borides precipitate at the grain boundaries and the alloy once again exhibits brittle intergranular fracture [97].

Both auger microprobe [13,98] and imaging atom probe [99,100,101] studies have shown that boron segregates strongly to grain boundaries in  $Ni_3Al$ , the extent of segregation varying from boundary to boundary. The depth of boron segregation is only a few layers adjacent to the boundaries.

It is important to note that boron segregation is an equilibrium segregation [102]. The segregation behaviour of boron has been expressed by the following equation ;

$$\frac{Y_B^\sigma (1-Y_B^\alpha)}{Y_B^\alpha (1-Y_B^\sigma)} = \exp\left[\frac{\Delta S_B}{k}\right] \exp\left[\frac{-\Delta H_B}{kT}\right] \quad (2.7)$$

where  $Y_B^\sigma$  = Equilibrium boron segregation to grain boundaries;

$Y_B^\alpha$  = Equilibrium boron concentration in the bulk;

$\Delta S_B$  = Entropy of adsorption of boron;

$\Delta H_B$  = Enthalpy of adsorption of boron.

It is clear from the above equation that the equilibrium grain boundary concentration of boron increases with increasing amount of boron content of bulk and decreasing temperature.

The change in ductility with temperature in boron-doped  $Ni_3Al$  has been observed by a number of workers [103,104]. Slow cooling from  $1050^\circ C$  enhances intergranular segregation of boron in the grain boundaries

while rapid quenching causes a low concentration of boron in the grain boundaries. This result is entirely reversible indicating the equilibrium nature [103] of the boron segregation in  $\text{Ni}_3\text{Al}$  grain boundaries. This observation implies that boron tends to segregate strongly to the grain boundaries at low temperatures while it boils off from the grain boundaries with increasing temperature at  $1050^\circ\text{C}$ . This thermal behaviour accounts for, at least partially, the high temperature weakness of the grain boundaries in this alloy.

#### 2.4.2.2. Other interstitial solutes

Among the interstitial solutes, apart from boron, the alloying behaviour of carbon has been studied in detail. Other interstitial elements like oxygen, nitrogen and hydrogen were excluded because they are gaseous elements. It is not easy to control the alloy composition, particularly of gaseous atoms.

Using X-ray diffractometry and Debye-Scherrer technique, Masahashi et al. [52] showed that, like boron, carbon also prefers to occupy the interstitial body centred position of  $\text{L1}_2$  structure. In rapidly solidified (i.e. non-equilibrium)  $\text{Ni}_3\text{Al}$  doped with carbon [105,106], carbon atoms interstitially occupy the body centred site in  $\text{Ni}_3\text{Al}$  and then induce further ordering of  $\text{Ni}_3\text{Al}$  through the cooperative ordering of the substitutional atoms (Ni and Al). The addition of carbon atoms, like boron, induces further ordering of constituent atoms. This is more significant at the off-stoichiometric compositions of  $\text{Ni}_3\text{Al}$  [52]. Masahashi et al. [52] proposed that the strongly attractive interaction between nickel and interstitial atoms stabilizes the  $\text{L1}_2$  structure of  $\text{Ni}_3\text{Al}$ .

Like boron, carbon also shows the tendency of segregating to the grain boundaries and causes a large strengthening effect [107].

Segregation of carbon atoms to the grain boundaries in rapidly solidified  $\text{Ni}_3\text{Al}$  has been detected by Auger electron microscopy also [108]. The amount of carbon segregation to the grain boundaries is controlled by the bulk concentration and is unaffected by matrix stoichiometry [108] and the grain boundaries get slightly enriched in aluminium also. Although carbon shows the tendency to segregate to the grain boundaries, it does not improve the ductility of  $\text{Ni}_3\text{Al}$  like boron [109]. The reason can be found in the light of the mechanism proposed by Chaki [110]. The carbon atoms do not form strong bonds with either nickel or aluminium atoms and therefore, can not reduce the strength of the directional bonding between nickel and aluminium atoms.

## 2.5. DIFFUSION IN BORON-FREE AND BORON-DOPED $\text{Ni}_3\text{Al}$

Diffusion of atoms in ordered intermetallics is comparatively difficult due to the constraints put by ordering. This is the main source of the high temperature capabilities of these alloys. In  $\text{Ni}_3\text{Al}$ , diffusivity studies have been carried out in both boron-free and boron-doped alloys [111,112,113].

Tracer diffusion measurements of Ni have been conducted in  $\text{Ni}_3\text{Al}$  for various aluminium contents in the range of 920–1200°C [111,112]. These studies indicated that the diffusivity of nickel is independent of composition and the activation energy for diffusion is insensitive to aluminium content. Therefore, the constitutional vacancies do not contribute to diffusion in off-stoichiometric alloys. Aoki and Izumi [45] also did not find any evidence for constitutional vacancies on either side of stoichiometry. Rather, substitutional anti-site defects occur.

Later work by Hoshino et al. [113] showed that the diffusivity of  $^{63}\text{Ni}$  in  $\text{Ni}_3\text{Al}$  is independent of aluminium content in binary  $\text{Ni}_3\text{Al}$  at

temperatures exceeding  $1000^{\circ}\text{C}$  but there is a minimum in diffusivity at 25 at.% Ni between  $692$  and  $1000^{\circ}\text{C}$ . Further the addition of boron resulted in increased diffusivity of nickel for all aluminium contents studied at  $1200^{\circ}\text{C}$  and in stoichiometric alloys at all temperatures in the range  $692$ - $1352^{\circ}\text{C}$ . The diffusivity of Ni in binary  $\text{Ni}_3\text{Al}$  is shown in Figure 2.19 [113]. The Arrhenius plot is curved. At lower temperatures, there is a small temperature independent vacancy concentration i.e. the constitutional vacancies. Boron seems to interact with vacancies in off-stoichiometric alloys. Earlier, positron annihilation studies showed such interaction only in nickel-rich alloys [114], indicating that boron can not diffuse to grain boundaries in stoichiometric or aluminium-rich alloys. Positron work indicated that these vacancies existed in both stoichiometric and off-stoichiometric alloys [114,115] while the tracer experiments indicated vacancy occupancy on the nickel-sublattice on either side of stoichiometry [113]. Figure 2.19 shows a good agreement in the temperature dependence of diffusivity of Ni in  $\text{Ni}_3\text{Al}$  by various workers, especially at high temperatures.

The diffusion constant ' $D_0$ ' measured above  $1000^{\circ}\text{C}$  is more than 100 times larger than that usually found for single vacancy controlled diffusion in fcc metals [113]. Also, the activation energy normalized for melting temperature  $T_m$  is 30 to 40% higher than usual, perhaps because of a higher activation energy for vacancy motion due to ordering.

However, previous work in the range  $800$ - $1212^{\circ}\text{C}$  indicated no effect of boron (or 0.5 at.% Hf) on the activation energy for diffusion of  $\text{Ni}_3\text{Al}$ ; also, aluminium contents in the range 23.5 - 26 at.% Al provided values of  $Q = 273$ - $301$  kJ/mol for volume diffusion with no clear trend with aluminium content [116].

Grain boundary diffusivities in  $\text{Ni}_3\text{Al}$  have been measured in

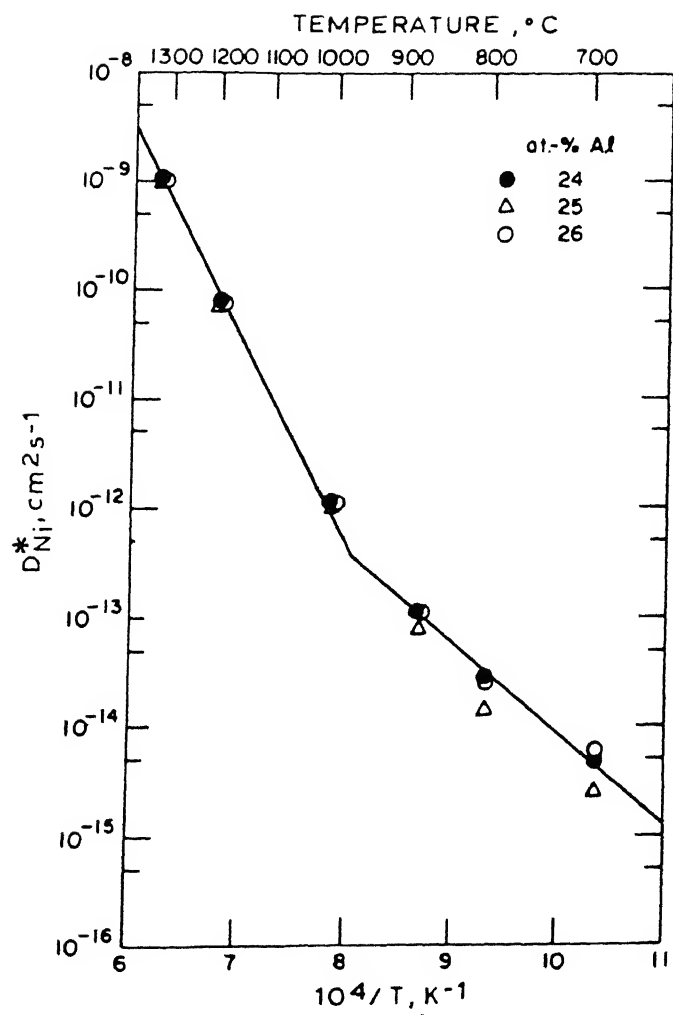


Fig. 2.19: Temperature dependence of  $D_{Ni}^*$  in  $\text{Ni}_3\text{Al}$  [113].

Ni/Ni<sub>3</sub>Al+B and Ni/Ni<sub>3</sub>Al+B+Hf couples at temperatures in the range of 955-1124°C [116]. It was concluded that the grain boundary diffusion of Ni is 5 - 6 orders of magnitude greater than the volume interdiffusion coefficient in this temperature range. However, the activation energy for grain boundary diffusion is higher than that for volume diffusion [116,117]. Minamino et al. [118] have shown that the diffusion behaviour of substitutional solutes like cobalt, chromium and titanium in Ni<sub>3</sub>Al is found to be closely associated with the substitution behaviour of these elements.

## 2.6. YIELDING BEHAVIOUR OF $\gamma'$

### 2.6.1. Temperature dependence of yield stress

The yield or flow stress of both single and polycrystalline Ni<sub>3</sub>Al has been observed to increase with increase in temperature. This anomalous variation in flow stress was first observed by Flinn [119] in polycrystalline Ni<sub>3</sub>Al. Figure 2.20 [120] shows the variation of yield stress of Ni<sub>3</sub>Al with temperature. Figure 2.20 also compares the yield strengths of Ni<sub>3</sub>Al alloys with conventional commercial alloys. The figure shows a peak in the yield stress of Ni<sub>3</sub>Al in the temperature range of 600-700°C. The position of the peak stress and its height has been found to be a function of crystal orientation, solute addition and grain size [11,121,122,123]

### 2.6.2. Mechanism of yielding

The yield stress anomaly is associated with a number of other effects which are listed below [124] :

**Slip systems :** The slip system over the temperature range of the yield stress anomaly is {111}<110>. Above the yield stress peak, slip transfers progressively to the cube plane and two new slip systems

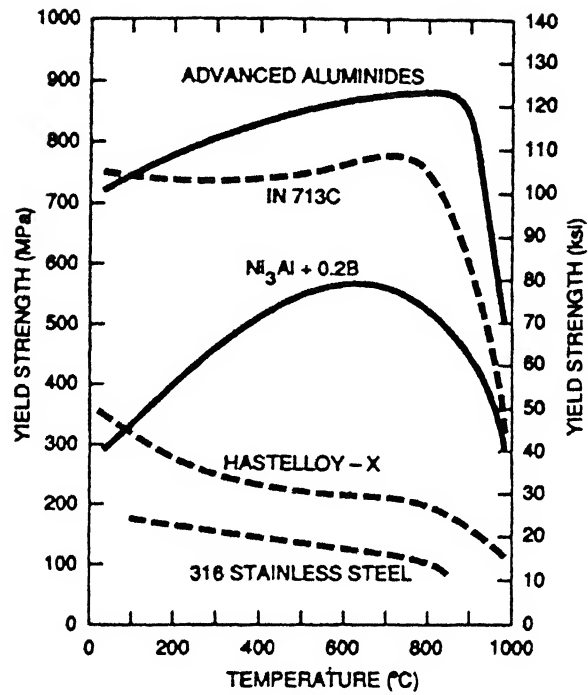


Fig. 2.20: Yield strength as a function of temperature for Ni<sub>3</sub>Al alloys (advanced aluminide alloy and Ni<sub>3</sub>Al+0.2B), compared with a few conventional commercial alloys (IN 713C, Hastelloy-X and 316 stainless steel) [120].



operate:  $\{001\}\langle 110 \rangle$  and  $\{001\}\langle 100 \rangle$  [125-127]. At low temperatures, there is evidence [128] for abundant cross-slip between (111) and  $(\bar{1}\bar{1}1)$ . The yield stress anomaly is associated specifically with the APB-coupled  $(111)[\bar{1}01]$  slip system.

$$[\bar{1}01] \longrightarrow 1/2[\bar{1}01] + \text{APB}(111) + 1/2[\bar{1}01] \quad (2.8)$$

**Rate sensitivity of the yield stress :** While the yield stress increases with temperature, it is very insensitive to changes in the imposed strain rate [129]. The rate sensitivity parameter is  $10^{-5} \text{ K}^{-1}$  over the whole temperature range and reaches a minimum to  $10^{-6} \text{ K}^{-1}$  close to the peak in the yield stress.

**Thermal reversibility of the yield stress :** If a specimen of  $\text{Ni}_3\text{Al}$  is deformed at a high temperature, then quenched and reformed at low temperature, its yield stress is exactly the same as that of a specimen being deformed for the first time at low temperature [130,131]. The yield stress can be said to be thermally reversible. At the first deformation work hardening of the specimen takes place and then at low temperature, the yield stress is the sum of the normal low temperature yield stress plus the work hardening increment [132].

**Disappearance of yield stress anomaly at low strain :** When the yield stress is measured at the conventional 0.2% strain, it is a strong function of temperature, but if, instead it is measured at very low plastic strain, say  $10^{-5}$  then the yield stress is almost independent of temperature [129, 133].

**Violation of Schmid's law :** Takeuchi and Kuramoto [134] showed that the CRSS for  $(111)[\bar{1}01]$  slip in  $\text{Ni}_3\text{Ga}$  (which is very similar to  $\text{Ni}_3\text{Al}$  in mechanical behaviour) under compression, increases as the deformation axis moves away from [001] in the standard  $[001][011][\bar{1}\bar{1}1]$  triangle. In addition to the orientation dependence, there is an asymmetry between tensile and compressive yield stresses [135]. The orientation dependence

and tension/compression asymmetry are also found in single crystals of  $\text{Ni}_3\text{Al}$  [123].

**Work hardening** : The temperature dependence of the initial work hardening rate is complicated but not unlike the rate sensitivity of the yield stress [124,126]. The work hardening rate has a minimum close to the peak of the yield stress.

**Inverse creep** : Inverse Creep is observed [136,137] in  $\text{Ni}_3\text{Al}$  alloys. The creep rate drops from its initial high value while the material deforms by primary and critical slip. After a small strain, the creep rate increases again as the material deforms on the cube cross slip plane. The accelerating creep rate indicates that the work-hardening rate which is small and positive at large strain rate near the peak temperature, becomes negative at low strain rates.

Any mechanism which explains the anomalous yield behaviour must at least satisfy the general characteristics of the anomalous flow behaviour stated above.

**Cross-slip models** : The yield anomaly behaviour has been explained based on the consideration of the instability of  $\langle 101 \rangle$  screw superdislocations on  $\{111\}$  slip planes [119,129,134,135, 138-143]. With the assistance of thermal activation,  $\langle 101 \rangle$  screw superdislocations have the tendency to cross slip from  $\{111\}$  to  $\{100\}$  planes and become less mobile. The driving forces for the cross slip have been identified as APB energy anisotropy [119] and elastic anisotropy [141].

The cross slip model was developed quantitatively by Takeuchi and Kuramoto [134] and Lall, Chin and Pope [135] and then further refined by Paider, Pope and Vitek [140], generally referred to as the PPV model. According to the model, the cross slip process is thermally activated and the number of cross slip pinning (CSP) points (Figure 2.21(a) [144]) increases with increasing temperature, leading to an increase in the

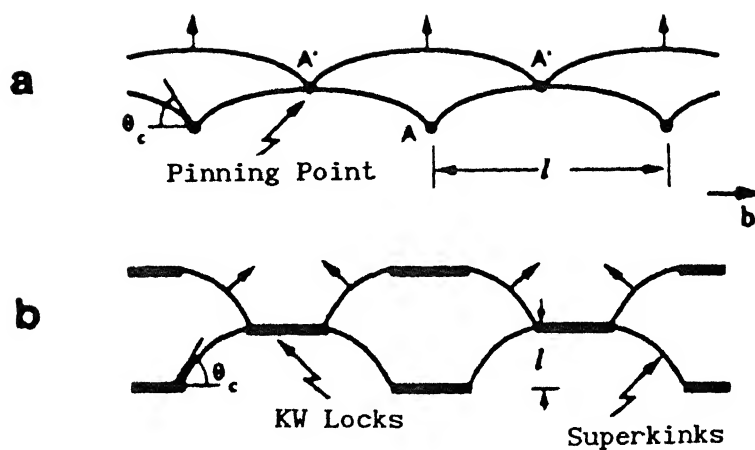


Fig. 2.21: Illustrations of successive positions for a superdislocation moving on the (111) plane by (a) bowing between cross-slip pinning (CSP) points as envisioned in the CSP models and (b) lateral motion of superkinks between Kear-Wilsdorf (KW) locks as envisioned in the superkinks models [144].

resistance to  $\{111\}\langle 110 \rangle$  slip. The yield strength decreases again when  $\{100\}\langle 110 \rangle$  slip becomes feasible. Yoo [141-143] has shown that cross slip pinning will occur only when

$$\left[ 3A/(A+2) \right] (\gamma_1/\gamma_0) > \sqrt{3} \quad (2.9)$$

where  $A = 2C_{44}/(C_{11}-C_{12})$  is Zener's ratio of elastic anisotropy;

$\gamma_1$  = The anti-phase energy of (111) plane;

$\gamma_0$  = The anti-phase energy of (010) plane.

In the case of  $\text{Ni}_3\text{Al}$ ,  $\gamma_1/\gamma_0$  is equal to 1.1 to 1.4. Equation 2.9 would not be satisfied for  $\text{Ni}_3\text{Al}$  if the elastic anisotropy is not considered (i.e.  $A=1$ ). The Zener anisotropy factor, which is not sensitive to temperature, was calculated to be 3.3 for  $\text{Ni}_3\text{Al}$ . Setting  $A = 3.3$  and  $\gamma_1/\gamma_0 = 1.2$ , the condition for the yield strength anomaly is well satisfied. Thus, the torque term derived from the elastic anisotropy plays a major role in the CSP process and yield strength anomaly observed for  $\text{Ni}_3\text{Al}$  [141,142].

All the models based on the idea of cross slip pinning of screw dislocation segments are very well discussed by Liu [120] and Hazzledine and Sun [124]. The PPV model [140] with the additional torque term developed by Yoo [141-143] has successfully explained many yield and flow phenomena in  $\text{Ni}_3\text{Al}$ , including the strong orientation dependence of the yield strength and tension/compression asymmetry [121,134,145]. However, the model has been troubled by some observations such as (i) a low strain rate sensitivity in the anomalous regime below the peak strength temperature [129,134,146], (ii) a large discontinuity in the activation volume at a temperature well below that of the peak [147] and (iii) observed superkinks between long and straight sessile screw segments analogous to Kear-Wilsdorf locks [138] in deformed  $\text{Ni}_3\text{Al}$

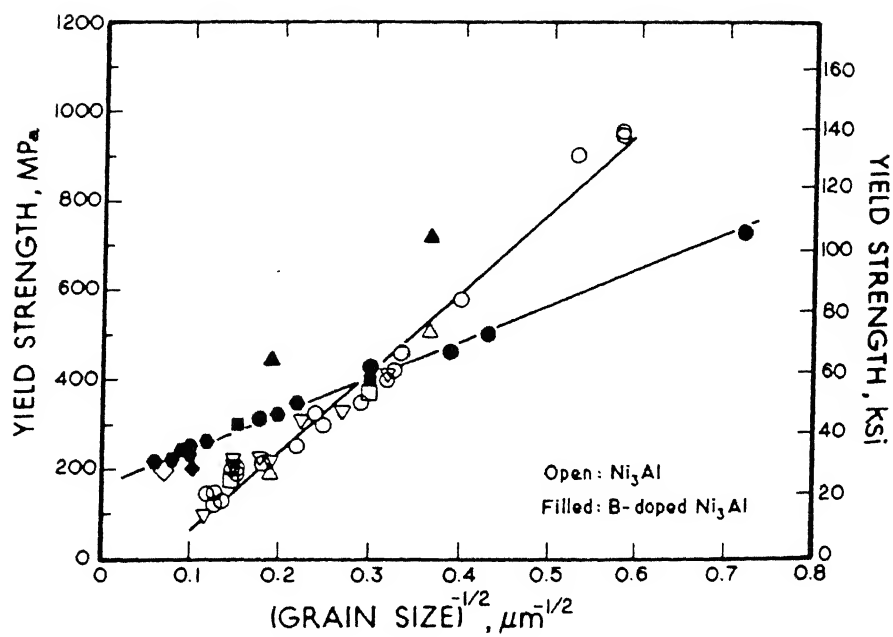


Fig. 2.22: Comparison of Hall-Petch relationships for alloys with and without boron [157].

Compositional variations have not been taken care of while drawing Figure 2.22. However, as pointed out by Takeyama and Liu [104] care must be taken to plot separately the results for materials of even slightly differing composition because of the great sensitivity of the properties of  $\text{Ni}_3\text{Al}$  to compositional changes. The following conclusions were drawn by Takeyama et al. [104] and Kim et al. [162]. Boron reduces the Petch slope by 25% for Ni-24 at% Al while it has little or no effect on the Petch slope for Ni-25 at% Al. Boron increases  $\sigma_0$ . The effect is three times higher for stoichiometric  $\text{Ni}_3\text{Al}$  than for the nickel-rich material. ' $\sigma_0$ ' is negative only for powder extruded material. Flow stresses also obey the Hall-Petch equation with both  $\sigma_0$  and  $k_y$  increasing with strain. On the basis of Luder's band extension model, Schulson et al. [156] have suggested that the grain size effects are better described by the relation having Hall-Petch exponent,  $n$ , equal to  $0.8 \pm 0.05$ .

Alternative models of the grain size dependence of yielding have been suggested by Li [163] and Conrad [164]. These are based on the assumption that dislocation density ( $\rho$ ) is dependent on grain diameter. According to Li and Conrad,  $\rho \propto d^{-1}$ . There is no experimental evidence on  $\text{Ni}_3\text{Al}$  to support (or refute) either point of view.

Hanada et al. [159] and Oya et al. [160] report respectively that the peak temperature,  $T_p$ , where the yield strength is maximum, is independent of grain size in the range of 12-70  $\mu\text{m}$  and of 4-275  $\mu\text{m}$ . However, Weihs et al. [161] report that the maximum can be entirely suppressed for the material with  $d = 2.9 \mu\text{m}$  due to the grain boundary sliding and the predominance of cube slip. Takeyama et al. [104] also report a lowering of the maximum temperature from  $800^\circ$  to  $600^\circ\text{C}$  with decreasing grain size in the range 173-15.3  $\mu\text{m}$  (Figure 2.23). This is consistent with the results of Weihs et al. [161]. At temperatures above  $700^\circ\text{C}$ , refining grain size weakens boron-doped  $\text{Ni}_3\text{Al}$ , in contrast to the

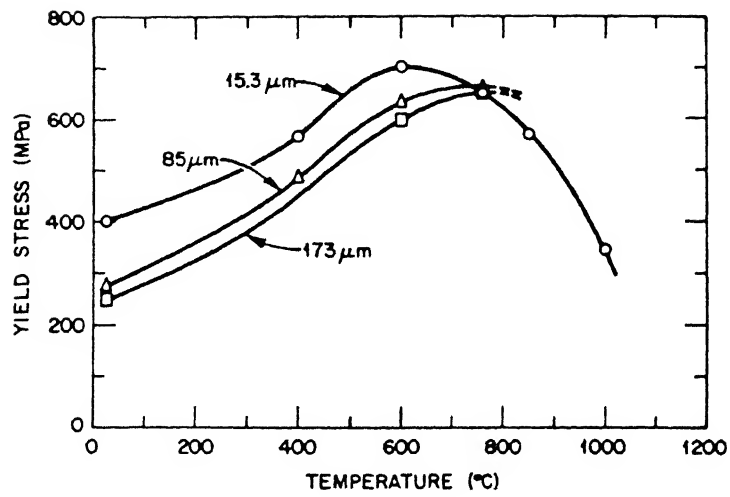


Fig. 2.23: Changes in yield stress with temperature for boron-doped  $\text{Ni}_3\text{Al}$  with a grain size of 15.3, 85 and 173  $\mu\text{m}$  [104].

observations at low temperatures [158,161]. Grain refinement lowers the thermal strengthening leading to thermal weakening [158].

#### 2.6.4. Effect of alloy stoichiometry

$\text{Ni}_3\text{Al}$  has a narrow composition range on either side of the stoichiometry and defect hardening [46] may also occur at off-stoichiometric regions. Hence, apart from the third element effect, effect of non-stoichiometry also plays an important role in strengthening of  $\text{Ni}_3\text{Al}$ . It is concluded [46] that the defect hardening in  $\text{Ni}_3\text{Al}$  is to be regarded as a sort of solid solution hardening and both hardening effects are controlled by the same mechanism. Aluminium-rich deviations from the stoichiometry leads to a more significant strengthening than nickel-rich deviations [61,165] and the strength is minimum at the stoichiometric composition [53]. This is clearly demonstrated in Figure 2.24 [53]. The positive temperature dependence of the strength of  $\text{Ni}_3\text{Al}$  is greater for aluminium-rich deviations than the nickel-rich deviations [46,53,62]. The temperature dependence of 0.2% flow stress of  $\text{Ni}_3\text{Al}$  alloys for various aluminium contents is shown in Figure 2.25 [53]. However, alloy stoichiometry apparently does not affect the temperature of peak strength of  $\text{Ni}_3\text{Al}$ . The changes in the activation constant of  $\text{Ni}_3\text{Al}$  derived from the flow stress increment appears to be discontinuous at stoichiometry. The non-straight change in the anomalous behaviour in the vicinity of stoichiometry was explained [53] quantitatively with the formation of cluster composed of three wrong bonds around each excess minority atom by  $\{111\}$  slip. It was concluded that such a cluster formation in aluminium-rich alloys increases the  $\{111\}$  APB energy and hence, the relatively lower  $\{100\}$  APB energy results in a high velocity for cross-slip onto the cube plane. Aoki and Izumi [46] explained the



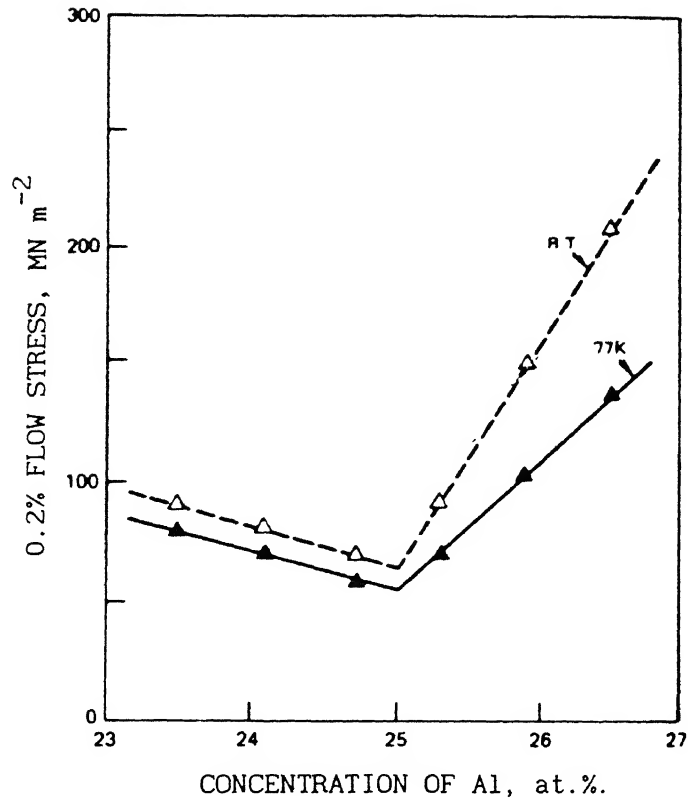


Fig. 2.24: Effect of stoichiometry on flow stress of  $\text{Ni}_3\text{Al}$  at 77 K and room temperature [53].

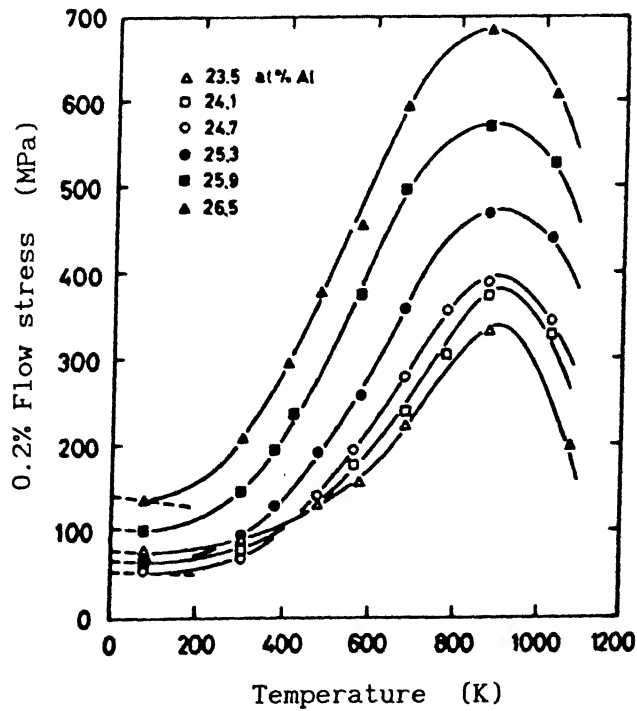


Fig. 2.25: Temperature dependence of the 0.2% flow stress of the

asymmetric defect hardening using Fleischer's solid solution hardening theory.

#### 2.6.5. Solid solution strengthening

The flow stress of  $\text{Ni}_3\text{Al}$  is known to be affected by addition of ternary elements that are soluble in  $\text{Ni}_3\text{Al}$ . It is known that the effects of solid solution strengthening in  $\text{Ni}_3\text{Al}$  can be divided into two parts, the strengthening at low temperatures by solid solution hardening and that at high temperatures by thermally activated process [166,167,168]. The solid solution strengthening effect can be evaluated by yield stress at a temperature near liquid nitrogen temperature and the magnitude of the positive temperature dependence of the yield stress can be evaluated by the activation energy. It has been proposed [166] that the yield stress versus temperature curve in the  $\text{L1}_2$  type alloys can be regarded as the sum of two temperature dependent terms. The stress component,  $\sigma_{\text{ath}}$ , has the ordinary negative temperature dependence of the stress arising from the shear modulus change with temperature, while,  $\sigma_{\text{th}}$ , has the positive temperature dependence of the stress caused by Kear-Wilsdorf mechanism [138]. Thus, the observed yield stress,  $\sigma_y$ , is expressed as

$$\sigma_y = \sigma_{\text{ath}} + \sigma_{\text{th}} \quad (2.11)$$

$$\sigma_{\text{ath}} = \sigma_0 (1+BT) \quad (2.12)$$

$$\sigma_{\text{th}} = A \exp(-U/RT) \quad (2.13)$$

where  $\sigma_0$  - The yield stress at 0 K;

U - The activation energy for the thermally activated process;

A and B - Constants;

R - Gas constant;

T - Temperature.

Effect of alloying elements on the positive temperature dependence of the yield stress : The yield stress level at temperatures below the peak of the yield stress versus temperature curves increases with increasing concentration of the additive alloy elements. On the other hand, the strengthening effects of the additive elements weaken or disappear at sufficiently high temperatures above the peak.

Suzuki and co-workers [169,170] have shown that the choice of the alloy chemistry to alter the electron-atom ratio ( $e/a$ ) in the compound and/or the atomic radius ratio of the components ( $R_B/R_A$ ), controls the magnitude of the mechanical anomaly by changing the phase stability of the  $L1_2$  crystal structure against other geometrically close packed (GCP) phases. The rate of activation energy change per atom percent of the ternary element,  $dU/dC$ , determines the tendency to enhance the magnitude of the positive temperature dependence of strength. The smaller the value of  $dU/dC$ , the larger is the tendency to enhance the magnitude of the positive temperature dependence of strength by the ternary additions. The results of Suzuki and coworkers [11, 122] and Zhang et al. [171] also demonstrate that the addition of such elements into  $Ni_3Al$  which increase its electron concentration ( $e/a$ ) and/or atomic radius ratio ( $R_B/R_A$ ) could reduce the stability of the phase with respect to other close packed phases, especially  $DO_{22}$  phase. This would result in a change in the fault energies such as an increase in anisotropy of APB energy between  $\{111\}$  planes and  $\{100\}$  planes for  $Ni_3Al$ . This favours the cross slip of screw dislocation from  $\{111\}$  to  $\{100\}$  planes, thereby enhancing the anomalous yield behaviour of  $Ni_3Al$ .

The activation energy for the thermally activated process can be calculated from the slope of  $\ln[\sigma_y - \sigma_o(1+BT)]$  versus  $1/T$  plot for each alloy element. It is noted that  $\sigma_o$  is the yield stress at 77 K for boron-free alloys and at 123 K for boron-doped alloys. The constant 'B' is related to the shear modulus change with temperature and can be supposed to be 0.0003 for  $Ni_3Al$  [53, 166,167,172]. The effect of each alloying element on the activation energy for the thermally activated process to cause the positive temperature dependence of the stress for  $Ni_3Al$  is shown in Figure 2.26 [11] as a function of concentration of transition metal elements. Similarly the effect of B-subgroup elements on the activation energy of  $Ni_3Al$  [122], the effect of transition elements on the activation energy of boron-doped directionally solidified  $Ni_3Al$  [171] have been studied. It is demonstrated that every alloying element in  $Ni_3Al$ , except for Zn and Ga, significantly reduces the value of the activation energy [122]. It is found that Zn is the only one solute element which reduces the anomalous mechanical behavior of  $Ni_3Al$ . It has been reported that the anomaly almost disappears by the addition of 6 at.% Zn [173].

The effects of interstitial alloying elements like boron and carbon along with Be (which is a substitutional alloying element) on the activation energy of  $Ni_3Al$  alloys have been studied [109]. It should be noted that the just stoichiometric undoped  $Ni_3Al$  alloy showed lower activation energy (about 6 kJ/mol) as compared to that of the off-stoichiometric one (about 12 kJ/mol). This trend agrees with the previous observations [53,165]. Interestingly, in just stoichiometric alloys, the activation energy versus atom percent of solute plot showed positive slope while in off-stoichiometric alloys, the negative slope was observed. This result suggests that the cross-slip process of dislocations from (111) to (100) planes can be modified by the addition

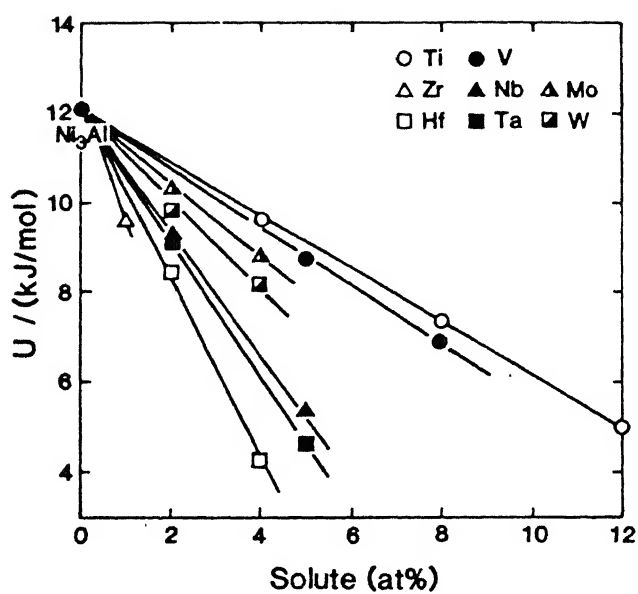


Fig. 2.26: Change in activation energy with solute concentration in ternary  $\text{Ni}_3\text{Al}$  with addition of transition metal elements [11].

of C, B and Be atoms in  $\text{Ni}_3\text{Al}$  [109].

Effects of alloying elements on solid solution hardening : In principle, the degree of solid solution hardening by the ternary additions should be evaluated by measuring the flow stress at zero absolute temperature, where the contribution of  $\sigma_{\text{th}}$  is absent. But experimental restrictions allow this to be done at a temperature only as low as 77 K at which in some alloys, there may still be some contribution from  $\sigma_{\text{th}}$ .

The 0.2% flow stress, as a function of concentration of the alloying element in undoped  $\text{Ni}_3\text{Al}$  at 77 K, is shown in Figure 2.27 [11] for transition metal elements. Similarly the effect of B-subgroup elements [122], the effect of interstitial elements along with beryllium [109] on the yield stress of undoped  $\text{Ni}_3\text{Al}$  and the effect of various transition elements along with silicon, which is a B-subgroup element, on the yield stress of boron-doped  $\text{Ni}_3\text{Al}$  [171] have been studied. The rate of solid solution hardening per atom percent of solute element,  $d\sigma/dc$ , as a function of lattice strain increment per atom percent of solute,  $d\epsilon/dc$ , for the addition of substitutional [11,61,62,109, 122,171] and interstitial [59,108,109] alloying elements is shown in Figure 2.28 [171]. In this figure, the yield stress increment per atom fraction was furthermore normalized by the shear modulus,  $G$ , using the value of  $6.5 \times 10^4$  MPa. The strain,  $d\epsilon$ , is equal to  $(a-a_0)/a_0$  where 'a' and 'a<sub>0</sub>' are the values of the lattice parameter of  $\text{Ni}_3\text{Al}$  alloys with and without the addition of the alloy element, respectively. For the additions of the different alloying elements (Figure 2.28), the experimental points are not normalized by a single correlation i.e., a single straight line, although based on the data reported by Zhang et al. [171], a straight line with a negative slope of  $1/2G$  could approximately be given for the additions of hafnium, tantalum and

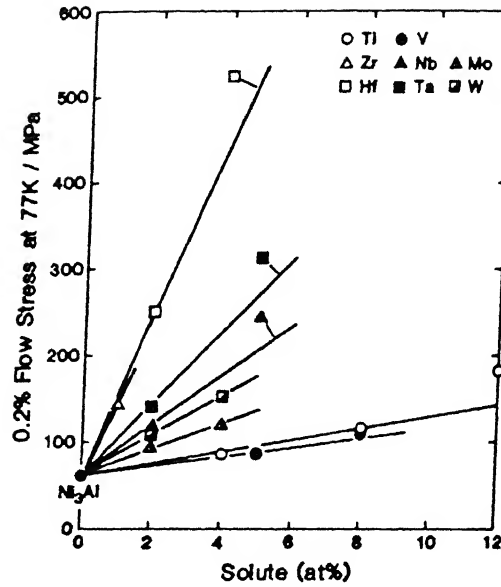


Fig. 2.27: Relation between 0.2% flow stress measured at 77 K and the solute concentration in ternary  $\text{Ni}_3\text{Al}$  with addition of transition elements [11].

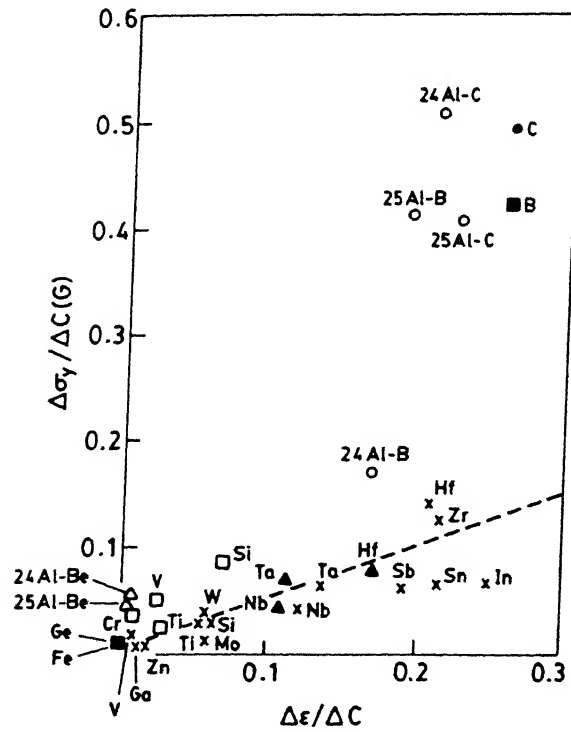


Fig. 2.28: Correlation of strengthening capacity,  $\delta\sigma_y/\delta C$ , to the lattice strain per atom fraction,  $\delta\epsilon/\delta C$ , for the addition of various ternary additions [171].

niobium in boron-doped DS-Ni<sub>3</sub>Al. Comparing the results of the substitutional atoms, the effect of the transition metal element, like hafnium, tantalum etc. on the solid solution hardening is stronger. From Figure 2.28, it is also shown that the interstitial elements such as carbon and boron stand out as particularly potent strengtheners. These results imply that the mechanisms of solid solution hardening in Ni<sub>3</sub>Al are different for interstitial and substitutional types of solutes and the mechanisms are also different for transition metal elements and B-subgroup elements. In a previous work [174], it was found that for the addition of transition metal elements, the extra strengthening could not be interpreted even if the modulus effect is taken into account. One possible interpretation of this deviation is that the hardening in the transition-metal containing alloys is not controlled by the elastic solute-dislocation interaction alone. It is possible that the transition metal solutes with larger atomic size affect the superdislocation core structure and cross-slip processes and thus provide an additional hardening effect [120]. Zhang et al. [171] has also tried to use the electronic effect to explain their results. Applying the concept of electronegativity of alloying elements to this phenomenon [171], it is found that the larger the electronegativity difference, the stronger the solid solution strengthening for the additions of transition metal elements like hafnium, tantalum and niobium in boron-doped Ni<sub>3</sub>Al.

## 2.7. DUCTILITY

### 2.7.1. Intrinsic brittleness of grain boundaries in Ni<sub>3</sub>Al

Intergranular fracture occurs in Ni<sub>3</sub>Al, prepared from ultra purity materials, without any appreciable segregation of impurities to the grain boundaries and therefore, the grain boundary brittleness appears to be an intrinsic property of Ni<sub>3</sub>Al [13,65,175-179]. The inherent



weakness of  $\text{Ni}_3\text{Al}$  grain boundaries has been variously attributed to the effects of electronegativity and valency of nickel and aluminium, the degree of order in the boundary regions and the structure, and the openness of the grain boundaries and may, in fact, derive from combination of these factors. Each of these approaches predicts that Ni-rich grain boundaries should possess greater strength.

Electrochemical factors, like valency difference and electronegativity difference between the constituent atoms, have been correlated to the grain boundary cohesive strength [65,175,180-185]. For example, the larger electronegativity difference between nickel and aluminium atoms imparts a poor grain boundary cohesive strength to  $\text{Ni}_3\text{Al}$  as compared to  $\text{Cu}_3\text{Au}$  where the electronegativity difference between Cu and Au atoms is less.

The lattice parameters of  $\text{Ni}_3\text{Al}$  and Ni are very similar while the lattice parameter of aluminium is much larger. The enrichment of nickel atoms in hypo-stoichiometric compounds is expected to create more homogeneous environment in the grain boundaries, resulting in higher grain boundary cohesion, and thus high alloy ductility [182]. In contrast, the aluminium rich boundaries have been shown to have high energy and associated with lower cohesive strength [95,186-189]. The cohesive strength of the grain boundaries in  $\text{Ni}_3\text{Al}$  is comparable to that of pure nickel [190]. But the yield stress of  $\text{Ni}_3\text{Al}$  is several times higher than that of pure nickel which favours cracking in the compound [186,191,192].

In the ordered compounds such as  $\text{Ni}_3\text{Al}$ , with high ordering energy the chemical order is preserved upto the grain boundary. As a consequence of this microcavities form on the grain boundaries which has been confirmed by many workers [189,193,194]. The formation of such

atomic size cavities on a symmetrical boundary is shown in Figure 2.29 [194]. These microcracks act as nuclei for intergranular fracture and as a result weakening of the grain boundaries occur. It has been shown [195,196] that lesser number of dislocation reactions are permissible at the ordered grain boundaries compared to the disordered grain boundaries. This inhibits slip compatibility between adjacent grains and makes the grain boundaries very brittle.

### 2.7.2. Effect of Boron

Microalloying with small amounts of boron has been found to improve the ductility of  $\text{Ni}_3\text{Al}$  significantly [12,13,97,197] and may completely suppress the intergranular fracture in  $\text{Ni}_3\text{Al}$  [13,178,179,184]. An equally important observation is that the addition of boron inhibits intergranular fracture only in non-stoichiometric nickel-rich alloys [13,178,179,184,197]. Figure 2.30 shows how a dramatic improvement in ductility of  $\text{Ni}_3\text{Al}$  takes place by boron doping [13]. Figure 2.31 [13] represents the effect of stoichiometry on the ductility of boron-doped alloy. Addition of boron to single crystals of  $\text{Ni}_3\text{Al}$  also shows a positive effect on both ductility and fracture stress at room temperature, but not at high temperatures [198-200].

### 2.7.3. Mechanism of ductilization by boron

Although the boron induced ductilization of hypostoichiometric  $\text{Ni}_3\text{Al}$  has been well established, the precise mechanism of this phenomenon is still controversial. At present, there are two models available, namely,

- (i) Boron enhanced cohesive strength model , and
- (ii) Boron facilitated slip-transfer model.

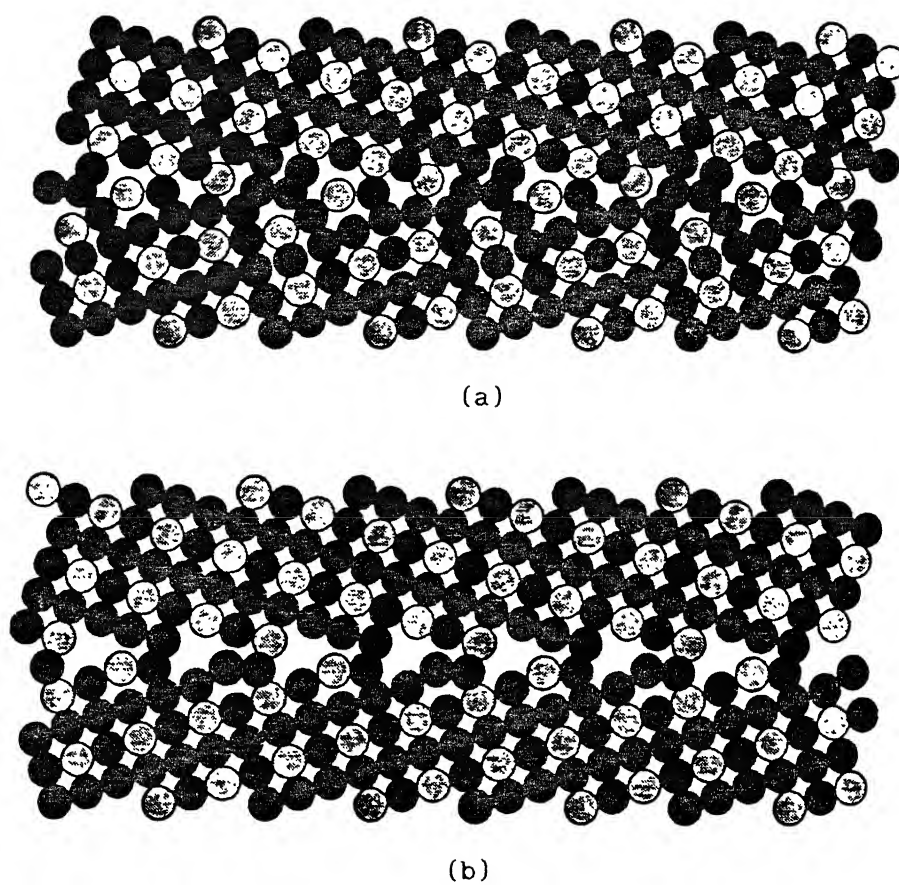


Fig. 2.29: Structure of the  $\Sigma=5(310)$  boundary in (a) stoichiometric  $\text{Cu}_3\text{Au}$ ; (b) stoichiometric  $\text{Ni}_3\text{Al}$  [194].

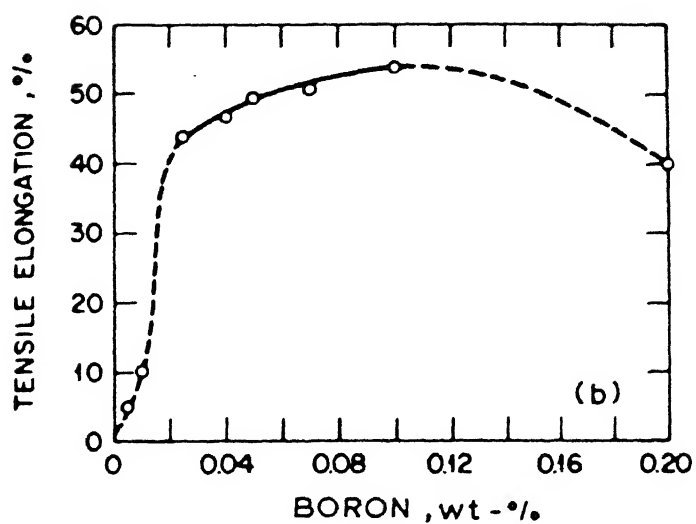
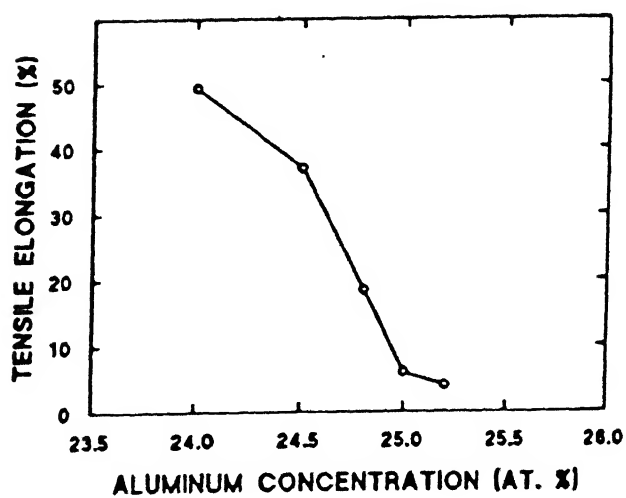


Fig. 2.30: Effect of boron concentration on the ductility of  $\text{Ni}_3\text{Al}$  [13].



2.31: Effect of aluminium concentration on the ductility of boron-doped  $\text{Ni}_3\text{Al}$  [13].

(i). Boron enhanced cohesive strength model : This model is based on the view that boron alters grain boundary chemistry (and possibly also grain boundary structure), thereby increasing grain boundary cohesive energy and strength. Increased grain boundary cohesion not only suppresses crack nucleation, but by providing increased crack-tip plastic deformation and blunting, also suppresses crack propagation. These effects are so pronounced in boron-doped  $\text{Ni}_3\text{Al}$  that ductility is dramatically increased and the alloy fractures in a transgranular fashion.

The cohesion model was first proposed on the basis of studies of grain boundary and free surface segregation in  $\text{Ni}_3\text{Al}$ . Boron shows a strong tendency to segregate to grain boundary but not to the surface [13,98,201]. The ideal work of fracture ( $\gamma_{id}$ ) which is required in the fracture of a perfect crystal is correlated to the surface energy ( $\gamma_s$ ) and grain boundary energy ( $\gamma_{gb}$ ) by the following relation :

$$\gamma_{id} = 2\gamma_s - \gamma_{gb} \quad (2.14)$$

According to the thermodynamic theory of Rice [202], this segregation behaviour leads to increase in ideal work of fracture ( $\gamma_{id}$ ).

Attempts to measure the actual work of separation ( $\gamma_{act}$ ) during grain boundary fracture inevitably indicate values significantly larger than  $\gamma_{id}$ . Discrepancies between  $\gamma_{act}$  and  $\gamma_{id}$  are generally attributed to the plastic work,  $\gamma_{pl}$ , associated with grain boundary crack propagation, which was not accounted by Griffith's model :

$$\gamma_{act} = \gamma_{id} + \gamma_{pl} = 2\gamma_s - \gamma_{gb} + \gamma_{pl} \quad (2.15)$$

Although  $\gamma_{id}$  is generally small compared to  $\gamma_{pl}$ , the latter quantity is

strongly dependent on cohesive strength ( $\sigma_{\max}$ ) of the boundary [203-205] which in turn is directly related to  $\gamma_{id}$ . According to the cohesive strength argument [206], boron increases the maximum stress that the grain boundary crack-tip can withstand. But, it is this local stress that is also the driving force for plastic deformation near the crack-tip. Therefore, changes in  $\gamma_{id}$  or  $\sigma_{\max}$ , even though these terms are very small, can result in large changes in the amount of plastic deformation accompanying crack propagation. According to this view  $\gamma_{id}$  (or more accurately  $\sigma_{\max}$ ) is the key factor that controls  $\gamma_{pl}$  and thus  $\gamma_{act}$ . An increase in  $\gamma_{id}$  by boron segregation would lead to retardation of crack propagation along the grain boundaries through a substantial increase in  $\gamma_{act}$ .

Theoretical analyses based on first-principle calculations as well as more empirical approaches [92,93,95] have concluded that boron does, in fact, enhance the cohesive strength of  $Ni_3Al$ . Further evidence for increased grain boundary cohesion resulting from the boron segregation in  $Ni_3Al$  comes from the work of Khadkikar et al. [207] who used finite element stress analysis to determine the stress to initiate grain boundary separation in a double notched tensile specimen and found that boron-doped  $Ni_3Al$  always required higher stresses than the undoped alloys.

(ii). Boron-facilitated slip transfer model : This model is based on the consideration that slip transfer is facilitated by boron segregation [157,158,208], thereby resulting in less stress concentration and reduced crack nucleation at grain boundaries. According to this view, boron disorders the grain boundary region, thereby increasing grain boundary dislocation mobility [209], the number of available dislocation reactions at the grain boundaries [210] or

both.

The experimental evidence to support the slip transfer model comes mainly from Hall-Petch type analysis of the grain size effect. Schulson and Baker [158,208,209] observed that boron segregation in  $\text{Ni}_3\text{Al}$  lowers the Hall-Petch slope for yielding,  $k_y$ , by 40%. The lowering of  $k_y$  is interpreted as an indication that boron segregation reduces the effectiveness with which the boundaries impede slip.

Stress-strain curves of conventional tensile tests from undoped Ni-rich and stoichiometric  $\text{Ni}_3\text{Al}$  alloys, showed a short Luder's plateau [156]. The Luder's strain is direct evidence that localized plasticity precedes fracture. Supporting this are the observations made during in-situ TEM straining of thin foils of doped and undoped stoichiometric alloys (Figure 2.32) [208]. Prior to fracture, plastic flow is localized within the slip bands. When the bands are formed, they terminate at grain boundaries, producing dislocation pile-ups. Upon further straining, the pile-ups (i.e. their stress fields) become large enough to initiate slip in the adjacent grains, where upon a new pile-up begins to form at another boundary. In this way, slip is transmitted from grain to grain, leading to global plasticity.

Baker and Schulson [211-214] observed a continuous disordered ( $\gamma$ ) grain boundary phase in boron-doped Ni-24 at.% Al alloy produced by powder metallurgy. This grain boundary phase has a thickness of ~20 nm with a boundary separating it from the ( $\gamma'$  phase) matrix. It has fcc crystal structure with a very low aluminium level. Presence of disordered regions of ~2 nm thickness were detected in the vicinity of large angle boundaries in Ni-24 at% Al doped with boron by HREM studies [215,216]. Observations using microdiffraction [217], showed partially ordered regions (~10 nm wide) adjacent to low angle boundaries in doped Ni-rich alloy. In addition, the results from STEM [218] and atom probe

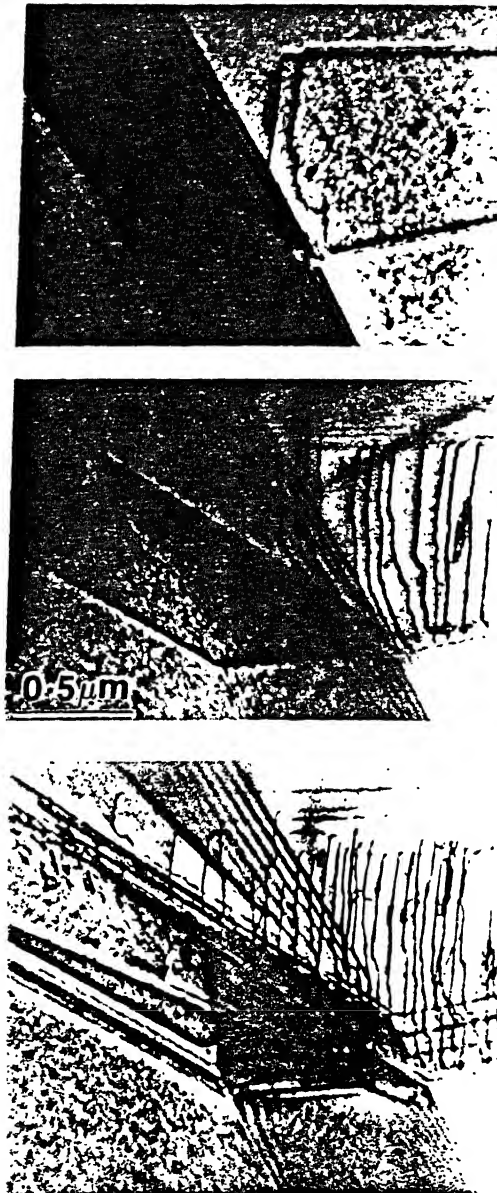


Fig. 2.32: Slip propagation across a boundary during TEM *in-situ* straining of boron-doped stoichiometric  $\text{Ni}_3\text{Al}$  [208].



analyses [101,219] of Ni and boron coenrichment at a grain boundary in doped Ni-rich  $\text{Ni}_3\text{Al}$  are also consistent with these features. Monte-Carlo calculations indicate that boron causes a small increase in the local disorder at  $\Sigma$  5(130) boundaries [220]. Boron attracts nickel to the boundaries and this leads to the same structural changes as in the cases of large deviations from stoichiometry [221].

Based on these observations coupled with the reduction in the grain boundary contribution to the yield stress of the doped ductile alloys, Baker and Schulson [222] suggested that a grain boundary which is at least partially disordered may be a requirement for the tensile ductility. Within this shell, the APB barrier,  $\gamma$ , to the nucleation of superlattice partial dislocations is eliminated. The disordered boundary also allows for the possibility that slip will be more easily transmitted across grain boundaries via direct passage of dislocations, because the order induced obstacles to the movement of the residual grain boundary dislocations are also eliminated [209]. In either way slip may be transmitted from grain to grain without the localization of tensile stress at the grain boundaries ahead of the dislocation pile-ups becoming sufficiently large to nucleate cracks. The enhanced transmission then leads to global plasticity.

The main criticism to the slip transfer model comes from the following observations :

(i). Using sharply notched bend bars tested in 3-point bending at a constant displacement rate, it was shown [223] that catastrophic fracture did not accompany crack initiation in  $\text{Ni}_3\text{Al}$ ; rather the plot of load versus crack opening displacement was indicative of stable crack growth.

(ii). The value of ' $k_y$ ' in Hall-Petch equation is influenced by a number of metallurgical factors like alloy chemistry, impurities etc. as

discussed by George et al. [206]. The observations of disordered phase along the grain boundaries [211-213] only complicates the analysis of 'k<sub>y</sub>'.

(iii). In-situ TEM work [224] suggests that the transmission appears to be spread out and to have initiated away from the tip when boron was present.

(iv). No grain boundary phase was observed in boron-doped  $\gamma'$  [13,225,226]. No disordering but only non-planarity of the boundary was observed [226].

(v). Preservation of ordering upto the grain boundary is reported [220,227-230].

(vi). Observation of grain boundary disordered phase even in boron free nickel-rich alloys [159,211].

(vii). Observation of lack of strong co-segregation of nickel and boron [231,232].

(viii). There is a strong opinion that the observed presence of grain boundary phase [211] may be due to compositional difference [225].

#### 2.7.4. Effect of substitutional elements

The ductility of Ni<sub>3</sub>Al can be improved by many substitutional elements also. Addition of Be can improve the room temperature ductility of Ni<sub>3</sub>Al but it is found to be ineffective at elevated temperatures [14]. According to Takasugi et al. [65], Fe additions ranging from 4 to 15 at.% replacing Al only resulted in an increase in room temperature ductility. Horton et al. [233] reported that the addition of 10 at.% Fe to Ni<sub>3</sub>Al replacing both Ni and Al produced the most fabricable alloys. Addition of about 6 at.% Mn to Ni<sub>3</sub>Al also improve room temperature ductility [65,234]. Dimiduk et al. [234] associated the ductilizing effect of Mn with the formation of second phase. Liu [235] has reported

that Mn improves the fabricability of B-doped  $\text{Ni}_3\text{Al}$  so that the ductilizing influence of these solute may be additive. The addition of 5 at.% Cr had no beneficial effect on room temperature bend ductility of  $\text{Ni}_3\text{Al}$  nor did it change the fracture mode [65]. Also, 6 at.% Cr reduced slightly the room temperature ductility of B-doped  $\text{Ni}_3\text{Al}$  [235]. However, 6-8 at.% Cr added to B-doped  $\text{Ni}_3\text{Al}$  produces remarkable improvement in ductility in air at elevated temperatures [236]. Hf also improves the fabricability of B-doped  $\text{Ni}_3\text{Al}$  [235]. An addition of only a few atom percent of Pd to Ni-rich  $\text{Ni}_3\text{Al}$  significantly improves its ductility [15,237]. Chiba et al. [16] have shown experimentally that the addition of  $\gamma$  formers such as Pt, Cu and Co as well as Pd, which degrades the ordering, are effective in improving the ductility of  $\text{Ni}_3\text{Al}$ . In contrast,  $\gamma'$  formers such as Si, Ti, V and Nb which enhance the ordering energy are ineffective. Hono et al. [83] also substantiate these findings.

#### 2.7.5. Mechanism of enhanced ductility by substitutional solutes

There are three models available to explain the effect of macroalloying on the ductility of  $\text{Ni}_3\text{Al}$ , namely, valency model, electronegativity model and ordering energy model.

(i). Valency model : According to this model, proposed by Takasugi et al. [65, 175], in  $\text{A}_3\text{B}$  alloys having  $\text{L1}_2$  structures such as  $\text{Ni}_3\text{Al}$ , the ternary element which has similar electronic bonding to 'A' suppress grain boundary embrittlement while other solute elements with dissimilar electronic structures have no beneficial effect. The valency difference between the third element and the solvent atom (Ni or Al), replaced by the solute, was taken as a semi-quantitative measure of the grain boundary strength in ternary alloys. Lack of clear physical relationship between valency and cohesive strength makes the valency model less

attractive [180].

(ii). Electronegativity model : According to this model, proposed by Taub et al. [180,181,238], the addition of any ternary element which decreases the electronegativity difference between Ni and Al enhances the grain boundary strength resulting in improved ductility.

Both electronegativity and valency models are based on the idea that the intergranular brittleness is due to localization of electronic charge. Both the models make similar predictions as to ductility.

(iii). Ordering energy model : Enomoto et al. [79], using cluster variation method, have shown that the order-disorder transformation temperature is raised by the addition of ternary element substituting for Ni site, meaning that the ordering energy of  $\text{Ni}_3\text{Al}$  is decreased by the addition of ternary element substituting for Ni site. Jia et al. [84] have shown experimentally that when a ternary element substitutes for Al site in  $\text{Ni}_3\text{Al}$  [63,239], the addition of such ternary element stabilizes  $\gamma'$  whereas, when a ternary element tends to substitute for Ni site,  $\gamma$  is stabilized. This means that the ordering energy is changed by the addition of third element.

Vitek et al. [221], on the basis of theoretical calculations have shown that the grain boundary structure is affected by ordering energy. King and Yoo [210] showed that the number of allowed dislocation reactions is significantly larger in a disordered alloy than in an ordered alloy. The above two investigations clearly indicate that ordering energy and ductility of  $\text{Ni}_3\text{Al}$  are closely related. If the ordering energy is degraded, dislocation reactions at the grain boundaries and the motion of grain boundary dislocations are promoted, resulting in ductility improvement [195,208,209,240]. In addition, it has been suggested that the stronger the tendency for a ternary element to substitute for Ni site, the more the ordering energy of  $\text{Ni}_3\text{Al}$

degrades [16,79]. Cahn et al. [241,242] and Enomoto et al. [79] have indicated that the ordering energy of  $\text{Ni}_3\text{Al}$  decreases with decreasing Al content also, suggesting better ductility of  $\text{Ni}_3\text{Al}$  with hypostoichiometric Al.

#### 2.7.6. Improvement in the ductility of hyper-stoichiometric alloys

Al-rich  $\text{Ni}_3\text{Al}$  is superior to Ni-rich  $\text{Ni}_3\text{Al}$  as a high temperature material. It has considerably higher temperature strength than stoichiometric and Ni-rich  $\text{Ni}_3\text{Al}$  [53]. Also, boron has a greater strengthening effect in Al-rich alloys than Ni-rich alloy [60,243]. Probably, Al-rich  $\text{Ni}_3\text{Al}$  is considered to be more resistant to oxidation than Ni-rich  $\text{Ni}_3\text{Al}$  because of its higher aluminium concentration. Therefore, ductile Al-rich  $\text{Ni}_3\text{Al}$  is desired to be developed.

The failure of boron to ductilize Al-rich alloys was attributed to the formation of boron clusters which reduces the concentration of boron available to the boundaries [114,219]. The presence of boron clusters also contributes to an increased lattice resistance to the dislocation motion [243].

Hirano [244] found a remarkable effect of unidirectional solidification by floating zone method (FZ-UDS) on the room temperature ductility of stoichiometric  $\text{Ni}_3\text{Al}$ . Hirano et al. [245] later confirmed the effectiveness of the method (Figure 2.33). It was suggested [245] that FZ-UDS produces structures with crystal orientations in which dislocation can easily transfer across the grain boundary.

#### 2.7.7. Effect of environment and temperature

The room temperature ductility of boron-doped  $\text{Ni}_3\text{Al}$  is not sensitive to environment (air versus vacuum) as reported by Masahashi et al. [109]. While, oxygen is particularly significant as an embrittler at

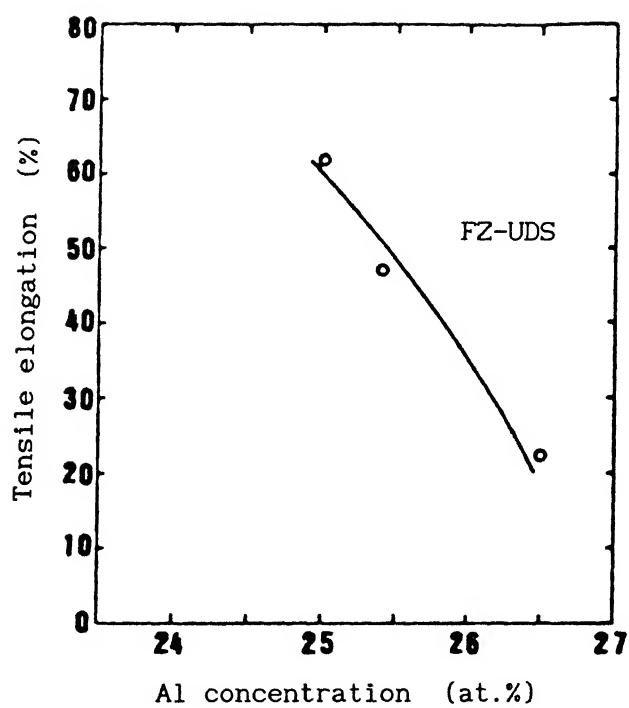


Fig. 2.33: Plot of room temperature tensile elongation as a function aluminium concentration [245].

elevated temperatures, water vapour (hydrogen) is more likely to be a problem for  $\text{Ni}_3\text{Al}$  at low temperatures [246,247]. Liu et al. [246,247] first discovered that the embrittlement in  $\text{Ni}_3\text{Al}$  is due to a dynamic rather than a static effect. Recently, Hippsley and Devan [248] have proposed a mechanism of 'Stress Assisted Grain Boundary Oxidation (SAGBO)' to explain the dynamic embrittlement in  $\text{Ni}_3\text{Al}$ .

The role of grain size on elevated temperature embrittlement is shown in Figure 2.34 [104]. Note that the ductility and fracture mode of  $\text{Ni}_3\text{Al}$  are little influenced by grain size upto about  $700^\circ\text{C}$ . At higher temperatures, intergranular fracture intervenes and then dominates. However, the ductility is higher in fine grained materials above about  $800^\circ\text{C}$  perhaps due to the occurrence of dynamic recrystallization [249].

Figure 2.35 [236] compares the tensile elongation of  $\text{Ni}_3\text{Al}$  alloy containing Hf and B, tested in air and in vacuum as a function of temperature. The alloy shows severe embrittlement in the temperature range of  $600\text{--}800^\circ\text{C}$ . Liu [235] has reported that  $\text{Ni}_3\text{Al}$  alloy containing Hf and B exhibited about 1% elongation when tested in air at  $760^\circ\text{C}$ . With a decrease in air pressure, the ductility increases continuously and reaches a value as high as 26% in a vacuum of  $10^{-5}$  Pa (Figure 2.36).

Two metallurgical solutions have proven effective in reducing the embrittlement. One is to control the grain shape in  $\text{Ni}_3\text{Al}$  alloys by processing techniques. This consists of producing columnar grains by directional solidification [235,250]. An alternative solution is to add moderate amounts of chromium to  $\text{Ni}_3\text{Al}$  alloys [236,251].

## 2.8. Substructure

The anomalous yield behaviour has been attributed to thermally activated cross-slip of  $a/2[\bar{1}01]$  screw dislocations from (111) to (010) which occurs due to the lower APB energy on (010) cross-slip plane

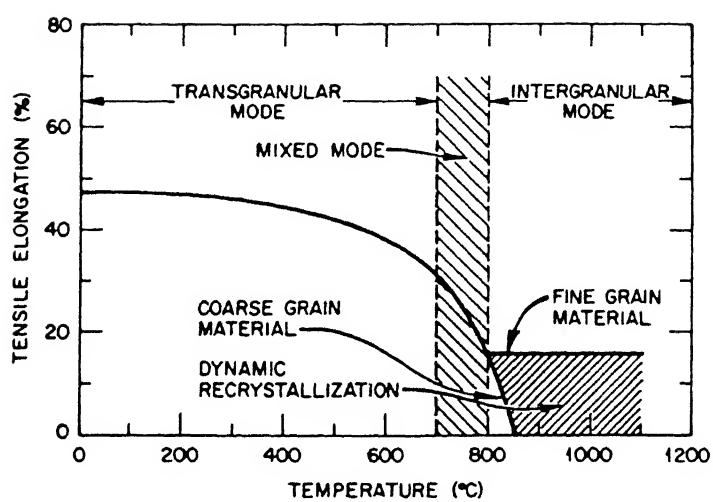


Fig. 2.34: Schematic variation of tensile elongation with temperature for boron-doped  $\text{Ni}_3\text{Al}$  [104].



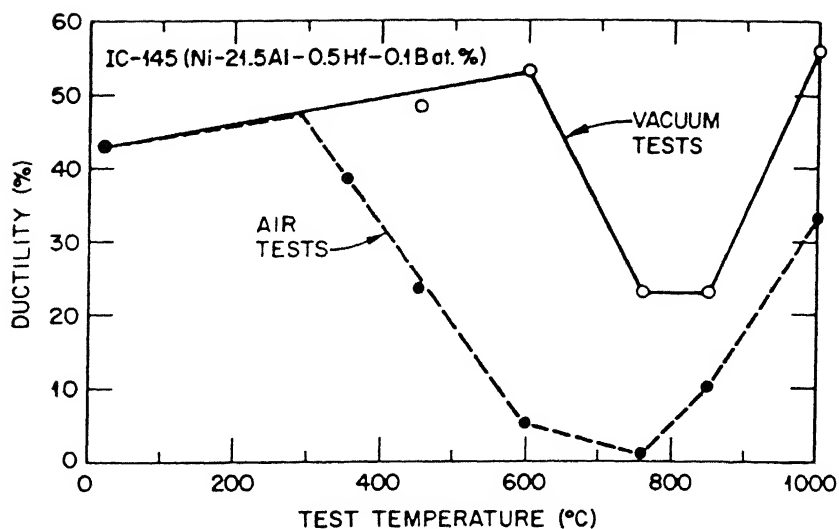


Fig. 2.35: Plot of tensile ductility as a function of test temperature for Ni-21.5% Al-0.5% Hf-0.1% B alloy tested in air and vacuum [236].

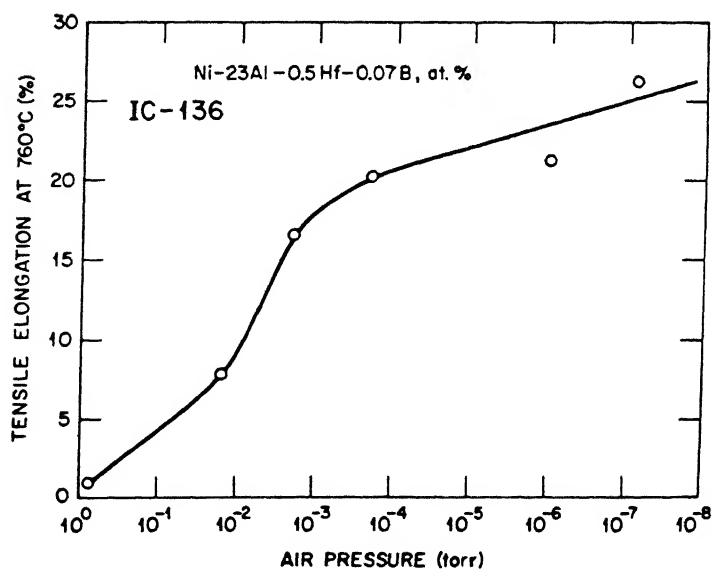


Fig. 2.36: Plot of tensile ductility as a function of air pressure for Ni-23% Al-0.5% Hf-0.07% B tested at 760°C [235].

[138]. A detailed discussion of fault types on  $\{111\}$  in  $L1_2$  are given by Pope and Ezz [121] and Paider et al. [140]. There are three types of important planar faults in  $L1_2$  structure, as shown in Figure 2.37 [252]. In the figure, when the layer A is displaced by a vector  $f_A$  with respect to the layer B, the configuration of atom neighbours across the fault is changed. This is the antiphase boundary (APB). The super lattice intrinsic stacking fault (SISF) is produced after a displacement of  $f_{SF}$ . The SISF does not involve any wrong bonds between unlike atoms. The complex stacking fault (CSF) is formed when the layer A is displaced by the vector  $f_C$  with respect to the layer B. The CSF is also a stacking fault but involves the effect of wrong bonds.

In  $L1_2$  structure slip always occurs along  $\langle 110 \rangle$  directions. Considering the deviation from the fault vectors predicted on the basis of the hard sphere model, six fold dissociation involving two CSFs, two APBs and an SISF, four fold dissociation involving two CSFs and an APB and two fold dissociation involving an APB or an SISF are proposed for  $a\langle 110 \rangle$  superlattice dislocation, as indicated in Figure 2.38 [253,254,255]. The energy of these planar faults varies in the order  $E_{CSF} > E_{APB} > E_{SISF}$ . An APB on (001) and an SISF are always stable at the displacement vectors derived from the hard sphere model [255].

Although there is a strong possibility for the existence of CSFs, none have been observed in  $Ni_3Al$  [100,121,140,256,257,258]. On the other hand, in addition to  $a/2[\bar{1}01]$  dislocations, it is well known that  $a/3\langle 112 \rangle$  bounded SISFs also occur in deformed  $Ni_3Al$  [208,259,260]. It appears that these SISFs nucleate in some manner from slip of  $\langle 110 \rangle$  dislocations although the exact mechanism has not been resolved [208,259]. Baker and Schulson [260] noted large number of SISFs at low temperatures with decreasing numbers at high temperatures. While most of the SISFs are generally confined to one plane, in a number of cases they

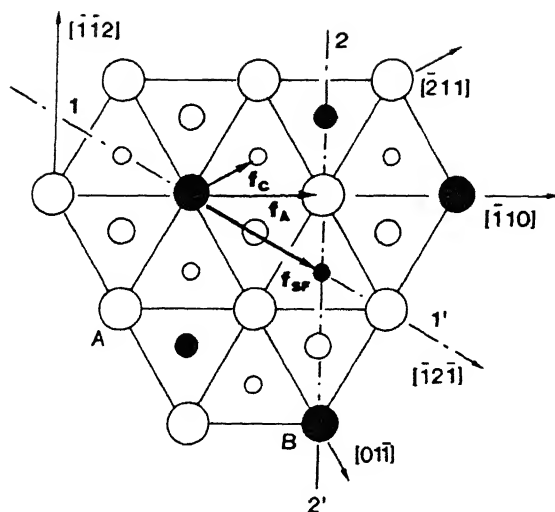


Fig. 2.37: The atomic arrangement on the (111) plane in an  $A_3B$  compound with the  $L1_2$  structure. Large, medium and small circles represent atoms on A, B and C layers respectively [252].

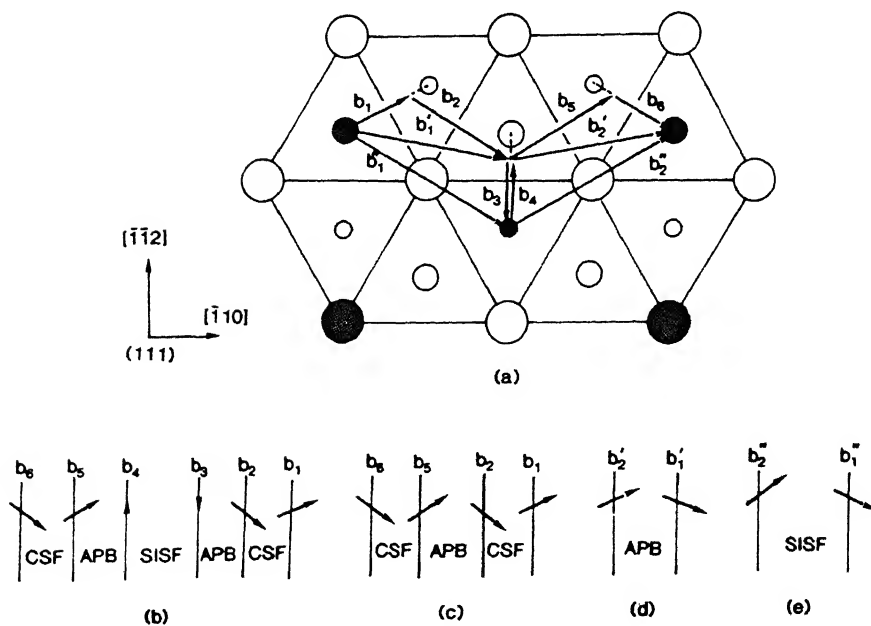


Fig. 2.38: Atomic arrangement and possible dissociation schemes for  $[110]$  dislocation on (111) in the  $L1_2$  structure. (a) Types of dissociation, (b) six-fold, (c) four fold (d) two-fold (APB-splitting) and (e) two-fold (SISF-splitting) dissociations [253,254,255].

are observed to be jogged between planes a few layers apart. Kinks such as these have been observed using weak beam spectroscopy [259] and it has been suggested that they occur due to cutting by  $\langle 110 \rangle$  superdislocations.

Using high resolution electron microscopy, Crimp et al. [261] have shown that  $a/3\langle 112 \rangle$  coupled SISFs lie on (111).  $a/2[\bar{1}01]$  super partials were always dissociated on (111) or ( $\bar{1}\bar{1}\bar{1}$ ) planes while APB plane was found to be (010). The APB width was found to increase significantly with increasing deformation temperature near the peak yield strength temperature. A number of researchers have also shown, using weak beam microscopy, that the screw partials are separated by APBs lying on the (010) plane, with the superpartials spaced roughly 5 nm apart [149,262].

TEM observations on SC-Ni<sub>3</sub>Al [149], compressed at room temperature along an axis near  $[\bar{1}11]$ , revealed many long straight screw dislocations. Also, it has been observed that cross-slip from (111) to (010) planes occurs. The microstructure that results from room temperature deformation of Ni<sub>3</sub>Al single crystals is dominated by screw dislocations that are mostly dissociated in their cube cross-slip plane [263].

In Ni<sub>3</sub>Al alloy deformed at 650°C, evidence was provided for glide of K-W locks on a{111} plane, accompanied by dragging of APBs [262]. The dislocation structure in Ni<sub>3</sub>(Al,Ti) deformed at 1073 K [264], a temperature above that at which the flow stress peaks, illustrates features of planar localized single slip. APB dragging is observed to operate locally but is not regarded as the rate controlling process for dislocation motion. Delocalization of the APB on several atomic planes parallel to the fault plane could be the reason for glide plane 'softening' and the formation of a planar structure. The primary cube  $a[\bar{1}\bar{1}0](001)$  slip system carries the deformation.

Sun and Hazzledine [148] observed dislocation configurations in the  $\gamma'$  particles of a  $\gamma/\gamma'$  superalloy after deformation at several temperatures. They [148] found that superdislocations in  $\gamma'$  are observed to glide on the primary octahedral slip plane by the formation and the lateral propagation of 'superkinks' on the (111) plane while the dissociation into superpartials is on the cube cross-slip plane (010). Similar structures have been observed by Mills et al. [128].

Clement et al. [265] deformed  $\gamma'$  single crystals *in situ* in a TEM at a variety of temperatures, while observing the dislocation motion. They [265] observed that the deformation was carried by long  $1/2[\bar{1}01]$  screw dislocations on (111) planes but bowing was never observed. Moreover, the motion of screw dislocations is jerky and the jerks correspond to changes in superpartial spacing. These changes are consistent with changes in the plane of the  $1/2[\bar{1}01]$  dislocation cores from (111) plane to  $(1\bar{1}1)$  and back again. Dislocations were also seen to move from (111) to (010) plane and back again.

High resolution electron microscopy work by Sun et al. [127] on  $\text{Ni}_3\text{Al}$  and  $\text{Ni}_3\text{Ga}$  has shown locked structures on the following dislocations: 30-degree  $\langle 112 \rangle / 3$  super-Shockley partials, edge  $\{001\} \langle 110 \rangle$  dislocations and 45-degree  $\{001\} \langle 100 \rangle$  dislocations,  $\langle 110 \rangle$  dislocations formed by reactions between two  $\{001\} \langle 100 \rangle$  systems,  $\langle 111 \rangle$  dislocations formed by reactions between  $\{001\} \langle 100 \rangle$  and  $\{001\} \langle 110 \rangle$  slip systems.

## 2.9. SCOPE OF THE PRESENT INVESTIGATION

The available literature shows that  $\text{Ni}_3\text{Al}$  alloyed with hafnium and boron is one of the most promising and needs to be investigated thoroughly. The constitution diagram of the  $\gamma'$ -rich region of Ni-Al-Hf system has not been established. The effect of boron on the phase boundaries of the  $\gamma'$ -rich region of Ni-Al-Hf system is not known.

According to available literature, there is still a lot of discrepancy over the substitutional behaviour of hafnium in  $\gamma'$  alloys.

In the present investigation the constitution diagram of  $\gamma'$ -rich region of boron-free and boron-doped Ni-Al-Hf system at 1130°C has been determined. The phase stability of boron-free and boron-doped stoichiometric binary  $\text{Ni}_3\text{Al}$  has been investigated over the temperature range, 800-1200°C. The substitutional and bonding characteristics of different amounts of hafnium in hypostoichiometric ( $\gamma'$  alloy containing less than 25 at.% Al), stoichiometric ( $\gamma'$  alloy containing 25 at.% Al) and hyperstoichiometric ( $\gamma'$  alloy containing more than 25 at.% Al)  $\gamma'$  alloys have been examined. The substitutional behaviour of boron has also been examined. Dislocation substructures of 2 to 3% strained samples of some selected boron-free and boron-doped alloys were observed. An attempt has been made to examine the effects of hafnium and boron on the mechanical properties of some selected alloys through compression testing.

## CHAPTER III

### EXPERIMENTAL PROCEDURE

#### 3.1. MATERIALS

The starting materials for alloys not containing boron were 99.9% pure nickel and 99.9% pure hafnium supplied by Morton Thiokol Inc., USA and 99.999% pure aluminum supplied by Unichem Limited, UK. The weight of each component required for melting of the alloys was calculated directly from the weight percent.

The starting material for alloys containing boron was boron-doped stoichiometric  $\text{Ni}_3\text{Al}$  which was supplied by Defence Metallurgical Research Laboratories (DMRL), Hyderabad, India. The boron content of  $\text{Ni}_3\text{Al}$  was 500 ppm. X-ray diffraction and microstructure of DMRL supplied material showed it to be homogeneous and single phase. For preparation of some alloys, 99% pure boron supplied by Morton Thiokol Inc., USA was used.

In order to make an alloy of the required composition, the DMRL supplied  $\text{Ni}_3\text{Al}$  was used and extra nickel, aluminum and hafnium were added as required. In weight percent calculations, boron was neglected because of its insignificant weight. An alloy of  $\text{Ni}_3\text{Al}$  with boron was also prepared by arc melting elemental nickel, aluminum and boron.

#### 3.2. ALLOY PREPARATION

The alloys were melted into buttons of approximately 20 grams weight in a nonconsumable tungsten electrode, water cooled copper hearth electric arc melting furnace. The alloys containing boron were arranged in such a way that a large flat piece of  $\text{Ni}_3\text{Al}$  containing boron remained at the top with other elemental pieces all around. One alloy containing boron was

prepared from the elemental pieces which were arranged in such a way that a flat nickel piece was at the center, aluminum pieces were around the nickel piece and boron was at the bottom. In case of non-boron alloys, a flat nickel piece was kept at the center and other elemental pieces were kept all around.

Before striking the arc, the furnace was evacuated and flushed with high purity argon. After each melting, the button was turned over, the furnace was evacuated and flushed with high purity argon gas and the button was remelted. Each alloy button was remelted three times in order to ensure chemical homogeneity. After melting, the buttons were weighed to obtain the weight loss. The percentage weight loss on melting is listed in Table 3.1. Some of the alloys were melted in DMRL by their nonconsumable arc melting unit. The same procedure stated above was used to melt the alloys. Table 3.1 shows the composition of the alloys and contains details concerning melting.

### 3.3. HOMOGENIZATION

The alloys were vacuum sealed in fused quartz tube using a vacuum pump to obtain a vacuum of the order of  $10^{-2}$  to  $10^{-3}$  torr. The homogenization heat treatment for each kind of alloy was established by measuring the lattice parameter as a function of time at a given temperature until the lattice parameter became constant, especially for hafnium containing alloys. The homogenization procedure for each kind of alloy is listed in Table 3.2. After completing homogenization, the samples were water quenched. The homogenization temperature was maintained within  $\pm 2^{\circ}\text{C}$  in a silicon carbide vertical tube furnace using an Indotherm proportional controller. The quartz capsules containing the alloys were kept in the constant temperature zone of the furnace.



Table 3.1  
List of alloys

No.	Nominal Composition, at.%. Ni                  Al                  Hf                  B*				Weight loss on melting, %
1.	75.0	25.0	-	-	0.030
2.	77.0	23.0	-	-	0.014
3.	73.0	27.0	-	-	0.029
4.	75.0	22.5	2.5	-	0.001
5.	75.0	20.0	5.0	-	0.004
6.	75.0	17.5	7.5	-	0.025
7.	77.5	20.0	2.5	-	0.020
8.	77.5	17.5	5.0	-	0.050
9.	80.0	17.5	2.5	-	0.019
10.	80.0	15.0	5.0	-	0.000
11.	72.5	25.0	2.5	-	0.012
12.	72.5	22.5	5.0	-	0.050
×13.	75.0	25.0	-	B	0.060
+14.	75.0	25.0	-	B	-
15.	77.0	23.0	-	B	0.044
16.	73.0	27.0	-	B	0.015
17.	75.0	22.5	2.5	B	0.040
18.	75.0	20.0	5.0	B	0.020
19.	75.0	17.5	7.5	B	0.040
20.	77.5	20.0	2.5	B	0.024
21.	77.5	17.5	5.0	B	0.020
22.	72.5	25.0	2.5	B	0.037
23.	72.5	22.5	5.0	B	0.080
*24.	70.0	27.5	2.5	B	0.026
*25.	70.0	25.0	5.0	B	0.050

× Alloy prepared by melting elemental nickel, aluminium and boron (Alloy A).

+ DMRL supplied stoichiometric  $\text{Ni}_3\text{Al}$  with boron (Alloy B).

\*B Indicates the presence of boron.

\* Alloys melted in DMRL.

### 3.4. EQUILIBRATION

The alloys were equilibrated at various temperatures in order to obtain the structure characteristic of that equilibration temperature. The homogenization temperature was taken as one of the equilibration temperatures. The other equilibration temperatures used for some of the alloys were 1200°C, 1130°C, 1000°C and 800°C. For equilibration, pieces were vacuum sealed as stated before, in fused quartz tubes and annealed at the equilibration temperatures maintained at  $\pm 2^\circ\text{C}$ . Boron-free and boron-doped stoichiometric  $\text{Ni}_3\text{Al}$  were equilibrated at 1200°C for 5 days, at 1130°C for 7 days, at 1000°C for 10 days and at 800°C for 20 days. The boron-free and boron-doped binary off-stoichiometric  $\text{Ni}_3\text{Al}$  alloys were equilibrated at 1130°C for 20 days. Hafnium containing  $\text{Ni}_3\text{Al}$  alloys with and without boron were also equilibrated at 1130°C for 20 days.

### 3.5. X-RAY DIFFRACTION

#### 3.5.1. Powder sample preparation

For  $\text{Ni}_3\text{Al}$  based alloys, powder for X-ray diffraction work was prepared by filing a piece of alloy button with hardened steel file or jewellers' diamond file. Before filing, the surface of the piece of alloy was cleaned by grinding on a belt grinder. This was done to ensure the removal of the oxide layer that might have formed on the surface. The powder sample was sealed under vacuum in fused quartz tube and then heated to the temperature of equilibration for 15 to 20 minutes in order to relieve the strains in the material without causing sintering of powders.

#### 3.5.2. X-ray diffraction conditions

The X-ray diffraction work was carried out on Iso-Debyeflex 2002 X-ray Diffractometer using copper target. A curved graphite crystal monochromator attachment at the diffracted beam side of the diffractometer

was used to cut down the stray radiation reaching the counter. The diffraction pattern was recorded on a strip chart recorder.

For taking X-ray diffraction pattern, at first a rapid scan was made from  $15^\circ$  to  $150^\circ$  ( $2\theta$  values) to see the positions of the diffraction peaks. In the second step, slow scanning was done near the peak positions in order to get more accurate  $2\theta$  values for the peak positions.

Conditions under which the diffraction patterns were obtained are as follows.

Rapid scanning :

Voltage	- 30 kV
Current	- 20 mA
Scanning speed	- $3^\circ$ per minute (in $2\theta$ values)
Chart speed	- 30 mm/min
Time constant	- 3 sec
Counts per second	- 200 mk
Beam slit	- 2 mm

Slow scanning :

Scanning speed	- $0.6^\circ$ per minute ( $2\theta$ values)
Counts per second	- changed with intensity of peaks
Chart speed	- 15 mm/min

Parameters such as scanning speed, chart speed and counts per second were different for peak to peak scanning.

In order to find out the error in the machine, a standard silicon sample was scanned at slow speed (same speed as mentioned in slow scanning). Error was calculated from the deviation of the recorded peak values from the theoretical values calculated from the lattice parameter of silicon. This correction factor when added to recorded angles for the diffraction peaks of the sample, gave the exact angular positions of the

diffraction peaks (that is the correct values of  $2\theta$ ). These corrected angles were later used in calculating precise lattice parameter of the alloy.

To illustrate the above procedure, a detailed calculation of the lattice parameter measurement of  $\text{Ni}_3\text{Al}$  is given below. Powders of  $\text{Ni}_3\text{Al}$  equilibrated at  $1000^\circ\text{C}$  for 10 days were stress relieved at  $1000^\circ\text{C}$  for 15 minutes. X-ray tracings of these powders and also of silicon standard recorded under exactly the same conditions are shown in Figure 3.1. The theoretical peak positions of the silicon standard and the peak positions measured experimentally are listed in Table 3.3. The errors in the measurement are obtained by subtracting the experimental values from the theoretical values of silicon standard. Using these values the measured peak positions of the alloy  $\text{Ni}_3\text{Al}$  were corrected and listed in Table 3.4. These corrected peak positions of  $\text{Ni}_3\text{Al}$  are fed into a computer program and the value of lattice parameter and the Nelson-Riley functions,  $(\cos^2\theta/\sin\theta + \cos^2\theta/\theta)$ , [266] were calculated. These are listed in Table 3.4 and plotted in Figure 3.2. The plot shows the least square line obtained from the computer program and the lattice parameter.

### 3.6. OPTICAL MICROSCOPY

Alloys were hot mounted, polished and etched. The etching reagent used was alcoholic ferric chloride. The composition of the etching solution is as follows :

Anhydrous ferric chloride	- 5 gm
Concentrated HCl	- 2 ml
Ethanol	- 96 ml
Etching time	- 20 to 30 sec
Temperature	- Room temperature

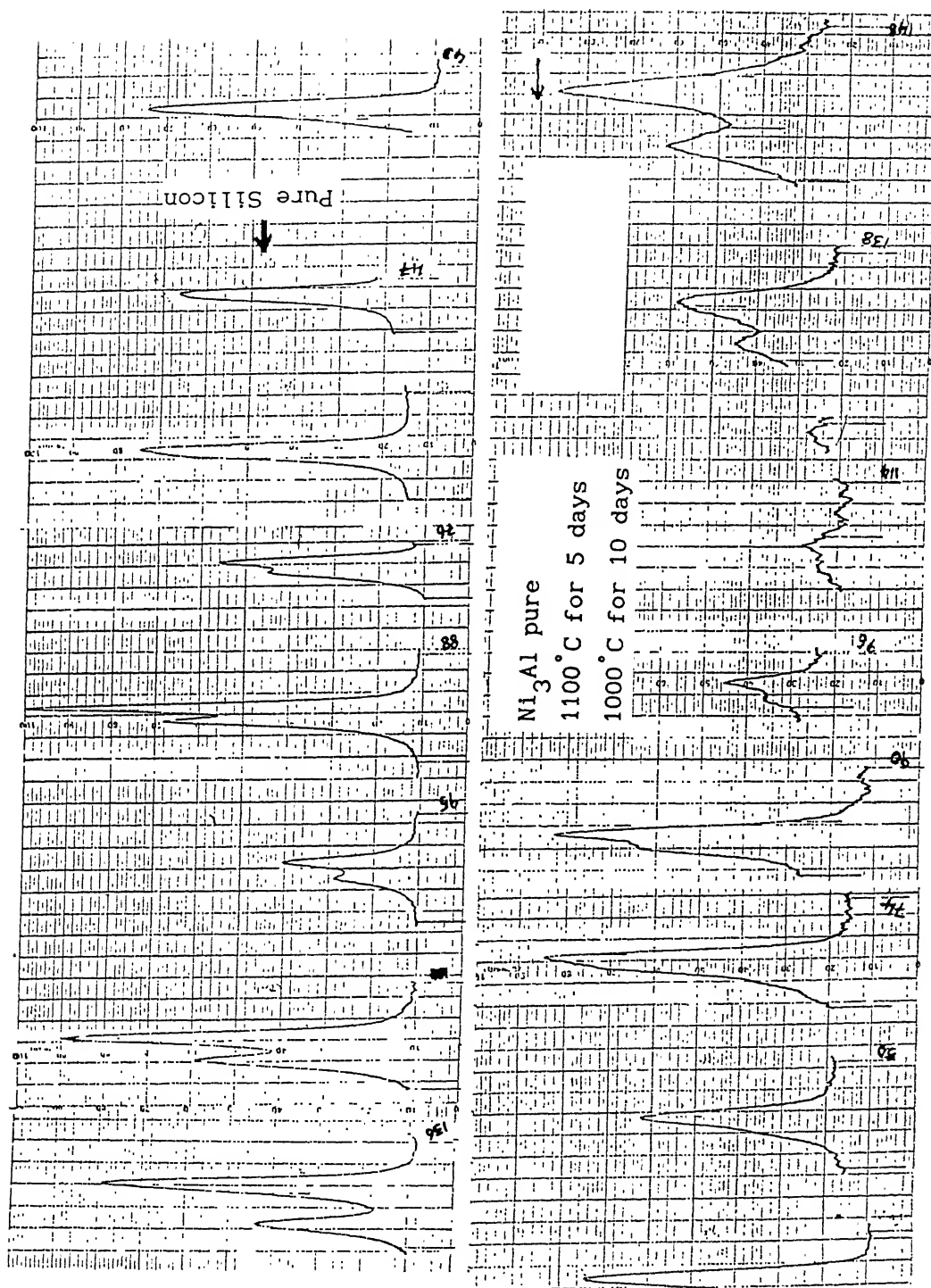


Fig. 3.1: X-ray diffraction pattern of boron-free stoichiometric  $\text{Ni}_3\text{Al}$ , homogenized at 1100°C for 5 days and then annealed at 1000°C for 10 days, along with that of silicon standard peaks.

Table 3.3

Calculation of errors using standard silicon sample

Lattice parameter of silicon,  $a_{\text{Si}} = 5.4305 \text{ \AA}$ 

$$\text{Cu } K_{\alpha} = 1.54178$$

$$\text{Cu } K_{\alpha 1} = 1.54051$$

$$\text{Cu } K_{\alpha 2} = 1.54433$$

Theoretical value of $2\theta$ for Silicon (in degrees)	Experimental value of $2\theta$ for Silicon (in degrees)	Error
47.3446	47.270	0.0746
76.4412	76.390	0.0512
88.1438	88.100	0.0438
95.0710	95.000	0.0710
114.2658	114.220	0.0458
137.1546	137.175	-0.0204

Table 3.4

Calculation of lattice parameter and Nelson-Riley Function for pure  
 $\text{Ni}_3\text{Al}$  using errors calculated for pure silicon sample

$2\theta_M$	$2\theta_C$	$\lambda$ (Å)	plane	d (Å)	a (Å)	NRF/2
43.760	43.8346	1.54178	(111)	2.0653	3.5771	2.2779
51.015	51.0896	1.54178	(200)	1.7877	3.5754	1.8568
75.140	75.1912	1.54178	(220)	1.2636	3.5739	0.9929
91.220	91.2638	1.54051	(311)	1.0775	3.5736	0.6490
96.560	96.6310	1.54051	(222)	1.0314	3.5728	0.5583
139.900	139.8796	1.54051	(331)	0.8200	3.5743	0.1108
140.695	140.6746	1.54433	(331)	0.8200	3.5742	0.1062
149.290	149.2696	1.54051	(420)	0.7988	3.5723	0.0634
150.370	150.3496	1.54433	(420)	0.7988	3.5721	0.0588

M : Measured;      C : Corrected;      NRF :  $\left[ \cos^2\theta/\sin\theta + \cos^2\theta/\theta \right]$ .

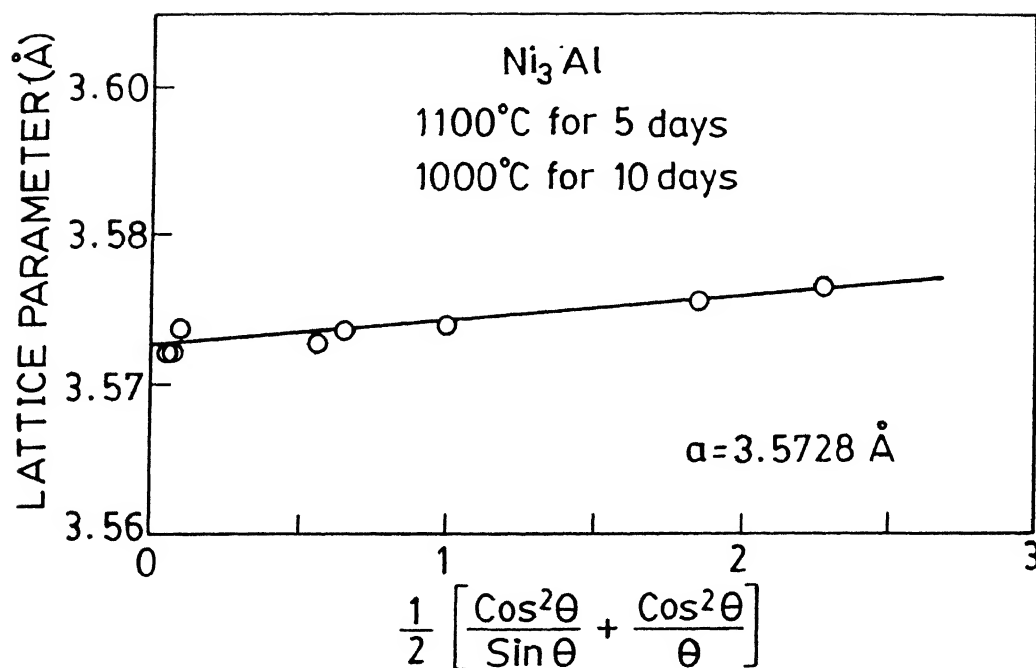


Fig. 3.2: Plot of Nelson-Riley function versus lattice parameter for boron-free stoichiometric  $\text{Ni}_3\text{Al}$ .



### 3.7. SCANNING ELECTRON MICROSCOPY

Scanning electron microscopy of the alloys having two or more phases was carried in JSM 840A JEOL scanning electron microscope (SEM). The compositional analysis was carried out using EDAX facility attached to SEM. For SEM work the samples prepared for optical microscopy were good enough except that they needed slight over etching.

The volume fractions of the second phases were also measured using high resolution scanning electron micrographs. Area fractions were calculated by superimposing transparent grid of small squares and counting the number of squares that fell on a phase. For each sample, the above procedure was repeated 20 times in order to ensure consistency. The area fraction was taken as the volume fraction of a phase.

### 3.8. TRANSMISSION ELECTRON MICROSCOPY

Initially alloy samples of 0.4 to 0.5 mm thick were cut in an Isomet cutter. These specimens were thinned down to 0.2 to 0.25 mm using fine waterproof emery papers. These specimens were, then, thinned down to 100  $\mu$ m thickness using Gatan disc grinder. Three millimeter discs were cut from these samples using a Spark erosion unit, Material Sciences, England. To avoid any overheating of the samples, they were well dipped in kerosene and then spark cut. These three millimeter disc specimens were further thinned by one of the two methods given below. The samples, on which no mechanical work was done, were thinned by using Fischione twin jet polisher. The conditions used here are given below :

Electrolyte - 10% perchloric acid in glacial acetic acid

Temperature - 5°C

Voltage - 25 V

For observing the dislocation substructures some the samples were deformed 2 to 3% by compression. These could not be satisfactorily thinned by the

above technique. These compressed samples were thinned by using 'Gatan Duo Ion Mill'. Each sample on an average took around 100 to 150 hours for thinning. This instrument was operated under following conditions :

Gun voltage	- 4kV
Gun current	- 1 DC mA
Specimen current	- 5 to 40 DC $\mu$ A
Gas	- high purity argon gas

### 3.9. HIGH TEMPERATURE COMPRESSION TEST

The compression testing specimens were cut by Isomet diamond wheel. Belt polisher was used to make the surface flat. The specimens were polished on 4/0 paper to make the surface smooth. The samples were compressed in a 10 ton MTS unit at various temperatures. The samples were heated with the help of a furnace which surround the compression jig. Temperature was measured with the help of three chromal-alumel thermocouples kept close to the samples. The arrangement is shown in Figure 3.3. The temperature of the furnace was maintained within  $\pm 2^{\circ}\text{C}$ . Generally, it took around one hour to reach the test temperatures and additional 10 to 15 minutes were given for stabilization. Following this, testing took around one hour. For all specimens, strain rate was kept at  $10^{-4}$ /s. The samples, after testing, were examined. There were no signs of oxidation.

Above  $650^{\circ}\text{C}$ , the material was too hard to be tested while being supported by tool bits. However, carbide tips were found to be suitable for supporting materials at temperatures up to  $700^{\circ}\text{C}$ .

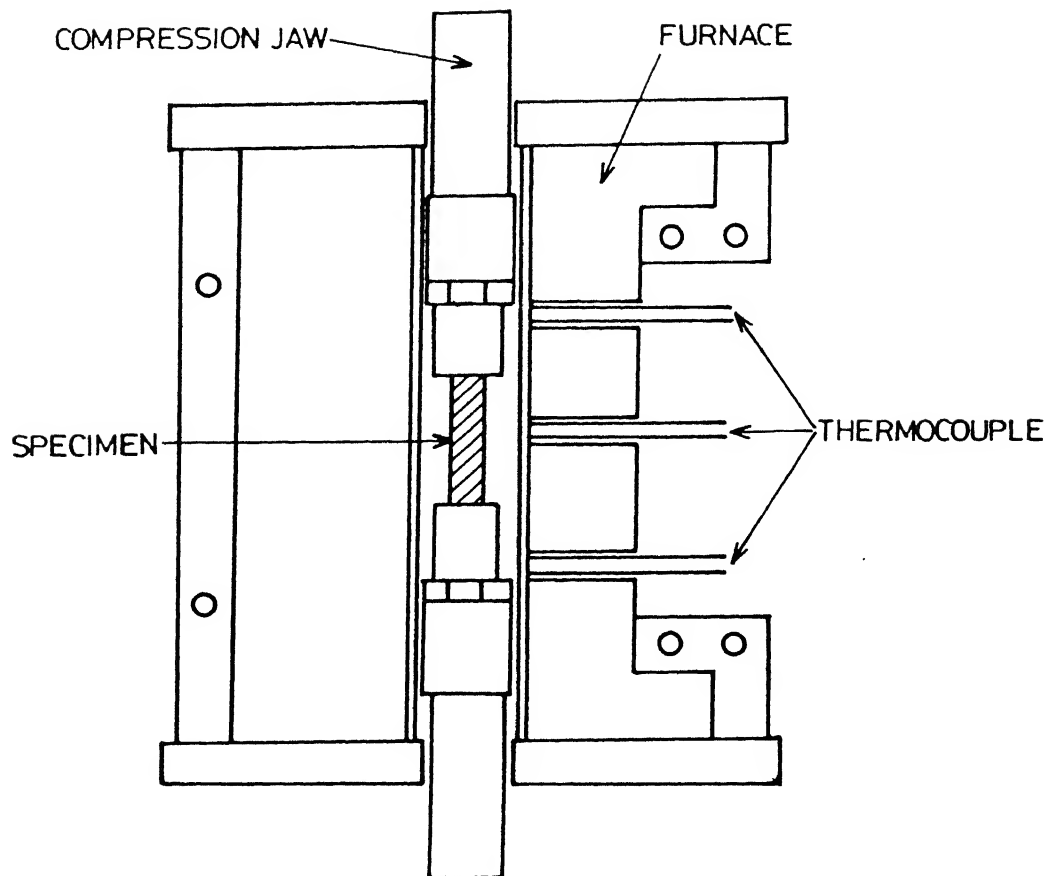


Fig. 3.3: Schematic plot of arrangements of compression testing machine.

## CHAPTER IV

PHASE EQUILIBRIA IN BORON-FREE AND BORON-DOPED  
 $\gamma'$ -RICH REGION OF THE Ni-Al-Hf SYSTEM4.1. THE TRINICKEL ALUMINIDE  $\gamma'$ 

## 4.1.1. The stoichiometric compound

A survey of literature showed that annealing at 1100°C for five days is adequate for homogenization of stoichiometric  $\text{Ni}_3\text{Al}$ . Consequently, the alloy was homogenized at 1100°C for 5 days. The microstructure of the homogenized sample of  $\text{Ni}_3\text{Al}$  (Figure 4.1) shows a homogeneous single phase structure. Annealing twins are also seen in this cubic  $\text{L1}_2$  ordered intermetallic compound. Some casting defects like cavities which are produced during arc melting of the alloy can also be seen in the microstructure.

The X-ray diffraction pattern of the alloy was recorded as described in Chapter III. The diffraction pattern showed the peaks due to  $\text{Ni}_3\text{Al}$  only. No extra peaks were observed. A typical diffraction pattern of  $\text{Ni}_3\text{Al}$  is shown in Figure 3.1.

The weight loss during arc melting of the alloy is given in Table 3.1. The weight loss on melting of this alloy is only 0.03%. Therefore, the composition calculated on the basis of weights of the component elements melted to produce the alloy is  $\text{Ni}_{75.0}\text{Al}_{25.0}$ . EDAX analysis was carried out in a JEOL scanning electron microscope in order to test for chemical homogeneity. Analysis was done at several spots which yielded consistent results. Hence, it was concluded that the alloy is homogeneous. This stoichiometric  $\text{Ni}_3\text{Al}$  was used as a standard for analyzing other alloy compositions based on  $\text{Ni}_3\text{Al}$ .

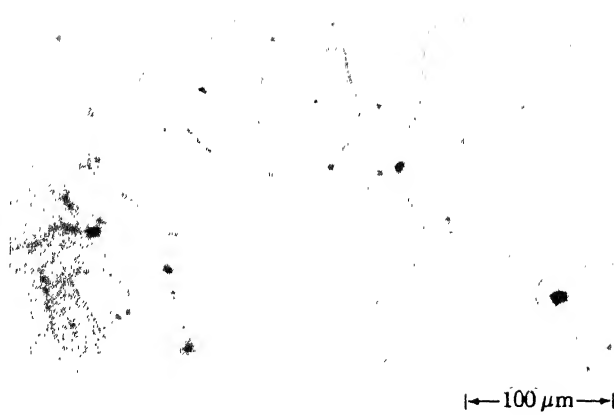


Fig. 4.1: Microstructure of stoichiometric Ni<sub>75</sub>Al<sub>25</sub> alloy homogenized at 1100°C for 5 days and water quenched.

#### 4.1.2. Nickel-rich $\gamma'$ of nominal composition $\text{Ni}_{77}\text{Al}_{23}$

Such alloys might contain second phase particles. Therefore, this alloy was homogenization annealed at  $1130^{\circ}\text{C}$  for 20 days, in order to ensure the attainment of equilibrium. The microstructure of the alloy (Figure 4.2) of nominal composition  $\text{Ni}_{77}\text{Al}_{23}$  (Table 3.1) shows a homogeneous single phase structure. Annealing twins which were seen in stoichiometric  $\text{Ni}_3\text{Al}$  are not seen in this alloy, but some casting defects are present. The X-ray diffraction pattern obtained for the alloy shows the lines due to nickel-rich  $\text{Ni}_3\text{Al}$  only. No extra lines were found.

EDAX analysis was carried out in a scanning electron microscope in order to confirm the homogeneity of the alloy. The analysis yielded consistent results at several spots using pure  $\text{Ni}_3\text{Al}$  as standard. The alloy composition was found to be  $\text{Ni}_{77.4}\text{Al}_{22.6}$  which is in excellent agreement with the composition,  $\text{Ni}_{77}\text{Al}_{23}$ , calculated on the basis of weights of the charge.

Taylor and Floyd [23] have found that at  $1150^{\circ}\text{C}$ , the Ni-Al alloy containing 25.1 at.% Al contains only  $\gamma'$  phase whereas the alloy containing 23.2 at.% Al contains a little bit of  $\gamma$ . In this investigation, it is found that at  $1130^{\circ}\text{C}$ ,  $\text{Ni}_3\text{Al}$  alloy containing 22.6 at.% Al gives a single phase structure. These results suggest that the phase boundary composition is slightly less than 22.6 at.% Al.

#### 4.1.3. Aluminium-rich $\gamma'$ of nominal composition $\text{Ni}_{73}\text{Al}_{27}$

This alloy may also contain second phase particles. Therefore, the alloy of nominal composition,  $\text{Ni}_{73}\text{Al}_{27}$  (Table 3.1), was homogenized at  $1130^{\circ}\text{C}$  for 20 days. The microstructure of the homogenized sample of the alloy (Figure 4.3) shows that the alloy has a two phase structure. The second phase was found mostly along the grain boundaries. Some second phase particles were found inside the grains as well. Annealing twins are

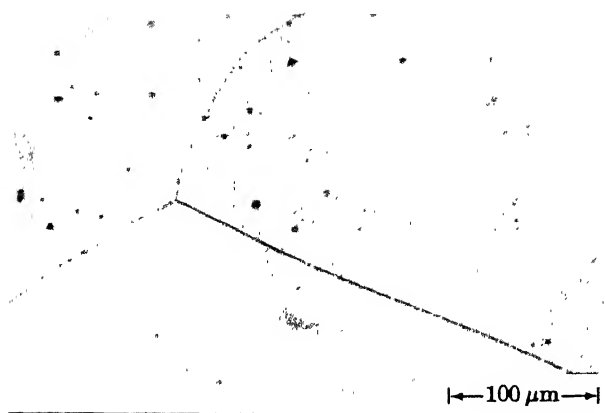


Fig. 4.2: Microstructure of the alloy  $\text{Ni}_{77.4}\text{Al}_{22.6}$  homogenized at  $1130^\circ\text{C}$  for 20 days and water quenched.

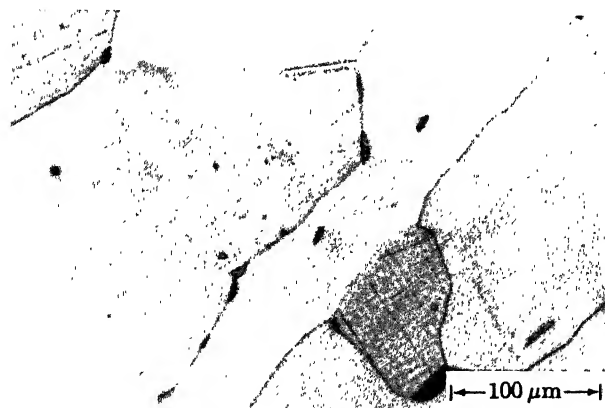


Fig. 4.3: Microstructure of the alloy of nominal composition  $\text{Ni}_{73}\text{Al}_{27}$  homogenized at  $1130^\circ\text{C}$  for 20 days and water quenched.

seen in this alloy although they are not found in the nickel-rich alloys. The volume percent of the second phase was measured metallographically and it was found to be 3.7%.

Even though the microstructure has shown a two phase structure, the X-ray pattern shows the lines due to the matrix only. There is no line observed for the second phase. This may be due to very low volume fraction of the second phase.

The weight loss due to arc melting of the alloy is negligible (0.029%). So the overall composition of the alloy, calculated from the weights of the charge before melting, is  $\text{Ni}_{73}\text{Al}_{27}$ .

EDAX analysis of the alloy was performed on both phases at several spots. It gave consistent results. The matrix composition was  $\text{Ni}_{72.9}\text{Al}_{27.1}$ . The average second phase composition was  $\text{Ni}_{65.2}\text{Al}_{34.8}$  which is in the  $\beta$  (NiAl) phase field and corresponds to the  $\beta$  phase, NiAl.

In order to check the internal consistency of these results, the overall nickel content of the alloy was calculated from the EDAX analyzed compositions of the two phases and the metallographically determined volume fractions of these two phases.

Let 'X' be the weight fraction of  $\text{Ni}_{65.2}\text{Al}_{34.8}$  in the two phase alloy and  $Y_{\text{Ni}_{65.2}\text{Al}_{34.8}}$  and  $Y_{\text{Ni}_{72.9}\text{Al}_{27.1}}$  be the weight fractions of Ni in  $\text{Ni}_{65.2}\text{Al}_{34.8}$  and  $\text{Ni}_{72.9}\text{Al}_{27.1}$  respectively. If 'Y' is the weight fraction of Ni in the overall alloy, then

$$100Y = 100 X Y_{\text{Ni}_{65.2}\text{Al}_{34.8}} + 100 (1-X) Y_{\text{Ni}_{72.9}\text{Al}_{27.1}} \quad (4.1)$$

$$X = \frac{3.7 \times \rho_{\text{Ni}_{65.2}\text{Al}_{34.8}}}{3.7 \times \rho_{\text{Ni}_{65.2}\text{Al}_{34.8}} + 96.3 \times \rho_{\text{Ni}_{72.9}\text{Al}_{27.1}}} \quad (4.2)$$

where  $\rho$  is the density.



The density of  $\text{Ni}_{65.2}\text{Al}_{34.8}$ , calculated from its lattice parameter (2.861Å) is 6.759 g/cc [267] and the density of  $\text{Ni}_{72.9}\text{Al}_{27.1}$  calculated from the lattice parameter (3.5808Å) is 7.247 g/cc. On the basis of these densities, Equation 4.2 yields 0.0346 for  $X_{\text{Ni}_{65.2}\text{Al}_{34.8}}$ . The weight percentages of nickel in  $\text{Ni}_{65.2}\text{Al}_{34.8}$  and  $\text{Ni}_{72.9}\text{Al}_{27.1}$  are 80.3 and 85.39 respectively. Substituting these data and the value of 'X' in the Equation 4.1, we get the overall weight percent of Ni in the alloy to be 85.21. Converting this into atom percent, yields 72.6. This value is in excellent agreement with the experimental value of 73 at.% Ni.

The present investigation shows that the aluminium-rich  $\text{Ni}_3\text{Al}$  at 1130°C has the composition 27.1 at.% Al. This is consistent with the results of Taylor et al. [23] who suggest that the phase boundary at 1150°C is between 26.4 and 27.8 at.% Al.

The composition of NiAl in equilibrium with  $\text{Ni}_3\text{Al}$  at 1130°C is found to be 34.8 at.% Al. This result is in excellent agreement with the solubility of  $\text{Ni}_3\text{Al}$  in NiAl of 35 at.% at 1130°C suggested by Lee and Nash [39].

## 4.2. HAFNIUM CONTAINING TRINICKEL ALUMINIDES

### 4.2.1. Homogenization

Hafnium is a high melting (2503 K) solute. Therefore, it is expected to diffuse slowly and the alloy is likely to take a long time to become homogeneous. In order to find the time suitable for homogenization,  $\text{Ni}_3\text{Al}$  containing 7.5 at.% Hf i.e. the alloy  $\text{Ni}_{75}\text{Al}_{17.5}\text{Hf}_{7.5}$ , was heat-treated as a function of time at 1130°C and the lattice parameter of the  $\gamma'$  phase present in the alloy was measured at room temperature. The plot of lattice parameter versus time for the above alloy is shown in Figure 4.4. From this it was concluded that the heat treatment at 1130°C for 20 days would

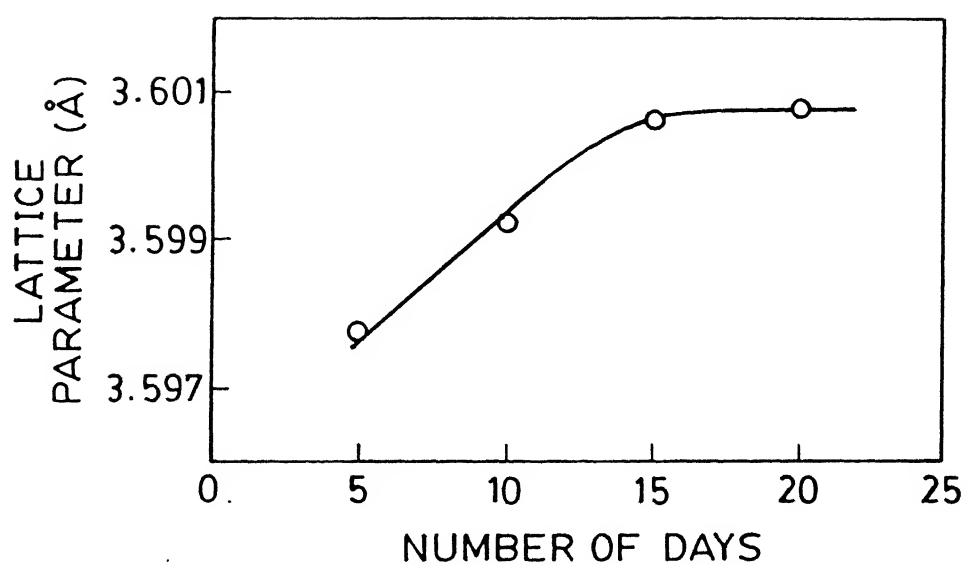


Fig. 4.4: Lattice parameter of the  $\gamma'$  phase present in the alloy of nominal composition  $\text{Ni}_{75}\text{Al}_{17.5}\text{Hf}_{7.5}$  as a function of homogenization time at  $1130^\circ\text{C}$ .

be sufficient for homogenization. Therefore, all the alloys containing hafnium were homogenized at 1130°C for 20 days.

The X-ray diffraction pattern of the alloy showed splitting of all the intensity peaks. Since, the structure of  $\gamma$  saturated with  $\text{Ni}_3\text{Al}$  is close to that of  $\text{Ni}_3\text{Al}$ , the two parts of the split peaks represent the phases,  $\gamma$  saturated with  $\text{Ni}_3\text{Al}$  and  $\text{Ni}_3\text{Al}$  containing hafnium. The separation between the peaks increased with time and the intensity of the peak of  $\gamma$  at the higher angle decreased with time as the  $\gamma$  content got reduced. The progress of the homogenization was followed from the shoulders of the diffraction peaks.

#### 4.2.2. The alloy of nominal composition $\text{Ni}_{75}\text{Al}_{22.5}\text{Hf}_{2.5}$

Figure 4.5. shows the microstructure of the homogenized sample of the alloy of nominal composition  $\text{Ni}_{75}\text{Al}_{22.5}\text{Hf}_{2.5}$  (Table 3.1). It shows a homogeneous single phase structure. No annealing twins were observed. Only casting defects like cavities were present.

To confirm the homogeneity of the alloy, EDAX analysis was carried out at several spots using stoichiometric  $\text{Ni}_3\text{Al}$  as standard which yielded consistent results. The alloy composition was found to be  $\text{Ni}_{75.7}\text{Al}_{21.5}\text{Hf}_{2.8}$ . This is very close to the overall composition,  $\text{Ni}_{75}\text{Al}_{22.5}\text{Hf}_{2.5}$ , calculated from the weights of the charge. The weight loss on melting of the alloy was negligible (0.001%).

X-ray diffraction pattern of the alloy shows the lines due to the  $\gamma'$  phase only. No extra lines were found.

#### 4.2.3. The alloy of nominal composition $\text{Ni}_{75}\text{Al}_{20}\text{Hf}_5$

Figure 4.6 shows the microstructure of the homogenized sample of the alloy of nominal composition,  $\text{Ni}_{75}\text{Al}_{20}\text{Hf}_5$ , (Table 3.1). A homogeneous

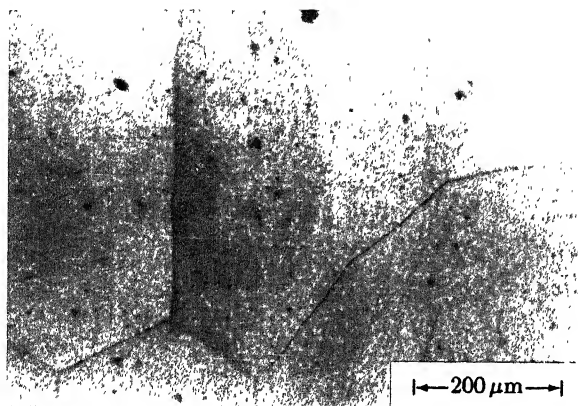


Fig. 4.5: Microstructure of the alloy  $\text{Ni}_{75.7}\text{Al}_{21.5}\text{Hf}_{2.8}$  homogenized at  $1130^\circ\text{C}$  for 20 days and water quenched.

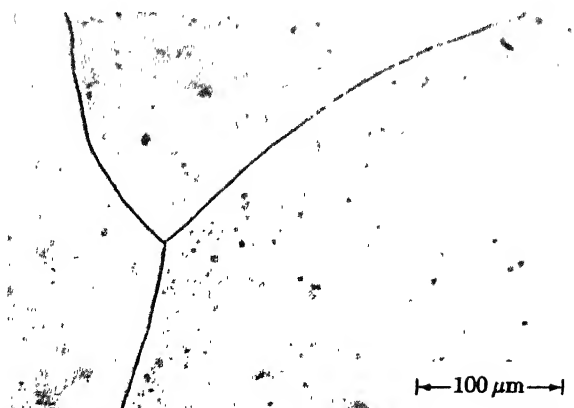


Fig. 4.6: Microstructure of the alloy  $\text{Ni}_{75.5}\text{Al}_{19.5}\text{Hf}_{5.0}$  homogenized at  $1130^\circ\text{C}$  for 20 days and water quenched.

single phase structure is seen in the micrograph. Here also, no annealing twins were observed. Only casting defects like cavities can be seen.

The X-ray diffraction pattern of the alloy showed the lines due to  $\gamma'$  phase only. No extra lines were found. This confirms the microstructural observations.

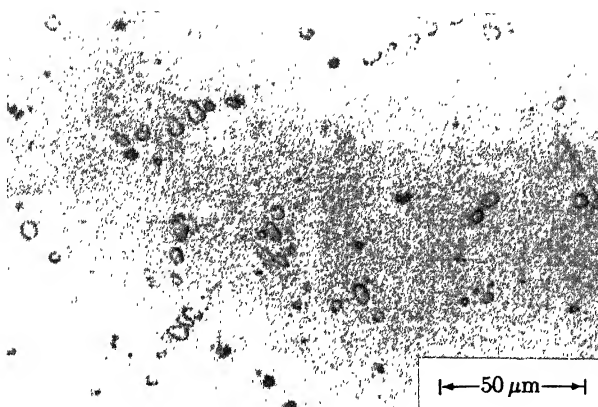
EDAX analysis was carried out in a scanning electron microscope in order to test the homogeneity of the alloy. Analysis was carried out on several spots which yielded consistent results. Hence, it was concluded that the alloy is homogeneous. The composition yielded by EDAX analysis was  $\text{Ni}_{75.5}\text{Al}_{19.5}\text{Hf}_{5.0}$ . Weight loss during arc melting of the alloy was calculated from the weights before and after melting. It was only 0.004% which is negligible. Therefore, the composition calculated on the basis of the weights of the charge,  $\text{Ni}_{75}\text{Al}_{20}\text{Hf}_5$ , compares well with the composition analyzed by the EDAX.

#### 4.2.4. The alloy of nominal composition $\text{Ni}_{75}\text{Al}_{17.5}\text{Hf}_{7.5}$

The microstructure of the homogenized sample of the alloy of nominal composition  $\text{Ni}_{75}\text{Al}_{17.5}\text{Hf}_{7.5}$  (Table 3.1) given in Figure 4.7(a) shows that the alloy has a two phase structure. The second phase particles are distributed throughout the material uniformly. The volume percent of the second phase was found to be 4.2%.

The weight loss during arc melting was calculated from the weights before and after melting and was found to be only 0.025%. It is negligible and hence, the overall composition of the alloy, on the basis of weights of the materials melted, is  $\text{Ni}_{75}\text{Al}_{17.5}\text{Hf}_{7.5}$ .

EDAX analysis of the two phases showed that the matrix composition was  $\text{Ni}_{74.8}\text{Al}_{17.8}\text{Hf}_{7.4}$  and the second phase composition was  $\text{Ni}_{78.8}\text{Al}_{0.1}\text{Hf}_{21.1}$  which correspond to the compound  $\eta_1$  ( $\text{Ni}_7\text{Hf}_2$ ). The



(a)



(b)

Fig. 4.7: Microstructure of the alloy of nominal composition  $\text{Ni}_{75}\text{Al}_{17.5}\text{Hf}_{7.5}$  homogenized at  $1130^\circ\text{C}$  for 20 days and water quenched;

(a). Optical microstructure;

(b). Scanning micrograph; 1 and 2 indicate the phases  $\gamma'$  and  $\eta_1$  respectively.

various regions analyzed are shown in Figure 4.7(b). The densities of  $\text{Ni}_{74.8}\text{Al}_{17.8}\text{Hf}_{7.4}$  and  $\text{Ni}_{78.8}\text{Al}_{0.1}\text{Hf}_{21.1}$ , calculated from the lattice parameters, were found to be 8.779 g/cc and 7.842 g/cc respectively. Using the procedure used earlier, these results yielded the overall composition given by  $\text{Ni}_{74.5}\text{Al}_{17.9}\text{Hf}_{7.6}$ . This is in excellent agreement with the composition  $\text{Ni}_{75}\text{Al}_{17.5}\text{Hf}_{7.5}$ , calculated from the weights of the charge.

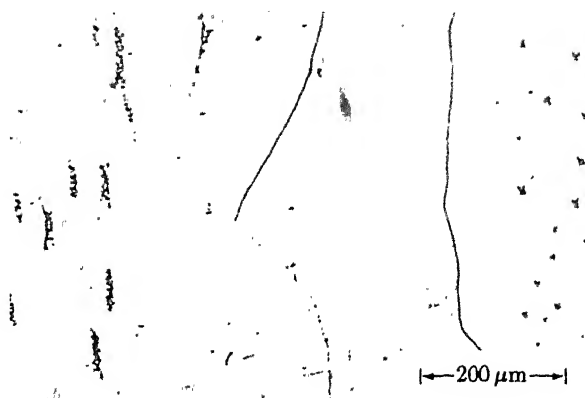
Even though the microstructure showed the presence of the  $\text{Ni}_7\text{Hf}_2$  phase also, X-ray diffraction pattern of the alloy yielded the lines due to the matrix phase,  $\gamma'$ , only. No extra lines were found. Because of the low volume percent of the second phase, the intensity of the lines due to this phase was probably very low to be detectable.

#### 4.2.5. The alloy of nominal composition $\text{Ni}_{77.5}\text{Al}_{20.0}\text{Hf}_{2.5}$

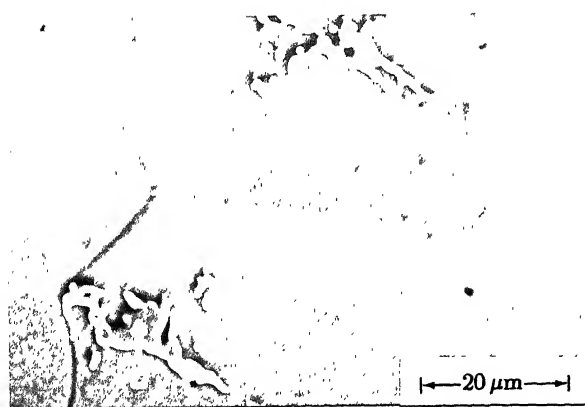
The microstructure of the homogenized alloy of nominal composition  $\text{Ni}_{77.5}\text{Al}_{20.0}\text{Hf}_{2.5}$  (Table 3.1) reveals (Figure 4.8(a)) that the alloy is a mixture of two phases. The second phase is distributed throughout the matrix. There are no annealing twins observed but some casting defects like cavities were found.

The X-ray diffraction pattern of the alloy shows the lines due to the matrix phase,  $\gamma'$ , and lines due to  $\gamma$  phase.

EDAX analysis performed on the alloy showed it to be a two phase material and the analyzed compositions were found to be  $\text{Ni}_{77.8}\text{Al}_{20.1}\text{Hf}_{2.1}$  for the matrix and  $\text{Ni}_{83.6}\text{Al}_{16.0}\text{Hf}_{0.4}$  for the  $\gamma$  phase. The various regions analyzed are indicated in Figure 4.8(b). The weight loss during arc melting of the alloy calculated from the weights before and after melting was only 0.02% which is negligible to change the overall composition of the alloy in a significant way.



(a)



(b)

Fig. 4.8: Microstructure of the alloy of nominal composition  $\text{Ni}_{77.5}\text{Al}_{20}\text{Hf}_{2.5}$  homogenized at  $1130^\circ\text{C}$  for 20 days and water quenched;

(a). Optical microstructure;

(b). Scanning micrograph; 1 and 2 indicate the phases  $\gamma'$  and  $\gamma$  respectively.



#### 4.2.6. The alloy of nominal composition $\text{Ni}_{77.5}\text{Al}_{17.5}\text{Hf}_{5.0}$

The weight loss during arc melting of the alloy was calculated from the weights before and after melting. It was only 0.05% which is negligible to change the composition drastically.

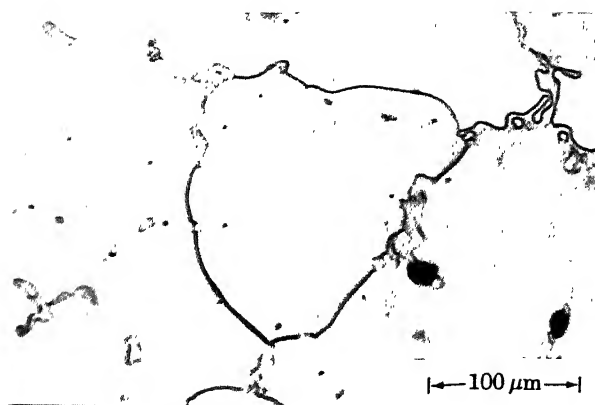
The microstructure of the homogenized alloy of nominal composition  $\text{Ni}_{77.5}\text{Al}_{17.5}\text{Hf}_{5.0}$  (Table 3.1) shows (Figure 4.9(a)) a three phase structure. Lot of casting defects were observed throughout the material. No annealing twins were found. However, the X-ray diffraction pattern of the alloy shows the lines due to the phases  $\gamma'$  and  $\gamma_1$  only. No line was observed for the third phase. It is likely to be due to the small volume fraction of the third phase.

EDAX analysis of the phases present in the alloy yielded the compositions  $\text{Ni}_{76.4}\text{Al}_{18.5}\text{Hf}_{5.1}$  for the matrix phase  $\gamma'$ ,  $\text{Ni}_{84.5}\text{Al}_{14.9}\text{Hf}_{0.6}$  for  $\gamma$  phase and  $\text{Ni}_{83.2}\text{Al}_{1.2}\text{Hf}_{15.6}$  for  $\gamma_1$  phase. The volume fraction as well as the particle size of  $\gamma_1$  were very small. Therefore, the chemical analysis of this phase was not very accurate because of the interference from the matrix. However, the measured composition is very close to the composition of  $\gamma_1$ . The phases analyzed are indicated in Figure 4.9(b).

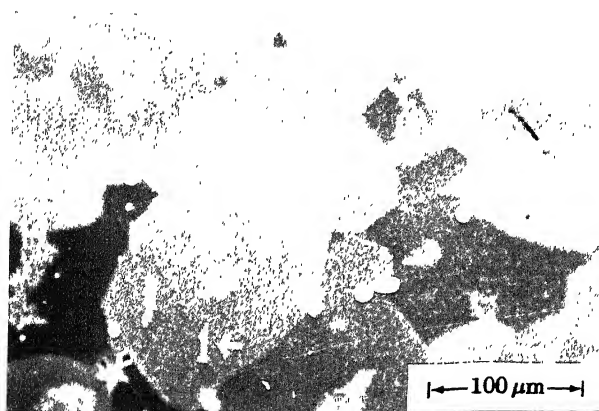
#### 4.2.7. The alloy of nominal composition $\text{Ni}_{80.0}\text{Al}_{17.5}\text{Hf}_{2.5}$

The microstructure of the homogenized alloy of nominal composition  $\text{Ni}_{80}\text{Al}_{17.5}\text{Hf}_{2.5}$  (Table 3.1) given in Figure 4.10(a) shows that the alloy has a two phase structure. The second phase particles are distributed uniformly all over the sample. The second phase also contains small particles embedded in it. However, the X-ray diffraction pattern of the alloy shows the lines due to the phases  $\gamma$  and  $\gamma'$  only.

EDAX analysis was carried out in order to find out the composition of the individual phases. The composition of the second phase was found to be  $\text{Ni}_{80}\text{Al}_{17.5}\text{Hf}_{2.5}$  which corresponds to nickel saturated with  $\text{Ni}_3\text{Al}$ . The

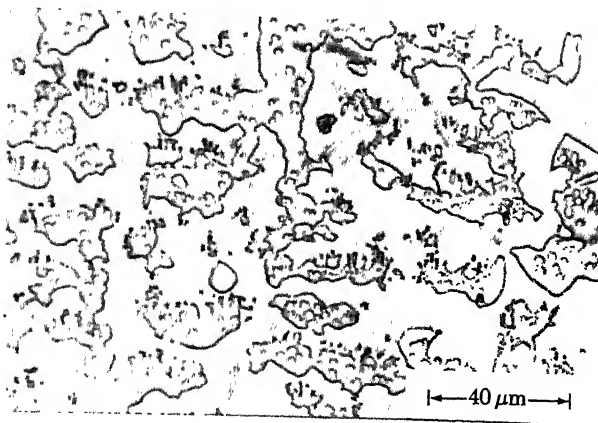


(a)

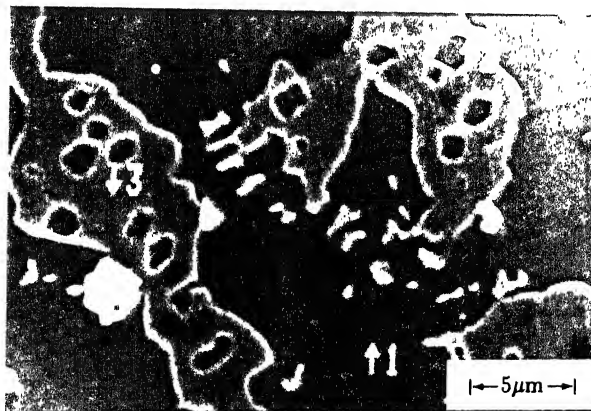


(b)

Fig. 4.9: Microstructure of the alloy of nominal composition  $\text{Ni}_{77.5}\text{Al}_{17.5}\text{Hf}_5$  homogenized at  $1130^\circ\text{C}$  for 20 days and water quenched;  
(a). Optical microstructure;  
(b). Scanning micrograph; 1 and 2 indicate the phases  $\gamma'$  and  $\gamma$  respectively.



(a)



(b)

Fig. 4.10: Microstructure of the alloy of nominal composition  $\text{Ni}_{80}\text{Al}_{17.5}\text{Hf}_{2.5}$  homogenized at  $1130^\circ\text{C}$  for 20 days and water quenched;

(a). Optical microstructure;

(b). Scanning micrograph; 1, 2 and 3 indicate the phases  $\gamma'$ ,  $\gamma'$  and  $\gamma$  respectively.

major phase as well as that present as small particles within the second phase represent the same matrix phase  $\gamma'$  of composition  $\text{Ni}_{78.0}\text{Al}_{18.8}\text{Hf}_{3.2}$ . The various phases analyzed are indicated in Figure 4.10(b).

The weight loss during arc melting of the alloy was calculated from the weights before and after melting and this was found to be 0.019%. Hence, on the basis of weights in the charge, the overall composition of the alloy is  $\text{Ni}_{80.0}\text{Al}_{17.5}\text{Hf}_{2.5}$ .

#### 4.2.8. The alloy of nominal composition $\text{Ni}_{80}\text{Al}_{15}\text{Hf}_5$

The microstructure of the homogenized alloy of nominal composition  $\text{Ni}_{80}\text{Al}_{15}\text{Hf}_5$ , given in Figure 4.11(a), shows the presence of several phases in the microstructure.

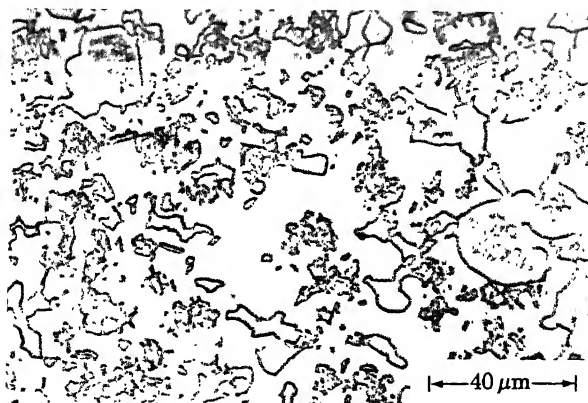
EDAX analysis was carried out in a scanning electron microscope to find out the composition of the individual phases. The analysis obtained is listed in Table 4.1. The phases  $\gamma'$ ,  $\gamma$ ,  $\gamma_1$  and  $\eta_1$  are indicated in Figure 4.11(b).

X-ray diffraction pattern of the alloy shows the lines due to the matrix phase  $\gamma'$  and lines due to  $\gamma$ . Those due to  $\eta_1$  ( $\text{Ni}_7\text{Hf}_2$ ) and  $\gamma_1$  ( $\text{Ni}_5\text{Hf}$ ) could not be detected presumably due to their low volume fractions.

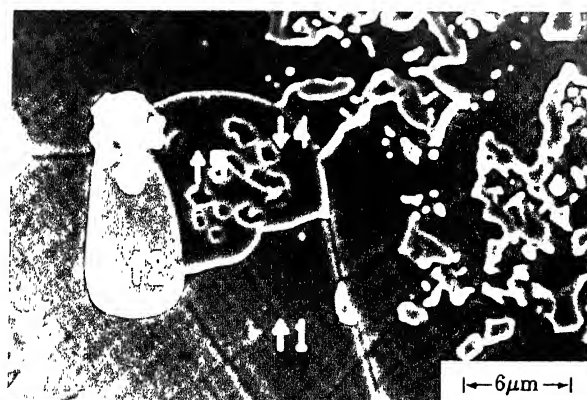
#### 4.2.9. The alloy of nominal composition $\text{Ni}_{72.5}\text{Al}_{25.0}\text{Hf}_{2.5}$

Figure 4.12(a) shows the microstructure of the homogenized sample of the alloy of nominal composition  $\text{Ni}_{72.5}\text{Al}_{25.0}\text{Hf}_{2.5}$  (Table 3.1). It clearly shows that the particles of a second phase are distributed along the grain boundaries as well as inside large grains.

EDAX analysis of several of the small second phase particles present within the grains as well as at the grain boundaries was carried out in a scanning electron microscope. All these had the same consistent



(a)



(b)

Fig. 4.11: Microstructure of the alloy of nominal composition  $\text{Ni}_{80}\text{Al}_{15}\text{Hf}_5$  homogenized at  $1130^\circ\text{C}$  for 20 days and water quenched;

(a). Optical microstructure;

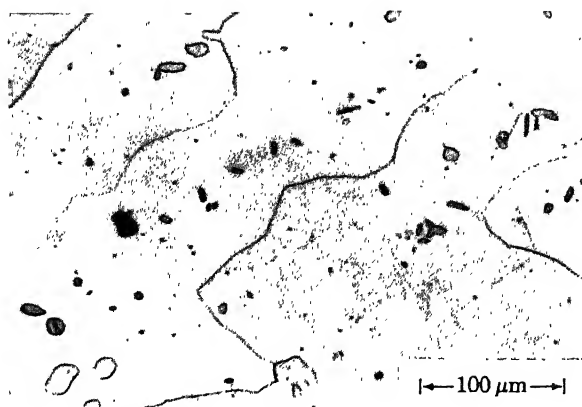
(b). Scanning micrograph, 1, 2, 3 and 5 indicate the phases  $\gamma'$ ,  $\eta_1$ ,  $\gamma_1$  and  $\gamma$  respectively and 4 indicates the overall composition of the alloy.

Table 4.1

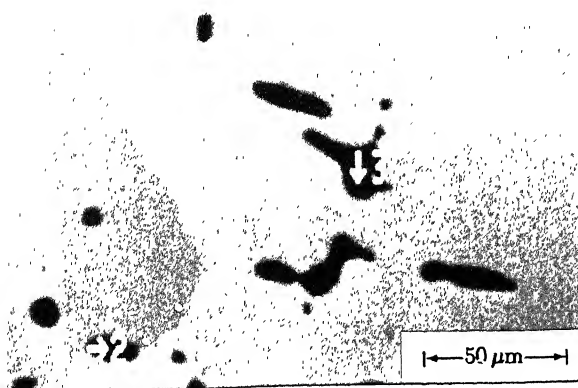
EDAX analysis of the various phases present in the alloy of nominal  
composition  $\text{Ni}_{80}\text{Al}_{15}\text{Hf}_5$

No.	Composition, at.%. NiAlHf			Phase
	Ni	Al	Hf	
1.	83.8	15.2	1.0	$\gamma$
2.	78.5	0.9	20.6	Ni <sub>7</sub> Hf <sub>2</sub> ( $\eta_1$ )
3.	84.9	0.8	14.3	Ni <sub>5</sub> Hf ( $\gamma_1$ )
4.	76.3	18.2	5.5	$\gamma'$

The phases  $\gamma'$ ,  $\gamma$ ,  $\gamma_1$  and  $\eta_1$  are indicated in Figure 4.11(b).



(a)



(b)

Fig. 4.12: Microstructure of the alloy of nominal composition  $\text{Ni}_{72.5}\text{Al}_{25}\text{Hf}_{2.5}$  homogenized at  $1130^{\circ}\text{C}$  for 20 days and water quenched;

(a). Optical microstructure;

(b). Scanning micrograph; 1 indicates the phase  $\gamma'$  and 2 and 3 indicate the phase  $\beta$ .

composition,  $\text{Ni}_{63.7}\text{Al}_{36.0}\text{Hf}_{0.3}$  with a scatter in the nickel percentage of about 2 at.%. This phase corresponds to the  $\beta$  phase (NiAl) of the Ni-Al-Hf system. The dark and bright etching matrix grains were also analyzed separately. They had an identical composition of  $\text{Ni}_{72.3}\text{Al}_{25.1}\text{Hf}_{2.6}$  which corresponds to the  $\gamma'$  phase. Thus, the alloy contains only two phases,  $\gamma'$  saturated with  $\beta$  and  $\beta$  saturated with  $\gamma'$ . The various regions analyzed are indicated in Figure 4.12(b).

The X-ray diffraction pattern of the alloy shows the lines due to the matrix  $\gamma'$  only. The lines due to  $\beta$  could not be detected.

The weight loss during arc melting of the alloy was calculated from the weights before and after melting and was found to be negligible. Hence, on the basis of the weight of the charge, the overall composition of the alloy is  $\text{Ni}_{72.5}\text{Al}_{25.0}\text{Hf}_{2.5}$ .

#### 4.2.10. The alloy of nominal composition $\text{Ni}_{72.5}\text{Al}_{22.5}\text{Hf}_{5.0}$

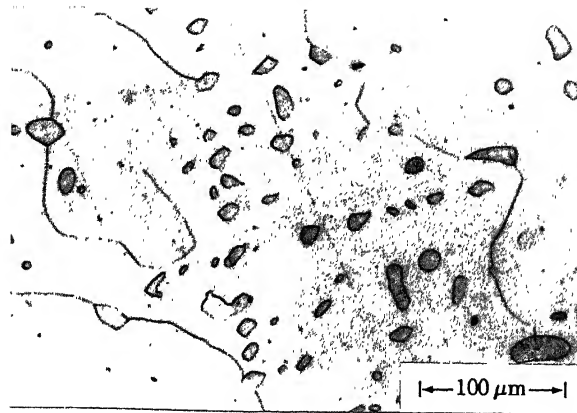
The microstructure of the homogenized alloy of nominal composition,  $\text{Ni}_{72.5}\text{Al}_{22.5}\text{Hf}_{5.0}$  (Table 3.1) is given in Figure 4.13(a). It shows clearly that there are two distinct phases present. The second phase particles are distributed along the grain boundaries as well as inside the grains.

EDAX analysis showed that the second phase particles have the composition  $\text{Ni}_{62.8}\text{Al}_{36.5}\text{Hf}_{0.7}$ . This phase corresponds to  $\beta$  (NiAl). The analysis of the matrix phase corresponds to  $\text{Ni}_{72.8}\text{Al}_{22.5}\text{Hf}_{4.7}$ . This phase corresponds to  $\gamma'$ . The phases analyzed are indicated in Figure 4.13(b). Thus, the alloy  $\text{Ni}_{72.5}\text{Al}_{22.5}\text{Hf}_{5.0}$  contains two phases, the  $\gamma'$  phase saturated with  $\beta$  and the  $\beta$  phase saturated with  $\gamma'$ .

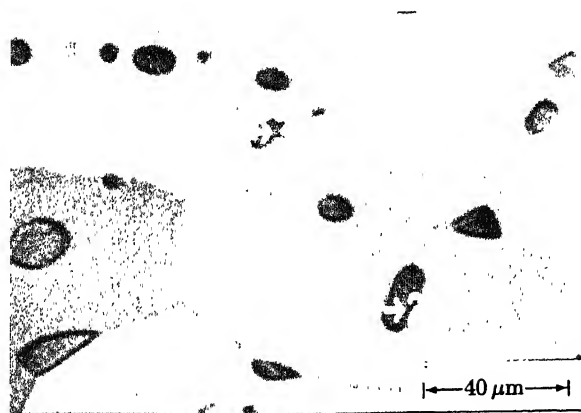
The X-ray diffraction pattern of the alloy showed the lines due to the parent phase only. The lines due to the  $\beta$  phase could not be detected although the volume percent of the second phase was close to about 10%.

The weight loss during arc melting of the alloy was calculated from





(a)



(b)

Fig. 4.13: Microstructure of the alloy of nominal composition  $\text{Ni}_{72.5}\text{Al}_{22.5}\text{Hf}_5$  homogenized at  $1130^\circ\text{C}$  for 20 days and water quenched;

(a). Optical microstructure;

(b). Scanning micrograph; 1 indicates the phase  $\gamma'$  and 2 and 3 indicate the phases  $\beta$ .

the weights before and after melting and this was found to be negligible. Hence, on the basis of the weights of the charge, the composition of the alloy is  $\text{Ni}_{72.5}\text{Al}_{22.5}\text{Hf}_{5.0}$ .

#### 4.3. THE $\gamma'$ -RICH REGION OF THE BORON-FREE Ni-Al-Hf SYSTEM

##### 4.3.1. Isothermal section

The compositions of all the phases present in the alloys of the Ni-Al-Hf system equilibrated at  $1130^\circ\text{C}$  are listed in Table 4.2. The results are represented as an isothermal section at 1403 K in Figure 4.14. In this figure,  $\gamma'$ ,  $\gamma$ ,  $\gamma_1$ ,  $\eta_1$  and  $\beta$  denote the phases  $\text{Ni}_3\text{Al}$ , nickel-rich terminal solid solution,  $\text{Ni}_5\text{Hf}$ ,  $\text{Ni}_7\text{Hf}_2$  and  $\text{NiAl}$  respectively. None of the alloys studied showed any liquid phase. This is consistent with the literature [35]. Alloys  $\text{Ni}_{75}\text{Al}_{25}$ ,  $\text{Ni}_{75.7}\text{Al}_{21.5}\text{Hf}_{2.8}$  and  $\text{Ni}_{75.5}\text{Al}_{19.5}\text{Hf}_{5.0}$  are single phase alloys. Out of the alloys that are close to the phase boundary,  $\text{Ni}_{77.4}\text{Al}_{22.6}$  is a single phase alloy whereas the rest of the alloys,  $\text{Ni}_{77.5}\text{Al}_{20.0}\text{Hf}_{2.5}$ ,  $\text{Ni}_{77.5}\text{Al}_{17.5}\text{Hf}_5$ ,  $\text{Ni}_{75}\text{Al}_{17.5}\text{Hf}_{7.5}$ ,  $\text{Ni}_{72.5}\text{Al}_{22.5}\text{Hf}_{5.0}$ ,  $\text{Ni}_{72.5}\text{Al}_{25}\text{Hf}_{2.5}$  and  $\text{Ni}_{73}\text{Al}_{27}$  contain very small percentages of other phases. The alloys having nominal compositions  $\text{Ni}_{73}\text{Al}_{27}$ ,  $\text{Ni}_{72.5}\text{Al}_{25.0}\text{Hf}_{2.5}$  and  $\text{Ni}_{72.5}\text{Al}_{22.5}\text{Hf}_5$  contain small percentages of  $\beta$ . The alloy  $\text{Ni}_{75}\text{Al}_{17.5}\text{Hf}_{7.5}$  contains a small percentage of  $\eta_1$  phase. The EDAX analysis of the alloy  $\text{Ni}_{77.5}\text{Al}_{20}\text{Hf}_{2.5}$  showed the presence of small volume percentages of  $\gamma$ . Similarly, the alloy  $\text{Ni}_{77.5}\text{Al}_{17.5}\text{Hf}_5$  showed the presence of very small percentages of the phases,  $\gamma$  and  $\gamma_1$ . The EDAX analysis of the alloy  $\text{Ni}_{80}\text{Al}_{17.5}\text{Hf}_{2.5}$  which is considerably outside the phase boundary showed the presence of  $\gamma'$  and  $\gamma$ . The alloy  $\text{Ni}_{80}\text{Al}_{15}\text{Hf}_5$  contained four phases  $\gamma'$ ,  $\gamma$ ,  $\eta_1$  and  $\gamma_1$  in equilibrium. All the compositions yielded by EDAX analysis as well as the tie lines are shown in Figure 4.14. The phase boundary of the  $\gamma'$  phase has been accordingly outlined and the parts of the  $\gamma$  and  $\beta$  phase boundaries are also indicated.

Table 4.2  
Composition of the phases present in boron-free Ni-Al-Hf system

Alloy No. from Table 3.1	Overall nominal composition calculated from the weights of materials used for arc melting (at.%)			Composition of individual phases given by EDAX analysis (at.%)											
				$\gamma'$ phase			$\gamma$ phase			$\beta$ phase			$\gamma_1$ phase		
				Ni	Al	Hf	Ni	Al	Hf	Ni	Al	Hf	Ni	Al	Hf
1	75.0	25.0	*	75.0	25.0	-	-	-	-	-	-	-	-	-	-
2	77.0	23.0	-	77.4	22.6	-	-	-	-	-	-	-	-	-	-
3	73.0	27.0	-	72.9	27.1	-	-	-	-	65.2	34.8	-	-	-	-
4	75.0	22.5	2.5	75.7	21.5	2.8	-	-	-	-	-	-	-	-	-
5	75.0	20.0	5.0	75.5	19.5	5.0	-	-	-	-	-	-	-	-	-
6	75.0	17.5	7.5	74.8	17.8	7.4	-	-	-	-	-	-	78.8	0.1	21.1
7	77.5	20.0	2.5	77.8	20.1	2.1	83.6	16.0	0.4	-	-	-	-	-	-
8	77.5	17.5	5.0	76.4	18.5	5.1	84.5	14.9	0.6	-	-	83.2	1.2	15.6	-
9	80.0	17.5	2.5	78.0	18.8	3.2	83.8	15.6	0.6	-	-	-	-	-	-
10	80.0	15.0	5.0	76.3	18.2	5.5	83.8	15.2	1.0	-	-	84.9	0.8	14.3	20.6
11	72.5	25.0	2.5	72.3	25.1	2.6	-	-	-	63.7	36.0	0.3	-	-	-
12	72.5	22.5	5.0	72.8	22.5	4.7	-	-	-	62.8	36.5	0.7	-	-	-

\* Absence of a phase or component is indicated by -.

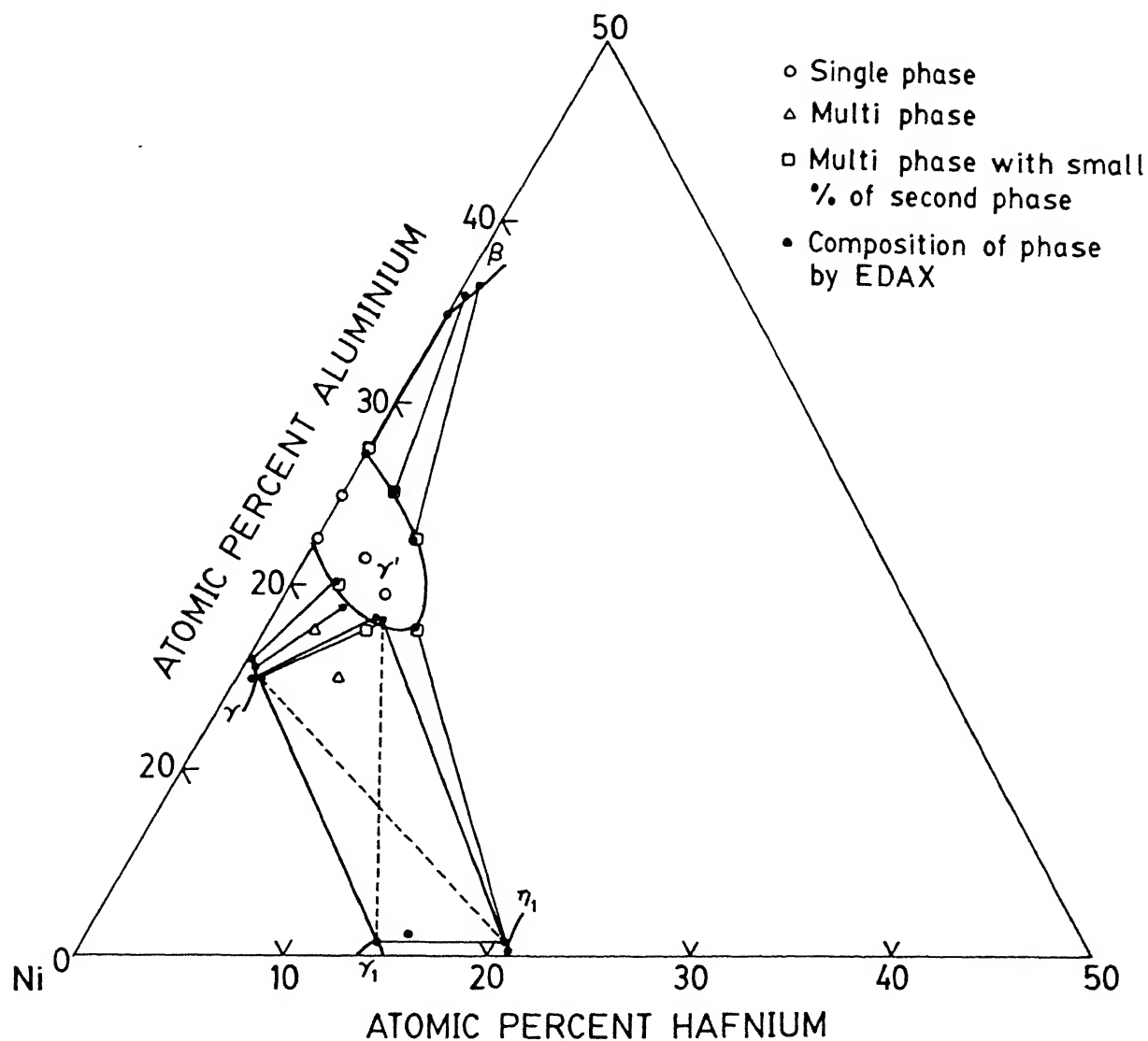


Fig. 4.14: Constitution diagram of boron-free Ni-Al-Hf system in its  $\gamma'$ -rich region at 1130°C.

Composition of  $\gamma_1$  found in one of the alloys falls outside the  $\gamma_1$  phase field as the accuracy of the compositional measurement is not high (see Section 4.2.6).

#### 4.3.2. Comparison with literature

Figure 4.15 shows the compositions of the phase boundaries of the  $\gamma'$  phase at 1000°C (1273 K) as dotted lines and at 1200°C (1473 K) as dashed lines [39]. Each of these boundaries is based on only two experimental points [35]. Therefore, the boundaries are not expected to have high degree of accuracy. The phase boundaries determined from the present investigation are also shown in Figure 4.15 as solid lines. These are based on a larger number of experimental points and are a much more accurate representation of the  $\gamma'$  phase field ( $\text{Ni}_3\text{Al}$  containing Hf). However, the phase boundaries reported in the literature are qualitatively satisfactory.

The multiphase reactions suggested from the present investigation at 1130°C are consistent with those suggested at 1000°C and 1200°C. This is demonstrated in Figure 4.15. The two phase equilibria,  $\gamma'-\beta$ ,  $\gamma'-\eta_1$  and  $\gamma'-\gamma$  have been found in this investigation at 1130°C. The two phase equilibria have also been found at 1000°C and 1200°C. The phase boundaries of the phases  $\gamma$  and  $\beta$  are consistent with the literature [24,39].

It is reported that at 1200°C, the ternary reactions,  $\gamma'-\eta_1-\gamma$  and  $\gamma-\gamma_1-\eta_1$  occur whereas at the lower temperature of 1000°C, these reactions change to ternary reactions,  $\gamma'-\eta_1-\gamma_1$  and  $\gamma'-\gamma_1-\gamma$ . It suggests that at a temperature between 1000°C and 1200°C, a quaternary reaction between  $\gamma'-\gamma-\eta_1-\gamma_1$  should exist. The phase rule states that the degree of freedom,  $F = C + 2 - P$  where 'C' is the number of components and 'P' is the number of phases. Since the number of components are three and the number of phases are four, the degree of freedom is one. Since, the pressure is kept

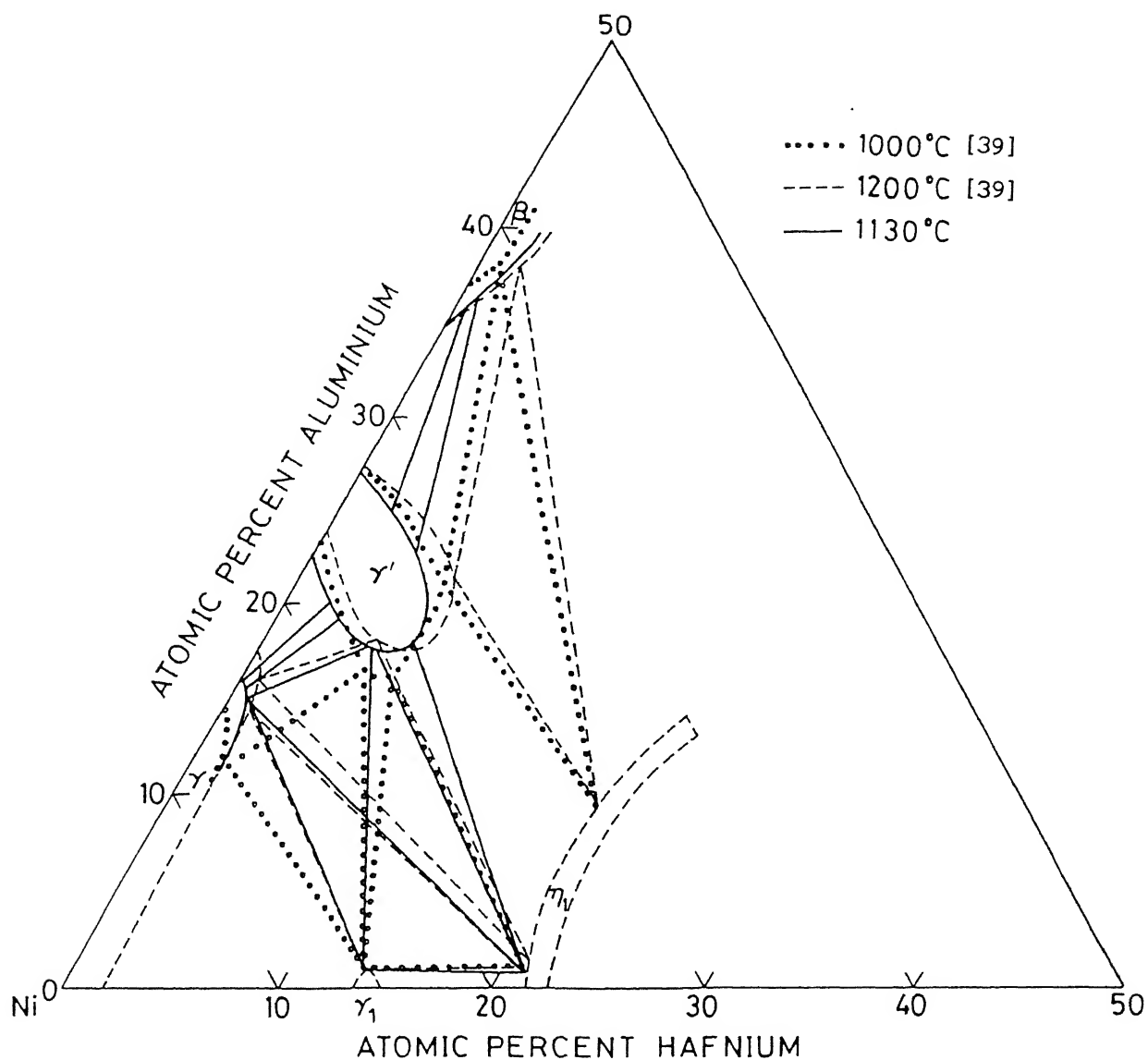
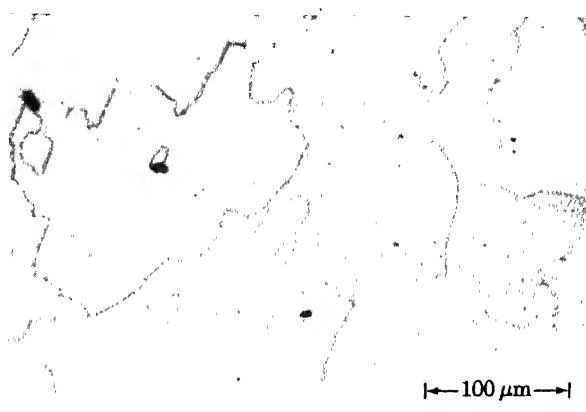
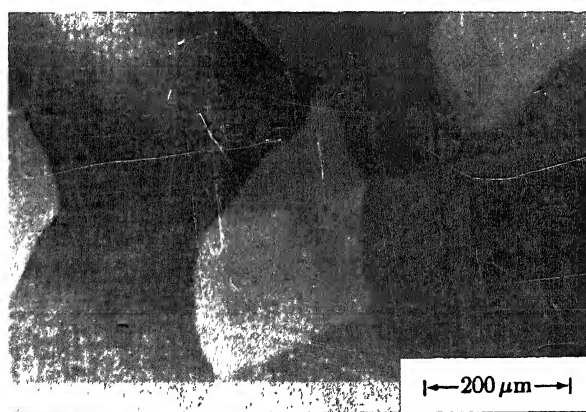


Fig. 4.15: Comparison of constitutional diagram of Ni-Al-Hf system determined in the present investigation with those reported in the literature.



(a)



(b)

Fig. 4.16: Microstructure of stoichiometric boron-doped  $\text{Ni}_{75}\text{Al}_{25}$  alloy homogenized at  $1100^{\circ}\text{C}$  for 5 days and water quenched;

(a). Alloy 'A' (see Table 3.1);

(b). Alloy 'B' (see Table 3.1).

of nominal composition  $\text{Ni}_{77}\text{Al}_{23}$  is shown in Figure 4.17. It shows a two phase structure while boron-free  $\text{Ni}_{77}\text{Al}_{23}$  was a single phase material (Figure 4.2). No annealing twins were detected but few casting defects were observed. EDAX analysis was carried out in a scanning electron microscope in order to find the compositions of the matrix phase as well as the second phase particles. Boron could not be detected in the EDAX system used but nickel and aluminium could be easily analyzed. The matrix phase composition was  $\text{Ni}_{76.9}\text{Al}_{23.1}$ . The second phase particles had the composition  $\text{Ni}_{83.9}\text{Al}_{16.1}$ , which might correspond to the composition of nickel-rich terminal solid solution which is in equilibrium with  $\gamma'$ .

In the case of boron-doped alloy of nominal composition  $\text{Ni}_{73}\text{Al}_{27}$ , the microstructure (Figure 4.18) of the homogenized alloy shows a single phase although boron-free  $\text{Ni}_{73}\text{Al}_{27}$  was a two phase alloy (Figure 4.3). EDAX analysis of the alloy yielded the composition  $\text{Ni}_{73.2}\text{Al}_{26.8}$ .

In case of both of these alloys, X-ray diffraction patterns show lines due to the  $\gamma'$  phase only. No extra lines were observed even in the two phase boron-doped alloy  $\text{Ni}_{77}\text{Al}_{23}$ .

#### 4.5. EFFECT OF BORON ON TRINICKEL ALUMINIDE CONTAINING HAFNIUM

All the alloys containing hafnium and boron were homogenized at  $1130^{\circ}\text{C}$  for 20 days. The procedure for homogenization is given in section 4.2.1. The weight losses on melting of all these alloys were negligible as seen in Table.3.1.

##### 4.5.1. Boron-doped alloy of nominal composition $\text{Ni}_{75}\text{Al}_{22.5}\text{Hf}_{2.5}$ :

Figure 4.19 shows that the homogenized sample of  $\text{Ni}_{75.0}\text{Al}_{22.5}\text{Hf}_{2.5}$  containing boron has a single phase microstructure. Lot of casting defects like cavities are observed, but no twins are seen. X-ray diffraction pattern of the alloy shows lines due to the  $\gamma'$  phase only.



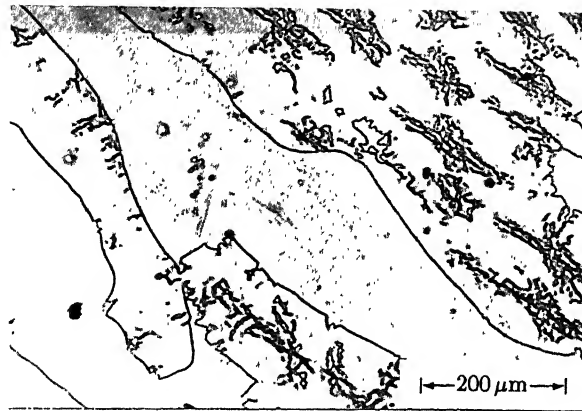


Fig. 4.17: Microstructure of boron-doped alloy of nominal composition  $\text{Ni}_{77}\text{Al}_{23}$  homogenized at  $1130^\circ\text{C}$  for 20 days and water quenched;

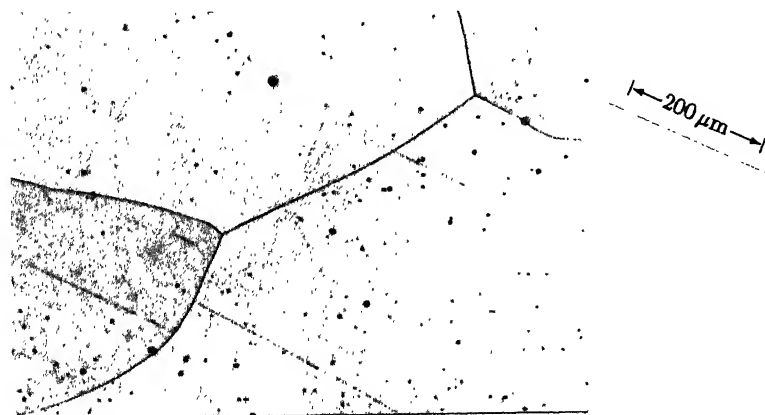


Fig. 4.18: Microstructure of boron-doped alloy  $\text{Ni}_{73.2}\text{Al}_{26.8}$  homogenized at  $1130^\circ\text{C}$  for 20 days and water quenched.

EDAX analysis, carried out in order to find the composition and homogeneity of the alloy, has indicated that the alloy has the overall composition  $\text{Ni}_{75.3}\text{Al}_{22.3}\text{Hf}_{2.4}$  which is close to the nominal composition  $\text{Ni}_{75}\text{Al}_{22.5}\text{Hf}_{2.5}$  calculated from the weights of the charges for arc melting.

#### 4.5.2. Boron-doped alloy of nominal composition $\text{Ni}_{75}\text{Al}_{20}\text{Hf}_5$ :

Figure 4.20 shows that the homogenized sample of  $\text{Ni}_{75}\text{Al}_{20}\text{Hf}_5$  containing boron has a single phase structure. Very few casting defects are seen in the micrograph and no twins are observed. X-ray diffraction pattern of the alloy shows that the lines are due to the  $\gamma'$  phase only. No extra lines are observed. The weight loss during arc melting of the alloy was found to be negligible. The composition of the alloy can, therefore, be calculated on the basis of the weights charged for melting and that gives  $\text{Ni}_{75}\text{Al}_{20}\text{Hf}_5$ . This is also confirmed from the results of the EDAX analysis carried out on the alloy which gives the composition as  $\text{Ni}_{75.2}\text{Al}_{19.7}\text{Hf}_{5.1}$ . This is very close to the composition calculated on the basis of the weights charged.

#### 4.5.3. Boron-doped alloy of nominal composition $\text{Ni}_{75}\text{Al}_{17.5}\text{Hf}_{7.5}$ :

The weight loss on melting of the alloy of nominal composition,  $\text{Ni}_{75}\text{Al}_{17.5}\text{Hf}_{7.5}$ , was negligible (Table.3.1) and the composition of the alloy was, therefore, calculated on the basis of the weights of the materials charged for melting. The optical and SEM microstructures of the homogenized alloy containing boron are presented, respectively, in Figures 4.21(a) and (b). Clearly, the alloy has a two phase structure. The second phase particles are distributed uniformly throughout the sample. The volume percentage of the second phase was 8.1%.

EDAX analysis of the two phases showed that the matrix phase

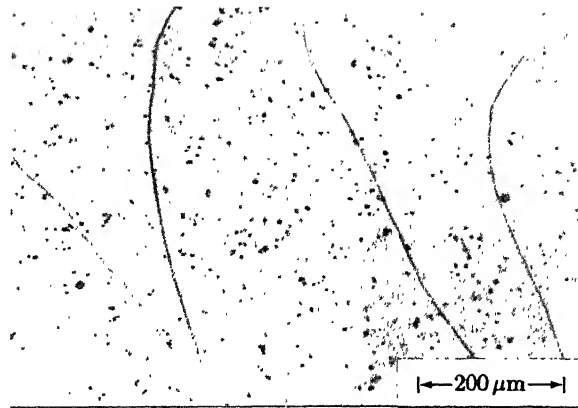


Fig. 4.19: Microstructure of boron-doped alloy  $\text{Ni}_{75.3}\text{Al}_{22.3}\text{Hf}_{2.4}$  homogenized at  $1130^{\circ}\text{C}$  for 20 days and water quenched.

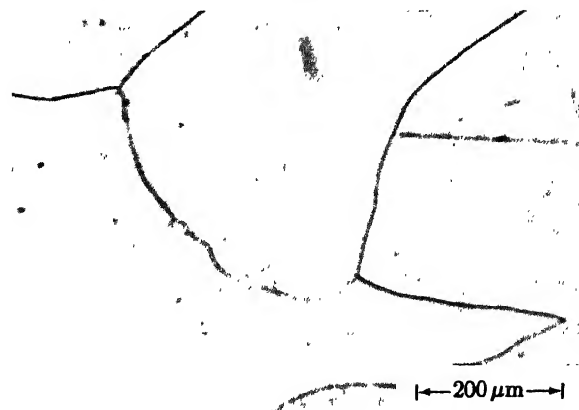
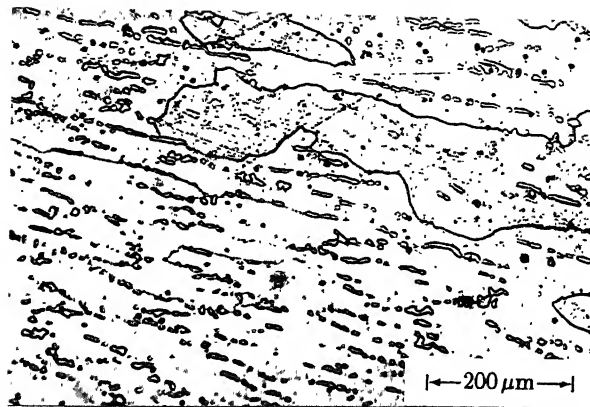
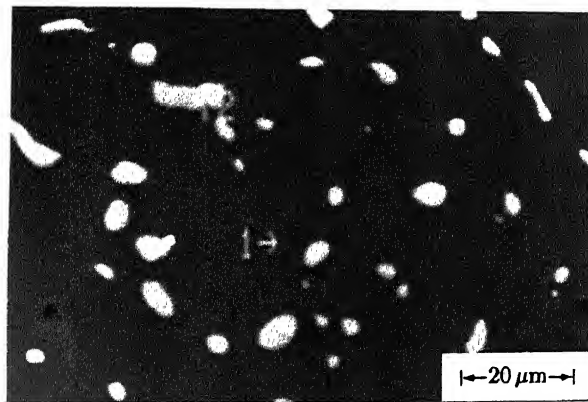


Fig. 4.20: Microstructure of boron-doped alloy  $\text{Ni}_{75.2}\text{Al}_{19.7}\text{Hf}_{5.1}$  homogenized at  $1130^{\circ}\text{C}$  for 20 days and water quenched.



(a)



(b)

Fig. 4.21: Microstructure of boron-doped alloy of nominal composition  $\text{Ni}_{75}\text{Al}_{17.5}\text{Hf}_{7.5}$  homogenized at  $1130^\circ\text{C}$  for 20 days and water quenched;

(a). Optical microstructure;

(b). Scanning micrograph; 1 and 2 indicate the phases  $\gamma'$  and  $\eta_1$  respectively.

composition was  $\text{Ni}_{75.3}\text{Al}_{17.7}\text{Hf}_{7.0}$  and the second phase composition was  $\text{Ni}_{78.3}\text{Al}_{0.3}\text{Hf}_{21.4}$  which corresponds to the compound,  $\text{Ni}_7\text{Hf}_2$  ( $\eta_1$  phase).

Even though the microstructures shows two phases, the X-ray pattern indicates that the lines are due to the matrix phase  $\gamma'$  only. No extra lines could be detected. This may be due to the low percentage of the second phase.

#### 4.5.4. Boron-doped alloy of nominal composition $\text{Ni}_{72.5}\text{Al}_{25}\text{Hf}_{2.5}$ :

Figure 4.22 shows that the microstructure of the homogenized alloy consists only of a single phase. In spite of repeated careful polishing, the series of lines inside the grains could not be removed. It is believed that these are related to some structural characteristics of the alloy. X-ray diffraction pattern of the alloy shows diffraction lines due to the  $\gamma'$  phase only. No extra lines were seen. EDAX analysis was carried out in a scanning electron microscope in order to find out the composition of the alloy. The analysis shows that the alloy composition is  $\text{Ni}_{72.5}\text{Al}_{25.2}\text{Hf}_{2.3}$  which is in excellent agreement with the composition,  $\text{Ni}_{72.5}\text{Al}_{25.0}\text{Hf}_{2.5}$ , calculated on the basis of weights charged for melting.

#### 4.5.5. Boron-doped alloy of nominal composition $\text{Ni}_{72.5}\text{Al}_{22.5}\text{Hf}_5$ :

The microstructure of the homogenized sample of the alloy given in Figure 4.23 clearly shows that the alloy has a single phase structure. Some casting defects can also be seen. X-ray pattern of the alloy shows lines due to the  $\gamma'$  phase only. No extra lines are seen. EDAX analysis of the alloy shows that the alloy composition is  $\text{Ni}_{72.3}\text{Al}_{23.1}\text{Hf}_{4.6}$  which is close to the nominal composition,  $\text{Ni}_{72.5}\text{Al}_{22.5}\text{Hf}_{5.0}$ , calculated on the basis of the weights charged for melting. The weight loss during melting of the alloy was negligible.



Fig. 4.22: Microstructure of boron-doped alloy  $\text{Ni}_{72.5}\text{Al}_{25.2}\text{Hf}_{2.3}$  homogenized at  $1130^{\circ}\text{C}$  for 20 days and water quenched.

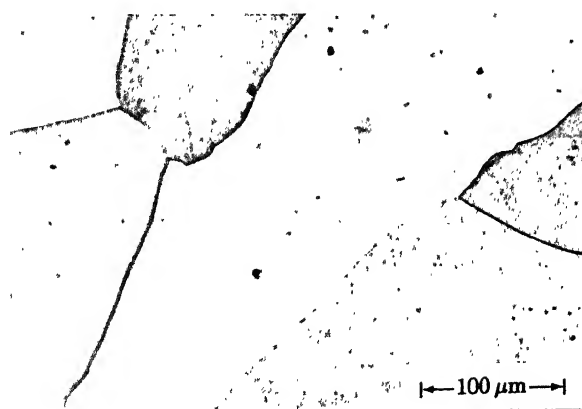


Fig. 4.23: Microstructure of boron-doped alloy  $\text{Ni}_{72.3}\text{Al}_{23.1}\text{Hf}_{4.6}$  homogenized at  $1130^{\circ}\text{C}$  for 20 days and water quenched.

#### 4.5.6. Boron-doped alloy of nominal composition $\text{Ni}_{70}\text{Al}_{27.5}\text{Hf}_{2.5}$ :

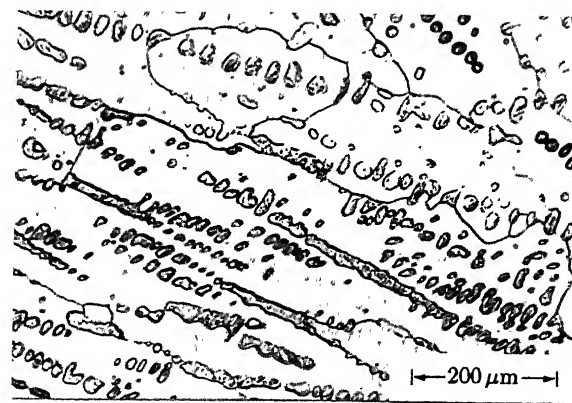
The microstructure of the homogenized alloy, shown in Figure 4.24(a), indicates that the alloy contains a two phase structure, with the second phase particles distributed throughout the matrix. The weight loss during arc melting of the alloy was calculated from the weights before and after melting and this was found to be negligible. Hence, on the basis of the weights of the charge, the overall composition of the alloy is  $\text{Ni}_{70}\text{Al}_{27.5}\text{Hf}_{2.5}$  only.

EDAX analysis of several of the small particles present was made. All these had the same composition,  $\text{Ni}_{63.1}\text{Al}_{36.6}\text{Hf}_{0.3}$ , which corresponds to the  $\beta$  phase in Ni-Al-Hf system. The matrix composition was analyzed and found to be  $\text{Ni}_{71.8}\text{Al}_{25.3}\text{Hf}_{2.9}$ . The various phases analyzed are indicated in Figure 4.24(b). The X-ray diffraction pattern of the alloy shows diffraction lines due to the matrix phase only. No extra lines due to the  $\beta$  phase could be seen.

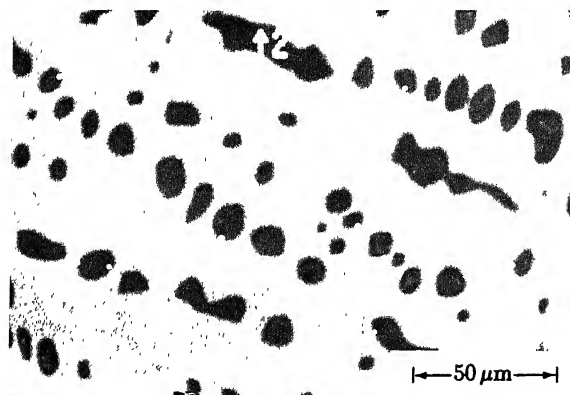
#### 4.5.7. Boron-doped alloy of nominal composition $\text{Ni}_{70}\text{Al}_{25}\text{Hf}_5$ :

The microstructure of the homogenized alloy of nominal composition  $\text{Ni}_{70}\text{Al}_{25}\text{Hf}_5$ , given in Figure 4.25(a), clearly shows that it has a two phase structure. The second phase particles are distributed throughout the material. The weight loss during arc melting of the alloy was calculated from the weights before and after melting and this was found to be negligible. Hence, on the basis of the weights taken for melting, the composition of the alloy is  $\text{Ni}_{70}\text{Al}_{25}\text{Hf}_5$ .

EDAX analysis showed that the second phase particles have the composition  $\text{Ni}_{62.2}\text{Al}_{37.4}\text{Hf}_{0.4}$  which corresponds to the  $\beta$  phase (NiAl) in the Ni-Al-Hf system. The composition of the matrix phase is  $\text{Ni}_{72.5}\text{Al}_{21.3}\text{Hf}_{6.2}$  which corresponds to the  $\gamma'$  phase in Ni-Al-Hf system. Thus, the alloy  $\text{Ni}_{70}\text{Al}_{25}\text{Hf}_5$  containing boron, contains two phases, namely



(a)



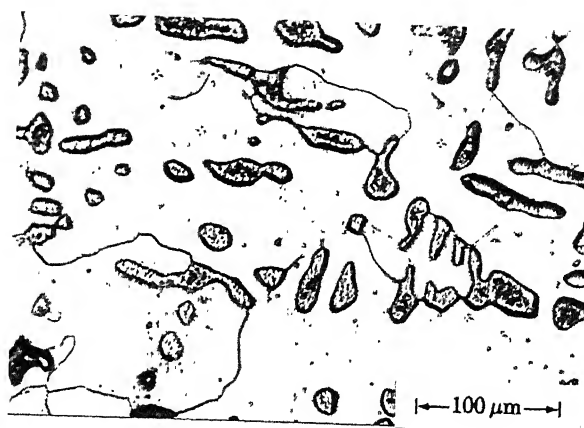
(b)

Fig. 4.24: Microstructure of boron-doped alloy of nominal composition  $\text{Ni}_{70}\text{Al}_{27.5}\text{Hf}_{2.5}$  homogenized at  $1130^{\circ}\text{C}$  for 20 days and water quenched;

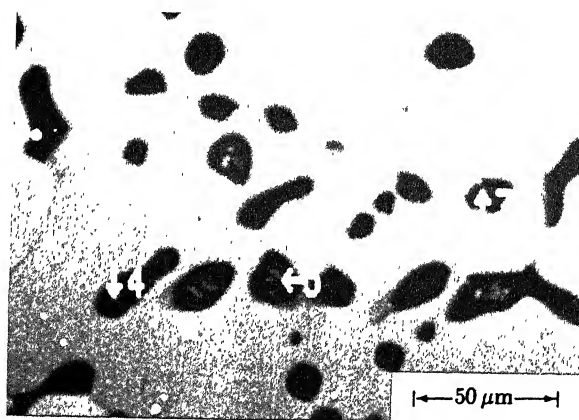
(a). Optical microstructure;

(b). Scanning micrograph; 1 and 2 indicate the phases  $\gamma'$  and  $\beta$  respectively.





(a)



(b)

Fig. 4.25: Microstructure of boron-doped alloy of nominal composition  $\text{Ni}_{70}\text{Al}_{25}\text{Hf}_5$  homogenized at  $1130^\circ\text{C}$  for 20 days and water quenched;  
 (a). Optical microstructure;  
 (b). Scanning micrograph; 1 and 2 indicate the phase  $\gamma'$  and 3, 4 and 5 indicate the phase  $\beta$ .

the  $\gamma'$  phase saturated with  $\beta$  and the  $\beta$  phase saturated with  $\gamma'$ . The phases  $\gamma'$  and  $\beta$  are indicated in Figure 4.25(b).

The X-ray diffraction pattern of the alloy shows lines due to parent phase only. The diffraction lines due to the  $\beta$  phase could not be detected.

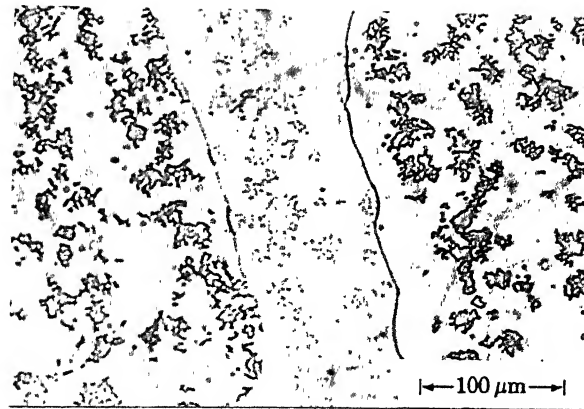
#### 4.5.8. Boron-doped alloy of nominal composition $\text{Ni}_{77.5}\text{Al}_{20}\text{Hf}_{2.5}$ :

Figures 4.26(a) show the microstructure of the alloy of nominal composition  $\text{Ni}_{77.5}\text{Al}_{20}\text{Hf}_{2.5}$  (Table 3.1). These clearly show that the alloy has a two phase structure. No casting defects were observed in the microstructure. No annealing twins could also be seen. The weight loss during arc melting was calculated and it was found to be only 0.02% which is negligible. Hence, the overall composition of the alloy on the basis of the weights charged is  $\text{Ni}_{77.5}\text{Al}_{20}\text{Hf}_{2.5}$ .

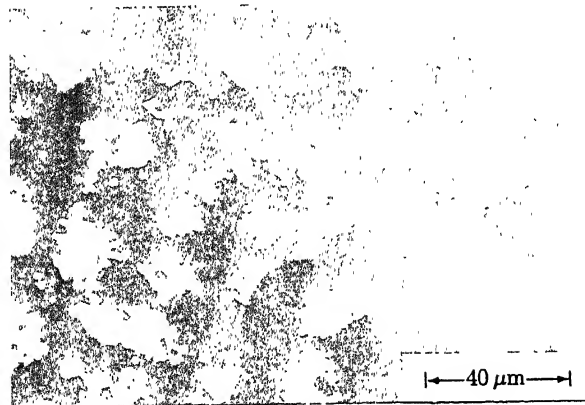
X-ray diffraction pattern of the homogenized sample of the alloy shows lines for the  $\gamma'$  phase only. No extra lines due to the presence of the other phase could be seen. EDAX analysis showed that the second phase particles have the composition  $\text{Ni}_{84.1}\text{Al}_{15.1}\text{Hf}_{0.8}$ . This phase corresponds to the  $\gamma$  phase which is the nickel-rich terminal solid solution saturated with  $\gamma'$  phase in the Ni-Al-Hf system. The analysis of the matrix phase corresponds to  $\text{Ni}_{77.1}\text{Al}_{20.1}\text{Hf}_{2.8}$  which is the  $\gamma'$  phase ( $\text{Ni}_3\text{Al}$ ) saturated with the  $\gamma$  phase. The phases analyzed are indicated in Figure 4.26(b).

#### 4.5.9. Boron-doped alloy of nominal composition $\text{Ni}_{77.5}\text{Al}_{17.5}\text{Hf}_{5.0}$

The microstructures of the homogenized sample of the alloy of nominal composition  $\text{Ni}_{77.5}\text{Al}_{17.5}\text{Hf}_{5.0}$  (Table 3.1) are given in Figures 4.27(a) and (b). These clearly indicate that the alloy has a two phase structure. The second phase particles are distributed throughout the matrix. The weight loss during arc melting of the alloy was calculated from the



(a)

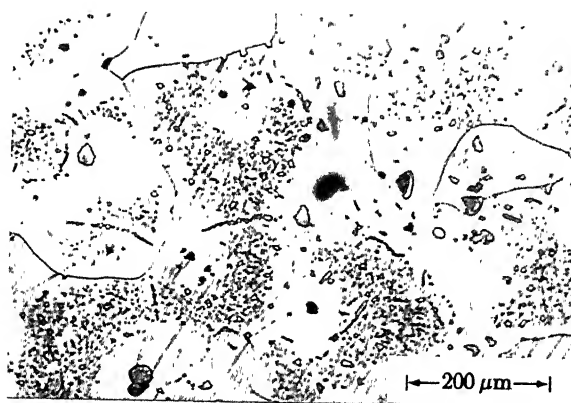


(b)

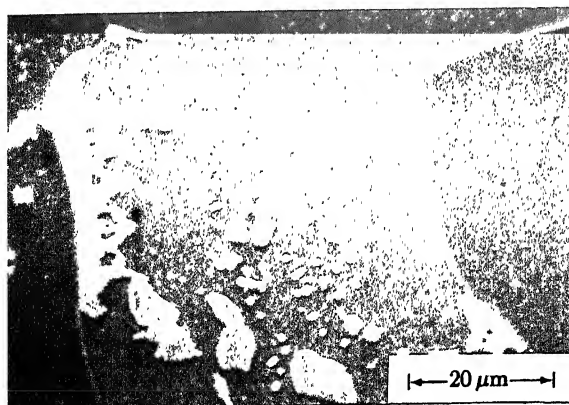
Fig. 4.26: Microstructure of boron-doped alloy of nominal composition  $\text{Ni}_{77.5}\text{Al}_{20}\text{Hf}_{2.5}$  homogenized at  $1130^{\circ}\text{C}$  for 20 days and water quenched;

(a). Optical microstructure;

(b). Scanning micrograph; 1 and 2 indicate the phases  $\gamma'$  and  $\gamma$  respectively.



(a)



(b)

Fig. 4.27: Microstructure of boron-doped alloy of nominal composition  $\text{Ni}_{77.5}\text{Al}_{17.5}\text{Hf}_5$  homogenized at  $1130^\circ\text{C}$  for 20 days and water quenched;  
(a). Optical microstructure;  
(b). Scanning micrograph; 1 and 2 indicate the phases  $\gamma'$  and  $\gamma$  respectively.

weights before and after melting and it was found to be 0.020% only. Hence, the overall nominal composition of the alloy calculated on the basis of the weights charged is  $\text{Ni}_{77.5}\text{Al}_{17.5}\text{Hf}_{5.0}$ . The EDAX analysis carried out in a scanning electron microscope showed that the second phase particles have the composition  $\text{Ni}_{85.6}\text{Al}_{13.3}\text{Hf}_{1.1}$  which corresponds to the  $\gamma$  phase, that is, the nickel-rich terminal solid solution. The analysis of the matrix phase corresponds to  $\text{Ni}_{77.7}\text{Al}_{17.6}\text{Hf}_{4.7}$ . This is the  $\gamma'$  phase ( $\text{Ni}_3\text{Al}$ ). Thus, the alloy contains two phases, the  $\gamma'$  phase saturated with  $\gamma$  phase and the  $\gamma$  phase saturated with  $\gamma'$ . The various phases analyzed are indicated in Figure 4.27(b). However, the X-ray diffraction pattern of the alloy showed the lines due to parent phase only.

#### 4.6. THE $\gamma'$ -RICH REGION OF THE BORON-DOPED Ni-Al-Hf SYSTEM

##### 4.6.1. Isothermal section

The compositions of all the phases present in the boron-doped alloys of the Ni-Al-Hf system are listed in Table 4.3. There is hardly any evidence in the literature about the phases and their compositions in different alloys based on the boron-doped Ni-Al-Hf system. The constitutional results at 1403 K (1130°C) are represented in Figure 4.28 as an isothermal section. None of the alloys studied showed any liquid phase at that temperature. Amongst the boron-doped alloys,  $\text{Ni}_{75}\text{Al}_{25}$ ,  $\text{Ni}_{75.3}\text{Al}_{22.3}\text{Hf}_{2.4}$  and  $\text{Ni}_{75.2}\text{Al}_{19.7}\text{Hf}_{5.1}$  are single phase alloys. Out of the alloys that are close to the phase boundary,  $\text{Ni}_{73.2}\text{Al}_{26.8}$ ,  $\text{Ni}_{72.5}\text{Al}_{25.2}\text{Hf}_{2.3}$  and  $\text{Ni}_{72.3}\text{Al}_{23.1}\text{Hf}_{4.6}$  are single phase alloys whereas the rest of the alloys,  $\text{Ni}_{75}\text{Al}_{17.5}\text{Hf}_{7.5}$ ,  $\text{Ni}_{77.5}\text{Al}_{17.5}\text{Hf}_{5.0}$ ,  $\text{Ni}_{77.5}\text{Al}_{20.0}\text{Hf}_{2.5}$  and  $\text{Ni}_{77}\text{Al}_{23}$  contain very small percentage of other phases. The alloys having compositions,  $\text{Ni}_{77}\text{Al}_{23}$ ,  $\text{Ni}_{77.5}\text{Al}_{20}\text{Hf}_{2.5}$  and  $\text{Ni}_{77.5}\text{Al}_{17.5}\text{Hf}_{5.0}$  contain small percentage of  $\gamma$ . The alloy  $\text{Ni}_{75}\text{Al}_{17.5}\text{Hf}_{7.5}$  contains a small percentage of  $\eta_1$  phase. The EDAX analysis of the alloys

Table 4.3

Composition of the phases present in the boron-doped Ni-Al-Hf system

Alloy No. from Table 3.1	Overall nominal composition calculated from the weights of materials used for arc melting (at%)			Composition of individual phase given by EDAX analysis (at.%)											
				$\gamma'$ phase			$\gamma$ phase			$\beta$ phase			$\eta_1$ phase		
				Ni	Al	Hf	Ni	Al	Hf	Ni	Al	Hf	Ni	Al	Hf
14	75.0	25.0	*	75.0	25.0	-	-	-	-	-	-	-	-	-	-
15	77.0	23.0	-	76.9	23.1	-	83.9	16.1	-	-	-	-	-	-	-
16	73.0	27.0	-	73.2	26.8	-	-	-	-	-	-	-	-	-	-
17	75.0	22.5	2.5	75.3	22.3	2.4	-	-	-	-	-	-	-	-	-
18	75.0	20.0	5.0	75.2	19.7	5.1	-	-	-	-	-	-	-	-	-
19	75.0	17.5	7.5	75.3	17.7	7.0	-	-	-	-	-	-	78.3	0.3	21.4
20	77.5	20.0	2.5	77.1	20.1	2.8	84.1	15.1	0.8	-	-	-	-	-	-
21	77.5	17.5	5.0	77.7	17.6	4.7	85.6	13.3	1.1	-	-	-	-	-	-
22	72.5	25.0	2.5	72.5	25.2	2.3	-	-	-	-	-	-	-	-	-
23	72.5	22.5	5.0	72.3	23.1	4.6	-	-	-	-	-	-	-	-	-
24	70.0	27.5	2.5	71.8	25.3	2.9	-	-	-	63.1	36.6	0.3	-	-	-
25	70.0	25.0	5.0	72.5	21.3	6.2	-	-	-	62.2	37.4	0.4	-	-	-

\* Absence of phase or component is indicated by -.

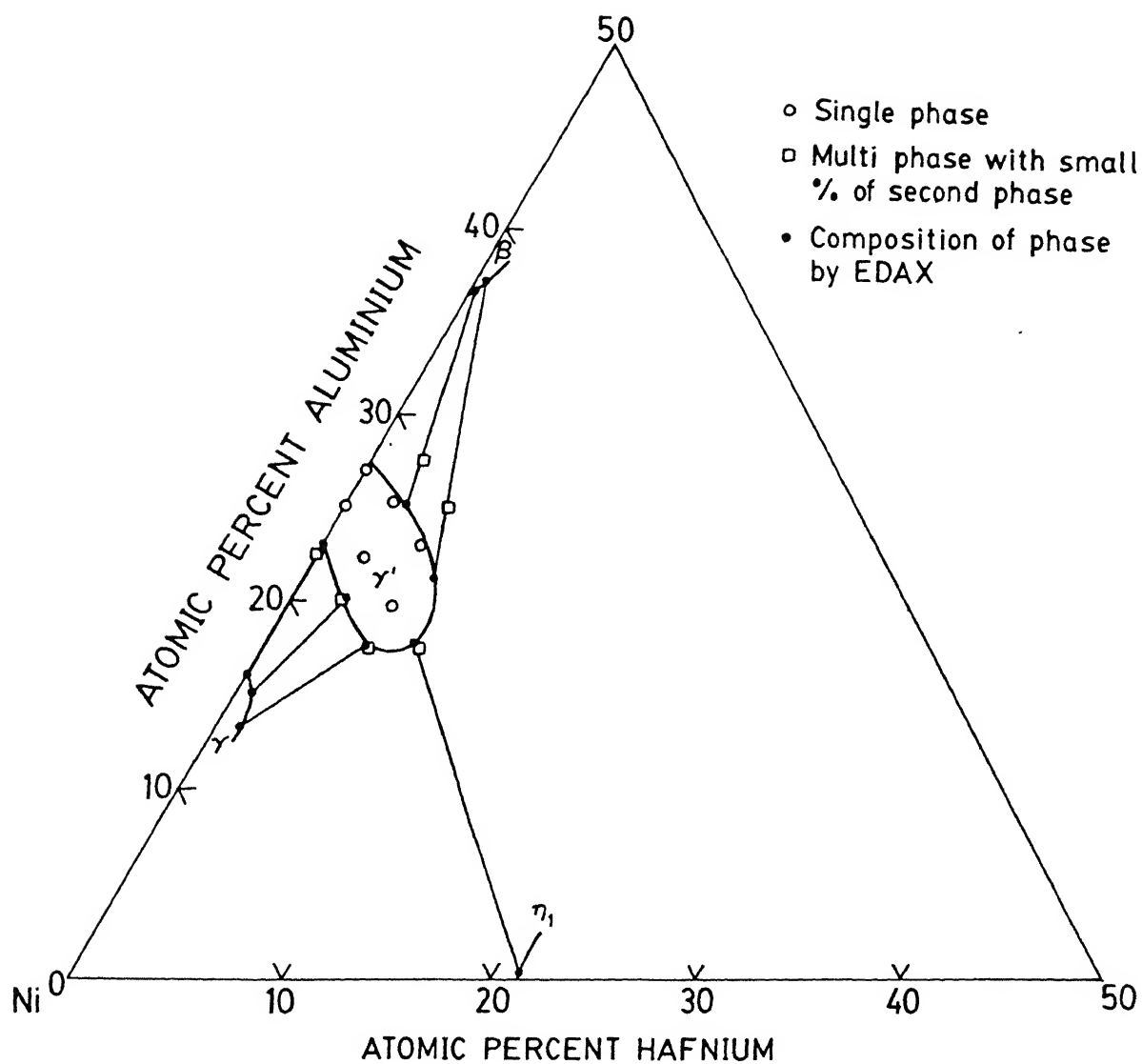


Fig. 4.28: Constitution diagram of boron-doped Ni-Al-Hf system in its  $\gamma'$ -rich region at 1130°C.

having compositions which are considerably outside the phase boundary, such as,  $\text{Ni}_{70}\text{Al}_{27.5}\text{Hf}_{2.5}$  and  $\text{Ni}_{70}\text{Al}_{25}\text{Hf}_5$ , showed the presence of  $\gamma'$  and  $\beta$ . None of the alloys showed either three or four phase equilibria. All the compositions yielded by EDAX analysis as well as the tie lines are shown in Figure 4.28. The phase boundary of the  $\gamma'$  phase has been accordingly outlined and the parts of  $\gamma$  and  $\beta$  phase boundaries are also indicated. There is no literature on the constitutional diagram for boron-doped Ni-Al-Hf ternary system. However, the results are very similar to those obtained for boron-free Ni-Al-Hf system.

#### 4.6.2. Comparison with boron-free constitutional diagram

Figure 4.29 shows the isothermal section containing the  $\gamma'$ -rich region of the constitutional diagram for boron-free and boron-doped Ni-Al-Hf systems. The phase boundaries of the four phases namely,  $\gamma$ ,  $\gamma'$ ,  $\beta$  and  $\eta_1$  are shown as dotted lines for boron-doped system and as full lines for boron-free system. It can be noted that the boundaries in the boron-doped alloys have shifted appreciably with respect to those in the boron-free alloys. In the presence of boron, the solubility of Ni in the  $\gamma'$  phase is reduced whereas that of Al in the  $\gamma'$  phase is increased. It suggests that in the presence of boron it is easier for aluminium and hafnium to occupy nickel sites while it is difficult for nickel to occupy aluminium sublattice. The solubility of aluminium in the  $\gamma$  phase does not change appreciably while that of nickel in the  $\beta$  phase is reduced by about 1.25 at% in the boron-doped state. The solubilities of nickel and aluminium are decreased by 0.5 at.% in  $\eta_1$  phase in the presence of boron. It is to be noted that although the boron content is very small (of the order of 0.1 at.%), the solubilities of the substitutional solutes showed changes of about 1 at.%. The presence of boron in Ni-Al-Hf system does not introduce any new phase or any new phase equilibria.



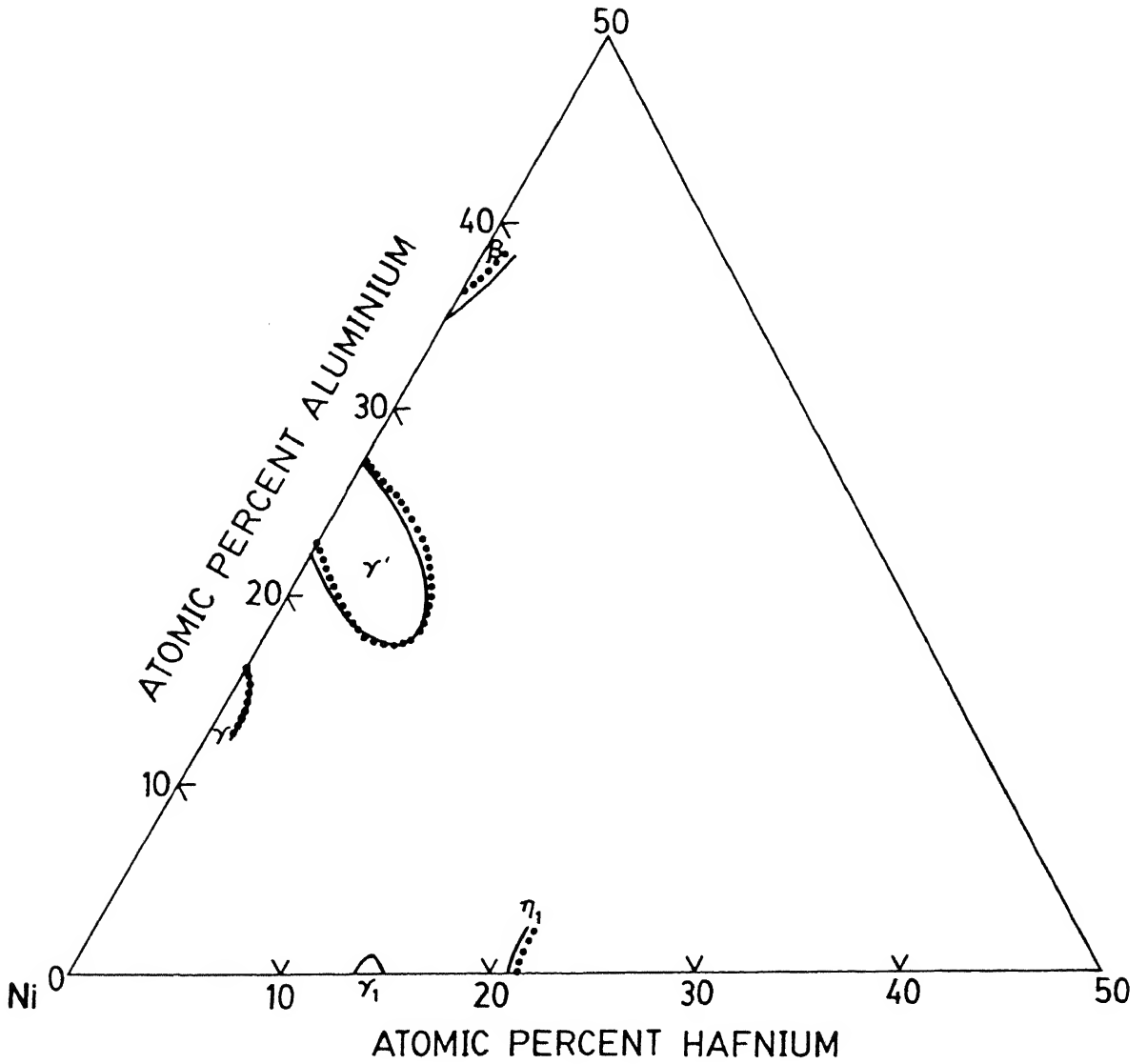


Fig. 4.29: Comparison of phase boundaries of boron-free and boron-doped Ni-Al-Hf system at 1130°C.

The size of boron atom (1.68 Å) is much larger than that of the interstitial holes (1.07 Å) in  $L1_2$  structure of  $Ni_3Al$ . The boron atom tends to push away the neighbouring substitutional atoms and expand the lattice. Therefore, it should have been easier for  $Ni_3Al$  to accept excess nickel atoms rather than aluminium atoms which are much larger than the nickel atoms. However, the phase boundary of  $Ni_3Al$  shows that it is easier for  $Ni_3Al$  to accept more of aluminium and hafnium atoms rather than nickel atoms. Thus, the size factor does not appear to be important in determining the alloying behaviour. The stronger interaction of Al-B and Hf-B compared with that between Ni and B can encourage the acceptance of more aluminium and hafnium atoms rather than nickel atoms by  $Ni_3Al$ . It is, therefore, suggested that the interaction between B and Ni is much weaker than those between B and Al and B and Hf. This aspect is discussed in greater detail in the following chapter.

## CHAPTER V

### STRUCTURAL CHARACTERISTICS OF $\gamma'$

#### 5.1. LATTICE PARAMETER

##### 5.1.1. Stoichiometric $\gamma'$

The homogenized samples of  $\gamma'$  were equilibrated at 1200°C, 1130°C, 1000°C and 800°C. The lattice parameters were measured at room temperature with samples quenched from the equilibration temperatures. The equilibration time was upto 5 days at 1200°C, 7 days at 1130°C, 10 days at 1000°C and 20 days at 800°C. The measured lattice parameters are listed in Table 5.1.

The lattice parameter of  $\text{Ni}_{75}\text{Al}_{25}$  has been shown in Figure 5.1 as a function of the equilibration temperature. Figure 5.1 does indicate changes in lattice parameter with change in quenching temperature. This is expected as it is well known that the lattice parameter of  $\text{Ni}_3\text{Al}$  is sensitive to heat treatment [23,52,54-56].

The available literature values of lattice parameters of the alloys and their heat treatments are listed in Table 5.2. Bradley et al. [55] found that the alloy  $\text{Ni}_{75}\text{Al}_{25}$  yielded higher lattice parameter (3.5745 Å) after slow cooling from 900°C than after quenching from the same temperature (3.5675 Å). Young et al. [56] have also measured the lattice parameter of  $\text{Ni}_3\text{Al}$  after slow cooling from 1100°C. This value was found to be 3.552 Å which is much lower than that of Bradley et al. [55]. Increases in the lattice parameters due to slow cooling rather than quenching from 900°C was also observed for the alloys containing 23.37 at.% Al and 26.25 at.% Al. Thus, according to Bradley et al. [55] in both stoichiometric and off-stoichiometric  $\text{Ni}_3\text{Al}$ , the lattice parameter increases due to slow

Table 5.1

Lattice parameter of boron-free  $\text{Ni}_3\text{Al}$  homogenized at  $1100^\circ\text{C}$  for 5 days  
as a function of equilibration temperature

Alloy (at.%)		Lattice parameter ( $\text{\AA}$ ) at $25^\circ\text{C}$ of specimens quenched from equilibration temperature ( $^\circ\text{C}$ )			
Ni	Al	800	1000	1130	1200
77.4	22.6			3.5697	
75.0	25.0	3.5705	3.5728	3.5726	3.5726
73.8	26.2			3.5808	

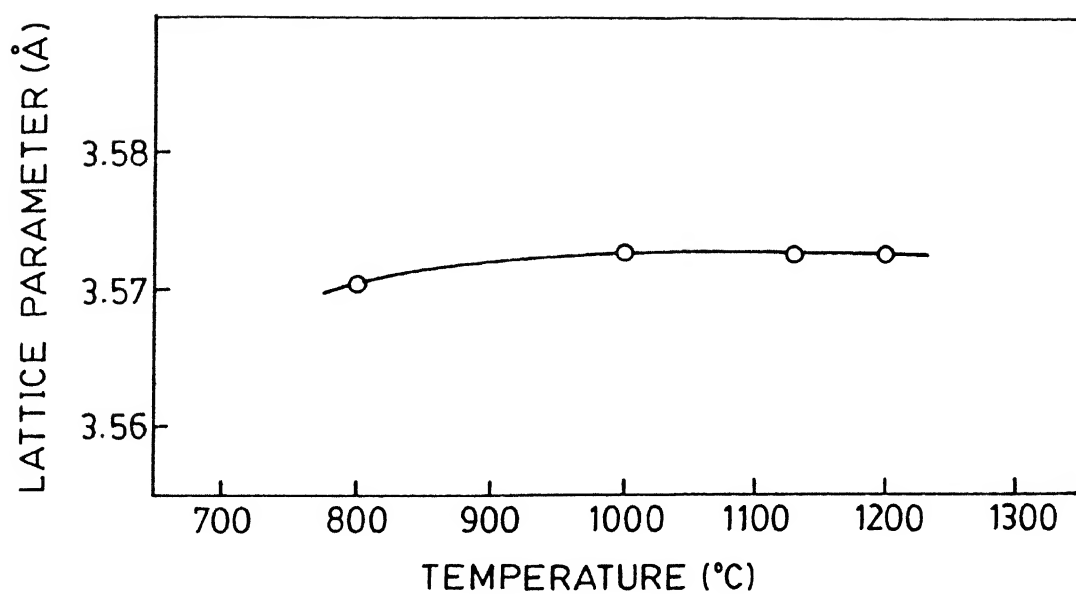


Fig. 5.1: Variation of lattice parameter of binary boron-free  $\text{Ni}_{75}\text{Al}_{25}$  as a function of equilibration temperature.

Table 5.2

Heat treatment and lattice parameter of boron-free  $\gamma'$  available  
in the literature

Atom percent aluminium	Heat treatment	Lattice parameter (Å)	Reference
25.1	Quenched from 1150°C	3.5663	Taylor et al. [23]
	Quenched from 1000°C	3.5668	"
	Quenched from 850°C	3.5677	"
	Quenched from 750°C	3.5678	"
26.4	Quenched from 1150°C	3.5706	"
	Quenched from 1000°C	3.5707	"
	Quenched from 850°C	3.5703	"
	Quenched from 750°C	3.5699	"
23.4	1050°C/48h/FC	3.5650	Masahashi et al. [52]
24.3	1050°C/48h/FC	3.5670	"
23.5	Slow cooled from 1000°C	3.5663	Ramesh et al. [54]
24.5	Slow cooled from 1000°C	3.5722	"
23.37	Slow cooled from 900°C	3.5819	Bradley et al. [55]
	Quenched from 900°C	3.5641	"
	Quenched from 600°C	3.5660	"
25	Slow cooled from 900°C	3.5745	"
	Quenched from 900°C	3.5675	"
	Quenched from 600°C	3.5676	"
25.25	Quenched from 900°C	3.5670	"
26.25	Slow cooled from 900°C	3.5896	"
	Quenched from 900°C	3.5671	"
	Quenched from 600°C	3.5676	"
25	900°C/5h/AC + 1100°C/5h/AC	3.5520	Young et al. [56]

cooling and the lattice parameter has the tendency to increase slightly with decrease in quenching temperature. However, Taylor et al. [23] found that decrease in quenching temperature from 1150°C to 750°C increases the lattice parameter in the alloy containing 25.1 at.% Al, but the lattice parameters of off-stoichiometric  $\gamma'$  containing 26.4 at.% Al shows a decrease in lattice parameter with decrease in quenching temperature. There is, therefore, a lot of inconsistency in the published lattice parameter values. Nevertheless, it is clear that heat treatment of samples leads to appreciable changes in the lattice parameter.

It is difficult to compare the reported values of lattice parameters of  $\gamma'$  with those of the present results (Figure 5.1) as the heat treatments are not always clearly specified in the literature. As only a trace amount of a solute can affect the lattice parameter, the lattice parameter values reported by various workers may not be directly comparable to the values obtained in the present investigation. The lattice parameters of  $\gamma'$  containing 25 at.% Al that were reported by Bradley et al. [55] yield a slight negative dependence of lattice parameter on quenching temperature. However, according to Taylor et al. [23], the temperature dependence of the lattice parameter of  $\gamma'$  containing 25.1 at.% Al for samples quenched from 1150°C, 1000°C, 850°C and 750°C is same as that obtained from the present results above 1000°C (Figure 5.1). Taylor et al. [23] also measured the lattice parameter of off-stoichiometric  $\gamma'$  alloy containing 26.4 at.% Al as a function of temperature. These results show a decrease in lattice parameter with decrease in quenching temperature which is identical with the present observation.

### 5.1.2. Off-stoichiometric $\gamma'$

The alloy of nominal composition  $\text{Ni}_{73}\text{Al}_{27}$  contains the phases

$\text{Ni}_{72.9}\text{Al}_{27.1}$  ( $\gamma'$  phase) and  $\text{Ni}_{65.2}\text{Al}_{34.8}$  ( $\beta$  phase). The lattice parameter of the  $\gamma'$  phase in this alloy homogenized at  $1130^\circ\text{C}$  for 20 days was measured and the value is listed in Table 5.1.

The alloy  $\text{Ni}_{77.4}\text{Al}_{22.6}$  is a single phase alloy. The lattice parameter of this alloy homogenized at  $1130^\circ\text{C}$  for 20 days was measured and this value is also listed in Table 5.1.

The dependence of the lattice parameter of  $\text{Ni}_3\text{Al}$  quenched from  $1130^\circ\text{C}$  is shown in Figure 5.2 as a function of aluminium content of the alloy. A number of values for the lattice parameter of  $\text{Ni}_3\text{Al}$ , as a function of its composition, are also available in the literature [23,52,54,55]. However, these values are widely different from one another mainly because of the differences in heat treatments given to different samples. Therefore, direct comparison of these values with those of the present investigation is not possible. However, the literature values show an increase in lattice parameter with increase in aluminium content which is also observed to be the case in the present work (Figure 5.2).

### 5.1.3. Hafnium containing $\gamma'$

As mentioned earlier, hafnium containing  $\gamma'$  alloys were homogenized at  $1130^\circ\text{C}$  up to 20 days in order to ensure complete homogenization (Figure 4.4). The lattice parameters of the  $\gamma'$  phase present in all the hafnium containing alloys measured after homogenization at  $1130^\circ\text{C}$  for 20 days are listed in Table 5.3.

Lattice parameters of some of the hafnium containing alloys are available in the literature [58]. However, as the compositions of these alloys are different from those investigated in this study, direct comparison is not possible.



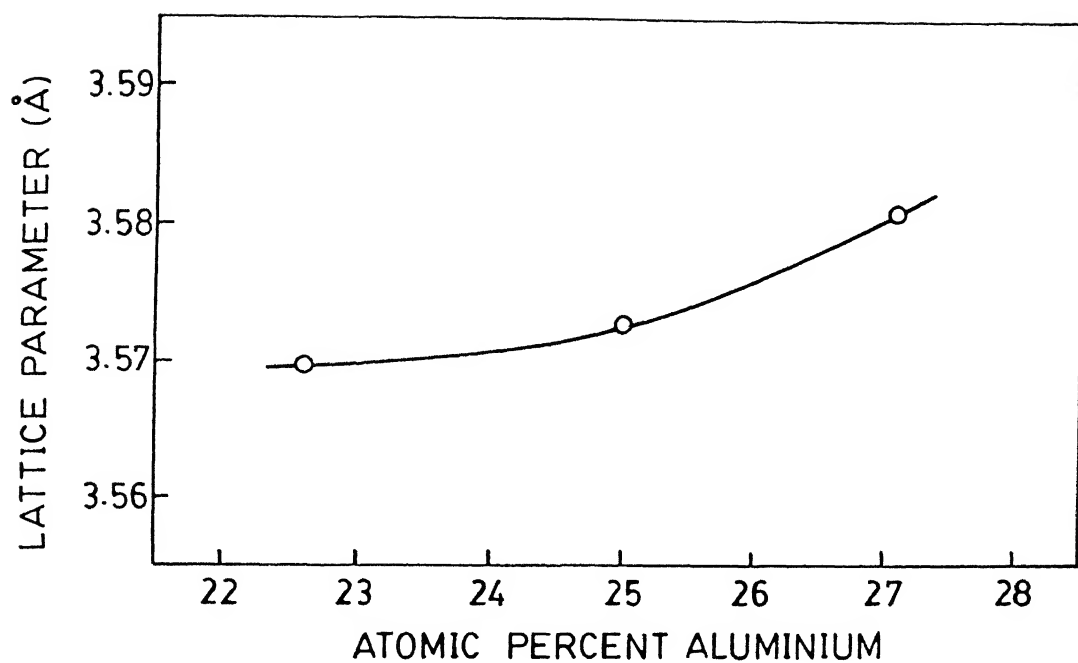


Fig. 5.2: Variation of lattice parameter of binary boron-free  $\text{Ni}_{75}\text{Al}_{25}$  as a function of aluminium content.

Table 5.3

Lattice parameter of boron-free  $\gamma'$  alloys at 25°C quenched from 1130°C

Alloy number from Table 3.1	Composition of $\gamma'$ phase (at.%)			Lattice parameter (Å)	
	Ni	Al	Hf	Measured	Calculated after Equation 5.9 <sup>*</sup>
1	75.0	25.0	-	3.5726	3.5726
2	77.4	22.6	-	3.5697	3.5681
3	72.9	27.1	-	3.5808	3.5826
4	75.7	21.5	2.8	3.5789	3.5776
5	75.5	19.5	5.0	3.5865	3.5872
6	74.8	17.8	7.4	3.6008	3.5996
7	77.8	20.1	2.1	3.5802	3.5767
8	76.4	18.5	5.1	3.5901	3.5896
9	78.0	18.8	3.2	3.5775	3.5832
10	76.3	18.2	5.5	3.5940	3.5919
11	72.3	25.1	2.6	3.5916	3.5852
12	72.8	22.5	4.7	3.5807	3.5867

\* Please see Section 5.2.2.

#### 5.1.4. Effect of boron

(a). Hafnium free  $\gamma'$  : The homogenized samples of boron-doped stoichiometric  $\gamma'$  were equilibrated at 1200°C, 1130°C, 1000°C and 800°C just like the corresponding boron-free stoichiometric compound. The lattice parameters were measured at room temperature with samples quenched from different equilibration temperatures. The equilibration time was upto 5 days at 1200°C, 7 days at 1130°C, 10 days at 1000°C and 20 days at 800°C. The measured lattice parameters are listed in Table 5.4. Figure 5.3 illustrates the temperature dependence of the lattice parameter of boron-doped  $\text{Ni}_3\text{Al}$ . The unusual temperature dependence of the lattice parameter is similar to that of the corresponding boron-free alloys (Figure 5.1). In order to highlight the similarity, the temperature dependence of boron-free  $\text{Ni}_3\text{Al}$  is shown in Figure 5.3 as a dashed line.

The available literature values of lattice parameters of different alloys and their heat treatments are listed in Table 5.5 and the data from the literature in graphical form are reported in Figures 2.13 to 2.16 (Chapter-II). The literature values suggest a wide variation of lattice parameter with heat treatment. Figure 2.16 [60] shows that the lattice parameters of furnace and air cooled samples can vary by as much as 0.0025 Å. It is, thus, not possible to compare the values of lattice parameters of  $\gamma'$  available in the literature with those of present results as the heat treatments given are not the same in the two cases.

Boron-doped aluminium rich  $\gamma'$  alloy  $\text{Ni}_{73.2}\text{Al}_{26.8}$  is a single phase alloy. The lattice parameter of the alloy homogenized at 1130°C for 20 days was measured and it is listed in Table 5.4.

Boron-doped nickel-rich alloy of nominal composition  $\text{Ni}_{77}\text{Al}_{23}$  contains two phases, namely, the parent phase  $\gamma'$  ( $\text{Ni}_{76.9}\text{Al}_{23.1}$ ) and nickel-rich terminal solid solution  $\gamma$  ( $\text{Ni}_{83.9}\text{Al}_{16.1}$ ). The lattice parameter of the  $\gamma'$  phase in the alloy homogenized at 1130°C for 20 days

Table 5.4

Lattice parameter of boron-doped  $\text{Ni}_3\text{Al}$  homogenized at  $1100^\circ\text{C}$  for 5 days  
as a function of equilibration temperature

Alloy (at.%)		Lattice parameter (Å) at $25^\circ\text{C}$ of specimens quenched from equilibration temperature ( $^\circ\text{C}$ )			
Ni	Al	800	1000	1130	1200
76.9	23.1			3.5731	
<sup>x</sup> 75.0	25.0	3.5711	3.5757		3.5731
<sup>+</sup> 75.0	25.0	3.5738	3.5770	3.5756	3.5745
73.2	26.8			3.5798	

- × Alloy prepared by melting elemental nickel, aluminium and boron and is designated as Alloy 'A' (See Table 3.1);
- + Boron-doped stoichiometric  $\text{Ni}_3\text{Al}$  supplied by Defence Metallurgical Research Laboratory (DMRL), Hyderabad, India and is designated as Alloy 'B' (See Table 3.1).

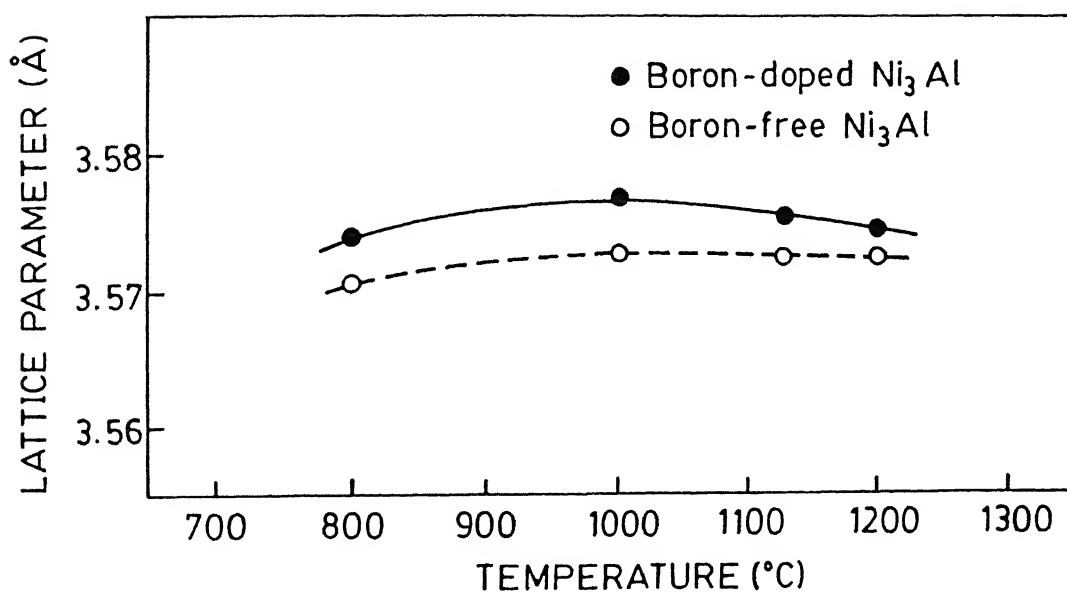


Fig. 5.3: Variation of lattice parameter of binary boron-doped Ni<sub>3</sub>Al (Alloy B) as a function equilibration temperature; Dashed line shows the temperature dependence of lattice parameter of boron-free Ni<sub>3</sub>Al (from Figure 5.1).

Table 5.5  
Heat treatment and lattice parameter of boron-doped  $\gamma'$  available  
in the literature

Atom percent aluminium	Amount of boron	Heat treatment	Lattice parameter (Å)	Reference
24.6	0.1 wt.%	Slow cooled from 1000°C	3.5791	Ramesh et al. [54]
23.6	0.1 wt.%	Slow cooled from 1000°C	3.5710	"
25	0.1 wt.%	800°C/3h/AC	3.5670	Young et al. [56]
25	0.1 wt.%	900°C/5h/AC	3.5630	"
25	0.1 wt.%	1100°C/5h/AC	3.5570	"
25	0.05 wt.%	1100°C/5h/AC	3.5530	"
25	0.1 wt.%	Rapidly solidified	3.5610	"
25	0.1 at.%	Furnace cooled from 900°C	3.5714	Baker et al. [60]

was measured and it is listed in Table 5.4.

The dependence of lattice parameter of  $\gamma'$ , quenched from 1130°C, on composition is shown in Figure 5.4 as a function of aluminium content of the alloy. As the aluminium content of the alloy is increased, aluminium replaces nickel in the lattice. The atomic size of aluminium is 14% greater than that of nickel. Therefore, the lattice parameter increases with aluminium content of the alloy. This behaviour is similar to that in the corresponding boron-free alloy (Figure 5.2). The composition dependence of the lattice parameter of boron-free  $\gamma'$  is shown as a dashed line in Figure 5.4 for comparison.

(b). Hafnium containing  $\gamma'$  : The boron-doped alloys containing hafnium were homogenized at 1130°C for 20 days. The lattice parameters of the  $\gamma'$  phase in all the alloys containing hafnium were measured. These are listed in Table 5.6.

#### 5.1.5. The $\gamma$ phase coexisting with $\gamma'$

It was shown in the earlier chapter that a number of alloys contain phases other than  $\gamma'$  at equilibrium. Out of the different phases, the lattice parameters of the boron-free phase  $\gamma$  could only be accurately measured. These values are listed in Table 5.7.

### 5.2. STABILITY

#### 5.2.1. Effect of temperature

Figure 5.3 shows the variation of lattice parameter with quenching temperature for boron-free and boron-doped (Alloy 'B', Table 3.1) stoichiometric  $\text{Ni}_3\text{Al}$ . In both the materials, the lattice parameter tends to increase with increase in the quenching temperature upto about 1000°C and then decreases slightly beyond 1000°C. This behaviour is more prominent in boron-doped alloys than in boron-free alloys.

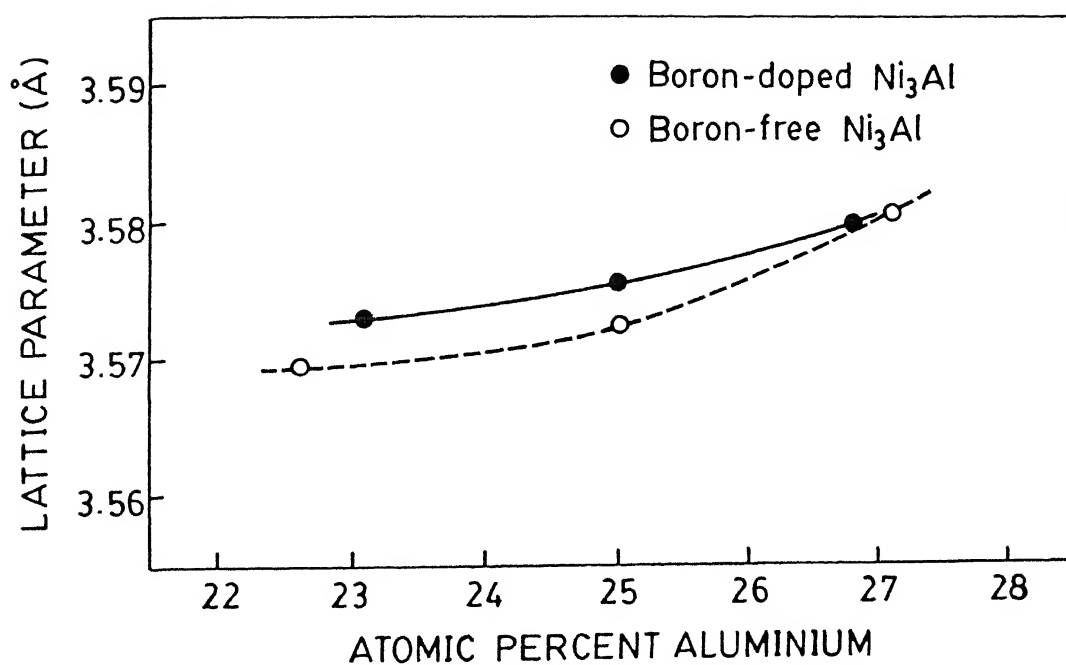


Fig. 5.4: Variation of lattice parameter of binary boron-doped Ni<sub>3</sub>Al (Alloy B) as function of aluminium content; Dashed line shows variation of lattice parameter of boron-free Ni<sub>3</sub>Al as function of aluminium content (from Figure 5.2).



Table 5.6

Lattice parameter of boron-doped  $\gamma'$  alloys at 25°C quenched from 1130°C

Alloy number from Table 3.1	Composition of $\gamma'$ phase (at.%)			Lattice parameter (Å)	
	Ni	Al	Hf	Measured	Calculated after Equation 5.13 <sup>*</sup>
14	75.0	25.0	-	3.5756	3.5756
15	76.9	23.1	-	3.5731	3.5739
16	73.2	26.8	-	3.5796	3.5818
17	75.3	22.3	2.4	3.5816	3.5803
18	75.2	19.7	5.1	3.5888	3.5921
19	75.3	17.7	7.0	3.6077	3.6045
20	77.1	20.1	2.8	3.5872	3.5841
21	77.7	17.6	4.7	3.5949	3.5974
22	72.5	25.2	2.3	3.5858	3.5860
23	72.3	23.1	4.6	3.5887	3.5918
24	71.8	25.3	2.9	3.5936	3.5898
25	72.5	21.3	6.2	3.5973	3.5976

<sup>\*</sup> Please see Section 5.2.2.

Table 5.7  
Lattice parameter of boron-free  $\gamma$  phase

Alloy number from Table 3.1	Composition of $\gamma$ phase (at.%)			Lattice parameter (Å)
	Ni	Al	Hf	
7	83.6	16.0	0.4	3.5764
8	84.5	14.9	0.6	3.5692
9	83.8	15.6	0.6	3.5554
10	83.8	15.2	1.0	3.5484

The change in lattice parameter with quenching temperature is consistent with the large number of observations in the literature that the lattice parameter changes appreciably with heat treatment (Table 5.2). This aspect is discussed in the earlier section. However, the unusual dependence of lattice parameter on quenching temperature as mentioned above has not been reported earlier. As discussed below, on the basis of the structural evidence obtained on  $\text{Ni}_3\text{Al}$  at various temperatures, one might expect such a behaviour.

Hoshino et al. [113] have reported the variation of the diffusion coefficient of nickel in  $\text{Ni}_3\text{Al}$  as a function of temperature. Their data reveal that above the temperature of  $1000^\circ\text{C}$ , the values of the activation energy,  $Q^*$  and the pre-exponential factor,  $D_0$  are 346.9 kJ/mole and  $146 \text{ cm}^2/\text{sec}$  respectively. On the other hand, these have values of 141 kJ/mole and  $1.1 \times 10^{-7} \text{ cm}^2/\text{sec}$  respectively below  $1000^\circ\text{C}$ . The activation energy at low temperature is less than half of that at high temperature. Also, the  $D_0$  values at low temperature is many orders of magnitude less than that at high temperature. These results imply a change of defect structure responsible for diffusion at high and low temperatures. From Figure 2.19 [113], it is clear that the low temperature process dominates below about  $1000^\circ\text{C}$  and the high temperature process occurs above about  $1000^\circ\text{C}$ . Thus, the unusual temperature dependence of lattice parameter of  $\text{Ni}_3\text{Al}$  may be expected to be related to the changes in the defect structure of  $\text{Ni}_3\text{Al}$  as a function of temperature. The possible nature of the defects is considered separately in the following paragraphs.

**High temperature region** : Removal of aluminium atoms from  $\text{Ni}_3\text{Al}$  lattice leaves a body centered tetragonal (bct) unit cell with the same interatomic distance as shown in Figure 5.5. In other words, nickel atoms are always in contact with other nickel atoms. At high temperatures, diffusion occurs by the process of vacancy creation and migration [50,51]

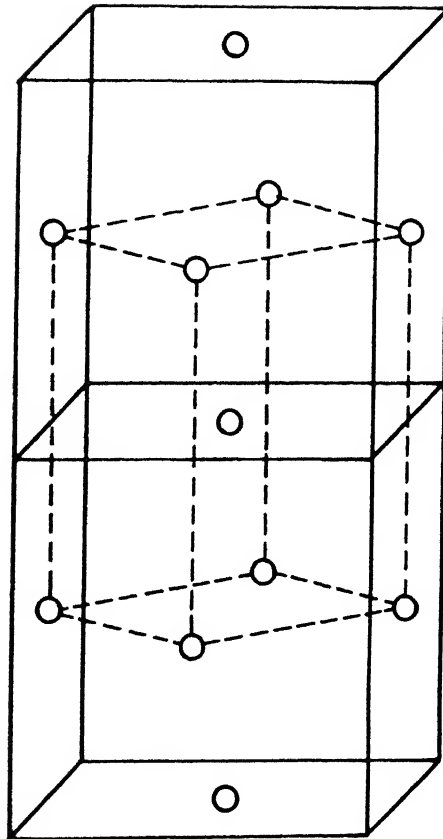


Fig. 5.5: Outline of body-centered tetragonal cell shown (dotted lines) inside the  $\text{Ni}_3\text{Al}$  lattice using face-centered nickel atoms.

in nickel sublattice. Thus, thermal vacancies are primarily responsible for diffusion. The increase in temperature increases the thermal vacancy concentration [268] and thereby slightly reducing the lattice parameter which is experimentally observed. In the presence of boron, because of high binding energy between boron and vacancy [113], more vacancies are retained on quenching. Therefore, the decrease in lattice parameter with increase in temperature above  $1000^{\circ}\text{C}$  is more appreciable.

Low temperature region : At temperatures below  $1000^{\circ}\text{C}$ , the activation energy is only half of the sum of the energies for vacancy formation and vacancy migration [268]. A few kilojoule difference between the activation energies for diffusion in stoichiometric and off-stoichiometric alloys may be attributed to the increase in activation energy for migration [269] due to change in the degree of order in off-stoichiometric composition [13]. However, 50% reduction in activation energy can not be accounted for in this manner. Also,  $D_0$  is extremely low at these temperatures.

Low activation energy and low  $D_0$  values could arise due to diffusion along short circuiting paths such as through grain boundaries, dislocations etc. However, experimental evidences rule out the possibility of diffusion along the short circuiting paths [113]. The other possibility is the existence of the temperature independent vacancy concentration. Such vacancy concentrations could arise either due to constitutional vacancies or due to vacancies introduced by impurities. Gupta et al. [114] have shown the existence of temperature independent vacancy concentrations in stoichiometric and off-stoichiometric alloys. However, the vacancy concentration which is independent of composition can not explain the decrease in lattice parameter with decrease in quenching temperature.

It has been recently reported that there is complete order in  $\text{Ni}_3\text{Al}$  upto about  $600^{\circ}\text{C}$ . Above this temperature, the degree of order decreases [54]. It is well known that decrease in degree of order tends to increase

the lattice parameter as in the case of  $\text{Cu}_3\text{Au}$  [270]. Since, the degree of order in  $\text{Ni}_3\text{Al}$  is lower at higher temperature, the lattice parameter of  $\text{Ni}_3\text{Al}$  is expected to increase with increase in quenching temperature and this is exactly the behaviour observed below  $1000^\circ\text{C}$  (Figure 5.3).

Thus, it may be concluded that the unusual dependence of lattice parameter of  $\text{Ni}_3\text{Al}$  on quenching temperature is due to the decrease in the degree of order with increase in equilibration temperature below  $1000^\circ\text{C}$  where the degree of order is expected to change rapidly with decrease in temperature and thermal vacancy effect would be small. The slight decrease in the lattice parameter observed above about  $1000^\circ\text{C}$  may be attributed to increase in the concentration of thermal vacancies as the effect of thermal vacancy at high temperature is quite appreciable and that of change in the degree of order would be negligible. In the presence of boron, the quenched-in thermal vacancy effects are slightly magnified because of higher concentration of quenched-in vacancies due to higher boron-vacancy binding energy [113]. The influences of thermal vacancies and degree of order are schematically illustrated in Figure 5.6.

### 5.2.2. Effect of composition

The  $\gamma'$  phase, investigated in this study, has three components, namely, nickel, aluminium and hafnium. Therefore, the system at constant temperature and pressure can be specified by two composition variables. We consider nickel content and aluminium content as variables. Once these two are fixed, hafnium content would be automatically fixed. It is convenient to express the composition of an alloy by the deviations from the stoichiometric composition of  $\gamma'$ . Hence, the nickel content  $X'_1$ , aluminium content  $X'_2$  and hafnium content  $X'_3$  can be expressed as

$$X'_1 = X_1 - 0.75 \quad (5.1)$$

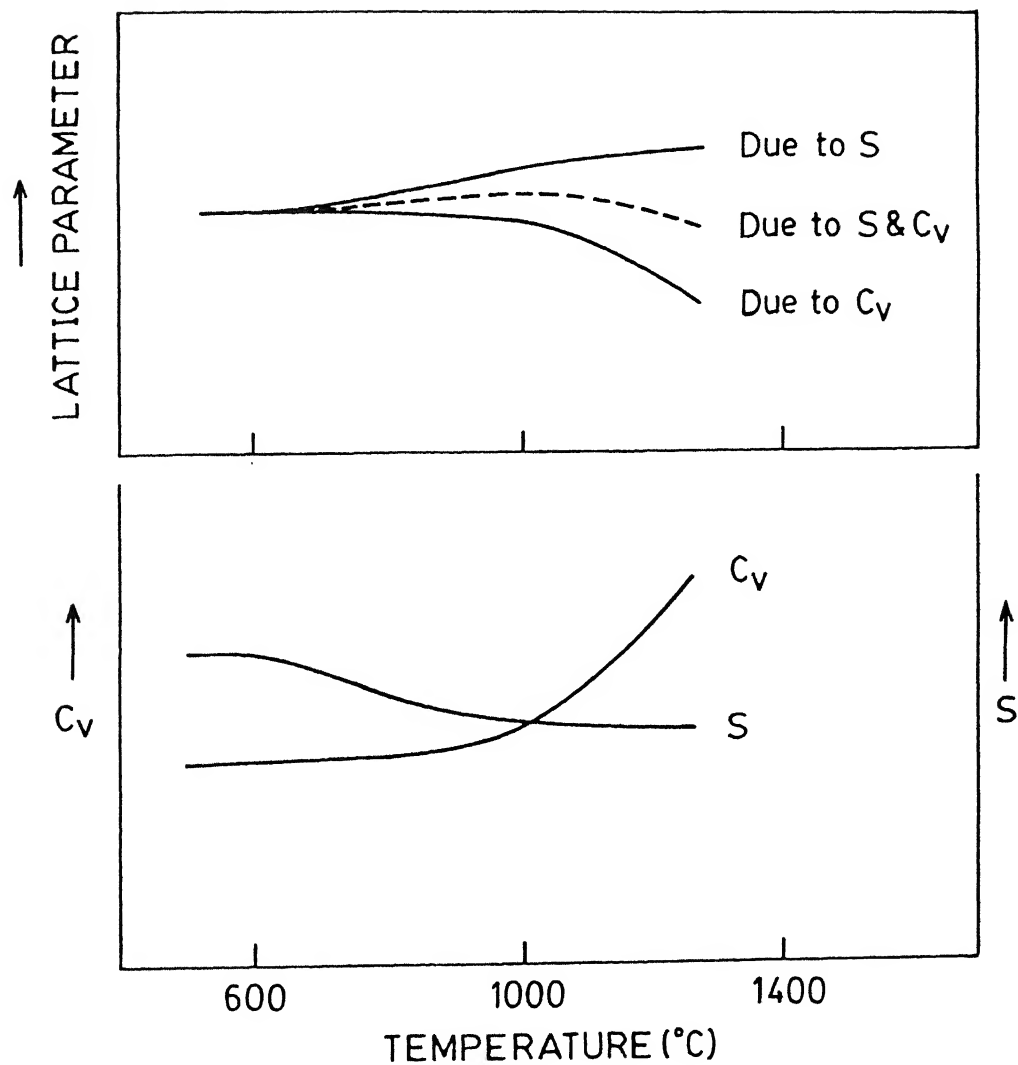


Fig. 5.6: Schematic plot of the effect of temperature on the vacancy concentration ( $C_v$ ), the degree of order ( $S$ ) and the lattice parameter.

$$X_2' = X_2 - 0.25 \quad (5.2)$$

$$X_3' = X_3 \quad (5.3)$$

where  $X_1$ ,  $X_2$  and  $X_3$  are the atom fractions of nickel aluminium and hafnium respectively in the alloy considered. Hence,

$$X_1 + X_2 + X_3 = 1 \quad (5.4)$$

$$X_1' + X_2' + X_3' = 0 \quad (5.5)$$

The lattice parameter 'a' of the  $\gamma'$  phase may be expressed as the following since the lattice parameter tends to increase monotonically with increase in aluminium content (Figure 5.2)

$$a = f(X_1', X_2') \quad (5.6)$$

Writing this function as polynomial and truncating the polynomial after second order terms, we get,

$$a = a_o + a_1 X_1' + a_2 X_2' + a_{11} (X_1')^2 + a_{22} (X_2')^2 + a_{12} X_1' X_2' \quad (5.7)$$

It may be noted from the equation, written in this form, that when  $X_1'$  and  $X_2'$  are zero, the composition corresponds to stoichiometric  $\gamma'$  phase and the lattice parameter 'a' equals 'a<sub>o</sub>' which is the lattice parameter of stoichiometric  $\text{Ni}_3\text{Al}$ . It has been measured accurately in this investigation as 3.5726 Å.

The values of  $X_1$ ,  $X_2$  and the lattice parameter values measured on a number of  $\gamma'$  alloys are listed in Table 5.3. Using the data from the table



and Equations 5.1 and 5.2,  $X_1'$  and  $X_2'$  are calculated for each alloy. Using the values of  $X_1'$ ,  $X_2'$  and the experimentally determined values of 'a' from Table 5.3 and  $a_0 = 3.5726 \text{ \AA}$ , the best fit obtained using Minitab, Data analysis software, Release 1.1, Student edition, Minitab Inc. 1988, was

$$a = 3.5726 - 0.427X_1' - 0.085X_2' + 1.54(X_1')^2 + 3.89(X_2')^2 - 0.98X_1'X_2' \quad (5.8)$$

where 'a', the lattice parameter of the alloy, is in  $\text{\AA}$ . Using Equations 5.1 and 5.2, Equation 5.8 can be written as

$$a = 4.839725 - 2.492X_1 - 1.295X_2 + 1.54(X_1)^2 + 3.89(X_2)^2 - 0.98X_1X_2 \quad (5.9)$$

Using Equation 5.9, the lattice parameter of all the  $\gamma'$  alloys were calculated and are listed in Table 5.3. A plot of calculated lattice parameter versus experimental lattice parameter is shown in Figure 5.7. Ideally, for zero scatter, all the points should lie on a straight line drawn at  $45^\circ$  to the X-axis. The figure shows the points are scattered uniformly on both sides of such a line. The standard deviation calculated using the experimental lattice parameters and the calculated lattice parameters was  $0.0023 \text{ \AA}$ . The lattice parameter of  $\text{Ni}_3\text{Al}$  containing hafnium available in the literature [58] can not be compared with the present results as the heat treatments in the two cases are different.

Using the lattice parameters, we can calculate the variation of partial volumes of the three components nickel, aluminium and hafnium for various compositions. In the  $\text{Ni}_3\text{Al}$  structure, nickel and aluminium substitute for each other in the off-stoichiometric compositions. Therefore, the number of atoms per unit cell is four and the specific

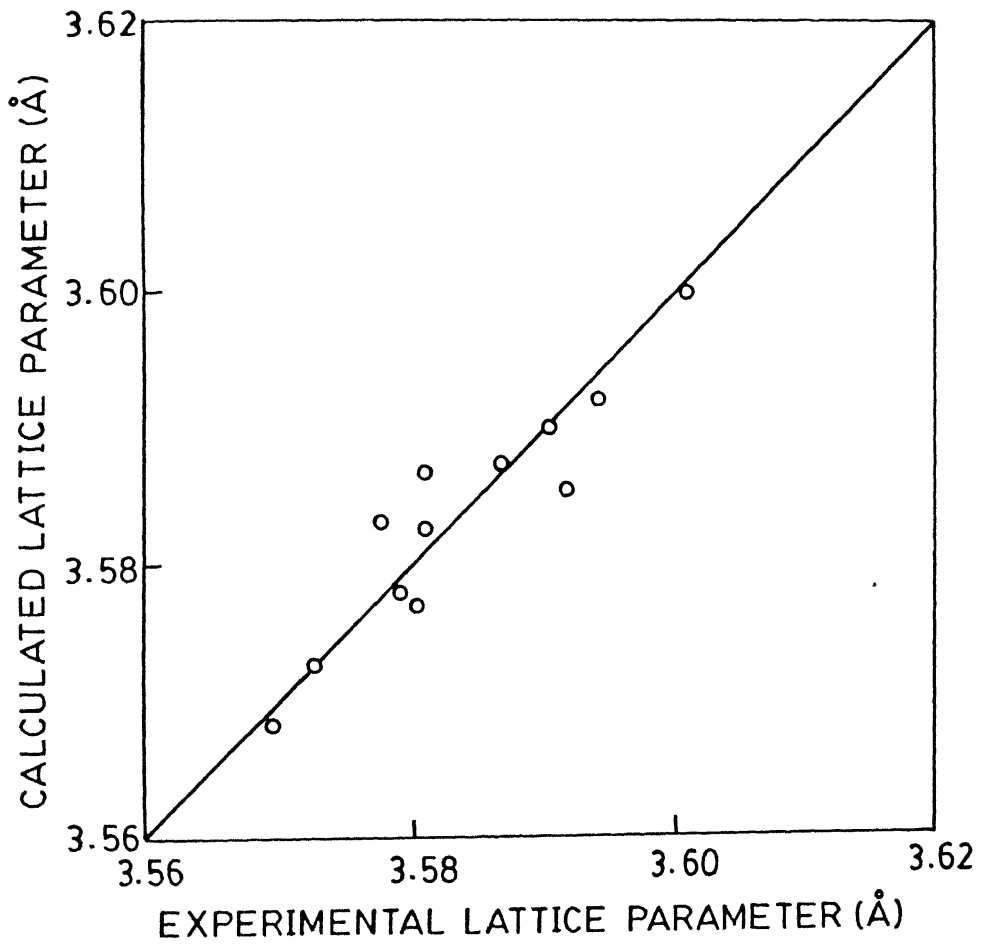


Fig. 5.7: Plot of experimental lattice parameter versus calculated lattice parameter for boron-free  $\gamma'$  alloys.

volume 'V' in  $\text{cm}^3$  per g-atom of the alloy is given by

$$V = 0.1506a^3 \text{ cm}^3/\text{g-atom} \quad (5.10)$$

where 'a' is in Å.

The partial volume,  $\bar{V}_i$ , of the element 'i' in the ternary system consisting of i, j and k having atom fractions X, Y and Z respectively, is given by

$$\bar{V}_i = V + (1-X)(dV/dX)_{Z/Y} \quad (5.11)$$

Equations 5.9, 5.10 and 5.11 are used to calculate the partial volumes. The computer programme used for this is given in Appendix I. The partial volumes obtained in this manner for a number of selected alloys are listed in Table 5.8. In order to find the composition dependence of the partial volumes, the data have been plotted in Figures 5.8, 5.9 and 5.10.

In Figure 5.8, the specific volume of  $\gamma'$  phase has also been indicated against atom percent aluminium. It shows continuous increase with increase in aluminium content. This is consistent with the fact that the molar volume of aluminium,  $V_{\text{Al}}^\circ$ , is much larger than the specific volume of nickel,  $V_{\text{Ni}}^\circ$ .

The smooth monotonic increase in specific volume of  $\gamma'$  with increase in aluminium content without any anomaly at stoichiometric composition of  $\text{Ni}_3\text{Al}$  is exactly same as that of  $\text{Cu}_3\text{Au}$  [118,271]. The specific volume of  $\text{Cu}_3\text{Au}$  also increases smoothly with increase in gold content without any anomalous behaviour at the stoichiometric  $\text{Cu}_3\text{Au}$  composition. The specific volume of Au,  $V_{\text{Au}}^\circ$  ( $10.22 \text{ cm}^3/\text{g-atom}$ ) is also much larger than that of Cu,  $V_{\text{Cu}}^\circ$  ( $7.11 \text{ cm}^3/\text{g-atom}$ ) just as  $V_{\text{Al}}^\circ$  ( $10 \text{ cm}^3/\text{g-atom}$ ) is larger than  $V_{\text{Ni}}^\circ$  ( $6.59 \text{ cm}^3/\text{g-atom}$ ). The partial molar volume of nickel,  $\bar{V}_{\text{Ni}}$  in nickel

Table 5.8

Calculated partial gram-atomic volumes of components in boron-free  $\gamma'$ 

Composition of $\gamma'$ (at.%)			$\bar{V}_{Ni}$	$\bar{V}_{Al}$	$\bar{V}_{Hf}$
Ni	Al	Hf	(cm <sup>3</sup> /g-atom)	(cm <sup>3</sup> /g-atom)	(cm <sup>3</sup> /g-atom)
73	27	0	6.0273	9.5050	8.9345
73	26	1	6.1585	9.1341	9.0115
73	25	2	6.2850	8.7599	9.0848
73	24	3	6.4071	8.3817	9.1547
73	23	4	6.5249	7.9990	9.2211
73	22	5	6.6385	7.6115	9.2843
75	25	0	6.4067	8.4057	8.8404
75	24	1	6.5270	8.0282	8.9089
75	23	2	6.6430	7.6461	8.9740
75	22	3	6.7549	7.2589	9.0357
75	21	4	6.8629	6.8659	9.0940
75	20	5	6.9669	6.4666	9.1490
77	23	0	6.7525	7.2898	8.7232
77	22	1	6.8629	6.9026	8.7834
77	21	2	6.9694	6.5094	8.8402
77	20	3	7.0721	6.1098	8.8936
77	19	4	7.1711	5.7030	8.9436
77	18	5	7.2665	5.2885	8.9902

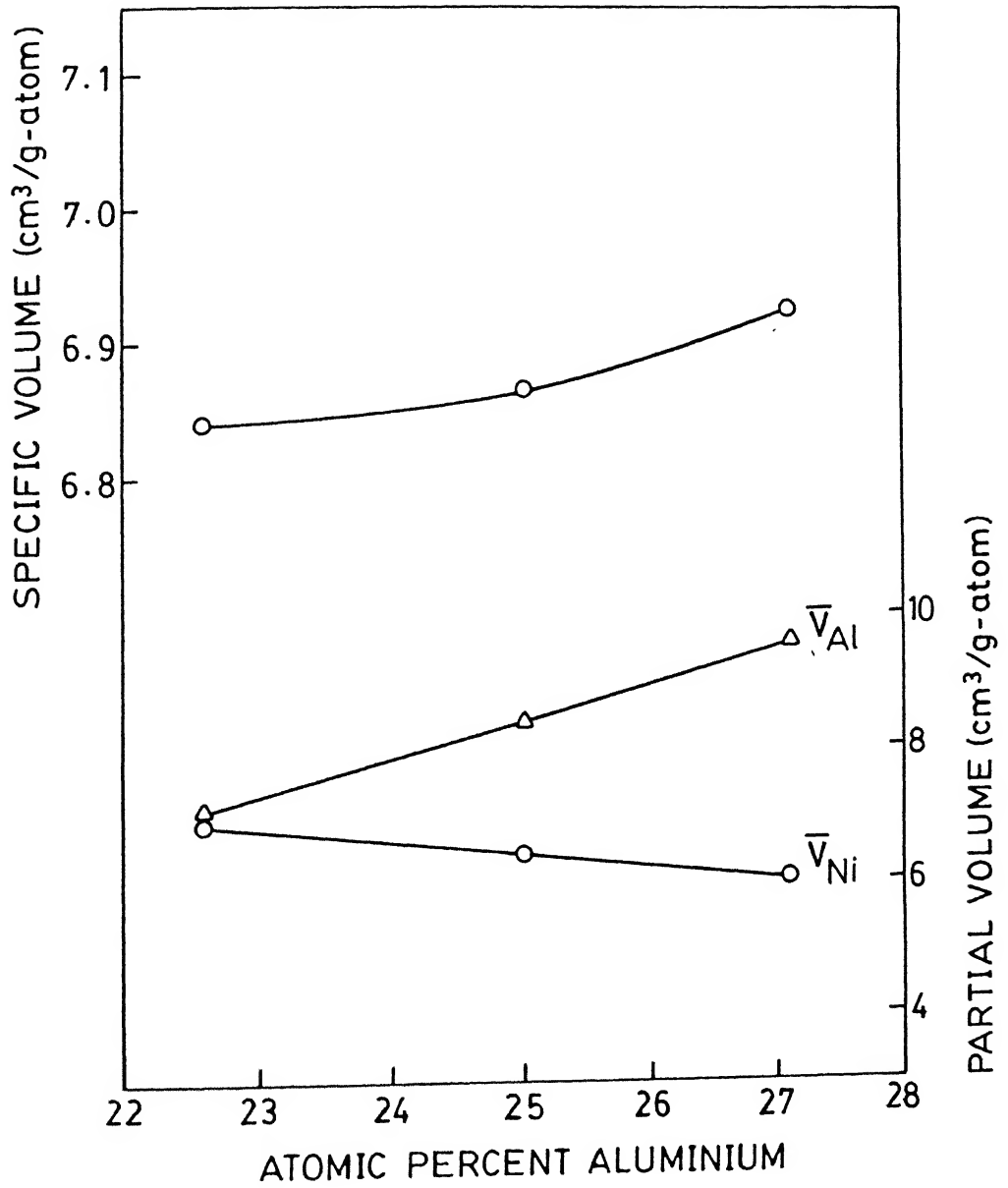


Fig. 5.8: Variation of specific and partial volumes as a function of atomic percent aluminium in boron-free binary Ni<sub>3</sub>Al alloys.

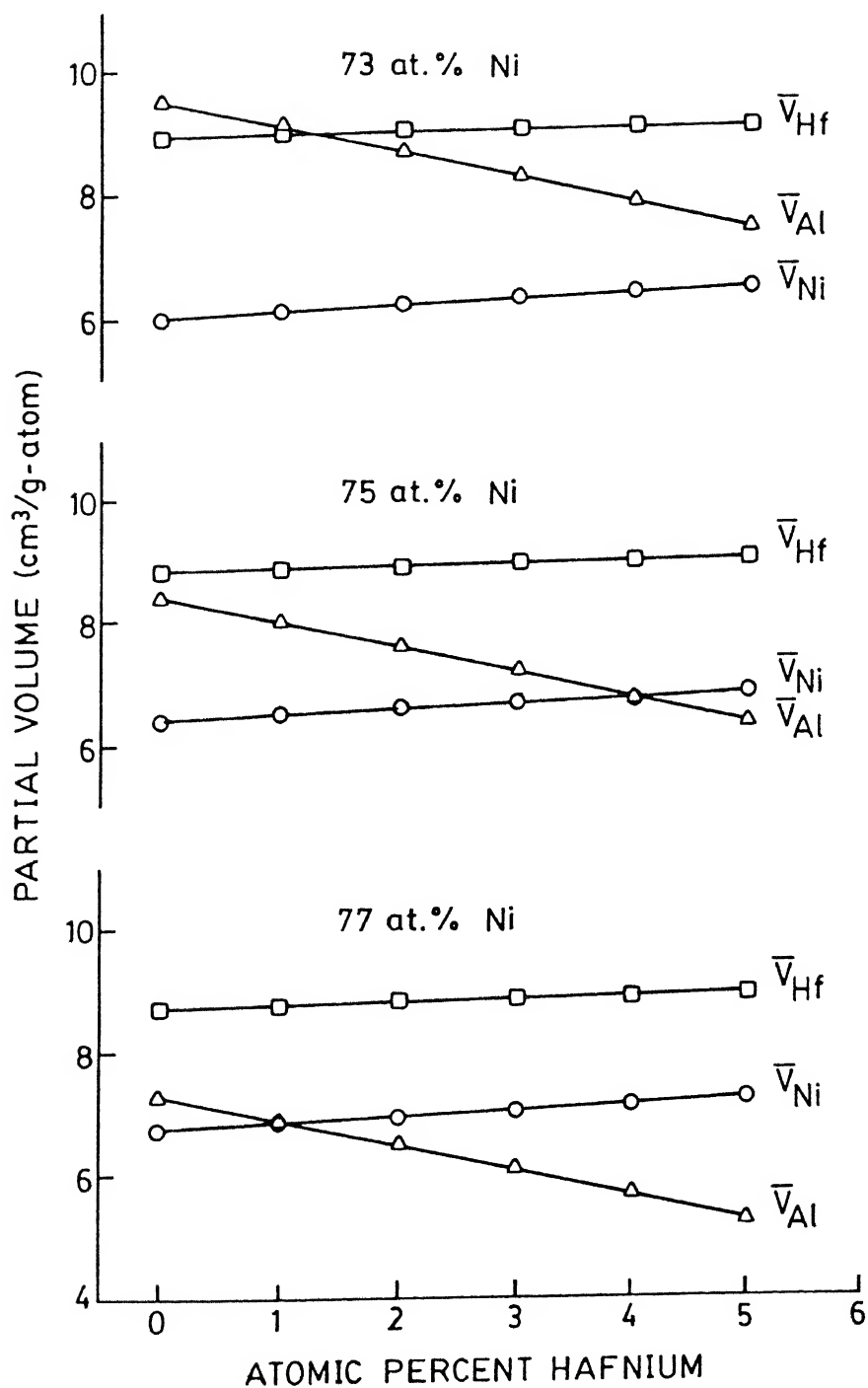


Fig. 5.9: Variation of partial volumes as a function of atomic percent hafnium in boron-free ternary Ni-Al-Hf alloys.

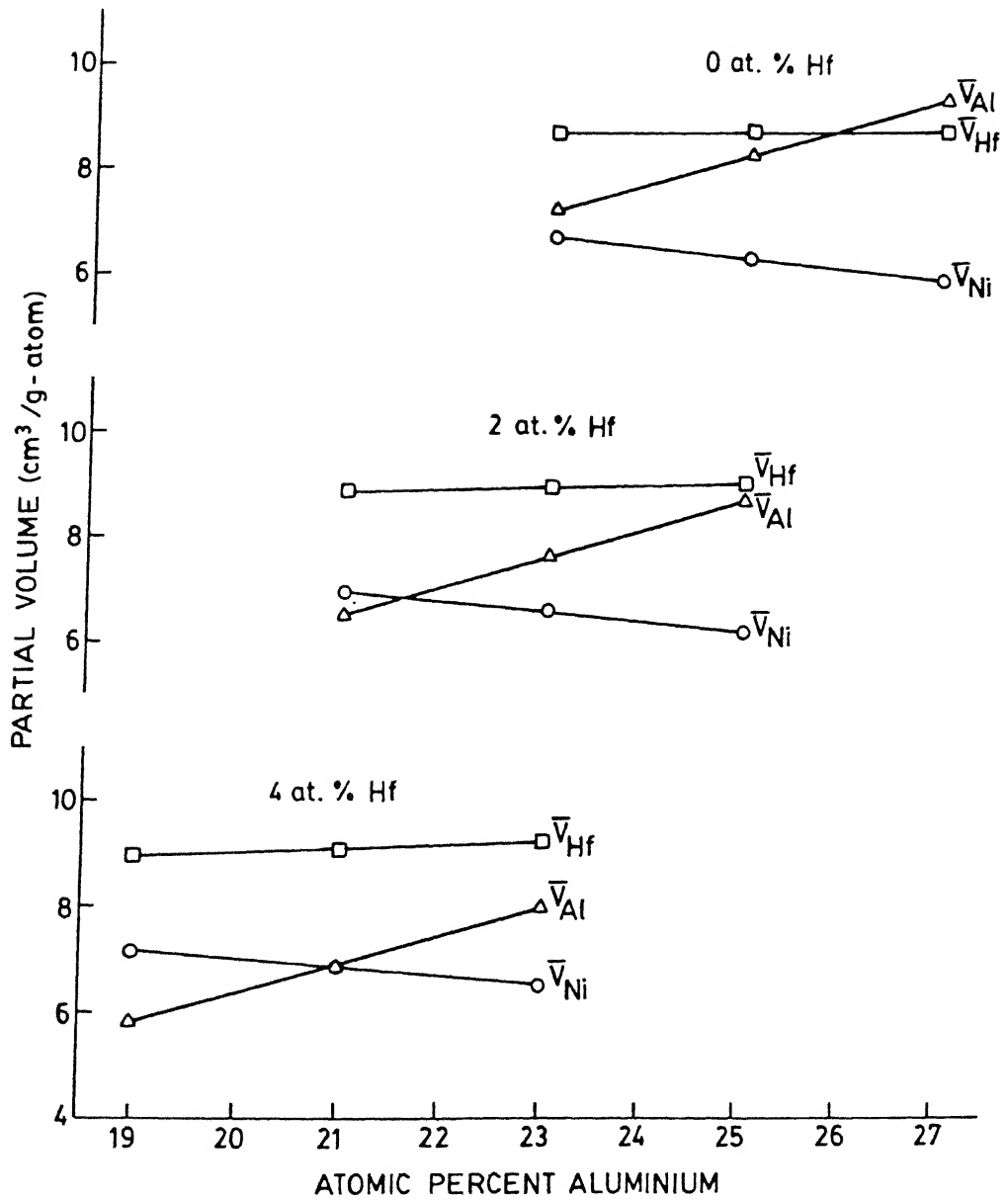


Fig. 5.10: Variation of partial volumes as a function of atomic percent aluminium in boron-free ternary Ni-Al-Hf alloys.

saturated  $\gamma'$ , is almost same as  $V_{Ni}^\circ$  and in aluminium saturated  $\gamma'$ ,  $\bar{V}_{Ni}$  decreases by about 9%. In contrast, although  $\bar{V}_{Al}$  in aluminium saturated  $Ni_3Al$  is almost same as that of  $V_{Al}^\circ$ ,  $\bar{V}_{Al}$  in nickel saturated  $\gamma'$  is reduced considerably (by about 30%).

Figure 5.9 shows the variation of the partial volumes of the three components, namely nickel, aluminium and hafnium as a function of hafnium content for constant atom percent of nickel. These results show that the  $\bar{V}_{Ni}$  is close to that of  $V_{Ni}^\circ$  and does not change with hafnium content appreciably. Although,  $\bar{V}_{Hf}$  is reduced by about 34% compared with the  $V_{Hf}^\circ$  ( $13.35 \text{ cm}^3/\text{g-atom}$ ), the magnitude is close to that of  $\bar{V}_{Al}$  in hafnium free alloys and  $\bar{V}_{Hf}$  also does not change appreciably with composition. However, in all the alloys,  $\bar{V}_{Al}$  decreases considerably by about 35% with increase in hafnium content. The magnitude of  $\bar{V}_{Al}$  is lower in nickel-rich alloys as was found in the binary  $\gamma'$ .

The partial volumes of the three components are plotted in Figure 5.10 as a function of aluminium content for constant atom percent of hafnium. The same trend, observed in Figure 5.9, are also noted here. Thus,  $\bar{V}_{Ni}$  is close to  $V_{Ni}^\circ$  and does not change much with change in composition.  $\bar{V}_{Hf}$ , at hafnium content equal to zero atom percent, undergoes a reduction of 35% and becomes equal to  $\bar{V}_{Al}$ . However,  $\bar{V}_{Hf}$  does not change appreciably with change in composition. On the other hand,  $\bar{V}_{Al}$  is reduced considerably from 5% to 47% during alloying. The above results suggest that the large variation of  $\bar{V}_{Al}$  is likely to be due to appreciable changes in its bonding characteristics.

### 5.2.3. Effect of boron

The lattice parameter 'a' of the  $\gamma'$  phase in boron-doped alloys can be expressed in the form of Equation 5.7 just as in the case of boron-free alloys. Here, the lattice parameter of the stoichiometric  $Ni_3Al$  containing



boron, quenched from 1130°C, was measured accurately and it was found to be 3.5756 Å. Hence, 'a<sub>0</sub>' of the equation equals 3.5756 Å. The values of X<sub>1</sub>, X<sub>2</sub> and the lattice parameter values measured on a number of γ' alloys containing boron are listed in Table 5.6. The mole fraction of boron is very small (of the order of 0.001 approximately). Therefore, the mole fraction of boron is ignored in the calculation. However, it is assumed that the boron content is same in all the alloys.

Using the data from Table 5.6. and Equations 5.1 and 5.2, X<sub>1</sub>' and X<sub>2</sub>' were calculated for each alloy. Using the values of X<sub>1</sub>', X<sub>2</sub>', the experimentally determined values of 'a' from Table 5.6 and a<sub>0</sub> (3.5756 Å), the best fit obtained using Minitab, Data analysis software, Release 1.1, Student edition, Minitab Inc. 1988, was

$$a = 3.5756 - 0.315X_1' - 0.095X_2' + 4.47(X_1')^2 + 4.38(X_2')^2 + 2.00X_1'X_2' \quad (5.12)$$

Using Equations 5.1 and 5.2, the above equation can be written as

$$a = 6.998725 - 7.52X_1 - 3.785X_2 + 4.47(X_1)^2 + 4.38(X_2)^2 + 2.00X_1X_2 \quad (5.13)$$

Using Equation 5.13 the lattice parameter of all the boron-doped γ' alloys were calculated and are listed in Table 5.6. A plot of calculated lattice parameter versus experimental lattice parameter is shown in Figure 5.11. Here also, the scatter was uniform on both sides of the line drawn at 45° to the X-axis. The standard deviation using the experimental and calculated lattice parameters was 0.0014 Å.

The specific volume 'V' in cm<sup>3</sup>/g-atom of the alloy and the partial volume,  $\bar{V}$ , of the components of the boron-doped ternary system can be

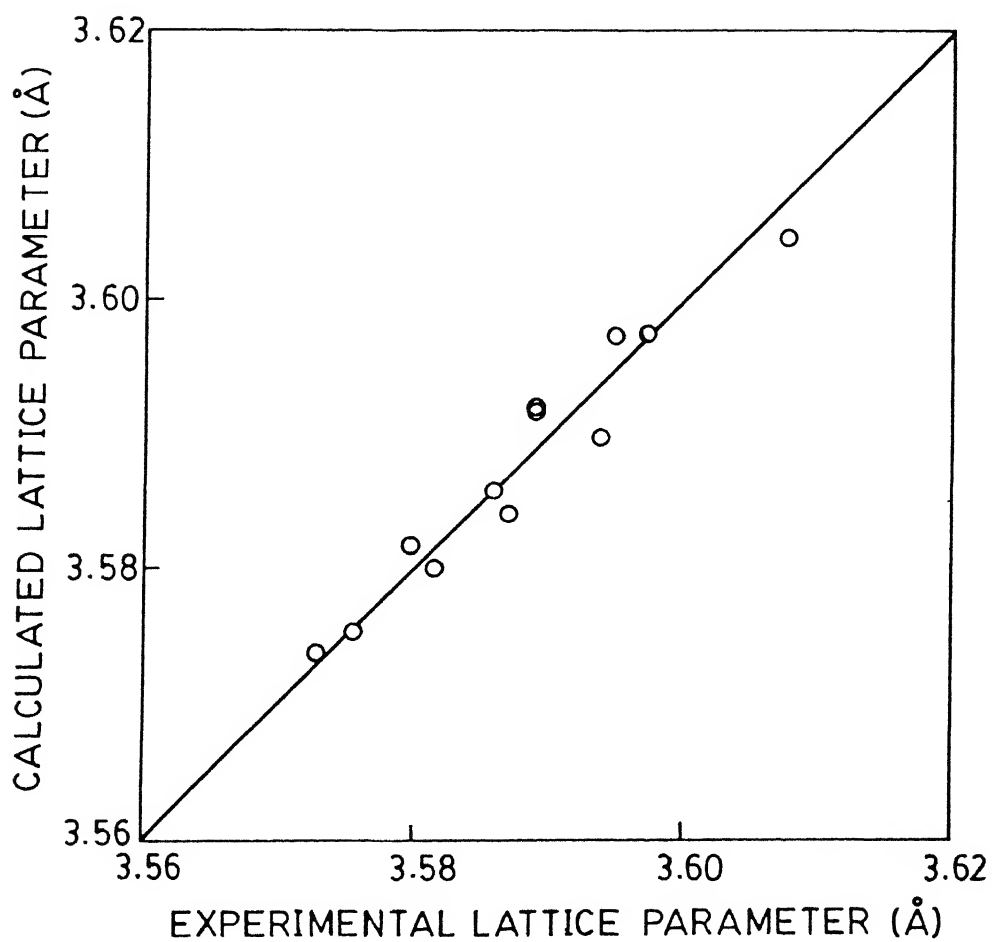


Fig. 5.11: Plot of experimental lattice parameter versus calculated lattice parameter for boron-doped  $\gamma'$  alloys.

calculated using Equations 5.10 and 5.11 just as in the case of boron-free alloys. The partial volumes obtained are listed in Table 5.9 for various compositions. In order to find the composition dependence of the partial volumes, the data have been plotted in Figures 5.12, 5.13 and 5.14.

The specific volume of boron-doped alloys is more than that of the boron-free alloys. The partial volume of nickel also tends to increase in the presence of boron. However, the partial volume of aluminium shows considerable reduction. In hafnium containing alloys, the partial volume of nickel always shows an increase in the presence of boron. However, partial volume of aluminium tends to decrease in the presence of boron. The partial volume of hafnium behaves in an unusual manner. It shows a decrease in the presence of boron when hafnium content is low and shows an increase when hafnium content is high. Thus, in the presence of boron,  $\bar{V}_{Ni}$  shows a slight increase and  $\bar{V}_{Al}$  shows slight decrease in all 75 at.% Ni, 77 at.% Ni and 73 at.% Ni containing alloys. However,  $\bar{V}_{Hf}$  shows a decrease at low hafnium content and considerable increase at high hafnium content. Such behaviour may be related to the specialized occupancy by solute atoms.

#### 5.2.4. Solute substitution and bonding characteristics

The  $L1_2$  structure of ordered  $Ni_3Al$  (Figure 2.7, Chapter-II) is generated when one of the sublattices is occupied by only aluminium atoms. Here, each aluminium atom in the aluminium sublattice will have only nickel atoms as the nearest neighbours. Each nickel atom in its sublattice will have four aluminium atoms and eight nickel atoms as nearest neighbours. Thus, the structure has only Al-Ni bonds and some Ni-Ni bonds and no Al-Al bond. Fifty percent of the bonds in the alloy are Al-Ni type and rest are Ni-Ni type. The solute substitution behaviour and the bonding characteristics of both stoichiometric and off-stoichiometric  $\gamma'$  with and

Table 5.9

Calculated partial gram-atomic volumes of components in boron-doped  $\gamma'$ 

Composition of $\gamma'$ (at.%)			$\bar{V}_{\text{Ni}}$	$\bar{V}_{\text{Al}}$	$\bar{V}_{\text{Hf}}$
Ni	Al	Hf	(cm <sup>3</sup> /g-atom)	(cm <sup>3</sup> /g-atom)	(cm <sup>3</sup> /g-atom)
73	27	0	6.1932	9.0756	8.8198
73	26	1	6.2936	8.7889	9.0380
73	25	2	6.3889	8.4979	9.2522
73	24	3	6.4792	8.2021	9.4629
73	23	4	6.5647	7.9012	9.6703
73	22	5	6.6453	7.5947	9.8745
75	25	0	6.5974	7.9051	8.4245
75	24	1	6.6897	7.6123	8.6354
75	23	2	6.7772	7.3142	8.8426
75	22	3	6.8600	7.0103	9.0462
75	21	4	6.9383	6.7002	9.2466
75	20	5	7.0121	6.3834	9.4440
77	23	0	6.9673	6.7121	8.0046
77	22	1	7.0523	6.4105	8.2082
77	21	2	7.1328	6.1026	8.4082
77	20	3	7.2089	5.7878	8.6047
77	19	4	7.2807	5.4656	8.7979
77	18	5	7.3482	5.1354	8.9882

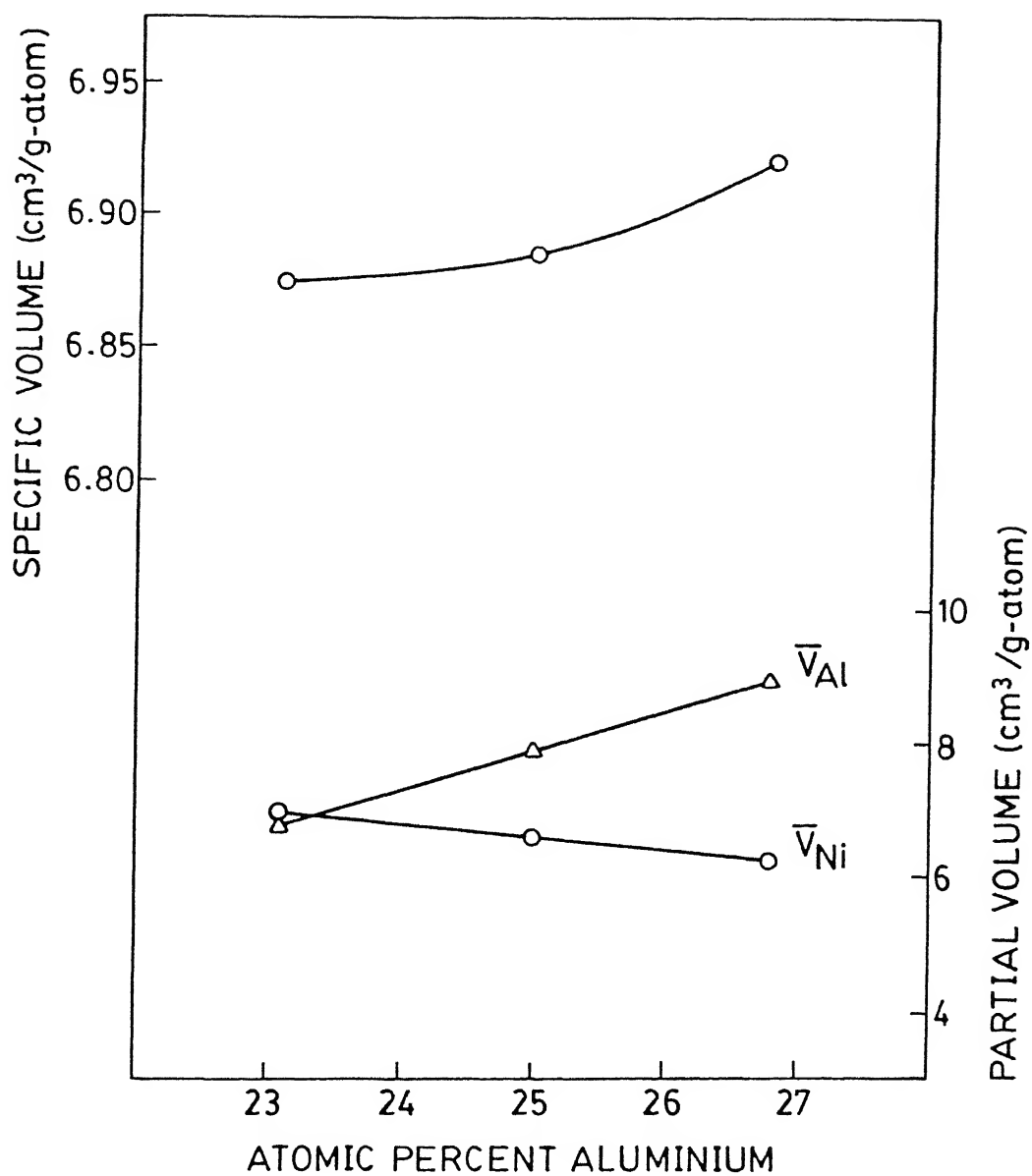


Fig. 5.12: Variation of specific and partial volumes as a function of atomic percent aluminium in boron-doped binary  $\text{Ni}_3\text{Al}$  alloys.

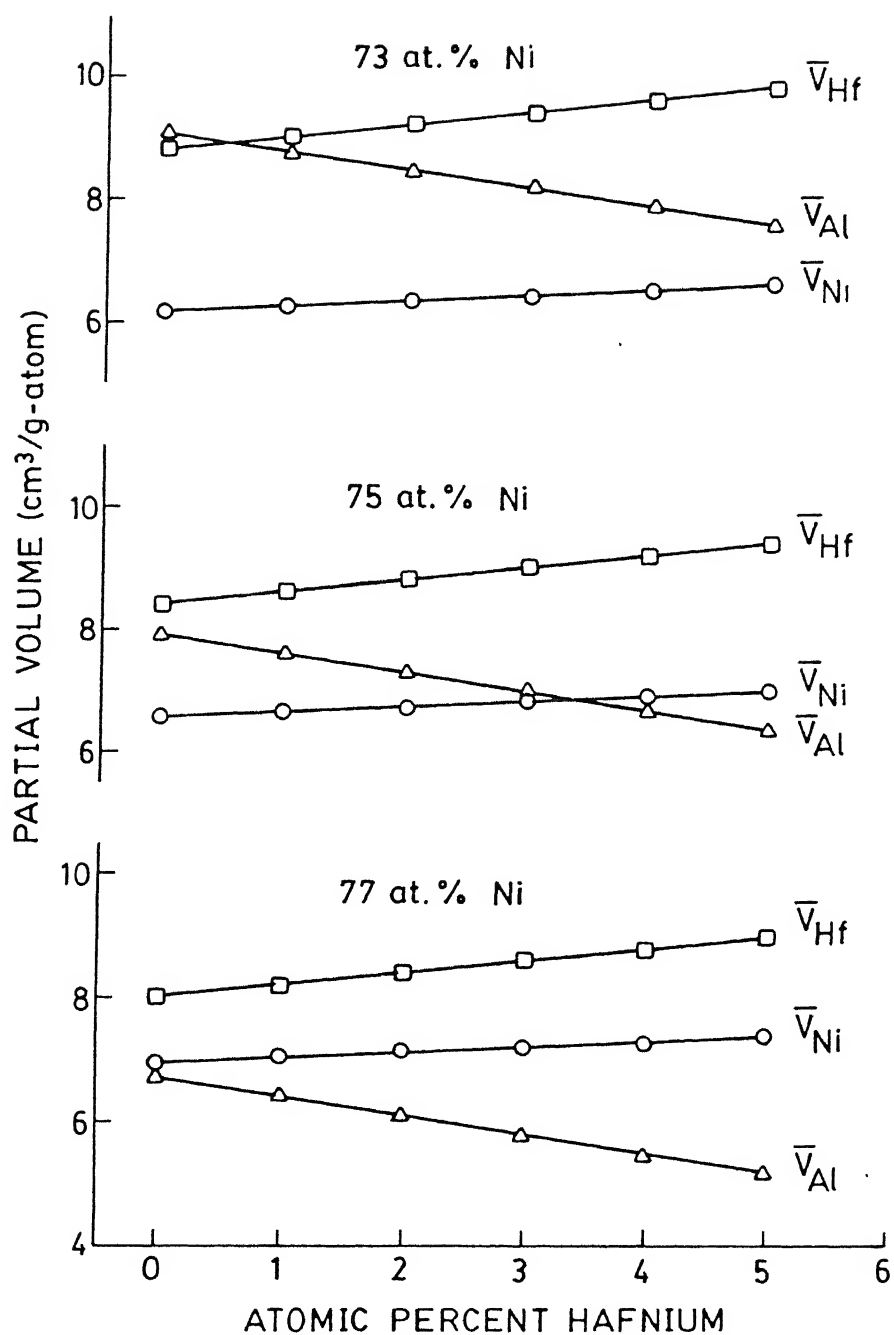


Fig. 5.13: Variation of partial volumes as a function of atomic percent hafnium in boron-doped ternary Ni-Al-Hf alloys.

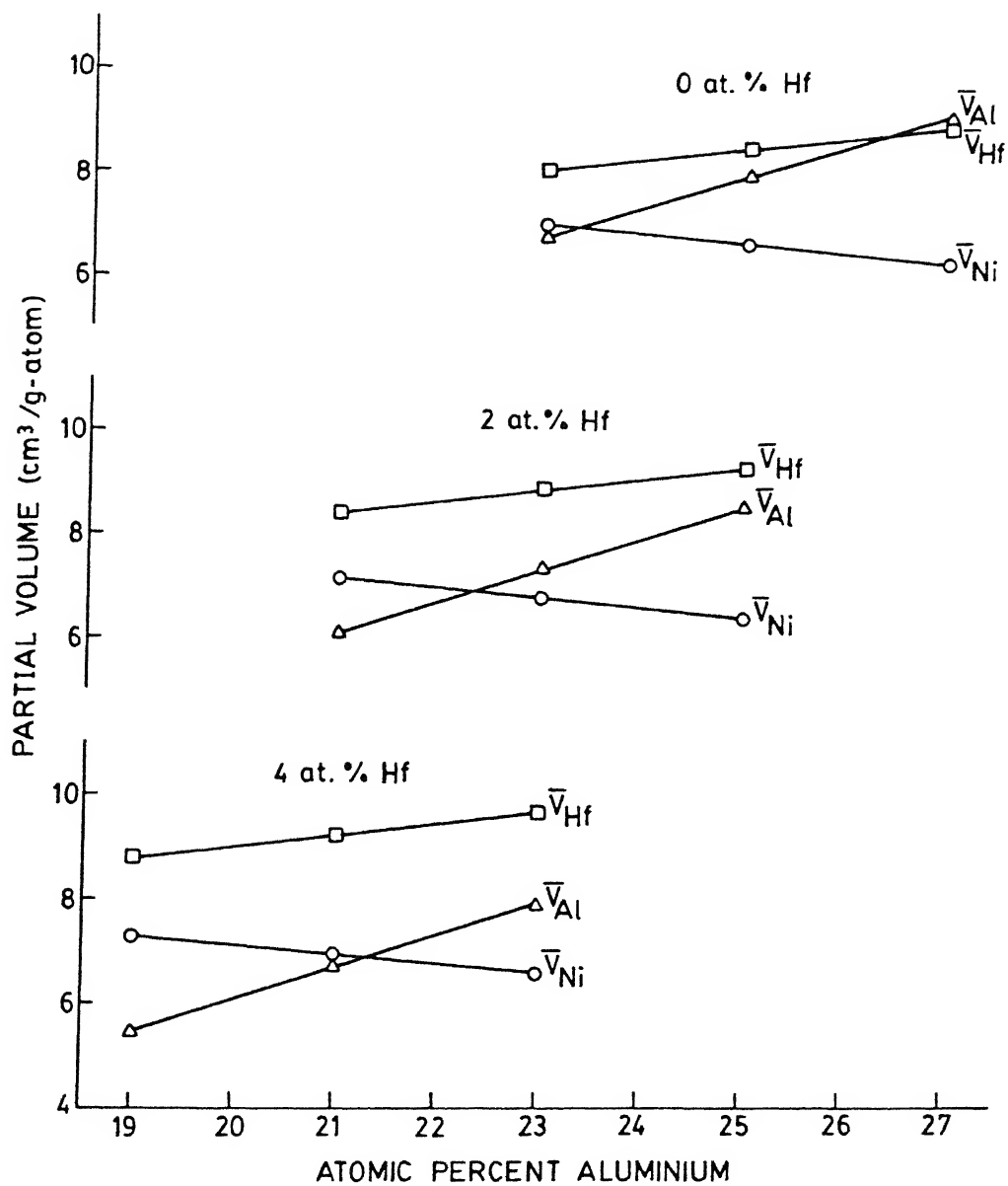


Fig. 5.14: Variation of partial volumes as a function of atomic percent aluminium in boron-doped ternary Ni-Al-Hf alloys.

without boron and/or hafnium are considered below.

(a).  $\gamma'$  containing 75 at.% Ni : The phase field of the  $\gamma'$  phase in this investigation (see Figure 4.14) shows that, with increase in hafnium content, the phase field extends along the constant 75 at.% Ni line. In Ni-Al-Hf alloys, nickel remains constant at 75 atom percent while aluminium decreases and hafnium increases so that aluminium and hafnium together remain at 25 atom percent. It suggests that hafnium has the tendency to replace part of aluminium in aluminium sublattice while nickel in nickel sublattice remains unchanged.

The partial volumes of the components of 75 at.% Ni containing  $\gamma'$  alloys is given in Figure 5.9 as a function of hafnium content. The partial volumes may be compared with the molar volumes of the pure components,  $V_{Ni}^{\circ}$  (6.59 cm<sup>3</sup>/g-atom),  $V_{Al}^{\circ}$  (10 cm<sup>3</sup>/g-atom) and  $V_{Hf}^{\circ}$  (13.35 cm<sup>3</sup>/g-atom). At hafnium content equal to zero,  $\bar{V}_{Ni}$  is reduced by only 3% while  $\bar{V}_{Al}$  and  $\bar{V}_{Hf}$  are reduced by 16% and 34% respectively, and  $\bar{V}_{Hf}$  is approximately equal to  $\bar{V}_{Al}$ . The similar partial volumes are consistent with the fact that aluminium and hafnium occupy lattice sites in the same sublattice. When the hafnium content is increased to five atom percent,  $\bar{V}_{Ni}$  expands by 8% and  $\bar{V}_{Hf}$  also expands by 2%. However,  $\bar{V}_{Al}$  is reduced by 35%. Thus, as the hafnium content is increased,  $\bar{V}_{Hf}$  and  $\bar{V}_{Ni}$  expand slightly while  $\bar{V}_{Al}$  is reduced considerably. Since, the atomic volume of hafnium is much larger than those of nickel and aluminium, general expansion of lattice due to the increase in hafnium is expected. This explains the observed increase in  $\bar{V}_{Hf}$  and  $\bar{V}_{Ni}$ . The considerable reduction in  $\bar{V}_{Al}$  is likely to be related to the bonding characteristics.

The available atomic and covalent radii for nickel, aluminium and hafnium [272] are listed in Table 5.10. It may be noted that the covalent radii cause 33% reduction in atomic volume of aluminium, 21% reduction in the atomic volume of hafnium and 21% reduction in the atomic volume of



Table 5.10  
Atomic and covalent radii and related properties of  
nickel, aluminium and hafnium

No.	Property	Ni	Al	Hf
1.	Atomic radii, Å	1.246 Å	1.430 Å	1.560 Å
2.	Covalent radii, Å	1.150 Å	1.250 Å	1.440 Å
3.	% reduction in volume due to covalent bonding	21	33	21
4.	% change in partial volume			
	(i) At atomic % Hf $\rightarrow$ 0	-3	-16	-34
	(ii) At atomic % Hf $\rightarrow$ 5	+5	-35	-32

nickel. The changes in the partial volumes of the components, nickel, aluminium and hafnium, in the 75 at.% Ni containing alloys are -3, -16 and -34% respectively, when hafnium content is zero. In contrast, the changes in the volumes are +5, -35 and -32% for nickel, aluminium and hafnium respectively, when the hafnium content is 5 at.% (Table 5.10). We note that the changes in the partial volumes of nickel and hafnium are very small while that of aluminium is appreciable (Figure 5.9). The partial volume of hafnium is about 34% less in all the alloys containing 0 to 5 at.% Hf while that of aluminium is reduced to about 35% when hafnium content is increased from 0 to 5 at.%. Thus, the partial volume of hafnium is reduced to a volume that may be characterized as due to covalent bonding and remains unchanged with change in hafnium content. On the other hand, the partial volume of aluminium changes appreciably with increase in hafnium content and these values are characteristic of covalent bonding. This result suggests that hafnium has considerable covalent character while the covalent character of aluminium increases appreciably as hafnium content is increased from 0 to 5 at.%.

The change in the bonding characteristics can also be inferred from the heats of formation of the alloys. Miedema and coworkers [82,273-275] demonstrated that a cellular model can give an excellent account of the heat of formation of binary alloys. The energy effect is derived from two contributions. Firstly, there is a negative contribution to the heat of formation arising from the requirement of equality of chemical potential for electrons in the different cells. This well-known electronegativity effect favours alloying. Secondly, an unfavourable positive contribution to the heat of formation has been shown to be related to the difference in density of electrons at the boundary of the Wigner-Seitz cells for the two atoms. They have provided equations to calculate the heat of formation of any alloy system. They have also listed the constants to evaluate all

the values in the equations. We have used an available computer programme and calculated the heat of formation of Ni-Hf and Ni-Al alloys. These results are listed below.

$$\Delta H (\text{Ni-25 at.\% Hf, Disordered}) = -34 \text{ kJ/mole};$$

$$\Delta H (\text{Ni-25 at.\% Al, Disordered}) = -25 \text{ kJ/mole}.$$

These two values suggest that the Ni-Hf bonds are much stronger than Ni-Al bonds and it is likely that, in the presence of hafnium, bonding with aluminium will become stronger.

(b). Boron-doped  $\gamma'$  containing 75 at.\% Ni : The addition of boron causes increase in  $\bar{V}_{\text{Ni}}$  but decrease in  $\bar{V}_{\text{Al}}$  in all hafnium containing  $\text{Ni}_3\text{Al}$  alloys (see Figures 5.9 and 5.13). But  $\bar{V}_{\text{Hf}}$  shows considerable reduction at hafnium content approaching zero while showing expansion as hafnium content approaches five atom percent. This can be understood in terms of the occupancy of boron atoms in the interstitial sites.

There are two types of interstitial sites which boron atom can occupy (Figure 5.15). Site-I has only nickel atoms as nearest neighbours and has the hole size of 1.08 Å in x, y and z directions. Site-II also is of the same type but out of six neighbours, two are aluminium atoms and four are nickel atoms. The latter also has a hole size of 1.08 Å in y and z directions and 0.71 Å in x direction. The atomic diameter of boron atom is 1.68 Å [272]. Since, the diameter of boron is much larger than the hole size, it causes general expansion of the lattice. This is demonstrated by the increase in  $\Delta\bar{V}_{\text{Ni}}$   $\left[ \Delta\bar{V}_{\text{Ni}} = (\bar{V}_{\text{Ni(B)}} - \bar{V}_{\text{Ni}}) \right]$  where  $\bar{V}_{\text{Ni(B)}}$  and  $\bar{V}_{\text{Ni}}$  are the partial volume of nickel in boron-doped and boron-free alloys, as shown in Figure 5.16. When boron occupies the site II, it is going to compress aluminium atoms appreciably in order to occupy the site as illustrated in Figure 5.17. Therefore,  $\bar{V}_{\text{Al}}$  should show a decrease as seen in Figure 5.13. The atomic diameter of hafnium (3.12 Å) is much more than that of aluminium (2.86 Å). Since, hafnium replaces aluminium in its sublattice,

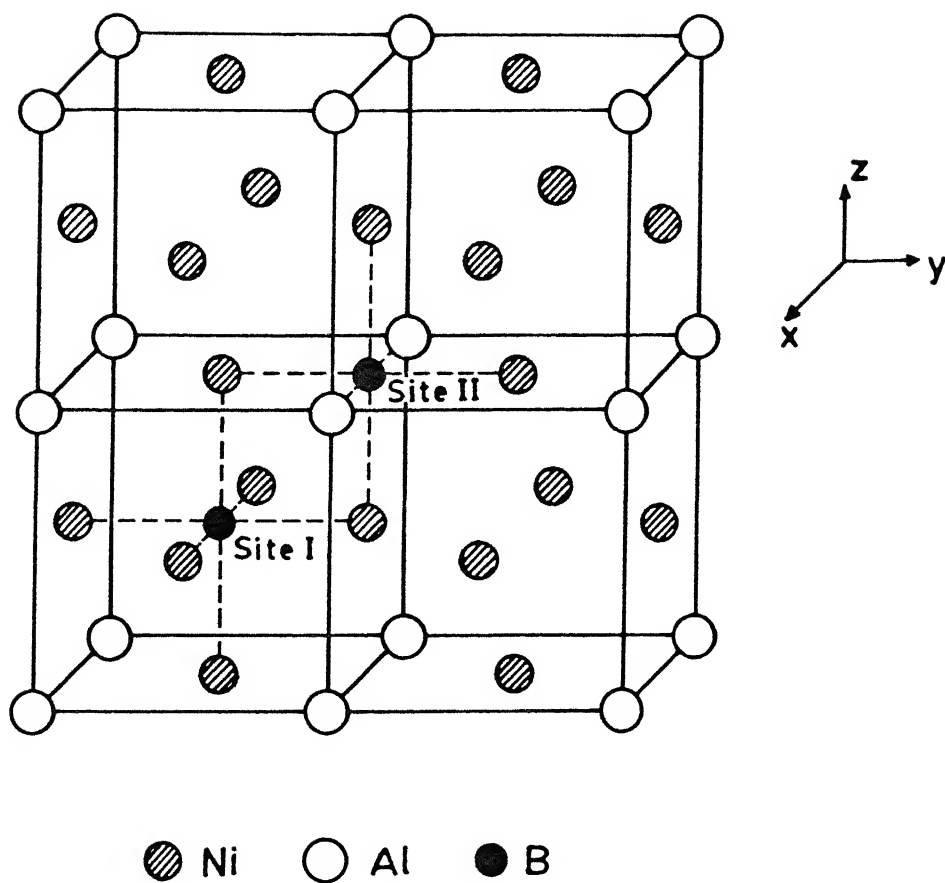


Fig. 5.15: Two different octahedral sites for  $\text{Ni}_3\text{Al}$  structure [52].

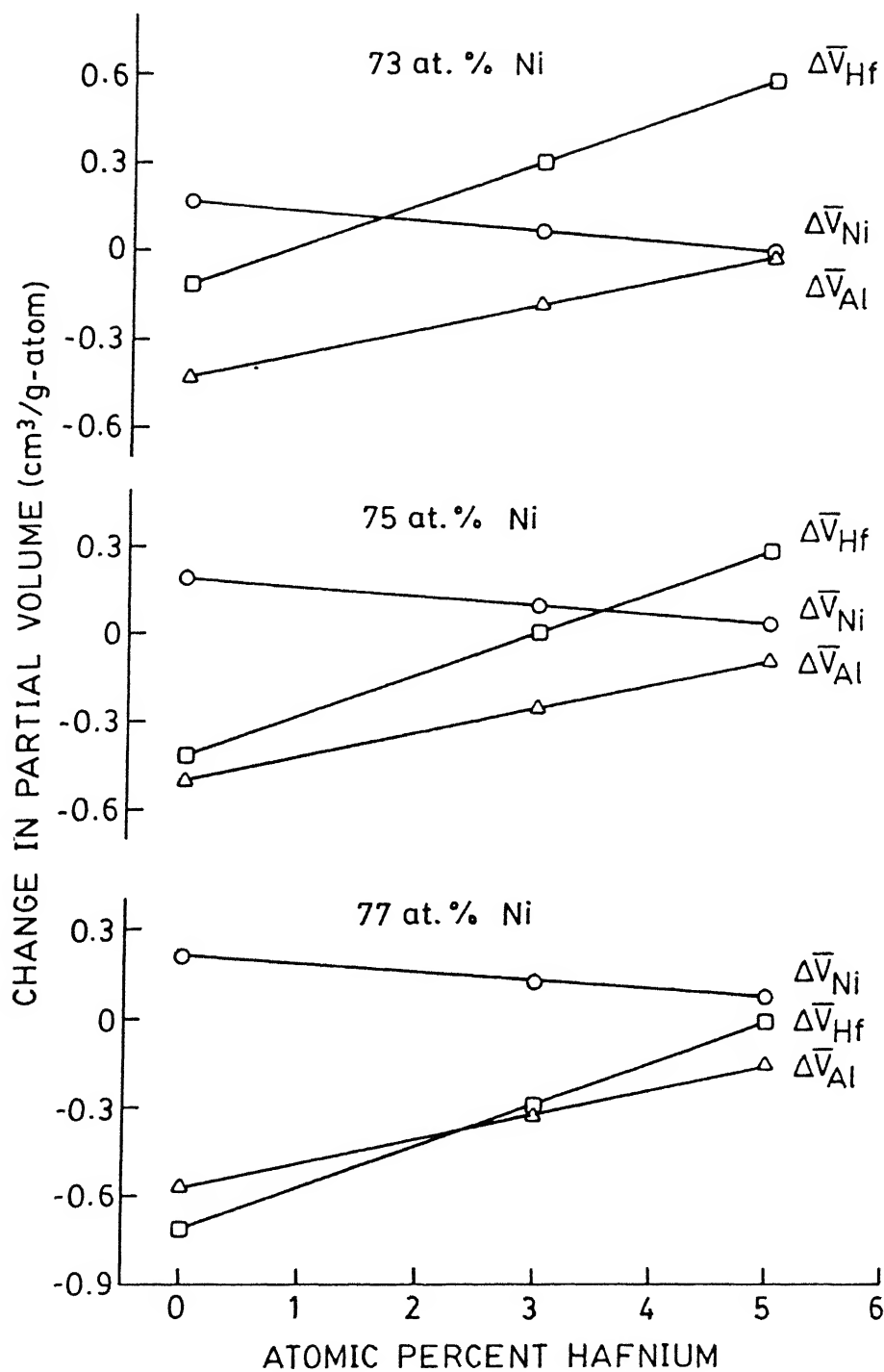


Fig. 5.16: Change in partial volumes ( $\Delta \bar{V}$ ) as a function of atomic percent hafnium in ternary Ni-Al-Hf alloys.

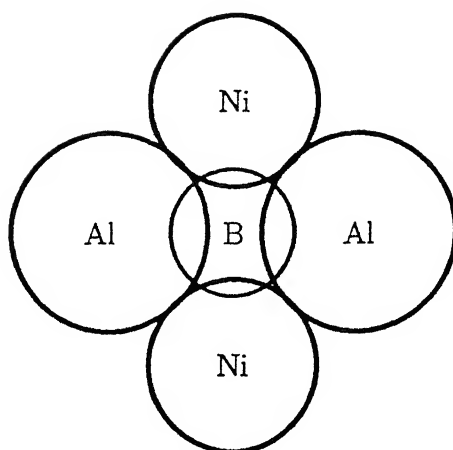


Fig. 5.17: Location of boron in one of the interstitial sites.  
(Site II) on (100) plane of  $\text{Ni}_3\text{Al}$ .

hafnium and aluminium will be neighbours of boron in site-II. Because of the large diameter of hafnium, the boron atom occupying site-II, is expected to compress hafnium more, thereby causing larger reduction in partial volume of hafnium. We see from Figure 5.16 that as hafnium content approaches zero,  $\Delta\bar{V}_{\text{Hf}}$  is appreciably negative. As the hafnium content is increased,  $\bar{V}_{\text{Ni}}$  does not change. However,  $\Delta\bar{V}_{\text{Hf}}$  and  $\Delta\bar{V}_{\text{Al}}$  increase appreciably with increase in hafnium content and  $\Delta\bar{V}_{\text{Hf}}$  becomes positive. This is possible when aluminium and hafnium atoms occupy nickel sites in addition to occupying the aluminium sites so that boron does not have larger hafnium and aluminium atoms as its neighbours. Since  $\Delta\bar{V}_{\text{Al}}$  remains negative, it is unlikely that the boron atom preferentially occupies site-I in order that hafnium atoms avert contact with boron atoms.

(c). Nickel-rich  $\gamma'$  containing 77 at.% Ni : Higher nickel content in the alloy (more than the stoichiometric composition) means that aluminium content is less than the stoichiometric composition. As the size of the aluminium atom is larger than that of nickel, there will be a general contraction of the lattice in the nickel-rich  $\gamma'$  alloys. This is reflected in the values of  $\bar{V}_{\text{Hf}}$  and  $\bar{V}_{\text{Al}}$  which are lower than the corresponding values in  $\gamma'$  alloys containing stoichiometric nickel content (Figure 5.9). However,  $\bar{V}_{\text{Ni}}$  values are larger in the 77 at.% Ni alloys since nickel now occupies aluminium sites which are associated with higher specific volume. As pointed out earlier (Section 5.2.3(a)), with the increase in hafnium content considerable reduction in the value of  $\bar{V}_{\text{Al}}$  (47%) occurs, and this suggests that the bonding between nickel and aluminium becomes stronger.

(d). Boron-doped nickel-rich  $\gamma'$  containing 77 at.% Ni : The addition of boron atoms causes an increase in  $\bar{V}_{\text{Ni}}$  but a decrease in  $\bar{V}_{\text{Al}}$  at all hafnium contents, just as in the case of boron-doped stoichiometric nickel-containing  $\gamma'$  alloys (Figure 5.16). The  $\bar{V}_{\text{Hf}}$  also behaves in a similar manner as in the boron-doped 75 at.%  $\gamma'$  alloys. The net expansion

in  $\bar{V}_{\text{Hf}}$  as hafnium content increases from 0 to 5 at.%, is  $0.70 \text{ cm}^3/\text{g-atom}$  for this alloy, which is identical to that of the boron-doped 75 at.%  $\gamma'$  alloy. When the hafnium content is increased, the  $\Delta\bar{V}_{\text{Hf}}$  is much less negative suggesting that the hafnium atoms tend to move towards nickel sites. At 5 at.% Hf, the  $\Delta\bar{V}_{\text{Hf}}$  is still negative compared to boron-free alloys suggesting that in these alloys boron may be occupying site I.

(e). Aluminium rich  $\gamma'$  containing 73 at.% Ni : As the size of aluminium atom is larger than that of nickel atom, there is a general expansion in the lattice. This is seen from the increase in the values of  $\bar{V}_{\text{Al}}$  and  $\bar{V}_{\text{Hf}}$  (Figure 5.9). However, the excess aluminium atoms go to nickel sites. So, the nickel atoms have more number of aluminium atoms as their neighbours. In other words, more number of nickel-aluminium bonds are formed which are stronger than nickel-nickel bonds. This gives rise to contraction and hence,  $\bar{V}_{\text{Ni}}$  is smaller compared to its value in 75 at.% Ni  $\gamma'$  alloys. As the hafnium content is increased from 0 to 5 at.%,  $\bar{V}_{\text{Ni}}$  and  $\bar{V}_{\text{Hf}}$  tend to increase as a result of the general increase in the volume of the lattice. However,  $\bar{V}_{\text{Al}}$  tends to decrease because of stronger interaction between nickel and aluminium as discussed earlier (Section 5.2.3(a)).

(f). Boron-doped aluminium rich  $\gamma'$  containing 73 at.% Ni: Figure 5.16 shows that  $\bar{V}_{\text{Ni}}$  changes only slightly due to the addition of boron as well as due to the addition of hafnium.  $\Delta\bar{V}_{\text{Al}}$  increases with hafnium content. The net expansion in  $\bar{V}_{\text{Hf}}$  is same as that of stoichiometric and nickel-rich alloys. But the values of  $\Delta\bar{V}_{\text{Al}}$  and  $\Delta\bar{V}_{\text{Hf}}$  at all hafnium content is higher than those of stoichiometric alloys. This is consistent with the substitution of nickel by both aluminium and hafnium in the nickel sublattice.



### 5.3. OCCURRENCE OF TWINS

#### 5.3.1. Boron-free $\gamma'$

The optical microstructures presented in Chapter-IV show the presence of twins in stoichiometric  $\text{Ni}_3\text{Al}$  (Figure 4.1) and aluminium-rich  $\gamma'$  of nominal composition  $\text{Ni}_{73}\text{Al}_{27}$  (Figure 4.3). Twins are not observed either in nickel-rich binary or in hafnium containing  $\gamma'$ . The presence or absence of twins is related to the variation of the stacking fault energy (SFE) of the phase with alloy content.

The change of the stacking fault energy with alloying is often derived from the measurement of faulting probability. The faulting probability and the stacking fault energy are related by a simple relationship [276];

$$\alpha = k\rho/\gamma \quad (5.14)$$

where,  $k$  is a constant,  $\rho$  is the dislocation density,  $\alpha$  is the faulting probability and  $\gamma$  is the stacking fault energy. It is normally assumed that ' $k\rho$ ' is independent of alloy composition. Although in some cases, this can be shown to be a poor assumption [276], it is reasonable to conclude that  $\alpha$  and  $\gamma$  are inversely proportional and a material with a low stacking fault energy will have a high faulting probability.

The faulting probability ( $\alpha$ ) in alloys of nickel with B-subgroup elements reveals that antimony and tin are more effective than titanium in increasing  $\alpha$ , while germanium, silicon, indium and aluminium are about as effective as molybdenum and tungsten (Figure 5.18) [277]. Therefore, in aluminium-rich alloys of nickel, the faulting probability ( $\alpha$ ) is expected to be higher. Therefore, the stacking fault energy,  $\gamma$ , should decrease with the addition of aluminium and more twins are expected to form. This may be the case with aluminium-rich  $\gamma'$  in which twins are observed. In the

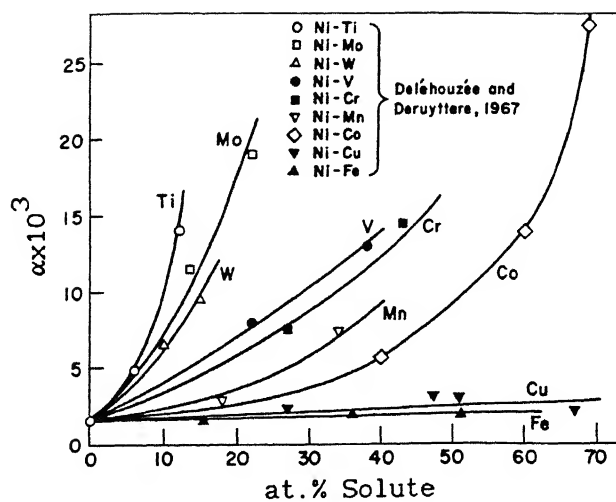


Fig. 5.18: Room temperature determination of the variation of the faulting probability,  $\alpha$ , as a function of atomic percent solute in nickel-base alloys [277].

case of nickel-rich  $\gamma'$ , which are poor in aluminium, twins are not observed.

The decrease in the stacking fault energy of nickel due to a solute is also generally greater when the separation between nickel group and that of the solute in the periodic table is greater [239]. Therefore, the presence of hafnium (Group IV) should decrease the stacking fault energy of nickel (Group VIII) and hence, twins should be observed in the hafnium containing alloys. However, experimentally twins are not observed in hafnium containing alloys. This behaviour may be attributed to the fact that hafnium replaces aluminium in  $\gamma'$  and hafnium may not be as effective as aluminium in reducing the stacking fault energy of  $\gamma'$  and to produce twins.

#### 5.3.2. Effect of boron

In boron-free alloys, twins were observed in stoichiometric  $\text{Ni}_3\text{Al}$  and aluminium-rich  $\gamma'$  of nominal composition  $\text{Ni}_{73}\text{Al}_{27}$ . But in the case of boron-doped alloys, whether aluminium-rich or nickel-rich, no twins could be observed. In the case of boron-free alloys, the presence or absence of twins is attributed to the variation of stacking fault energy (SFE) of the phase with alloy content. It is suggested that the presence of excess aluminium may decrease the stacking fault energy and hence, result in the formation twins. In boron-doped alloys, the presence of boron may be responsible in increasing the stacking fault energy resulting in a decrease and total disappearance of twins.

#### 5.4. SUBSTRUCTURE OF $\text{Ni}_3\text{Al}$ ( $\gamma'$ ) ALLOYS

None of the annealed single phase  $\gamma'$  alloys examined under the transmission electron microscope showed any features excepting grain boundaries. In order to study the dislocation substructures of these

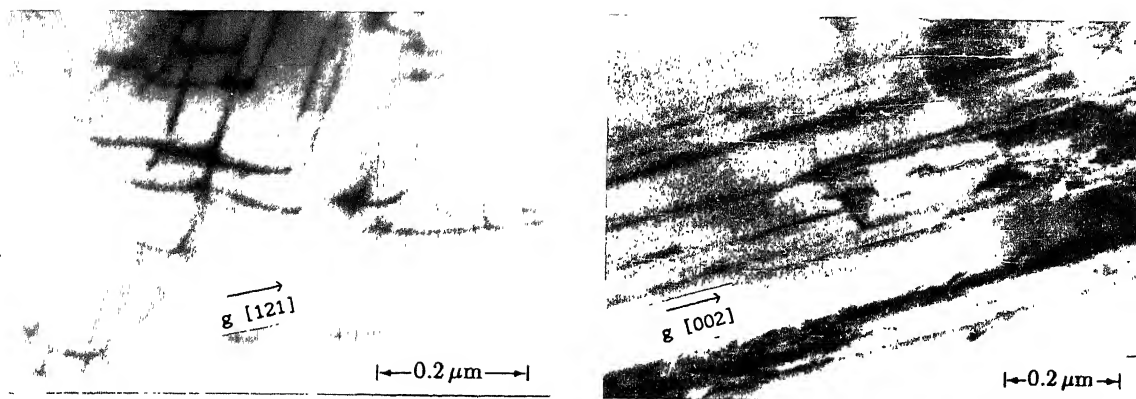
alloys, thin foils were prepared after prestraining upto 2 to 3 percent. Substructures in stoichiometric  $\text{Ni}_3\text{Al}$ , boron-doped  $\text{Ni}_3\text{Al}$ , hafnium containing  $\text{Ni}_3\text{Al}$  and boron-doped hafnium containing  $\text{Ni}_3\text{Al}$  have been studied. Apart from these alloys which are all single phase, only one two phase boron-doped  $\text{Ni}_3\text{Al}$  alloy containing 7.5 at.% Hf was analyzed without giving any prestraining to the sample.

#### 5.4.1. Stoichiometric $\text{Ni}_3\text{Al}$

Typical microstructures of boron-free  $\text{Ni}_3\text{Al}$  are shown in Figures 5.19(a) to (f). Figure 5.19(a) shows an area with a large number of dislocations, most of them straight but some are curved. The beam direction in this is  $[\bar{1}3\bar{7}]$ . Very often long nearly parallel dislocations are also observed (Figure 5.19(b)). The beam direction, here, is  $[\bar{1}\bar{1}0]$ . Sometimes two sets of nearly parallel dislocations are seen crossing each other making an angle of approximately  $60^\circ$  (Figure 5.19(c)). Again in some areas, three sets of dislocation lines are found criss-crossing one another making an angle of approximately  $60^\circ$  (Figure 5.19(d)). Features similar to those of stacking faults can also be seen at a few places in this micrograph (Figure 5.19(d)). Figure 5.19(e) shows an area containing mostly stacking fault like features and a few straight dislocation lines. Intersecting twin-like features and stacking faults have also been observed at a few places (Figure 5.19(f)). Careful examination of a number of foils reveals that the stacking faults and long straight dislocation lines appear with nearly equal probability in this alloy.

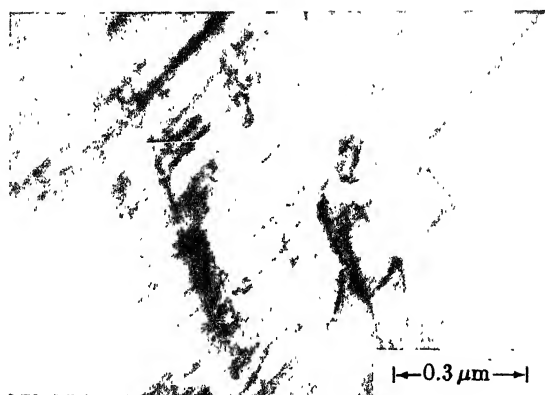
#### 5.4.2. Boron-doped $\text{Ni}_3\text{Al}$

Contrary to what has been observed in the case of stoichiometric  $\text{Ni}_3\text{Al}$ , the boron-doped  $\text{Ni}_3\text{Al}$  showed a distinctly different substructure. These are shown typically in Figures 5.20(a) to (d). Very often the



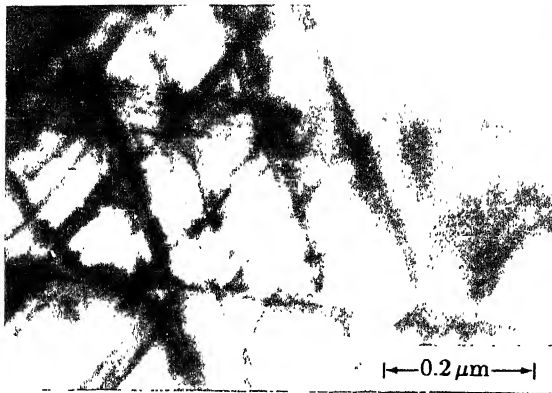
(a)

(b)

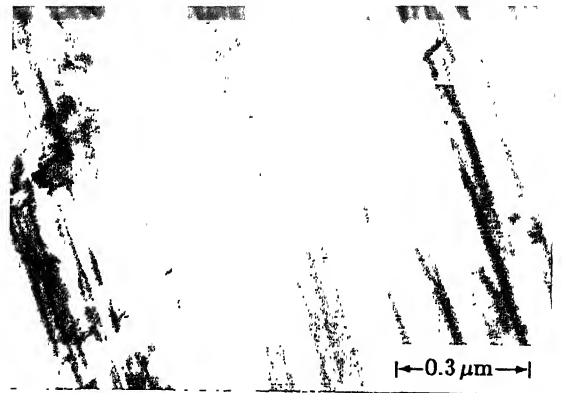


(c)

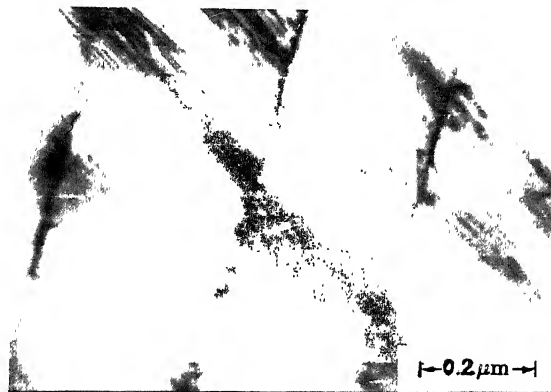
Fig. 5.19: Typical dislocation configurations in prestrained (2-3 %) boron-free  $\text{Ni}_3\text{Al}$  ((a), (b) and (c)).



(d)

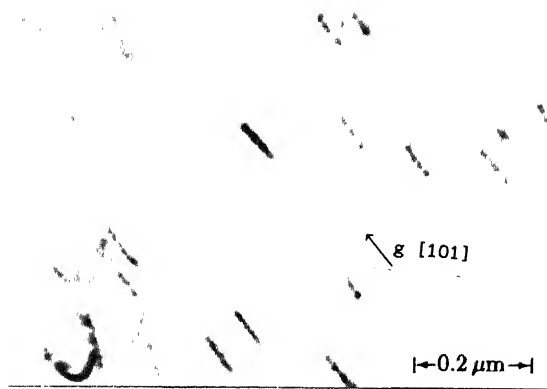


(e)

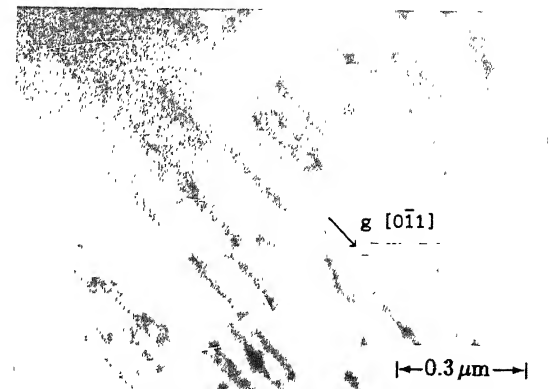


(f)

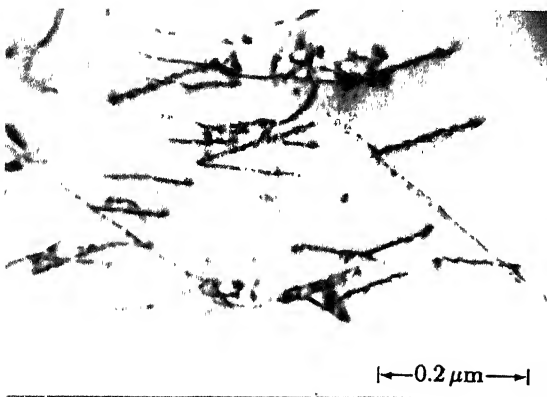
Fig. 5.19: Typical dislocation configurations in prestrained (2-3 %) boron-free  $\text{Ni}_3\text{Al}$  ((d), (e) and (f)).



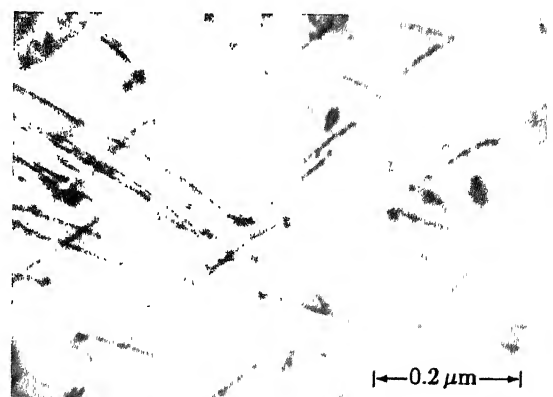
(a)



(b)



(c)



(d)

Fig. 5.20: Typical dislocation configurations in prestrained (2-3 %) boron-doped  $\text{Ni}_3\text{Al}$  ((a), (b), (c) and (d)).

substructure consists of short straight dislocation segments lying parallel to one another (Figure 5.20(a)). The beam direction in this case is  $[\bar{1}31]$ . At a few places dislocation dipoles are also observed in addition to the straight dislocation lines (Figure 5.20(b)). Sometimes pile-ups of dislocation lines against some kind of obstacles can also be seen (Figure 5.20(c)). At a few places, two distinct sets of dislocation lines making an angle of nearly  $60^\circ$  with each other can also be observed (Figure 5.20(d)). It is interesting to note that none of the foils of this alloy that were examined under transmission electron microscope, showed any stacking fault like features or twins which were very common in the substructure of boron-free stoichiometric  $\text{Ni}_3\text{Al}$ .

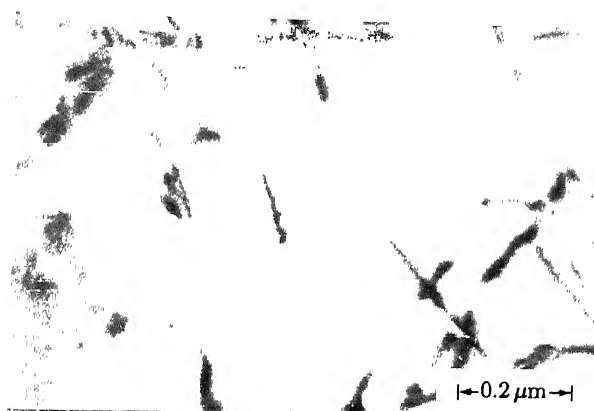
#### 5.4.3. Hafnium containing $\gamma'$

Foils of  $\text{Ni}_3\text{Al}$  containing 5 at.% Hf were examined under the electron microscope (Figures 5.21(a) to (d)). Figure 5.21(a) shows typically the dislocation pattern which is obtained in this alloy. Sometimes, long parallel dislocation lines are found (Figure 5.21(b)). At a few places a criss-cross arrangement of two sets of dislocation lines is also seen (Figure 5.21(c)). The beam direction, here, is  $[\bar{1}10]$ . Very rarely, parallel dislocation lines making a wavy pattern are observed as shown in Figure 5.21(d). No stacking fault like feature could be observed in any one of the foils prepared from this alloy.

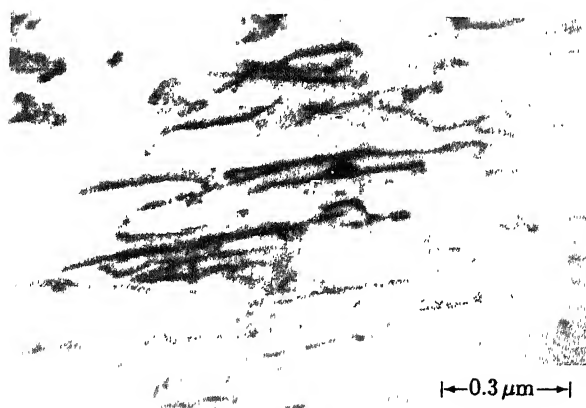
#### 5.4.4. Boron-doped $\gamma'$ alloy containing hafnium

The arrangement of dislocations in the boron-doped  $\text{Ni}_3\text{Al}$  alloy containing 5 at.% Hf is shown typically in Figure 5.22(a). Sometimes, long dislocation lines tend to align themselves in nearly parallel fashion (Figure 5.22(b)). The beam direction in this case is  $[\bar{1}\bar{1}5]$ . It is interesting to note that the hafnium containing alloys with and without





(a)



(b)

Fig. 5.22: Typical dislocation configurations in prestrained (2-3 %) boron-doped alloy  $\text{Ni}_{75.2}\text{Al}_{19.7}\text{Hf}_{5.1}$  ((a) and (b)).

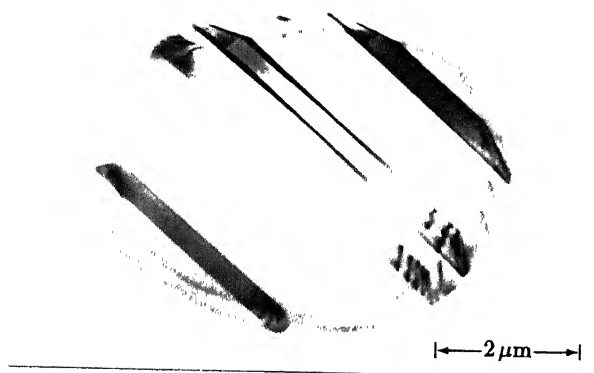
boron do not show any stacking fault in their substructures.

#### 5.4.5. Boron-doped hafnium containing $\gamma'$ -rich alloy having two phase structure

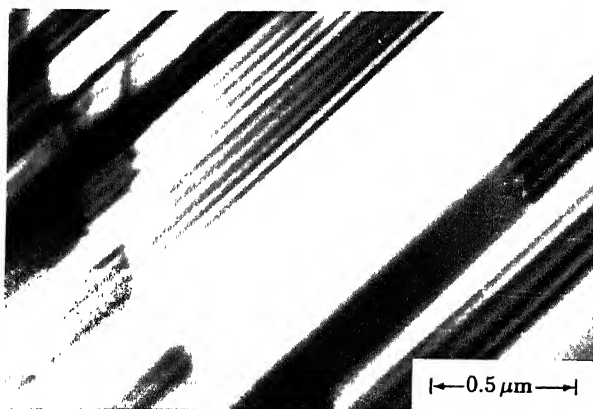
One foil made from boron-doped  $\text{Ni}_3\text{Al}$  alloy containing 7.5 at.% Hf was examined under the transmission electron microscope. It was found previously that this alloy consisted of mostly the  $\gamma'$  phase with some second phase  $\eta_1$  ( $\text{Ni}_7\text{Hf}_2$ ) particles. The substructure of the  $\gamma'$  phase does not show any stacking fault although the second phase contains a large number of faults within it. Figures 5.23(a) and 5.23(b) show the images of these stacking faults under two different magnifications.

#### 5.4.6. Discussion

As stated earlier, the stoichiometric  $\text{Ni}_3\text{Al}$  shows a substructure made-up of isolated dislocations as well as stacking faults. This has been observed by early workers also [278]. Although the stacking fault energy (SFE) of  $\text{Ni}_3\text{Al}$  is not known, Gottstein et al. [279] have suggested that the stacking fault energy of  $\text{Ni}_3\text{Al}$  must be greater than the antiphase boundary (APB) energy on the (111) planes which has been determined as  $111 \text{ mJm}^{-2}$  [256]. The shear modulus  $\mu$  for  $\text{Ni}_3\text{Al}$  is quite high, about 80 GPa [280]. These values are quite comparable with those of pure nickel which has  $\gamma_{\text{SFE}} = 150 \text{ mJm}^{-2}$  and  $\mu = 80 \text{ GPa}$  [281-283]. The lattice parameter of  $\text{Ni}_3\text{Al}$  as measured in this investigation is about 3.57 Å which is not very far from the lattice parameter of nickel which is 3.52 Å. Thus, whether we compare the  $\gamma_{\text{SFE}}$  values or  $\gamma/\mu b$  values of  $\text{Ni}_3\text{Al}$  with those of pure nickel, there is practically not much of a difference. Pure nickel does not show any stacking faults in its microstructure because of its reasonably high value of the stacking fault energy. It is, therefore, quite surprising that profusion of stacking faults is obtained in the substructure of



(a)



(b)

Fig. 5.23: Typical microstructures of the boron-doped alloy of nominal composition  $\text{Ni}_{75.0}\text{Al}_{17.5}\text{Hf}_{7.5}$  showing stacking faults in the  $\eta_1$  phase ((a) and (b)).

$\text{Ni}_3\text{Al}$ . In fact, the stacking faults are known to occur only in low stacking fault energy materials such as Cu-high Zn alloys or Ni-high Co alloy etc. The stacking fault energy of a Ni-10 wt.%Co alloy has been measured as  $111.8 \text{ mJm}^{-2}$ . Yet this alloy has not been found to show any stacking faults [284].

Different types of faults that occur in  $\text{L1}_2 \text{Ni}_3\text{Al}$  are discussed in section 2.8, Chapter-II. A major experimental difficulty is normally encountered in the unambiguous identification of the partial dislocations present after dissociation, largely because the separation between the partials is often too small to permit resolution and identification with simple diffraction-contrast TEM methods. This has been the reason why it was not possible in the present investigation to identify the fault type in  $\text{Ni}_3\text{Al}$ . In view of what has been stated above, we may safely conclude that the stacking faults observed are not the ones commonly observed in fcc metals and alloys with low stacking fault energy (the so-called complex stacking faults as mentioned above). In fact, no CSF's have been observed in  $\text{Ni}_3\text{Al}$  [100,121,140,256-258]. On the other hand, plenty of SISF's have been found to occur in  $\text{Ni}_3\text{Al}$  [208,259,260]. Therefore, we conclude that the faults observed in the present alloys are, in all probability, the superlattice intrinsic stacking faults.

The addition of boron has been found to effectively suppress the formation of superlattice intrinsic stacking faults in  $\text{Ni}_3\text{Al}$  (Figure 5.20(a) to (d)). This has been suggested to be due to the segregation of boron atoms to the dislocations, thereby, preventing the nucleation of  $1/3\langle 112 \rangle$  partials [278]. It has been further suggested that for such mechanism to operate, the boron atmosphere has to keep up with the moving dislocations. All these will amount to saying that the addition of boron may simply cause easier glide by the  $\langle 110 \rangle$  dislocations [278].

The effect of the addition of hafnium to  $\text{Ni}_3\text{Al}$  has been found to be

rather similar to that of boron in the sense that, in the single phase  $\text{Ni}_3\text{Al}$  containing 5 at.% Hf, no stacking faults could be observed. The precise mechanism by which hafnium prevents the formation of SISF's in  $\text{Ni}_3\text{Al}$  is not known yet. As expected, the boron-doped  $\text{Ni}_3\text{Al}$  containing 5 at.% Hf also did not show the presence of any SISF's. Although the effect of addition of boron or hafnium to  $\text{Ni}_3\text{Al}$  is found to be similar in so far as the substructure formation is concerned, it is difficult to visualize these two elements operating in the same way to prevent the formation of SISF's. The total concentration of hafnium atoms is about fifty times that of boron concentration in the present alloys. Thus, we may expect a much more uniform distribution of hafnium atoms throughout the  $\text{Ni}_3\text{Al}$  matrix. Whether some of the hafnium atoms which may be segregating to the dislocations present will be effective enough to prevent the formation of SISF's in the same manner as that of boron can not be stated with any certainty at this moment.

## CHAPTER VI

### MECHANICAL BEHAVIOUR OF $\gamma'$ IN COMPRESSION

#### 6.1. INTRODUCTION

A large number of alloy compositions were prepared during this investigation for the purpose of the determination of phase equilibria and structural characteristics. It would be interesting to compare the mechanical behaviour of these alloys with those of the host of alloys of similar compositions which have been reported in the literature from time to time. It was mainly with these ideas that a limited amount of mechanical testing (compression tests) was undertaken on selected alloy compositions. The results of these experiments along with comparison of the observed data with those reported in the literature will be described below.

#### 6.2. DEFORMATION OF STOICHIOMETRIC $\gamma'$

##### 6.2.1. Stress-Strain behaviour

The yield behaviour of  $\text{Ni}_3\text{Al}$  has been studied by many investigators [11,53,123] through compression tests and tension tests as a function of temperature. It is well known that the 0.2% flow stress of  $\text{Ni}_3\text{Al}$  increases with temperature and after reaching the peak value, it starts to decrease. In order to check the behaviour of the material used in the present investigation, compression tests on stoichiometric  $\text{Ni}_3\text{Al}$  was carried out at different temperatures. Some of the plots, available in the literature, of 0.2% flow stress of stoichiometric  $\text{Ni}_3\text{Al}$  versus temperature along with those of off-stoichiometric alloys are shown in Figure 2.25 (Chapter II). The temperature at which the peak of the proof stress occurs has been

reported [53] to be around  $650^{\circ}\text{C}$ . Therefore, the samples of  $\text{Ni}_3\text{Al}$  used in the present investigation were tested at  $650^{\circ}\text{C}$ .

The load versus the change in length curve for boron-free stoichiometric  $\text{Ni}_3\text{Al}$ , recorded at a strain rate of  $10^{-4} \text{ sec}^{-1}$ , is shown in Figure 6.1. From the graph, it is seen that the load initially increases with decrease in the length of the specimen and then decreases after reaching the peak value. The increase in load is due to the work hardening of the specimen as well as due to the increase in the cross-sectional area of the specimen. Since, there is no necking possible under compression the decrease in load after reaching the peak occurs when cracks are formed in the material. Thus, the strain corresponding to the peak load may be taken as the ductility of the material before the formation of cracks.

From the experimental load versus the change in length plot, the true stress versus the true strain graph can be plotted using the following relationships;

$$\text{True stress } \sigma' = P/A_0 \left[ L/L_0 \right] \quad (6.1)$$

$$\text{True strain } \epsilon' = \int_{L_0}^L dL/L_0 = \ln \left[ L/L_0 \right] \quad (6.2)$$

where P - The load at any instant;

$A_0$  - Original cross-sectional area;

$L_0$  - Original gauge length;

L - Final gauge length.

The true stress values were calculated from corresponding true strain values in the plastic region of the plot. The true stress versus the true strain curve for stoichiometric boron-free  $\text{Ni}_3\text{Al}$  deformed at  $650^{\circ}\text{C}$  is shown in Figure 6.2. The 0.2% flow stress calculated was found to be

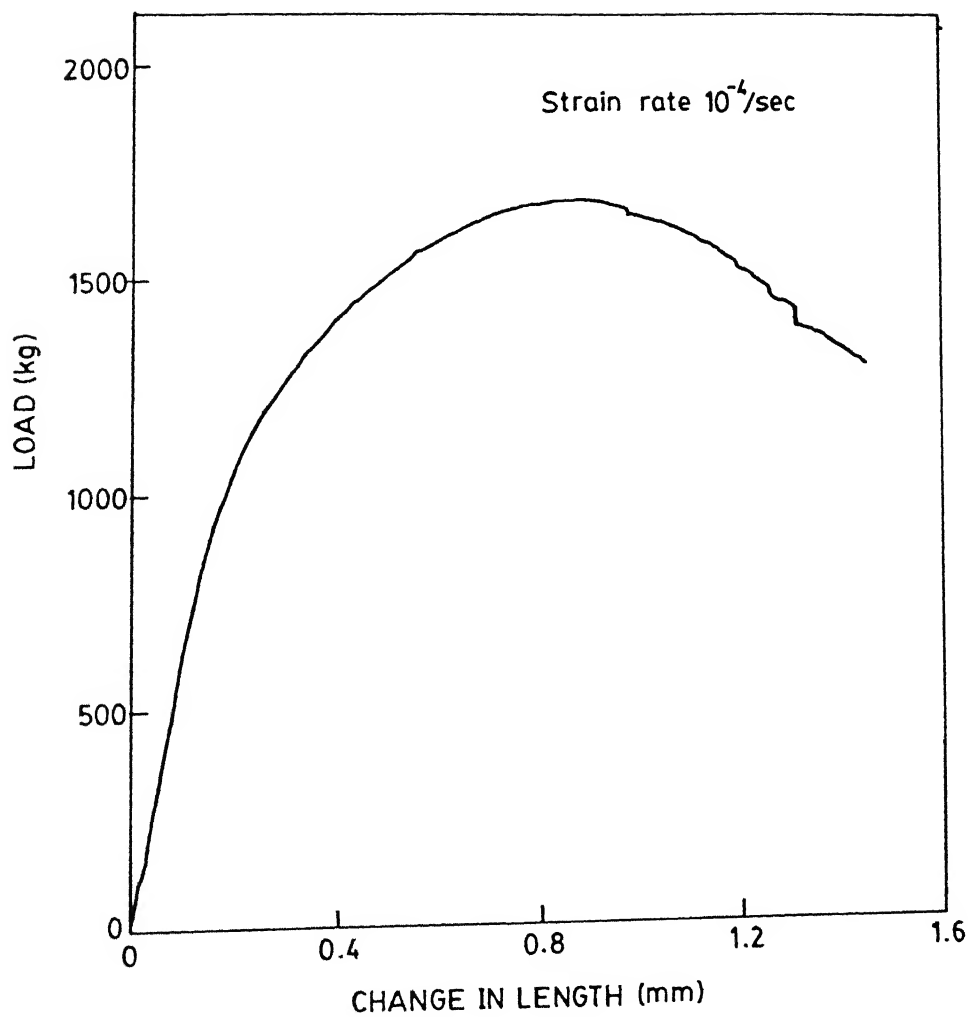


Fig. 6.1: Load versus change in length plot of boron-free stoichiometric  $\text{Ni}_3\text{Al}$  alloy at  $650^\circ\text{C}$ .



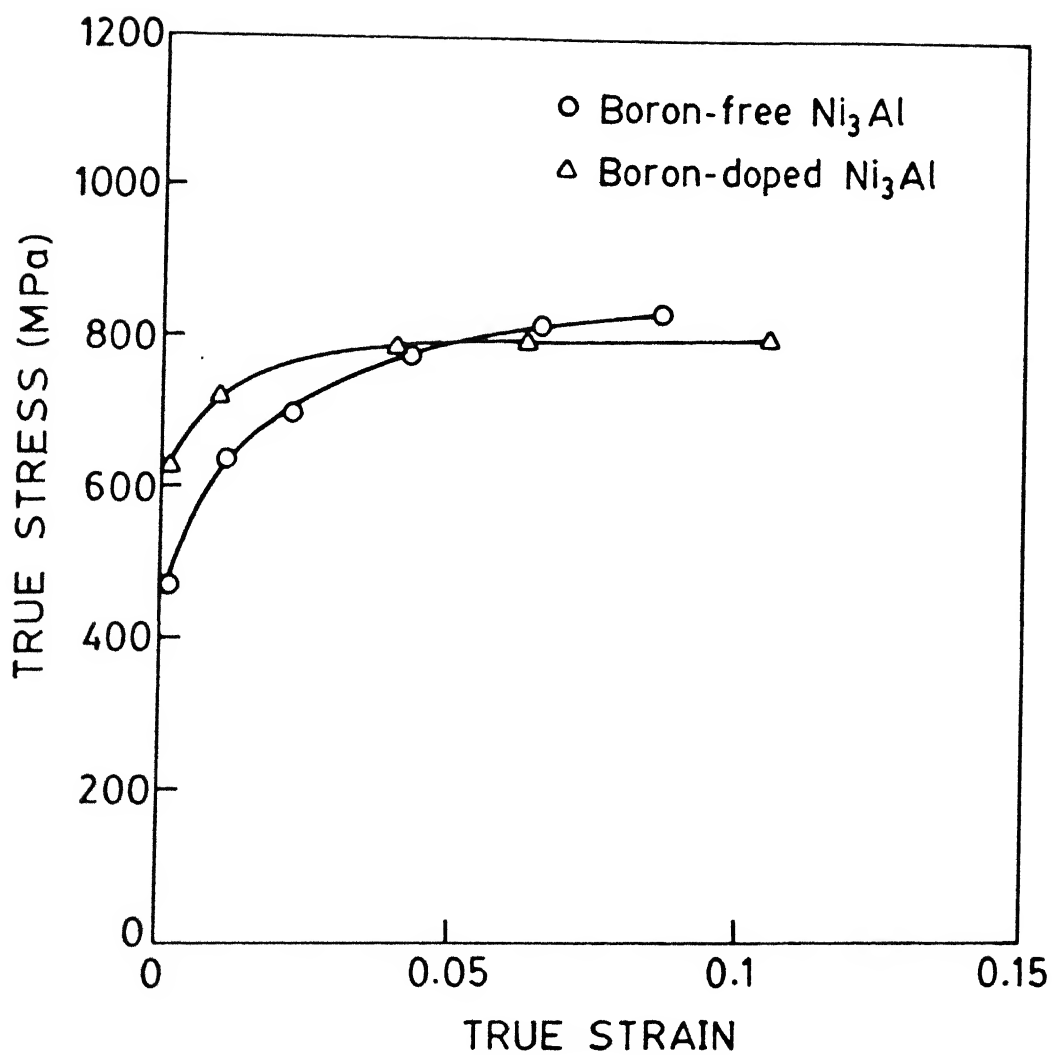


Fig. 6.2: True stress versus true strain plot of boron-free and boron-doped stoichiometric  $\text{Ni}_3\text{Al}$  alloy at  $650^\circ\text{C}$ .

476 MPa which compares well with the literature value of 475 MPa [53]. The strain required for crack initiation was found to be 8%.

The true stress versus the true strain curve for boron-free stoichiometric  $\text{Ni}_3\text{Al}$ , compression tested at room temperature ( $25^\circ\text{C}$ ) is shown in Figure 6.3. Here, the stress initially increases with strain due to work hardening, followed by a more rapid increase of flow stress beyond a strain value of 2%. Hence, the strain corresponding to the crack initiation could not be measured. The 0.2% flow stress calculated was found to be 153 MPa which is higher compared to the literature value of 100 MPa [53].

#### 6.2.2. Effect of boron doping

In order to find out the effect of boron, compression test was performed on boron-doped stoichiometric  $\text{Ni}_3\text{Al}$  (Alloy 'B', Table 3.1). This material was also tested at  $650^\circ\text{C}$  just as in the case of boron-free stoichiometric  $\text{Ni}_3\text{Al}$ . The true stress and the true strain values were calculated from the load versus the change in length graph and the plot of true stress versus true strain is shown in Figure 6.2. The 0.2% flow stress was calculated to be 623 MPa which is much higher compared to that of boron-free stoichiometric  $\text{Ni}_3\text{Al}$  alloy and the strain required for the crack initiation was found to be 10%.

The compression test on the alloy 'B' was also performed at room temperature. The true stress versus the true strain plot was made from the load versus the change in length graph and this is shown in Figure 6.3. The 0.2% flow stress was calculated to be 161 MPa which is marginally higher compared to the 0.2% flow stress value of boron-free  $\text{Ni}_3\text{Al}$  at room temperature. The strain required for the crack initiation could not be measured because of stage II hardening.

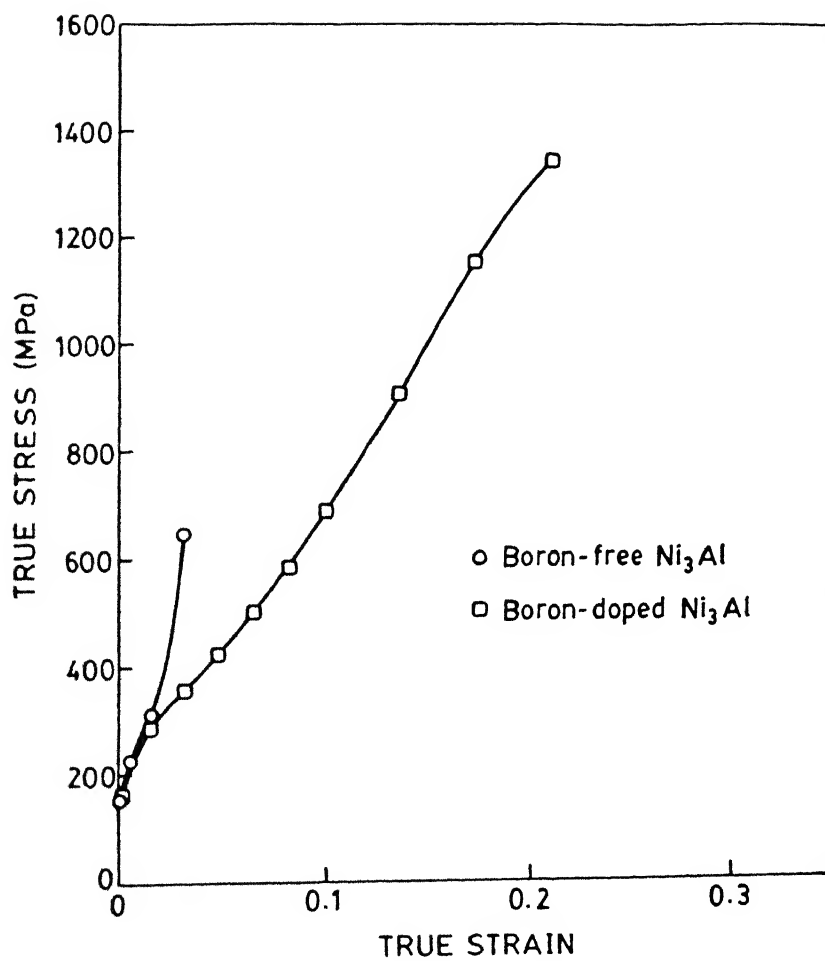


Fig. 6.3: True stress versus true strain plot of boron-free and boron-doped stoichiometric  $\text{Ni}_3\text{Al}$  alloy at  $25^\circ\text{C}$ .

### 6.3. DEFORMATION OF HAFNIUM CONTAINING $\gamma'$

#### 6.3.1. Stress-strain behaviour

The temperatures at which the proof stress of hafnium containing  $\text{Ni}_3\text{Al}$  alloys peaked were collected from the literature [11] and are plotted in Figure 6.4 as a function of hafnium content. The peak temperature at which 0.2% flow stress becomes maximum was determined for various percentages of hafnium in the experimental alloys of this investigation. In order to check the consistency of the present results with the literature, the compression tests of the alloy  $\text{Ni}_{75.5}\text{Al}_{19.5}\text{Hf}_5$ , which has a homogeneous single phase structure, were performed at various temperatures near the peak.

From the load versus the change in length plot, the true stress and the true strain values were calculated and the plot of true stress versus true strain for the alloy  $\text{Ni}_{75.5}\text{Al}_{19.5}\text{Hf}_5$  at 375°C, 400°C, 500°C and 600°C is drawn in Figure 6.5.

Compression tests were also performed for boron-free alloy  $\text{Ni}_{75.5}\text{Al}_{19.5}\text{Hf}_5$  and boron-doped alloy  $\text{Ni}_{75.2}\text{Al}_{19.7}\text{Hf}_{5.1}$  at room temperature. The true stress versus the true strain plots are shown in Figure 6.6. From this figure, it is seen that the 0.2% flow stress at room temperature for both boron-free and boron-doped alloys are almost identical. This value is comparable with the literature value of 1040 MPa [11].

#### 6.3.2. Effect of temperature

The 0.2% flow stress values determined for the boron-free alloy  $\text{Ni}_{75.5}\text{Hf}_{19.5}\text{Al}_5$  as a function of temperature are plotted in Figure 6.7. The 0.2% flow stress increases with increasing temperature and then decreases after reaching the peak. The peak temperature was found to be 475°C which is comparable with the literature value of 455°C [11]. The

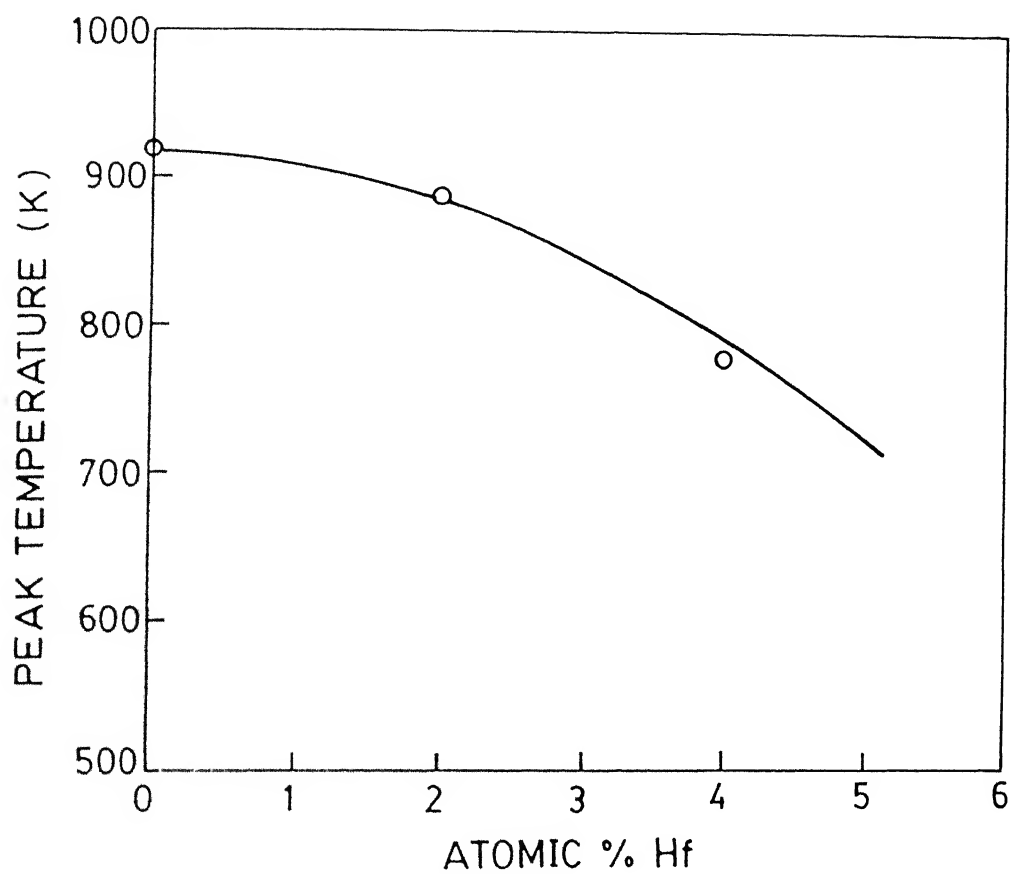


Fig. 6.4: Plot of peak temperature as a function of atomic percent hafnium [11].

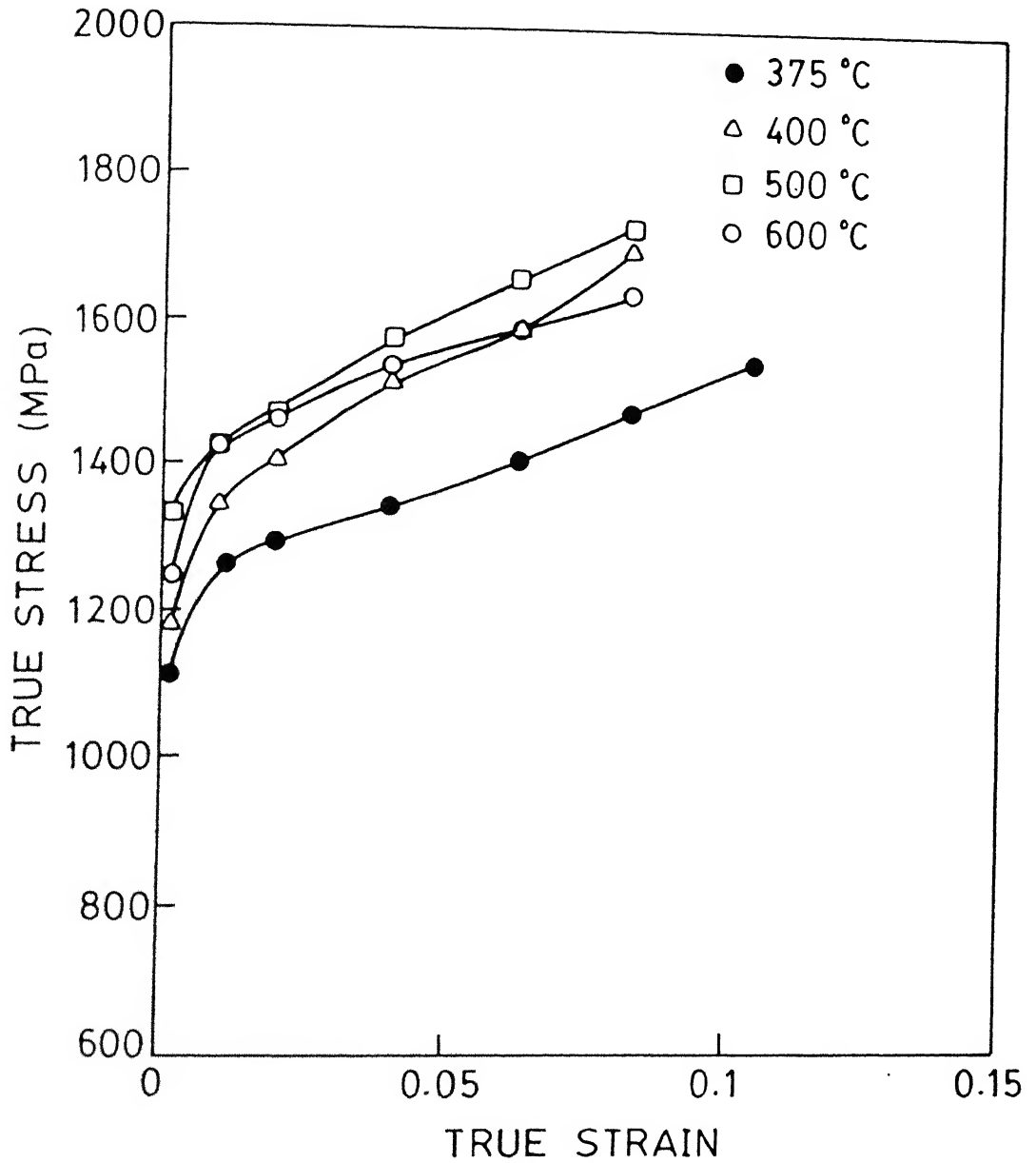


Fig. 6.5: True stress versus true strain plot of boron-free alloy  $\text{Ni}_{75.5}\text{Al}_{19.5}\text{Hf}_{5.0}$  at various temperatures.

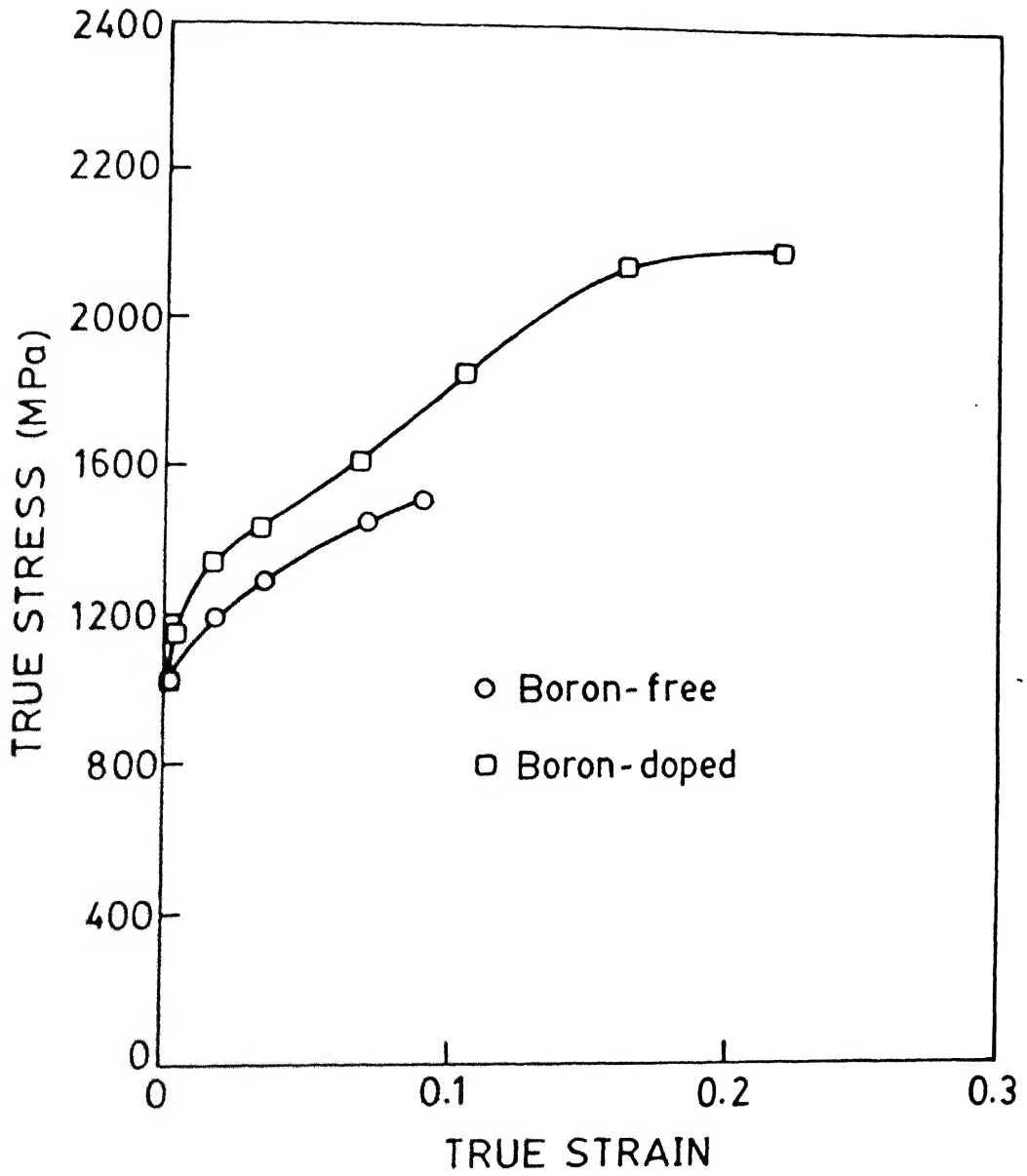


Fig. 6.6: True stress versus true strain plot for boron-free alloy  $\text{Ni}_{75.5}\text{Al}_{19.5}\text{Hf}_{5.0}$  and boron-doped alloy  $\text{Ni}_{75.2}\text{Al}_{19.7}\text{Hf}_{5.1}$  at 25°C.

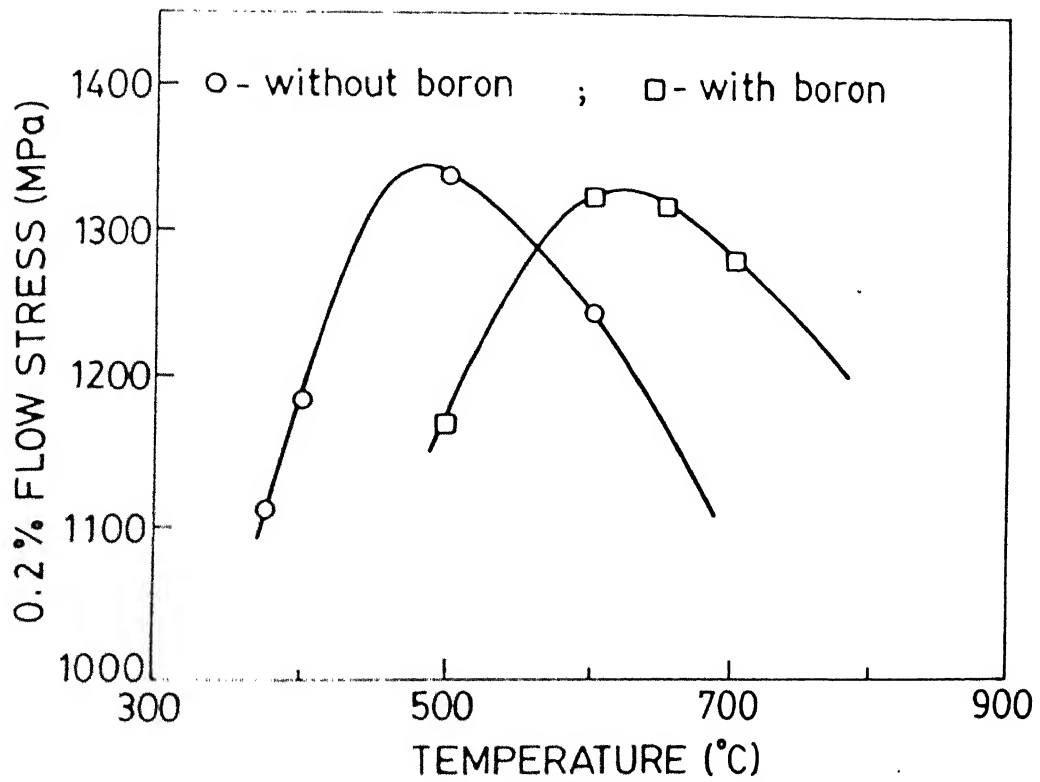


Fig. 6.7: Plot of 0.2% flow stress as a function of temperature for boron-free alloy  $\text{Ni}_{75.5}\text{Al}_{19.5}\text{Hf}_{5.0}$  and boron-doped alloy  $\text{Ni}_{75.2}\text{Al}_{19.7}\text{Hf}_{5.1}$ .



effect of boron doping will be discussed in section 6.3.4.

### 6.3.3. Effect of hafnium content

From Figure 6.4, the temperature at which the 0.2% flow stress is maximum was calculated for the alloy  $\text{Ni}_{75.7}\text{Al}_{21.5}\text{Hf}_{2.8}$ . The compression test was performed at that temperature. The true stress versus the true strain graph was plotted from the load versus the change in length curve and it is shown in Figure 6.8. The 0.2% flow stress was calculated and it was found to be 850 MPa.

The 0.2% proof stress was measured at the peak temperature for the alloys containing 0, 2.5 and 5 at.% Hf. The plot of 0.2% flow stress at peak temperature versus atomic percent hafnium was drawn and is shown in Figure 6.9 along with the literature curve [11]. From this figure, it is seen that the present results agree well with those of the literature results [11].

### 6.3.4. Effect of boron-doping

In order to find out the effect of boron on the peak temperature, the compression tests were performed for the boron-doped alloy  $\text{Ni}_{75.2}\text{Al}_{19.7}\text{Hf}_{5.1}$  at 500°C, 600°C, 650°C and 700°C. The true stress versus the true strain curve for each temperature was drawn. These are shown in Figure 6.10.

The 0.2% flow stress was calculated for each temperature and is plotted as a function of temperature (Figure 6.7). From Figure 6.7, it is seen that the boron addition tends to increase the peak temperature.

## 6.4. FRACTURE BEHAVIOUR

During the compression test, not all the alloys studied got fractured. Hence, the fracture behaviour has been investigated only for

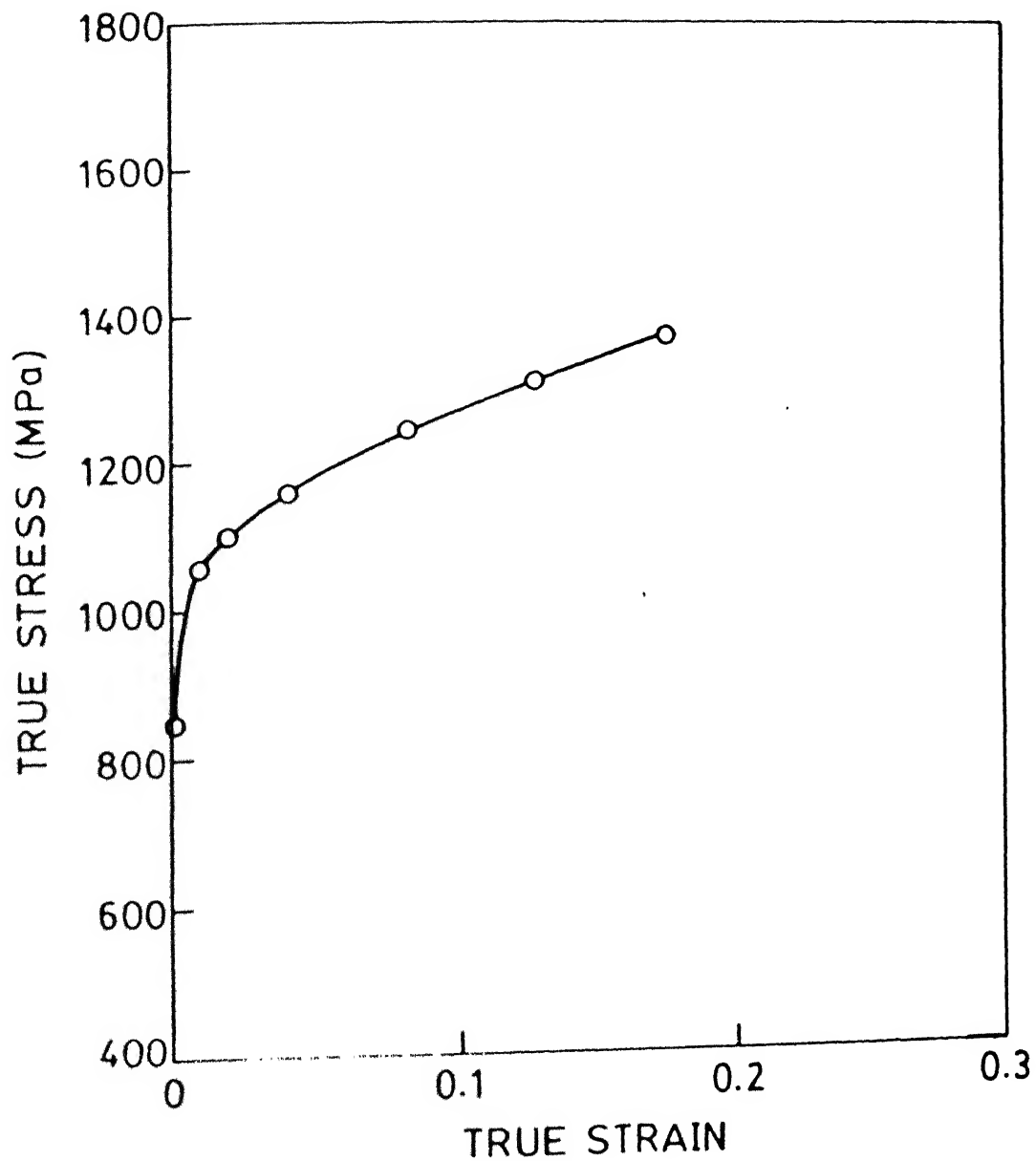


Fig. 6.8: True stress versus true strain plot of boron-free alloy  $\text{Ni}_{75.7}\text{Al}_{21.5}\text{Hf}_{2.8}$  at  $600^{\circ}\text{C}$ .

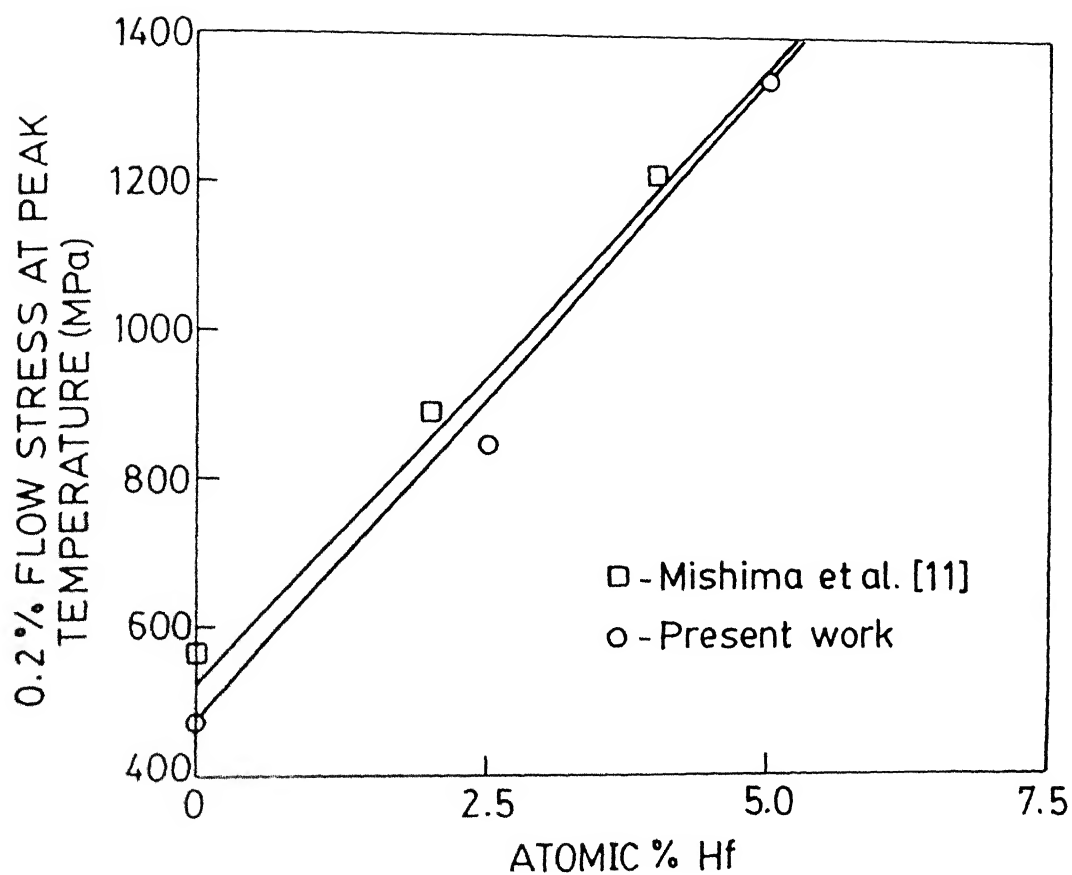


Fig. 6.9: Plot of 0.2% flow stress at peak temperature as a function of atomic percent hafnium.

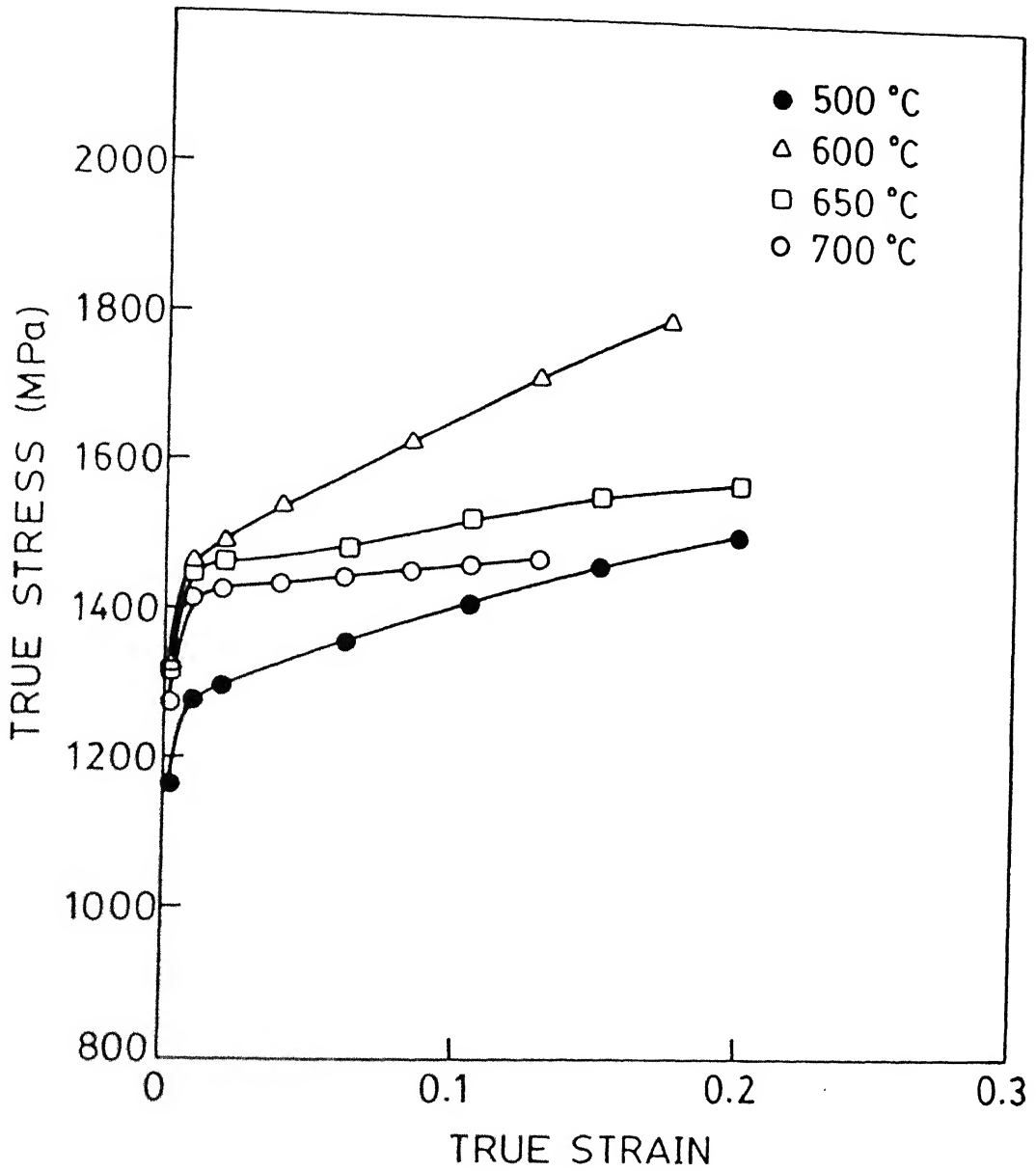
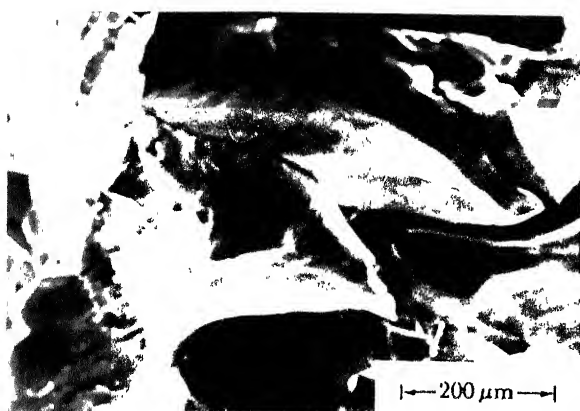


Fig. 6.10: True stress versus true strain plot of boron-doped alloy  $\text{Ni}_{75.2}\text{Al}_{19.7}\text{Hf}_{5.1}$  at various temperatures.

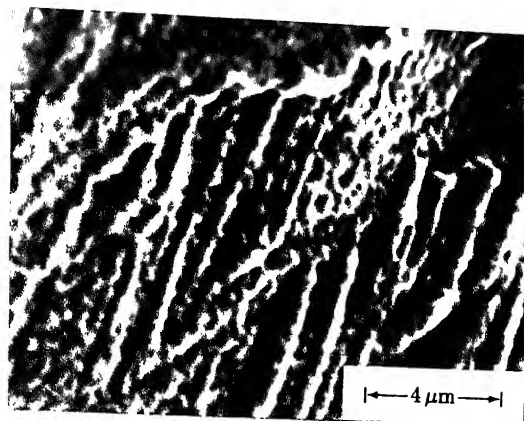
the alloys containing hafnium which fractured during the compression testing. Figure 6.11(a) shows the scanning electron microscope fractograph of the alloy having composition  $\text{Ni}_{75.5}\text{Al}_{19.5}\text{Hf}_5$ , compression tested at  $600^\circ\text{C}$ . The fractograph shows mainly intergranular fracture and also transgranular fracture at a few places. At a few small localized regions characteristic of ductile failure can also be seen (Figure 6.11(b)). Figure 6.12(a) shows the fractograph of the alloy  $\text{Ni}_{75.5}\text{Al}_{19.5}\text{Hf}_5$  compression tested at room temperature. Although the addition of hafnium increases only the high temperature ductility, the room temperature fractograph (Figure 6.12(a)) shows transgranular fracture at few places in addition to intergranular failure. Figure 6.12(b) shows an area comprising of two large grains in which one shows complete transgranular fracture while a profusion of deep striations are observed in the other.

A few typical fractographs from the fractured surfaces of the boron-doped alloy  $\text{Ni}_{75.2}\text{Al}_{19.7}\text{Hf}_{5.1}$  are presented in Figures 6.13 and 6.14. Figure 6.13(a) shows a fractograph of the alloy compression tested at  $700^\circ\text{C}$ . The fracture here is transgranular in nature. Figure 6.13(b) shows a still higher magnified image of the fractured surface indicating a ductile failure. In contrast, the room temperature compression tested samples showed a mixed mode of failure (Figure 6.14(a)) exhibiting the characteristics of both ductile and brittle fracture. At a number of places, a clear evidence of tearing representing transgranular fracture can be observed (Figure 6.14(b)).

An analysis of the features present on the fracture surfaces of the two alloys clearly indicate that the boron-doped alloy has perceptibly higher ductility as compared to the boron-free hafnium containing  $\gamma'$  alloy.

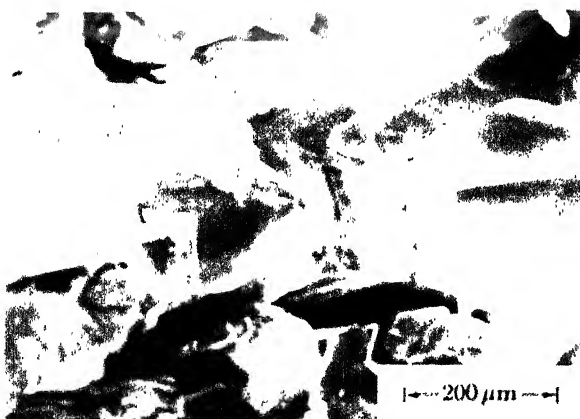


(a)

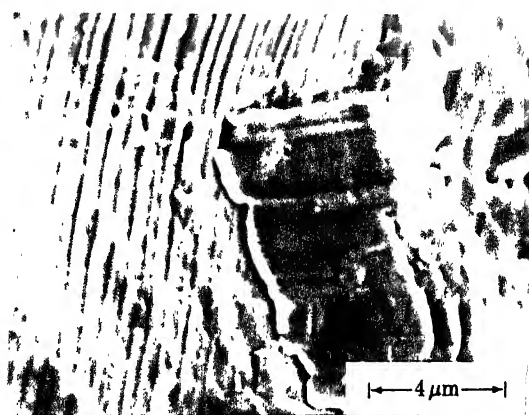


(b)

Fig. 6.11: SEM fractographs of the boron-free alloy  $\text{Ni}_{75.5}\text{Al}_{19.5}\text{Hf}_5$  compression tested at  $600^\circ\text{C}$  ((a) and (b)).

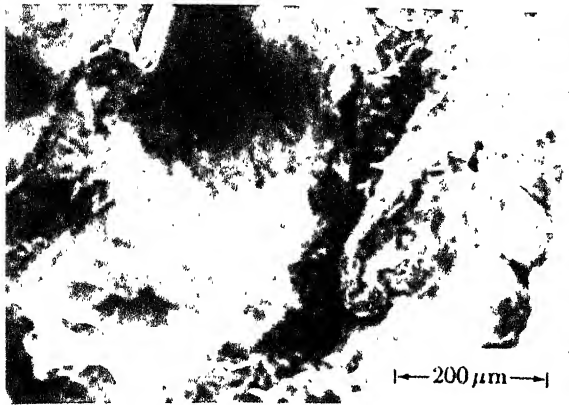


(a)

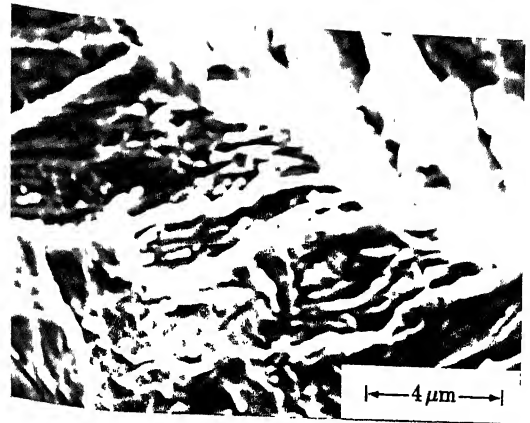


(b)

Fig. 6.12: SEM fractographs of the boron-free alloy  $\text{Ni}_{75.5}\text{Al}_{19.5}\text{Hf}_5$  compression tested at  $25^\circ\text{C}$  ((a) and (b)).

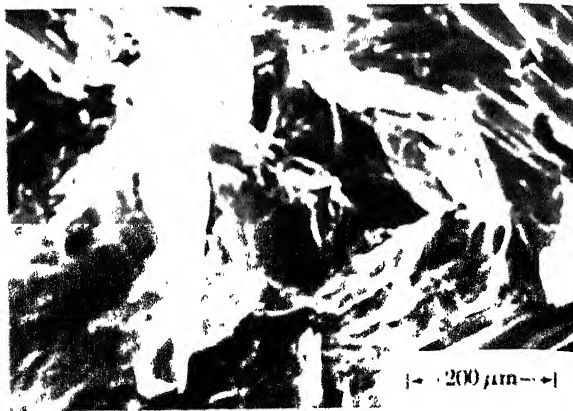


(a)

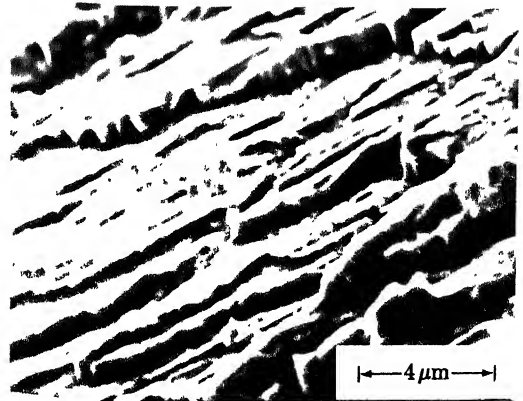


(b)

Fig. 6.13: SEM fractographs of the boron-doped alloy  $\text{Ni}_{75.2}\text{Al}_{19.7}\text{Hf}_{5.1}$  compression tested at  $700^\circ\text{C}$  ((a) and (b)).



(a)



(b)

Fig. 6.14: SEM fractographs of the boron-doped alloy  $\text{Ni}_{75.2}\text{Al}_{19.7}\text{Hf}_{5.1}$  compression tested at  $25^\circ\text{C}$  ((a) and (b)).

## 6.5. DISCUSSION

The results of the compression tests are summarized in Table 6.1. Although the stoichiometric  $\text{Ni}_3\text{Al}$  sample used in the present investigation showed a good agreement in the value of proof stress at high temperature with literature values, it has shown unusually high value of proof stress at room temperature compared with the literature value. In the case of boron-doped  $\text{Ni}_3\text{Al}$ , it shows an increase in the proof stress value at high temperature compared with boron free  $\text{Ni}_3\text{Al}$  material, but at room temperature both have almost identical values of 0.2% proof stress. Both the materials, boron-doped and boron-free  $\text{Ni}_3\text{Al}$  samples, have shown higher ductilities compared to reported values in the literature. Considering the fact that the change in the proof stress values per atom percent deviation from the stoichiometry is quite high, the discrepancy in the value of proof stress is quite understandable.

As far as the dependence of proof stress with temperature is concerned, the hafnium containing  $\text{Ni}_3\text{Al}$  samples in the present investigation, for example the alloy having the composition  $\text{Ni}_{75.5}\text{Al}_{19.5}\text{Hf}_5$ , has shown behaviour similar to that in the literature. The proof stress initially increases with temperature and then decreases after reaching the peak value. The values of proof stress at peak temperature for various amounts of hafnium have also shown good agreement with the literature. The value of the proof stress of the alloy having the composition  $\text{Ni}_{75.5}\text{Al}_{19.5}\text{Hf}_5$  at room temperature is slightly lower than that of the value reported in the literature. The effect of boron addition seems to increase the peak temperature. The boron-doped alloys have similar values of proof stress at room temperature compared with boron-free alloys. Despite a good agreement in the proof stress values for hafnium containing alloys, it can be safely concluded that direct comparison is not possible with literature because of the nature of the



Table 6.1  
Results of the compression tests

Boron-free alloys			Boron-doped alloys		
Alloy	Temperature (°C)	0.2% Flow stress (MPa)	Alloy	Temperature (°C)	0.2% flow stress (MPa)
Ni <sub>75</sub> Al <sub>25</sub>	25	153.0	Ni <sub>75</sub> Al <sub>25</sub>	25	161.0
	650	476.0		650	624.4
Ni <sub>75.7</sub> Al <sub>21.5</sub> Hf <sub>2.8</sub>	600	850.0	Ni <sub>75.2</sub> Al <sub>19.7</sub> Hf <sub>5.1</sub>	25	1025.0
Ni <sub>75.5</sub> Al <sub>19.5</sub> Hf <sub>5.0</sub>	25	1035.0		500	1171.0
	375	1111.1		600	1326.0
	400	1184.1		650	1321.0
	500	1339.0		700	1276.7
	600	1246.0			

dependence of proof stress on temperature as well as the exact composition of the alloy. One can only say that the addition of boron increases the ductility of the hafnium containing alloys.

The mechanical properties of the hafnium containing boron-free alloys are summarized in Figure 6.15. In the earlier chapters, it has been shown that  $\gamma'$  can take up to 7.4 at.% Hf at 1130°C. Extrapolation of data in Figure 6.15 shows that this alloy is about ten times stronger than the hafnium-free alloy at 500 K. However, the peak temperature is reduced as the hafnium content of the alloy is increased. For the alloy containing 5 at.% Hf the reduction is about 210 K. The ductility does not decrease appreciably with the addition of hafnium. It decreases from 8% to 6% as the hafnium content is increased from 0 to 5 at.%. After boron doping, the alloy can still be retained in a single phase state with up to 7.0 at.% Hf. As expected, the addition of boron improves the proof stress, ductility and the peak temperature. Consequently, boron-doped hafnium containing  $\gamma'$  appears to have good promise.

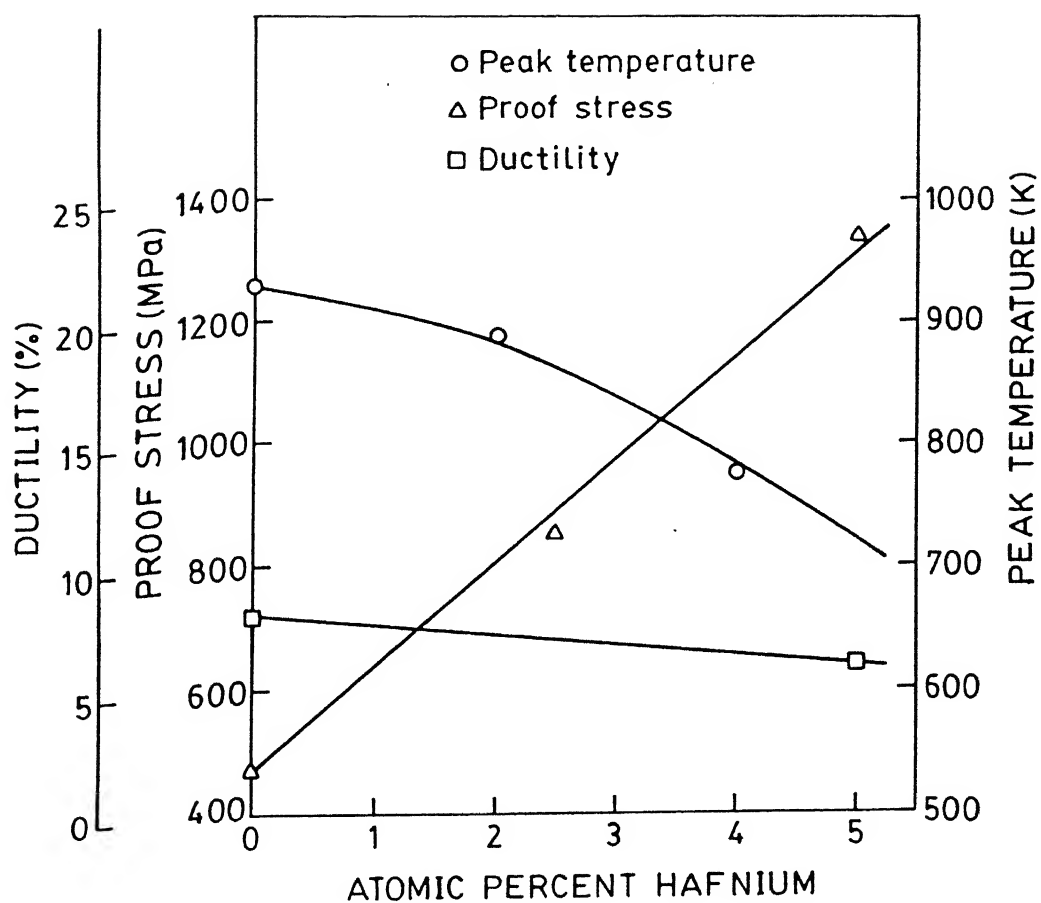


Fig. 6.15: Variation of the mechanical properties of boron-free  $\gamma'$  alloys with hafnium content

## CHAPTER VII

## SUMMARY AND CONCLUSIONS

1. In this investigation, binary  $\text{Ni}_3\text{Al}$  alloys containing 72.5, 75 and 77.5 at.% Ni, and binary  $\text{Ni}_3\text{Al}$  alloys of same compositions containing boron were prepared. Hafnium containing  $\text{Ni}_3\text{Al}$  alloys with 72.5, 77.5 and 80 at.% Ni and 2.5 and 5 at.% Hf together with hafnium containing  $\text{Ni}_3\text{Al}$  with 75 at.% Ni and 2.5, 5 and 7.5 at.% Hf were prepared. Hafnium containing boron-doped  $\text{Ni}_3\text{Al}$  alloys with 70, 72.5 and 77.5 at.% Ni and 2.5 and 5 at.% Hf, and hafnium containing boron-doped  $\text{Ni}_3\text{Al}$  alloys with 75 at.% Ni plus 2.5, 5 and 7.5 at.% Hf were made. In total twelve boron-free alloys and thirteen boron-doped alloys were prepared. The alloys were made using a non-consumable tungsten electrode arc melting furnace under high purity argon atmosphere. The arc melted alloys were vacuum sealed in fused quartz tubes and homogenized. The stoichiometric  $\text{Ni}_3\text{Al}$  alloys with and without boron were homogenized at  $1100^\circ\text{C}$  for 5 days and the rest of the alloys were homogenized at  $1130^\circ\text{C}$  for 20 days. The samples of the alloys were vacuum sealed and equilibrated at the required temperatures for predetermined lengths of time and then quenched in water. Boron-free and boron-doped stoichiometric  $\text{Ni}_3\text{Al}$  alloys were equilibrated at  $1200^\circ\text{C}$  for 5 days, at  $1130^\circ\text{C}$  for 7 days, at  $1000^\circ\text{C}$  for 10 days and at  $800^\circ\text{C}$  for 20 days. The off-stoichiometric  $\text{Ni}_3\text{Al}$  alloys and hafnium containing  $\gamma'$  alloys were equilibrated at  $1130^\circ\text{C}$  for 20 days.

Microstructural analysis of the homogenized and equilibrated specimens was carried out by both optical and scanning electron microscopy. Transmission electron microscopic studies of thin foils were also carried out. The lattice parameters of the various phases present in

the different alloys were accurately determined using X-ray diffraction tracings of powder samples of the alloys stress relieved at the equilibration temperatures. The composition of each phase present in the alloy was determined using EDAX facility attached to the scanning electron microscope. Compression tests on selected alloys were carried out using an MTS unit in the temperature range from room temperature to 700°C.

2. The ternary phase diagram around the  $\gamma'$  phase in boron-free Ni-Al-Hf system at 1130°C was determined and the phase boundary of  $\gamma'$  phase was established. The phase boundary of the other phases  $\gamma$ ,  $\gamma_1$ ,  $\beta$  and  $\eta_1$ , coexisting with  $\gamma'$ , were also determined. Three tie lines between  $\gamma'$  and  $\beta$  phases, three tie lines between  $\gamma'$  and  $\gamma$ , one tie line between  $\gamma'$  and  $\eta_1$ , a tie triangle between  $\gamma'$ ,  $\gamma$  and  $\gamma_1$  and a four phase equilibria between  $\gamma'$ ,  $\gamma$ ,  $\gamma_1$  and  $\eta_1$  were determined. The present results yielded adequate data to establish the phase boundaries of  $\gamma'$  phase and the coexisting phases in Ni-Al-Hf system at 1130°C. In the literature only two data points for  $\gamma'$  phase were available.

3. The ternary phase diagram around the  $\gamma'$  phase field in boron-doped Ni-Al-Hf system at 1130°C was determined and the phase boundary of  $\gamma'$  phase was established. The phase boundaries of other phases,  $\gamma$ ,  $\beta$  and  $\eta_1$ , coexisting with  $\gamma'$ , were also determined. Three tie lines between  $\gamma'$  and  $\beta$ , two tie lines between  $\gamma'$  and  $\gamma$  and one tie line between  $\gamma'$  and  $\eta_1$  were established. This information is completely new as no literature work regarding the phase equilibria of boron-doped system is available.

4. The phase boundaries in boron-doped alloys were found to shift appreciably with respect to those in the boron-free alloys. In the presence of boron, the solubility of nickel in  $\gamma'$  phase is reduced whereas that of aluminium in  $\gamma'$  phase is increased. This suggests that in the presence of boron, it is easier for aluminium and hafnium to occupy nickel sites while it is difficult for nickel to occupy the aluminium sublattice.

The solubility of aluminium in the  $\gamma$  phase does not change appreciably while that of nickel in the  $\beta$  phase is reduced by about 1.25 at.% in the boron-doped state. The solubilities of nickel and aluminium are decreased by 0.5 at.% in  $\eta_1$  phase in the presence of boron. However, the presence of boron in Ni-Al-Hf system does not introduce any new phase or any new phase equilibria.

5. Accurately determined lattice parameters of all the boron-free alloys, equilibrated at 1130°C, were used to develop a mathematical model expressing the lattice parameters in terms of the two variables; atom fraction of nickel,  $X_{Ni}$  and aluminium,  $X_{Al}$ . The lattice parameter,  $a$ , of the  $\gamma'$  phase was expressed in a polynomial equation truncated after the second order terms. The best fit was obtained using the Minitab, Data Analysis Software. The relation obtained is :

$$a = 4.839725 - 2.492X_{Ni} - 1.295X_{Al} + 1.54X_{Ni}^2 + 3.89X_{Al}^2 - 0.98X_{Ni}X_{Al}$$

Both experimental and calculated lattice parameters agreed well with each other with a standard deviation of 0.0023 Å.

6. Accurately measured lattice parameters of all the boron-doped alloys, equilibrated at 1130°C, were utilized to find the relation between lattice parameter and composition using the model developed for boron-free alloys. The relation obtained is :

$$a = 6.998725 - 7.52X_{Ni} - 3.785X_{Al} + 4.47X_{Ni}^2 + 4.38X_{Al}^2 + 2.00X_{Ni}X_{Al}$$

Both experimental and calculated lattice parameters agreed well with each other with a standard deviation of 0.0014 Å.

7. The lattice parameter of  $\gamma'$  phase of boron-free stoichiometric  $Ni_2Al$  tends to increase with increase in the quenching temperature up to

about  $1000^{\circ}\text{C}$  and then decreases slightly beyond  $1000^{\circ}\text{C}$ . This unusual dependence of the lattice parameter of  $\text{Ni}_3\text{Al}$  is interpreted in terms of the decrease in the degree of order with increase in the equilibration temperature up to  $1000^{\circ}\text{C}$  where the degree of order is expected to change rapidly with decrease in temperature and the thermal vacancy effect would be small. The slight decrease in the lattice parameter observed above  $1000^{\circ}\text{C}$  may be attributed to increase in the concentration of thermal vacancies as the effect of thermal vacancy at high temperature is appreciable and that of change in the degree of order would be negligible. The decrease in the lattice parameter beyond  $1000^{\circ}\text{C}$  is more prominent in boron-doped alloy than in boron-free alloy. In the presence of boron, the quenched-in thermal vacancy effect is slightly magnified because of higher concentration of quenched-in vacancies due to higher boron-vacancy binding energy.

8. Specific volumes were determined on the basis of extensively and accurately measured lattice parameters of the  $\gamma'$  phase of the alloys. In hafnium free binary  $\gamma'$  phase, the specific volume increases monotonically with increase in aluminium content. The partial volume of aluminium and nickel are almost identical in nickel saturated  $\gamma'$  phase. As the aluminium content increases, the partial volume of aluminium increases rapidly while that of nickel decreases slightly.

9. Alloying behaviour in ternary  $\gamma'$  phase was studied on the basis of partial volumes of the components, nickel, aluminium and hafnium, of the  $\gamma'$  phase. In boron-free hafnium containing alloys, the partial volume of aluminium changes significantly with changes in composition compared with the partial volume of nickel and hafnium. In alloys with 73, 75 and 77 at.% Ni, hafnium seems to have considerable covalent character and the covalent character of aluminium increases appreciably as the hafnium content is increased from 0 to 5 at.%.

10. In the boron-doped hafnium containing  $\gamma'$  alloys, the partial volumes of nickel, aluminium and hafnium behave in a similar manner as in boron-free alloys. However, the variation with composition suggest that in boron-doped  $\gamma'$  alloys containing 75 at.% Ni, the boron atoms occupy the edge centered octahedral sites of the  $L1_2$  structure. Hafnium atoms occupy the aluminium sites when hafnium content is low while it starts occupying nickel sites also when hafnium content is increased. However, in nickel-rich  $\gamma'$  alloy containing 77 at.% Ni, the boron atoms tend to occupy some of the body centered octahedral sites in addition to occupying the edge centered octahedral sites.

11. Twins were observed in boron-free stoichiometric and aluminium rich  $Ni_3Al$  alloys whereas they were not observed in the other alloys. The occurrence or absence of twins in these alloys was attributed to the effect of alloying elements on the stacking fault probability. Aluminium seems to increase the stacking fault probability while the presence of boron as well as hafnium seems to decrease it. Typical electron micrographs of slightly compressed boron-free stoichiometric  $Ni_3Al$  alloy consist of stacking fault like features and straight dislocations, two to three sets of which criss-cross one another at an angle of  $60^\circ$ . Substructures of boron-doped stoichiometric  $Ni_3Al$  alloy consist of short straight dislocation segments, dislocation dipoles and two sets of dislocation lines at an angles of  $60^\circ$ . Boron-free  $Ni_3Al$  alloy containing 5 at.% Hf showed long parallel dislocation lines and a criss-cross arrangement of two sets of dislocation lines at a few places. Boron-doped  $Ni_3Al$  containing 5 at.% Hf showed long dislocation lines. It was suggested that the faults observed in boron-free alloys are superlattice intrinsic stacking faults (SISF). The addition of boron seems to effectively suppress the formation of SISFs in  $Ni_3Al$ . The effect of the addition of hafnium to  $Ni_3Al$  has been found to be rather similar to that of boron in



the sense that in the single phase  $\text{Ni}_3\text{Al}$  containing 5 at.% Hf, no stacking fault could be observed.

12. The proof stress of stoichiometric  $\text{Ni}_3\text{Al}$  measured in this investigation is comparable to the values available in the literature. However, the proof stress of boron-doped alloy is found to be comparable with that of boron-free alloy at room temperature while the boron-doped alloy is 30% stronger at the proof stress peak temperature. The values of the proof stress at peak temperature for  $\gamma'$  alloys containing various amounts of hafnium have shown good agreement with those in the literature. The effect of boron addition increases the peak temperature by about  $150^\circ\text{C}$  for the alloy containing 5 at.% Hf. From the mechanical as well as microstructural studies it was concluded that the addition of boron to  $\gamma'$  was effective in suppressing the intergranular fracture considerably.

13. The  $\gamma'$  phase in its single phase state can retain in solution up to about 7.4 at.% Hf. This alloy is about ten times stronger (1980 MPa) than the hafnium-free alloy (200 MPa) at 500 K and possesses adequate ductility at high temperatures. On boron doping, the alloy can still be retained in a single phase state with up to 7.0 at.% Hf. Addition of boron also extends the usefulness of this alloy up to room temperature by improving its ductility and suppressing intergranular fracture. Therefore, boron containing  $\gamma'$  alloys with hafnium appears to have considerable promise.

## REFERENCES

1. R. W. Fawley, *'The Superalloys'*, eds. C. T. Sims and W. C. Hagel, John Wiley and Sons, New York, 1972, p. 3.
2. D. I. Roberts, S. N. Rosenwassen and J. F. Washton, Proc. Conf. on *'Alloys for the eighties'*, Ann Arbor, Michigan, June, 1980, Climax Molybdenum Co., 1981, p. 119.
3. J. B. Johnson, J. R. Nicholls, R. C. Hurst and P. Hancock, *Corrosion Science*, **18** (1978) 527.
4. K. J. Barton, V. L. Hill and R. Yurkewycz, Conf. Proc. on *'The properties and performance of materials in coal gasification environments'*, Pittsburgh, p. 8-10, September, 1980, ASM, Ohio, 1981, p. 65.
5. A. I. Asphansani and F. G. Hodge, Conf. Proc. on *'Alloys for the eighties'*, Ann Arbor, Michigan, June 1980, Climax Molybdenum Co., 1981, p. 329.
6. J. L. Bartons, Conf. Proc. on *'Optimization of processing, properties and service performance through microstructural control'*, Houston, 3-5 April, 1978, ASTM Philadelphia, 1979, p. 564.
7. S. Yamaguchi, H. Kobayashi, T. Matsumiya and S. Hayami, *Met. Technol.*, **6** (1979) 170.
8. S. W. K. Shaw, *Met. Progress*, **115**(3) (1979) 47.
9. P. Shankar, Conf. Proc. on *'Advances in Composite Materials'*, Vol. 2, Paris, France, August, 1980, p. 1439.
10. J. F. Kocis and W. M. Matlock, *Z. Werkstofftech*, **9**(4) (1978) 132.
11. Y. Mishima, S. Ochiai, M. Yodogawa and T. Suzuki, *Trans. Japan Inst. Met.*, **27** (1986) 41.
12. K. Aoki and O. Izumi, *J. Japan Inst. Met.*, **43** (1979) 1190.
13. C. T. Liu, C. L. White and J. A. Horton, *Acta Metall.*, **33** (1985) 213.

14. T. Takasugi, N. Masahashi and O. Izumi, *Scripta Metall.*, **20** (1986) 1317.
15. A. Chiba, S. Hanada and S. Watanabe, *Acta Metall. Mater.*, **39** (1991) 1799.
16. A. Chiba, S. Hanada and S. Watanabe, *Scripta Metall. Mater.*, **25** (1991) 303.
17. V. K. Sikka, *Mat. Res. Soc. Symp. Proc.*, **133** (1989) 487.
18. A. Fujita, T. Matsumoto, M. Nakamura and Y. Takeda, *Mat. Res. Soc. Symp. Proc.*, **133** (1989) 573.
19. J. H. Schneibel, G. F. Peterson and C. T. Liu, *J. Mater. Res.*, **1** (1986) 68.
20. R. S. Bellows, E. A. Schwarzkopf and T. K. Tien, *Metall. Trans. A*, **19A** (1988) 479.
21. W. O. Alexander and N. B. Vaughan, *J. Inst. Metals*, **61** (1937) 247.
22. M. Hansen and K. Anderko, '*Constitution of binary alloys*', (2nd edition), McGraw Hill, New York, 1958.
23. A. Taylor and R. W. Floyd, *J. Inst. Metals*, **81** (1952-53) 25.
24. T. B. Massalski, '*Binary alloy phase diagrams*', Vol. 1 and 2, ASM, Metals Park, Ohio, 1986.
25. K. Hilpert, D. Kobertz, V. Venugopal, M. Miller, H. Gerads, F. J. Bremer and H. Nickel, *Z. Naturforsch*, **42A** (1987) 1327.
26. F. J. Bremer, M. Beyss, E. Karthaus, A. Hellwig, T. Schober, J. M. Welter and H. Wenzl, *J. Cryst. Growth.*, **87** (1988) 185.
27. G. Ghosh, '*Ternary Alloys*', eds. G. Petzow and G. Effenberg, VCH Verlagsgesellschaft mbH, D-6940 Weinheim, Germany, Vol. 6, 1993, p.176.
28. P. Nash and A. Nash, *Bull. Alloy Phase Diagrams*, **4** (1983) 250.
29. L. Bsenko, *J. Less-Common Met.*, **63** (1979) 171.
30. V. N. Svechnikov, A. K. Schryn and G. P. Dimitriyeva, *Russ. Metall.*, **6** (1967) 95.

31. R. P. Elliott, 'Constitution of binary alloys', 1st supplement, McGraw Hill, New York, 1961.
32. L. Kaufman and H. Nesor, *Can. Metall. Q.*, **14** (1975) 221.
33. I. A. Tsygnova, M. A. Tylkina and E. M. Savitskiy, *Russ. Metall.*, **1** (1970) 107.
34. V. Ya. Markiv and V. V. Burnashova, *Russ. Metall.*, **6** (1969) 113.
35. P. Nash and D. R. F. West, *Metal Science*, **15** (1981) 347.
36. L. Kaufman and H. Nesor, 'Computer calculated phase diagrams for Ni-W-Al, Ni-Al-Hf, Ni-Cr-Hf and Co(Cr,Ni)-Ta-C Systems', NASA contract no. NAS 3-17304, National Aeronautics and Space Administration (NASA), Washington D.C 20546, 1974, p. 1.
37. L. Kaufman and H. Nesor, *Mater. Sci. & Engg.*, **23** (1976) 119.
38. K. S. Kumar, *Intl. Mat. Rev.*, **35** (1990) 293.
39. K. J. Lee and P. Nash, *J. Phase Equilibria*, **12** (1991) 94.
40. S. Ochiai, Y. Oya and T. Suzuki, *Bull. Prec. Mech. Elec.*, **52** (1983) 1.
41. V. Ya. Markiv and P. I. Kripyakevich, *Sov. Phys. Crystallogr.*, **11** (1967) 733.
42. V. Ya. Markiv, Y. Yu. Vorshilova, P. I. Kripyakwich and E. E. Cherka-shin, *Sov. Phys. Crystallogr.*, **9** (1965) 619.
43. V. Ya. Markiv and V. V. Burnashova, *Dupov. Akad. Nauk Ukr. RSR*, **A5** (1969) 463.
44. V. V. Pet'kov, V. Ya. Markiv and V. V. Gorsky, *Izv. Akad. Nauk. SSSR, . Met.*, **2** (1972) 188.
45. K. Aoki and O. Izumi, *Phys. Stat. Sol. (a)*, **32** (1975) 657.
46. K. Aoki and O. Izumi, *Phys. Stat. Sol. (a)*, **38** (1976) 587.
47. J. Schramm, *Z. Metallkde.*, **33** (1941) 347.
48. R. W. Guard and J. H. Westbrook, *Trans. Met. Soc. AIME*, **215** (1959) 871.
49. C. L. Corey and B. Lisowskey, *Trans Met. Soc. AIME*, **239** (1967) 239.

50. G. R. Stoeckinger and J. P. Newmann, *J Appl. Cryst.*, **3** (1970) 32.
51. D. P. Pope and J. L. Grasim, *J. Appl. Cryst.*, **10** (1977) 14.
52. N. Masahashi, T. Takasugi and O. Izumi, *Acta Metall.*, **36** (1988) 1815.
53. O. Noguchi, Y. Oya and T. Suzuki, *Metall. Trans. A*, **12A** (1981) 1647.
54. R. Ramesh, R. Vasudevan, B. Pathiraj and B. H. Kolster, *J. Mater. Sci.*, **27** (1992) 270.
55. A. J. Bradley and A. Taylor, *Proc. Roy. Soc.*, **A159** (1937) 56.
56. Young G. Kim, G. W. Yoon and N. S. Stoloff, *J. Mater. Sci. Letters*, **4** (1985) 1407.
57. W. B. Pearson, '*A Handbook of Lattice Spacings and Structure of Metals and alloys*', Pergamon Press, London, 1958.
58. Y. Mishima, S. Ochiai and T. Suzuki, *Acta Metall.*, **33** (1985) 1161.
59. S. C. Huang, A. I. Taub and K. M. Chang, *Acta Metall.*, **32** (1984) 1703.
60. I. Baker, B. Huang and E. M. Schulson, *Acta Metall.*, **36** (1988) 493.
61. R. W. Guard and J. H. Westbrook, *Trans. Met. Soc. AIME*, **215** (1959) 807.
62. R. D. Rawlings and A. E. Staton-Bevan, *J. Mater. Sci.*, **10** (1975) 505.
63. S. Ochiai, Y. Oya and T. Suzuki, *Acta Metall.*, **32** (1984) 289.
64. N. S. Stoloff, *Intl. Mat. Rev.*, **34** (1989) 153.
65. T. Takasugi, O. Izumi and N. Masahashi, *Acta Metall.*, **33** (1985) 1259.
66. M. K. Miller and J. A. Horton, *Mat. Res. Soc. Symp. Proc.*, **81** (1987) 117.
67. M. K. Miller and J. A. Horton, *Scripta Metall.*, **20** (1986) 1125.
68. J. Bentley, in '*Proc. of the 44th Annual Meeting of the Electron Microscopy Society of America*', Albuquerque, New Mexico, August, 1986; ed. G. W. Bailey, San Fransisco Press, San Fransisco, 1986, p. 704.
69. S. S. Brenner, D. D. Sieloff and M. G. Burke, *J. phys. (Orsay)*, Colloque suppl., **47 C2** (1986) 215.

86. M. P. Arbuzov, E. T. Kachkovskaya and B. V. Khayenko, *Fiz. Met. Matallov.*, **21** (1966) 854.
87. G. P. Sabol and R. Stickler, *Phys. Stat. Sol. (a)* **35** (1969) 11.
88. J. R. Nicholls, Ph.D Thesis, London University, 1974.
89. J. R. Nicholls and R. D. Rawlings, *Acta Metall.*, **25** (1977) 187.
90. Y. P. Wu, N. C. Tso, J. M. Sanchez and J. K. Tien, *Acta Metall.*, **37** (1989) 2835.
91. R. P. Messmer and C. L. Briant, *Acta Metall.*, **30** (1982) 457.
92. G. S. Painter and F. W. Averill, *Phys. Rev. Lett.*, **58** (1987) 234.
93. M. E. Eberhart and D. D. Vvedensky, *Phys. Rev. Lett.*, **58** (1987) 61.
94. K. Masudo-Jindo, *J. Phys.*, Colloque, **49** C5 (1988) 557.
95. S. P. Chen, A. F. Voter, R. C. Albers, A. M. Boring and P. J. Hay, *Scripta Metall.*, **23** (1989) 217.
96. T. K. Chaki, *Phil. Mag. Lett.*, **61** (1990) 5.
97. A. I. Taub, S. C. Huang and K. M. Chang, *Metall. Trans. A*, **15A** (1984) 399.
98. C. L. White, R. A. Padgett, C. T. Liu and S. M. Yalisove, *Scripta Metall.*, **18** (1984) 1417.
99. M. K. Miller and J. A. Horton, *J. Phys.*, Colloque, **47** C7 (1986) 263.
100. J. A. Horton and M. K. Miller, *Mat. Res. Soc. Symp. Proc.*, **81** (1987) 105.
101. D. D. Sieloff, S. S. Brenner and M. G. Burke, *Mat. Res. Soc. Symp. Proc.*, **81** (1987) 87.
102. A. Choudhury, C. L. White and C. R. Brooks, *Acta Metall. Mater.*, **40** (1992) 57.
103. A. Choudhury, C. L. White and C. R. Brooks, *Scripta Metall.*, **20** (1986) 1061.
104. M. Takeyama and C. T. Liu, *Acta Metall.*, **36** (1988) 1241.
105. L. J. Heutter and H. H. Stadelmaier, *Acta Metall.*, **6** (1958) 367.

106. K. H. Han and W. K. Choo, *Scripta Metall.*, **17** (1983) 281.
107. S. C. Huang, C. L. Briant, K. M. Chang, A. I. Taub and E. L. Hall, *J. Mater. Res.*, **1** (1986) 60.
108. C. L. Briant and S. C. Huang, *Metall. Trans. A*, **17A** (1986) 2084.
109. N. Masahashi, T. Takasugi and O. Izumi, *Acta Metall.*, **36** (1988) 1823.
110. T. K. Chaki, *Mat. Res. Soc. Symp. Proc.*, **213** (1991) 769.
111. G. F. Hancock, *Phys. Stat. Sol. (a)*, **7** (1971) 535.
112. M. B. Bronfin, G. S. Bulatov and I. A. Drugova, *Fiz. Met. Metalloved*, **40** (1975) 363.
113. K. Hoshino, S. J. Rothman and R. S. Averback, *Acta Metall.*, **36** (1988) 1271.
114. A. Dasgupta, L. C. Smedskjaer, D. G. Legnini and R. W. Siegel, *Mater. Lett.*, **3** (1985) 457.
115. Jian Sun and Dongliang Lin (T. L. Lin), *Acta Metall. Mater.*, **42** (1994) 195.
116. T. C. Chou and Y. T. Chou, *Mat. Res. Soc. Symp. Proc.*, **39** (1985) 461.
117. J. H. Schneibel and W. D. Porter, *J. Mater. Res.*, **3** (1988) 403.
118. Y. Minamino, S. B. Jung, T. Yamane and K. Hirao, *Metall. Trans. A*, **23A** (1992) 2783.
119. P. A. Flinn, *Trans. AIME*, **218** (1960) 145.
120. C. T. Liu, Proc. of the first Int. Symp. on 'Structural Intermetallics', September 26-30, 1993, p. 365.
121. D. P. Pope and S. S. Ezz, *Intl. Met. Rev.*, **29** (1984) 136.
122. Y. Mishima, S. Ochiai, M. Yodogawa and T. Suzuki, *Trans. Japan Inst. Met.*, **27** (1986) 32.
123. F. E. Heredia and D. P. Pope, *Acta Metall. Mater.*, **39** (1991) 2027.
124. P. M. Hazzledine and Y. Q. Sun, *Mat. Res. Soc. Symp. Proc.*, **213** (1991) 209.

125. A. E. Staton-Bevan and R. W. Rawlings, *Phys. Stat. Sol. (a)*, **29** (1975) 613.
126. Y. Q. Sun, D. Phil. Thesis, Oxford University, 1990.
127. Y. Q. Sun, P. M. Hazzledine and M. A. Crimp, *Mat. Res. Soc. Symp. Proc.*, **213** (1991) 311.
128. M. J. Mills, N. Baluc and H. P. Karnthaler, *Met. Res. Soc. Symp. Proc.*, **133** (1989) 203.
129. P. H. Thornton, R. G. Davies and T. L. Johnston, *Metall. Trans. A*, **1A** (1970) 207.
130. R. G. Davies and N.S. Stoloff, *Trans. Met. Soc. AIME*, **233** (1965) 714.
131. M. H. Yoo and C. T. Liu, *J. Mater. Res.*, **3** (1988) 845.
132. W. E. Dowling, Jr. and R. Gibala, *Mat. Res. Soc. Symp. Proc.*, **133** (1989) 209.
133. R. A. Mulford and D. P. Pope, *Acta Metall.*, **21** (1973) 1375.
134. S. Takeuchi and E. Kuramoto, *Acta Metall.*, **21** (1973) 415.
135. C. Lall, S. Chin and D. P. Pope, *Metall. Trans. A*, **10A** (1979) 1323.
136. K. J. Hemker and W. D. Nix, *Mat. Res. Soc. Symp. Proc.*, **133** (1989) 481.
137. P. M. Hazzledine and J. H. Schneibel, *Scripta Metall.*, **23** (1989) 1887.
138. B. H. Kear and H. G. F. Wilsdorf, *Trans. Met. Soc. AIME*, **224** (1962) 382.
139. B. H. Kear, *Acta Metall.*, **12** (1964) 555.
140. V. Paider, D. P. Pope and V. Vitek, *Acta Metall.*, **32** (1984) 435.
141. M. H. Yoo, *Scripta Metall.*, **20** (1986) 915.
142. M. H. Yoo, *Mat. Res. Soc. Symp. Proc.*, **81** (1987) 207.
143. M. H. Yoo, J. A. Horton and C. T. Liu, *Acta Metall.*, **36** (1988) 2935.
144. M. J. Mills and D. C. Chrzan, *Acta Metall. Mater.*, **40** (1992) 3051.



145. F. E. Heredia and D. P. Pope, *Mat. Res. Soc. Symp. Proc.*, **81** (1987) 213.
146. S. Miura, S. Ochiai, Y. Oya, Y. Mishima and T. Suzuki, *Mat. Res. Soc. Symp. Proc.*, **133** (1989) 341.
147. J. Bonneville and J. L. Martin, *Mat. Res. Soc. Symp. Proc.*, **213** (1991) 629.
148. Y. Q. Sun and P. M. Hazzledine, *Phil. Mag.*, **A58** (1988) 603.
149. A. Korner, *Phil. Mag. Lett.*, **58** (1988) 507.
150. P. Veyssi re, *Mat. Res. Soc. Symp. Proc.*, **133** (1989) 175.
151. P. B. Hirsch, *Scripta Metall. Mater.*, **25** (1991) 1725.
152. P. B. Hirsch, *Phil. Mag.*, **A65** (1992) 569.
153. M. Khantha, J. Cserti and V. Vitek, *Scripta Metall. Mater.*, **27** (1992) 481.
154. M. Khantha, J. Cserti and V. Vitek, *Scripta Metall. Mater.*, **27** (1992) 487.
155. A. de Bussac, G. Webb and S. D. Antolovich, *Mat. Res. Soc. Symp. Proc.*, **213** (1991) 235.
156. E. M. Schulson, T. P. Weihs, D. V. Viens and I. Baker, *Acta Metall.*, **33** (1985) 1587.
157. P. S. Khadkikar, K. Vedula and B. S. Shabel, *Metall. Trans. A*, **18A** (1987) 425.
158. E. M. Schulson, I. Baker and H. J. Frost, *Mat. Res. Soc. Symp. Proc.*, **81** (1987) 195.
159. S. Hanada, S. Watanabe and O. Izumi, *J. Mater. Sci.*, **21** (1986) 203.
160. Y. Oya, Y. Mishima, K. Yamada and T. Suzuki, *J Iron Steel Inst. Japan*, **70** (1984) 80.
161. T. P. Weihs, V. Zinoviev, D. V. Viens and E. M. Schulson, *Acta Metall.*, **35** (1987) 1109.

162. M. S. Kim, S. Hanada, S. Watanabe and O. Izumi, *Trans. Japan Inst. Met.*, **29** (1988) 274.
163. J. C. M. Li, *Trans. AIME*, **227** (1963) 239.
164. H. Conrad, *Acta Metall.*, **11** (1963) 75.
165. J. A. Lopez and G. F. Hancock, *Phys. Stat. Sol. (a)*, **2** (1970) 469.
166. T. Suzuki, Y. Oya and D. M. Wee, *Acta Metall.*, **28** (1980) 301.
167. D. M. Wee, O. Noguchi, Y. Oya and T. Suzuki, *Trans. Japan Inst. Met.*, **21** (1980) 237.
168. S. J. Liang and D. P. Pope, *Acta Metall.*, **25** (1977) 485.
169. D. M. Wee and T. Suzuki, *Trans. Japan Inst. Met.*, **20** (1979) 634.
170. Y. Mishima, Y. Oya and T. Suzuki, *Mat. Res. Soc. Symp. Proc.*, **39** (1985) 263.
171. Yun Zhang and Dongliang Lin (T. L. Lin), *Mat. Res. Soc. Symp. Proc.*, **213** (1991) 515.
172. T. Suzuki, Y. Oya and S. Ochiai, *Metall. Trans. A*, **15A** (1984) 173.
173. Y. Kuriki, S. Ochiai, M. Yodogaya and T. Suzuki, *Trans. Japan Inst. Met.*, **26** (1985) 213.
174. Y. Mishima, S. Ochiai, N. Hamao, M. Yodogawa and T. Suzuki, *Trans. Japan Inst. Met.*, **27** (1986) 648.
175. T. Takasugi and O. Izumi, *Acta Metall.*, **33** (1985) 1247.
176. T. Ogura, S. Hanada, T. Masumoto and O. Izumi, *Metall. Trans. A*, **16A** (1985) 441.
177. T. Takasugi, E. P. George, D. P. Pope and O. Izumi, *Scripta Metall.*, **19** (1985) 551.
178. O. Izumi and T. Takasugi, *J. Mater. Res.*, **3** (1988) 426.
179. C. T. Liu, *Mat. Res. Soc. Symp. Proc.*, **122** (1988) 429.
180. A. I. Taub, C. L. Briant, S. C. Huang, K. M. Chang and M. R. Jackson, *Scripta Metall.*, **20** (1986) 129.

181. A. I. Taub and C. L. Briant, *Mat. Res. Soc. Symp. Proc.*, **81** (1987) 343.
182. T. Takasugi, N. Masahashi and O. Izumi, *Acta Metall.*, **35** (1987), 381.
183. T. Takasugi and O. Izumi, *Scripta Metall. Mater.*, **25** (1991) 1243.
184. O. Izumi and T. Takasugi, *Mat. Res. Soc. Symp. Proc.*, **81** (1987) 173.
185. T. Takasugi and O. Izumi, *Materials Forum*, **12** (1988) 8.
186. S. P. Chen, A. F. Voter and D. J. Srolovitz, *Scripta Metall.*, **20** (1986) 1389.
187. S. P. Chen, A. F. Voter and D. J. Srolovitz, *Mat. Res. Soc. Symp. Proc.*, **81** (1987) 45.
188. S. P. Chen, A. F. Voter and D. J. Srolovitz, *J. Mater. Res.*, **4** (1989) 62.
189. S. P. Chen, A. F. Voter, R. C. Albers, A. M. Boring and P. J. Hay, *J. Mater. Res.*, **5** (1990) 955.
190. S. M. Foiles, *Mat. Res. Soc. Symp. Proc.*, **81** (1987) 51.
191. J. E. Hack, D. J. Srolovitz and S. P. Chen, *Scripta Metall.*, **20** (1986) 1699.
192. J. E. Hack, S. P. Chen and D. J. Srolovitz, *Acta Metall.*, **37** (1989) 1957.
193. J. J. Kruisman, V. Vitek and J. Th. M. De Hosson, *Acta Metall.*, **36** (1988) 2729.
194. G. J. Ackland and V. Vitek, *Mat. Res. Soc. Symp. Proc.*, **133** (1989) 105.
195. A. H. King and M. H. Yoo, *Scripta Metall.*, **21** (1987) 1115.
196. A. H. King, H. J. Frost and M. H. Yoo, *Scripta Metall. Mater.*, **25** (1991) 1249.
197. K. Aoki, *Mater. Trans. Japan Inst. Met.*, **31** (1990) 443.
198. F. E. Heredia and D. P. Pope, *Mat. Res. Soc. Symp. Proc.*, **133** (1989) 287.

199. F. E. Heredia and D. P. Pope, *Acta Metall. Mater.*, **39** (1991) 2017.
200. Guo. Jiangting, S. Chao, L. Hui, Z. Zhiya, T. Yajun and H. Zhuangqi, *Mat. Res. Soc. Symp. Proc.*, **213** (1991) 655.
201. C. L. White, C. T. Liu and R. A. Padgett.Jr., *Acta Metall.*, **36** (1988) 2229.
202. J. R. Rice, in 'Effects of hydrogen on the behaviour of materials', eds. A. W. Thompson and I. M. Bernstein, AIME, New York, 1976, p.455.
203. C. J. McMahon. Jr. and V. Vitek, *Acta Metall.*, **27** (1979) 507.
204. M. L. Jokl, V. Vitek and C. J. McMahon. Jr., *Acta Metall.*, **28** (1980) 1479.
205. H. Zhang, A. H. King and R. Thompson, *J. Mater. Res.*, **6** (1991) 314.
206. E. P. George, C. L. White and J. A. Horton, *Scripta Metall. Mater.*, **25** (1991) 1259.
207. P. S. Khadkikar, J. J. Lewandowski and K. Vedula, *Metall. Trans. A*, **20A** (1989) 1247.
208. I. Baker, E. M. Schulson and J. A. Horton, *Acta Metall.*, **35** (1987) 1533.
209. E. M. Schulson, T. P. Weihs, I. Baker, H. J. Frost and J. A. Horton, *Acta Metall.*, **34** (1986) 1395.
210. A. H. King and M. H. Yoo, *Mat. Res. Soc. Symp. Proc.*, **81** (1987) 99.
211. I. Baker and E. M. Schulson, *Scripta Metall.*, **23** (1989) 1883.
212. I. Baker, E. M. Schulson, J. R. Michael and R. A. Padgett, *J Phys.*, Colloque, **51 C1** (1990) 77.
213. I. Baker, E. M. Schulson, J. R. Michael and S. J. Pennycook, *Phil. Mag.*, **B62** (1990) 659.
214. E. M. Schulson and I. Baker, *Scripta Metall. Mater.*, **25** (1991) 1253.
215. R. A. D. Meckenzie and S. L. Sass, *Scripta Metall.*, **22** (1988) 1807.
216. H. Kung, D. R. Masmussen and S. L. Sass, *Scripta Metall. Mater.*, **25** (1991) 1277.

217. J. Zhu, Z. Y. Cheng and D. X. Zou, *Scripta Metall. Mater.*, **24** (1990) 439.
218. I. Baker, E. M. Schulson and J. R. Michael, *Phil. Mag.*, **B57** (1988) 379.
219. D. D. Sieloff, S. S. Brenner and Hua Ming-Jian, *Mat. Res. Soc. Symp. Proc.*, **133** (1989) 155.
220. M. J. Mills, S. H. Goods, S. M. Foiles and J. R. Whetstone, *Scripta Metall. Mater.*, **25** (1991) 1283.
221. V. Vitek and S. P. Chen, *Scripta Metall. Mater.*, **25** (1991) 1237.
222. I. Baker and E. M. Schulson, *Scripta Metall.*, **23** (1989) 345.
223. P. S. Khadkikar, J. D. Rigney, J. J. Lewandowski and K. Vedula, *Mat. Res. Soc. Symp. Proc.*, **133** (1989) 523.
224. G. M. Bond, I. M. Robertson and H. R. Birnbaum, *J. Mater. Res.*, **2** (1987) 436.
225. J. A. Horton and C. T. Liu, *Scripta Metall. Mater.*, **24** (1990) 1251.
226. J. A. Horton, C. T. Liu and S. J. Pennycook, *Mat. Res. Soc. Symp. Proc.*, **213** (1991) 417.
227. M. J. Mills, *Scripta Metall.*, **23** (1989) 2061.
228. G. Sasaki, D. Shindo, K. Hiraga, M. Hirabayashi and T. Takasugi, *Acta Metall.*, **38** (1990) 1417.
229. S. S. Brenner and H. Ming-Jian, *Scripta Metall. Mater.*, **24** (1990) 671.
230. J. A. Horton and M. K. Miller, *Acta Metall.*, **35** (1987) 133.
231. E. P. George, C. T. Liu and R. A. Padgett, *Scripta Metall.*, **23** (1989) 979.
232. S. S. Brenner and Hua Ming-Jian, *Scripta Metall. Mater.*, **25** (1991) 1271.
233. J. A. Horton, C. T. Liu and M. L. Santella, *Metall. Trans. A*, **18A** (1987) 1265.

234. D. M. Dimiduk, V. L. Weddington and H. A. Lipsitt, *Mat. Res. Soc. Symp. Proc.*, **81** (1987) 221.
235. C. T. Liu, *Mat. Res. Soc. Symp. Proc.*, **81** (1987) 355.
236. C. T. Liu and V. K. Sikka, *J. Met.*, **38**(5) (1986) 19.
237. A. Chiba, S. Hanada and S. Watanabe, *Mater. Trans. Japan Inst. Met.*, **31** (1990) 824.
238. A. I. Taub and C. L. Briant, *Acta Metall.*, **35** (1987) 1597.
239. A. K. Jena and M. C. Chaturvedi, *J. Mater. Sci.*, **19** (1984) 3121.
240. H. J. Frost, *Acta Metall.*, **36** (1988) 2199.
241. R. W. Cahn, P. A. Siemers, J. E. Geiger and P. Bardhan, *Acta Metall.*, **35** (1987) 2737.
242. R. W. Cahn, P. A. Siemers and E. L. Hall, *Acta Metall.*, **35** (1987) 2753.
243. J. A. Horton, M. K. Miller, C. T. Liu, E. P. George and J. Bentley, *Mat. Res. Soc. Symp. Proc.*, **133** (1989) 89.
244. T. Hirano, *Acta Metall. Mater.*, **38** (1990) 2667.
245. T. Hirano, S. S. Chung, Y. Mishima and T. Suzuki, *Mat. Res. Soc. Symp. Proc.*, **213** (1991) 635.
246. C. T. Liu, C. L. White and E. H. Lee, *Scripta Metall.*, **19** (1985) 1247.
247. C. T. Liu and C. L. White, *Acta Metall.*, **35** (1987) 643.
248. C. A. Hipsley and J. H. De Van, *Acta Metall.*, **37** (1989) 1485.
249. I. Baker, D. V. Viens and E. M. Schulson, *Scripta Metall.*, **18** (1984) 237.
250. C. T. Liu and B. F. Oliver, *J. Mater. Res.*, **4** (1989) 294.
251. J. A. Horton, J. V. Cathcart and C. T. Liu, *Oxid. Metals*, **29** (1988) 347.

252. Y. Umakoshi, in '*Plastic deformation and fracture of materials*', eds. R. W. Cahn, P. Haasen and E. J. Kramer, Vol. 6, VCH publishers Inc., NY, 1993, p. 251.
253. M. J. Marcinkowski, N. Brown and R. M. Fisher, *Acta Metall.*, **9** (1961) 129.
254. B. H. Kear, A. F. Giamei, J. M. Silcock and R. K. Ham, *Scripta Metall.*, **2** (1968) 287.
255. M. Yamaguchi, V. Vitek and D. P. Pope, *Phil. Mag.*, **A43** (1981) 1027.
256. J. Douin, P. Veyssière and P. Beauchamp, *Phil. Mag.*, **A54** (1986) 375.
257. P. Veyssière, D. L. Guan and J. Rabier, *Phil. Mag.*, **A49** (1984) 45.
258. R. J. Taunt and B. Ralph, *Phil. Mag.*, **30** (1974) 1379.
259. P. Veyssière, J. Douin and P. Beauchamp, *Phil. Mag.*, **A51** (1985) 469.
260. I. Baker and E. M. Schulson, *Phys. Stat. Sol. (a)*, **89** (1985) 163.
261. M. A. Crimp and P. M. Hazzledine, *Mat. Res. Soc. Symp. Proc.*, **133** (1989) 131.
262. P. Veyssière, J. A. Horton, M. H. Yoo and C. T. Liu, *Phil. Mag.*, **A57** (1988) 17.
263. C. Bontemps and P. Veyssière, *Phil. Mag. Lett.*, **61** (1990) 259.
264. A. Korner, *Phil. Mag. Lett.*, **60** (1989) 103.
265. D. Caillard, N. Clement, A. Couret, P. Lours and A. Coujou, *Phil. Mag. Lett.*, **58** (1988) 263.
266. H. P. Klug and L. E. Alexander, '*X-Ray Diffraction Procedures*', John Wiley and Sons, Inc., 1954, p. 464.
267. L. N. Guseva, *Doklady. Akad. Nauk, SSSR.*, **77** (1951) 415.
268. T. M. Wang, M. Shimotomai and M. Doyama, *J. Phys. F. : Metal Physics*, **14** (1984) 37.
269. M. Schoijet and L. A. Girifalco, *J. Phys. Chem. Solids*, **29** (1968) 911.
270. R. Feder, M. Mooney and A. S. Nowick, *Acta Metall.*, **6** (1958) 266.

271. F. C. Nix and D. MacNair, *Phys. Rev.*, **60** (1941) 320.
272. J. Emsley, '*The Elements*', ELBS with Oxford University Press, 1989.
273. A. R. Miedema, *J. Less-Common Met.*, **32** (1973) 117.
274. A. R. Miedema, R. Boom and F. R. de Boer, *J. Less-Common Met.*, **41** (1975) 283.
275. A. R. Miedema, *J. Less-Common Met.*, **46** (1976) 67.
276. P. C. J. Gallagher, *Metall. Trans. A*, **1A** (1970) 2429.
277. L. Deléhouzée and A. Deruyttere, *Acta Metall.*, **15** (1967) 727.
278. W. Yan, I. P. Jones and R. E. Smallman, *Scripta Metall.*, **21** (1987) 1511.
279. G. Gottstein, P. Nagpal and W. Kim, *Mat. Sci. & Engg.*, **A108** (1989) 375.
280. M. H. Yoo, *Acta Metall.*, **35** (1987) 1559.
281. G. Gottstein and U. F. Kocks, *Acta Metall.*, **31** (1983) 175.
282. G. A. Alers, J. R. Neighbours and H. Sato, *J. Phys. Chem. Solids*, **13** (1960) 40.
283. C. B. Carter and S. M. Holmes, *Phil. Mag.*, **35** (1977) 1161.
284. R. K. Ray (Unpublished results).



## APPENDIX I

PROGRAM FOR THE CALCULATION OF SPECIFIC AND PARTIAL VOLUMES  
 INPUT : ATOMIC FRACTIONS OF x(=N1), y(=A1)

```

                                program Partial_volume(input,output);
const
  a0  =  4.839725;
  a1  = -2.492;
  a2  = -1.295;
  a11 =  1.54;
  a22 =  3.89;
  a12 = -0.98;
var
  i,n : integer;
  x,y,pv : real;

function V(x,y,z : real):real;
var a : real;
begin
  a := (a0 + a1*x + a2*y);
  a := a + (a11*x*x + a22*y*y + a12*x*y);
  V := 0.1506 * a * a * a;
end;

function vbar(x,y:real):real;
var
  V1,Vp,kp,z:real;
  dx,dy,dz :real;
begin
  z := 1 - x - y;
  kp := z/y;

  V1 := V(x,y,z);

  dx := 0.0025;
  dy := -dx/(1+kp);
  dz := kp*dy;
  x := x + dx;
  y := y + dy;
  z := z + dz;

  Vp := V(x,y,z);
  writeln('Specific Volume, V : ',V1:8:5);
  vbar := V1 + (1 - x - dx)*(Vp - V1)/dx;
end;

begin
  write( 'Give no. of points: ');
  read(n);
  for i:= 1 to n do begin
    writeln('Give point ',i);
    write('  x: '); read(x);
    write('  y: '); read(y);
    writeln('X : ',x:5:3,' Y : ',y:5:3);
    pv := vbar(x,y);
    writeln('Partial Volume, Vbar : ',pv:8:5);
  end;
end.

```

A 21716

**A 121716**  
**Date Slip**

## Date Slip

This book is to be returned on the date last stamped.

This image shows a single sheet of white paper with horizontal blue or grey ruling lines. A solid vertical line runs down the center of the page, creating two equal-width columns. The lines are evenly spaced and extend across the entire width and height of the page. There is no handwriting or other markings on the paper.

MME - 1994 - D. NAG - PHD

